

UNIVERSITÉ DE GENÈVE
Département de Physique
Nucléaire et Corpusculaire

FACULTÉ DES SCIENCES
Prof. A. Blondel

**Constraining neutrino flux predictions with hadron
production data:
the NA61/SHINE measurements for the T2K experiment.**

THÈSE

présentée à la Faculté des Sciences de l'Université de Genève

pour obtenir le grade de Docteur ès sciences, mention physique

par

Nicolas Abgrall

de Saint-Julien-en-Genevois, France

Thèse N° 4351

GENÈVE

Atelier de reproduction ReproMail
2011





**UNIVERSITÉ
DE GENÈVE**

FACULTÉ DES SCIENCES

**Doctorat ès sciences
Mention physique**

Thèse de *Monsieur Nicolas ABGRALL*

intitulée :

**" Constraining Neutrino Flux Predictions with Hadron
Production Data :
The NA61/SHINE Measurements of the T2K Experiment "**

La Faculté des sciences, sur le préavis de Messieurs A. BLONDEL, professeur ordinaire et directeur de thèse (Département de physique nucléaire et corpusculaire), M. POHL, professeur ordinaire (Département de physique nucléaire et corpusculaire), A. MARCHIONNI, docteur (Institute for Particle Physics, Swiss Federal Institute of Technology Zurich, Switzerland), B. POPOV, docteur (Joint Institute for Nuclear Research, Dubna, Russia), autorise l'impression de la présente thèse, sans exprimer d'opinion sur les propositions qui y sont énoncées.

Genève, le 23 septembre 2011

Thèse - 4351 -


Le Doyen, Jean-Marc TRISCONÉ

N.B.- La thèse doit porter la déclaration précédente et remplir les conditions énumérées dans les "Informations relatives aux thèses de doctorat à l'Université de Genève".

Abstract

From hypothetical particles in the 30s, neutrinos have turned into the first hint for new physics beyond the Standard Model in the late 90s. The observation of a new phenomenon, referred to as *neutrino oscillations*, in which a neutrino of a given flavor transforms into a neutrino of another flavor after traveling over a sufficiently long distance, actually revealed properties of the leptonic sector of the Standard Model that were not described so far: neutrinos have mass, leptons mix, and consequently, there might be CP violation in the leptonic sector.

The T2K experiment at Tokai, Japan, will allow us to probe neutrino oscillations with an unprecedented precision on the oscillation parameters in the three-neutrino model. The experiment is designed to perform a precise measurement of the $\nu_\mu \rightarrow \nu_e$ oscillation driven by the atmospheric mass squared splitting $|\Delta m_{23}^2|$ and the so far unknown mixing angle θ_{13} . To achieve a sensitivity down to $\sin^2 2\theta_{13} = 0.006$ at 90% CL and a precision of $\delta(\Delta m_{23}^2) = 10^{-4} \text{ eV}^2$, the T2K experiment needs a high intensity neutrino beam and a precise prediction of neutrino fluxes. The first point is achieved by using a high intensity proton beam on target with a design beam power of 0.75 MW, the second point by tuning the original predictions of the T2K beam simulation with hadron production data measured by the NA61/SHINE collaboration at the CERN SPS. The latter performed measurements of $p + C$ interactions at 31 GeV/ c beam momentum on both a thin (4% λ_I) target and a full-size (1.9 λ_I) replica of the T2K production target. The current neutrino flux predictions in T2K are based on the usual approach, which consists in tuning the particle multiplicities of the simulated primary interactions with inclusive hadron production cross section measurements. The goal of this thesis is to develop a complementary approach in which the tuning of the flux predictions is done at the level of both primary and secondary interactions by using long target measurements. Such a tuning would actually constrain a larger fraction of the neutrino flux, with a potentially better control of systematic uncertainties.

The first chapter of this thesis is an overall introduction to neutrino physics and to the phenomenology of neutrino oscillations. The original beam simulation of the T2K experiment and corresponding flux predictions from different sources are presented in Chapter 2, together with modifications implemented in order to express the flux predictions in terms of hadron production measurements off thin and long targets. These studies stressed the importance of the long target measurements to constrain neutrino flux predictions. The first part of Chapter 3 is dedicated to the estimation of the statistics of the NA61/SHINE long target measurements based on the T2K physics requirements. The second part of the chapter presents the analysis of the NA61/SHINE 2007 long target data, which

provides a direct comparison of the total π^+ production simulated by the T2K hadron production model to the measured production over the full-size replica of the T2K target. In Chapter 4, a first method is proposed to use the NA61/SHINE long target data within the T2K beam simulation and re-weight the neutrino flux predictions accordingly. Finally, the recent results of the T2K ν_e appearance analysis are reported in Chapter 5, in particular, the usage of the NA61/SHINE thin target data for the neutrino flux predictions.

Acknowledgments

First I would like of course to thank my director Prof. Alain Blondel for giving me the opportunity to work on this subject and participate to the T2K neutrino oscillation experiment in Japan. Prof. Alain Blondel and I started our *cursus* at the University of Geneva at the same time, me as a simple student and he by teaching us our first year lecture of classical mechanics. We met again some years later. At that time, I joined the neutrino group that he led (and still does) with great enthusiasm, proposing a motivating field of research for my master thesis. Our collaboration continued over all these years and I would like to thank him for a very pleasant research framework, for giving me the opportunity to take responsibilities in our different collaboration activities, and for always reminding us that even in physics, simple ways can be found along a complicated journey. Among the Neutrino Group at the University of Geneva I must also thank Dr. Sandro Bravar. He strongly supported our commitment as a group to the NA61/SHINE collaboration and allowed me from the very beginning to join this effort in a friendly atmosphere. I owe him a large part of my hardware experience through the construction of the forward time-of-flight detector of NA61/SHINE.

At the very basis of my involvement in the Neutrino Group is a great person, former member of the group, Raphaël Schroeter, whom I would like to thank for the friendship and generosity that he gave me from the very beginning. I will never forget the long evenings he spent patiently teaching me all the computer basic skills I missed at that time ! Our friendship evolved along all these years, and I discovered a wonderful guy with a great sense of humor, a great taste for music (my best provider ever), an admiring compassion for others and a great sensitivity that I think we both share. So Raphaël, many thanks for being there, I hope our friendship will continue for many years more !

Continuing with the Neutrino Group I want of course to thank my office mates Melody, Fanny, Alexander, Sebastien and Alexis for the great atmosphere at the office and their help over different aspects of this thesis. In particular I want to thank Sebastien for all the time we spent together wrapping scintillators, working in the experimental area, traveling to great places, for all the morning coffees we shared, for all the parties, all the jokes and of course all our pen-and-paper beer breaks ! A very large part of this thesis could not have been done without such a great colleague, and I would certainly not have gone through all this without such a great friend.

Among many other colleagues and friends, I also want to thank Gauthier. I really appreciate his personality and his friendship was really important to me over the

last years.

Still at University of Geneva, I thank Tica, Peggy and Nathalie for their great support over all these years, they have made our lives much easier taking care of almost everything for us ! Many, many thanks to you !

There are many more colleagues I want to thank for their kindness and making research such a pleasant activity, but among all these people I am deeply indebted to Dr. Boris Popov for his tremendous help and sharing so much of his experience with me during the last 5 years. I cannot count anymore the hours we spent talking on Skype or the number of emails we exchanged over that period working on this thesis ! I have been constantly impressed by his broad knowledge, his intuition, his unconditional involvement for the community, his sense of sharing and his kindness. I was lucky enough to find him on my way and this has been for me a great journey. I will never thank him enough for all what he did and his support. I wish him and his kind family all the best for the future.

I must also thank Dr. Jacques Dumarchez for letting me use the office he shares with Boris at CERN. It was a great place to stay at calm over these long nights and weekends. I know I did not pay the rent yet Jacques, but I will bring enough Toblerone for a year in Paris next time !

Still among my colleagues from the LPNHE, I would like to thank Dr. Jean-Michel Levy for his precious comments, contributions and corrections to the manuscript. I am still very much impressed by his knowledge and his modesty. I met few people like Jean-Michel so far, whose deep understanding of what they are doing comes along with such great pedagogic capacities.

Il y a évidemment beaucoup d'amis que j'aimerais remercier, à tous ceux-là, merci beaucoup de m'avoir soutenu, merci pour tous les bons moments passés avec chacun de vous. J'ai la chance d'avoir beaucoup de monde autour de moi et d'avoir pu tisser des relations particulières avec chacune de ces personnes. Toutes ces relations me sont précieuses et m'ont fait avancer chacune à leur façon. Désolé de ne pas citer tout le monde, je suis sûr que vous vous reconnaitrez. Encore merci à tous.

J'aimerais remercier plus particulièrement Helena, Tariku, Sara. Pour ce que vous êtes, pour ce que vous m'apportez, pour tout ce que l'on partage, pour être vrais, pour accepter, pour comprendre. Mon refuge en Ethiopie. Tariku, *wendeme*, Helena, *yene fek'er*, *egzeryist'legn* !

Merci à ma famille, Maman, Papa, Hélène, mes grands-parents, pour être toujours là, pour votre support, pour croire en moi.

Merci à Guy, parce que tu auras toujours été fier pour nous deux, parce que du rocher à tes bras il n'y avait qu'un pas et que tu m'en vantais un exploit. L'exploit

de croire en moi...

Contents

1	Introduction to neutrino physics	1
1.1	Neutrinos in the Standard Model	1
1.2	Current picture of neutrino oscillations	10
1.2.1	The neutrino puzzles	10
1.2.2	Neutrino oscillations in vacuum and matter	15
1.3	Neutrino oscillations in the general three-flavor mixing framework .	29
1.4	Unresolved questions: where do we stand ?	37
2	Neutrino flux predictions for the T2K experiment	44
2.1	Experimental setup and physics goals	44
2.2	The T2K beamline simulation program	51
2.2.1	Simulation of the neutrino beam	51
2.2.2	Simulation of neutrino fluxes	54
2.2.3	Neutrino production history	59
2.3	Prediction of neutrino fluxes from different sources	63
2.3.1	Direct contribution and thin target measurements	68
2.3.2	Target contribution and long target measurements	69
2.3.3	Far-to-near ratio predictions	73
2.3.4	Model dependence of the neutrino flux predictions	83
3	The NA61/SHINE auxiliary hadron production measurements	90
3.1	The NA61 experimental setup	91
3.2	T2K requirements on the NA61 measurements	93
3.2.1	Measurement of the target contribution in NA61	93
3.2.2	Statistical estimations	95
3.3	The NA61 simulation chain	99
3.4	The NA61 reconstruction chain	108
3.4.1	Particle identification for the simulated data	110
3.5	Results from the thin target measurements	117
3.6	Measurements with the T2K replica target	117
3.6.1	Beam data	117
3.6.2	ToF and TPC data	125

3.7	The NA61 acceptance and analysis binning in $\{p, \theta, z\}$	132
3.8	Backward extrapolation to the surface of the target	138
3.9	Raw yields of positively charged pions on target	150
3.10	Efficiencies and Corrections	166
3.11	Re-weighting factors for the T2K beam simulation	168
3.12	Summary of the NA61 replica target data analysis	174
4	Re-weighting based on the NA61/SHINE replica target data	177
4.1	Target geometries	177
4.2	Re-weighting classes	179
4.3	Potential modifications of the T2K simulation	189
5	The first T2K results	193
5.1	Results from the ν_e appearance analysis	193
	Conclusion	200
	A Kinematics of an off-axis neutrino beam	204
	B Neutrino fluxes up to 10 GeV neutrino energy	210
	C $\{p, \theta\}$ phase space distributions	223
	D Raw yields of positively charged pions on target	232
	E Efficiencies and corrections	239
	F Re-weighting factors	241

List of Figures

1.1	Hadron production cross section around the Z resonance.	3
1.2	Total charged current $\nu_\mu(\bar{\nu}_\mu)$ -nucleon inclusive cross section.	4
1.3	The solar neutrino spectrum predicted by the BS05(OP) SSM.	11
1.4	The SSM predictions and total observed rates in solar experiments.	12
1.5	Zenith angle distribution of fully-contained events in SK.	13
1.6	Fluxes of ^8B solar neutrinos deduced from the SNO measurements.	15
1.7	Muon neutrino survival probability as a function of L/E (km/GeV).	20
1.8	$P(\nu_e \rightarrow \nu_\mu)$ as a function of L in vacuum and in matter.	22
1.9	Mass spectrum, fraction of ν_2 and fractional fluxes in the Sun.	24
1.10	Electron neutrino survival probability for the LMA solution.	25
1.11	The $\bar{\nu}_e$ survival probability measured by KamLAND.	26
1.12	Neutrino oscillation parameters from KamLAND and solar data.	26
1.13	Results of the L/E analysis of the SK-I atmospheric neutrino data.	27
1.14	MINOS allowed region for the $\nu_\mu \rightarrow \nu_\tau$ oscillation parameters.	28
1.15	Regions of oscillation parameters favored by various experiments.	30
1.16	Neutrino mass hierarchies.	33
1.17	ν_e survival probability in the three-neutrino model.	34
1.18	ν_μ survival probability in the three-neutrino model.	36
1.19	The MINOS allowed regions for $\sin^2 \theta_{23} \sin^2 2\theta_{13}$ as a function of δ_{CP}	38
2.1	Schematic of the T2K baseline	45
2.2	The T2K production target and focusing system.	46
2.3	Off-axis neutrino flux properties.	48
2.4	The layout of the T2K beamline geometry.	52
2.5	Production point of the neutrino parent particles in T2K.	63
2.6	Energy spectra for ν_μ , $\bar{\nu}_\mu$, ν_e and $\bar{\nu}_e$ at the ND280 near detector.	64
2.7	Composition of the ν_μ , $\bar{\nu}_\mu$, ν_e and $\bar{\nu}_e$ energy spectra at the ND280.	65
2.8	Composition of the ν_μ , $\bar{\nu}_\mu$, ν_e and $\bar{\nu}_e$ energy spectra at SK.	66
2.9	Parent direct contribution to the ν_μ flux in the far detector.	70
2.10	Parent direct contribution to the ν_e flux in the far detector.	71
2.11	Ratio of indirect to total contribution for the far detector.	72
2.12	Parent target contribution to the ν_μ flux in the far detector.	74

2.13	Parent target contribution to the ν_e flux in the far detector.	75
2.14	Ratio of non-target to total contribution for the far detector.	76
2.15	Far-to-near ratio for ν_μ , $\bar{\nu}_\mu$, ν_e and $\bar{\nu}_e$ fluxes (direct contribution). .	78
2.16	Far-to-near ratio for ν_μ , $\bar{\nu}_\mu$, ν_e and $\bar{\nu}_e$ fluxes (target contribution). .	79
2.17	$\{p, \theta\}$ distributions of secondary π^+	80
2.18	$\{p, \theta\}$ distributions of secondary K^+	81
2.19	$\{p, \theta\}$ distributions of protons and neutrons.	82
2.20	ν_μ and ν_e spectra predictions from different models.	84
2.21	Far-to-near ratio for ν_μ and ν_e species for different models.	85
2.22	Comparison of far-to-near ratio predictions from different models. .	86
2.23	Indirect and non-target contributions for different models.	87
3.1	The layout of the NA61/SHINE experiment at the CERN SPS. . .	92
3.2	The beam momentum distribution measured in the TPCs.	92
3.3	ν_μ flux from π^+ meson decays at near and far detectors.	94
3.4	Binning template over the relevant T2K phase space.	97
3.5	Recomputed neutrino fluxes for a single bin variation.	98
3.6	Recomputed neutrino fluxes for an overall 10 % variation.	99
3.7	Recomputed neutrino fluxes for 1000 overall 10 % variations.	100
3.8	Illustration of the cross section variation.	100
3.9	Recomputed neutrino fluxes for 1000 overall 10 % variations.	101
3.10	Recomputed neutrino fluxes for 1000 overall 5 % variations.	101
3.11	Recomputed neutrino fluxes for 1000 overall 5 % variations.	102
3.12	Simulated geometry of the NA61/SHINE detectors.	102
3.13	Divergence vs position of the beam in the x and y directions.	105
3.14	Simulated divergence, impact on target and radial distribution.	106
3.15	Cross sections calculated by the GFLUKA (Geant3.21) model.	107
3.16	Exit points on target for simulated tracks.	109
3.17	Parametrization of the width of the mass squared distributions.	112
3.18	Mass squared distribution for the real and simulated data.	113
3.19	Projections of the mass squared distribution.	114
3.20	Simulated energy loss as a function of the number of points.	115
3.21	Energy loss in the TPCs as a function of momentum.	115
3.22	Projections of the energy loss distribution.	116
3.23	Differential production cross section of π^- mesons.	118
3.24	Differential production cross section of π^+ mesons.	119
3.25	Time distribution of beam particles around the beam time.	120
3.26	Track multiplicity in the TPCs.	121
3.27	Residuals in BPD-2 for the x (left) and y (middle) directions.	122
3.28	Reconstructed beam position.	122
3.29	Reconstructed beam profile and radial distribution on target	123
3.30	Reconstructed beam profile and radial distribution after cut.	124

3.31	Example of reconstruction of a real data event.	126
3.32	Error on angle and momentum resolution of global rtracks.	127
3.33	Azimuthal coverage of NA61 and acceptance cut.	129
3.34	Azimuthal distribution for the real and simulated data.	129
3.35	Number of points, momentum, polar and azimuthal distributions. . .	131
3.36	$\{p, \theta\}$ coverage of the different topologies	133
3.37	$\{p, \theta\}$ coverage of tracks at the surface of the target	134
3.38	$\{p, \theta\}$ coverage of positive tracks at the surface of the target. . . .	134
3.39	Schematic representation of the NA61 acceptance calculation. . . .	135
3.40	The NA61 acceptance for the long target measurements.	136
3.41	Analysis binning of the replica target data in $\{p, \theta, z\}$	137
3.42	$\{p, \theta\}$ coverage of tracks at the surface of the target	137
3.43	The NA61 acceptance and analysis binning in $\{p, \theta, z\}$	138
3.44	Statistics per $\{p, \theta, z\}$ for the replica target data.	139
3.45	Acceptance of the NA61 apparatus over the analysis binning. . . .	140
3.46	Extrapolated position on target in the x-z and y-z projections. . . .	141
3.47	Extrapolated position on target in the x-y and z projections. . . .	142
3.48	Distribution of the error on the extrapolated transverse position. . .	143
3.49	Distribution of the point-of-closest-approach on target.	143
3.50	Extrapolation efficiency and purity for all global rtracks.	145
3.51	Distribution of the p.c.a. for all global rtracks.	147
3.52	Momentum, polar angle and longitudinal resolutions on target. . . .	148
3.53	Magnetic field in the target region.	150
3.54	Combined $\{dE/dx, ToF\}$ distributions.	151
3.55	Fitted distribution in the $\{dE/dx, ToF\}$ phase space.	155
3.56	Fitted simulated distribution in the $\{dE/dx, ToF\}$ phase space. . .	156
3.57	Raw π^+ yields extracted from the data.	158
3.58	Raw π^+ yields extracted from the FLUKA based simulation.	159
3.59	Combined $\{dE/dx, ToF\}$ distributions.	160
3.60	$\chi^2_{\lambda}/d.o.f.$ and p-value distributions for real and simulated data. . .	161
3.61	π^+ spectra over the first angular bin.	163
3.62	π^+ spectra over the second angular bin.	164
3.63	π^+ spectra over the third angular bin.	165
3.64	Time-of-flight efficiency.	167
3.65	NA61 and T2K beam profiles and divergence.	170
3.66	Re-weighting factors for the first angular bin.	171
3.67	Re-weighting factors for the second angular bin.	172
3.68	Re-weighting factors for the third angular bin.	173
4.1	Target geometries.	178
4.2	Tuned ν_μ flux at SK based on the NA61 thin target data.	180
4.3	Tuned ν_μ flux at SK based on the NA61/SHINE replica target data. .	182

4.4	Thin and replica target based tuning of the ν_μ flux at SK.	182
4.5	$\{p, \theta\}$ phase space of π^+ 's exiting the target.	183
4.6	Impact of uncovered phase space on the long target tuning.	183
4.7	Comparison of the thin target and long target tunings.	184
4.8	Re-weighted π^+ spectra over the first angular bin.	185
4.9	Re-weighted π^+ spectra over the first angular bin.	186
4.10	Re-weighted π^+ spectra over the first angular bin.	187
4.11	Current error envelopes for the ν_μ and ν_e fluxes at SK.	189
4.12	Neutrino fluxes at the far detector including decays at rest.	191
5.1	$\{p, \theta\}$ phase space of π^+ 's exiting the target.	194
5.2	Predicted neutrino fluxes at the far detector.	196
5.3	Measured momentum of ν_μ CC candidates in the near detector. . .	198
5.4	The T2K allowed regions for $\sin^2 2\theta_{13}$ as a function of $ \Delta m_{23}^2 $. . .	198
5.5	The T2K allowed regions for $\sin^2 2\theta_{13}$ as a function of δ_{CP}	199
B.1	Parent direct contribution to the ν_μ flux in the near detector.	211
B.2	Parent direct contribution to the ν_μ flux in the far detector.	212
B.3	Parent direct contribution to the ν_e flux in the near detector.	213
B.4	Parent direct contribution to the ν_e flux in the far detector.	214
B.5	Fraction of indirect contribution for the near detector.	215
B.6	Fraction of indirect contribution for the far detector.	216
B.7	Parent target contribution to the ν_μ flux in the near detector. . . .	217
B.8	Parent target contribution to the ν_μ flux in the far detector.	218
B.9	Parent target contribution to the ν_e flux in the near detector.	219
B.10	Parent target contribution to the ν_e flux in the far detector.	220
B.11	Fraction of non-target contribution for the near detector.	221
B.12	Fraction of non-target contribution for the far detector.	222
C.1	$\{p, \theta\}$ distributions of secondary π^- (far detector).	224
C.2	$\{p, \theta\}$ distributions of secondary K^- (far detector).	225
C.3	$\{p, \theta\}$ distributions of secondary K_L^0 (far detector).	226
C.4	$\{p, \theta\}$ distributions of secondary π^+ (near detector).	227
C.5	$\{p, \theta\}$ distributions of secondary π^- (near detector).	228
C.6	$\{p, \theta\}$ distributions of secondary K^+ (near detector).	229
C.7	$\{p, \theta\}$ distributions of secondary K^- (near detector).	230
C.8	$\{p, \theta\}$ distributions of secondary K_L^0 (near detector).	231

List of Tables

1.1	Neutrino sources and corresponding energy ranges.	10
2.1	Main parameters of the T2K beamline simulation.	51
2.2	Simulated decay channels and branching ratios.	55
2.3	Decay chains of secondary particles.	62
2.4	Composition of the neutrino beam at the ND280 near detector. . .	67
2.5	Composition of the neutrino beam at the far detector.	67
2.6	Composition of the beam at the ND280 (direct contribution). . . .	70
2.7	Composition of the beam at the ND280 (indirect contribution). . .	70
2.8	Composition of the beam at SK (direct contribution).	71
2.9	Composition of the beam at SK (indirect contribution).	71
2.10	Composition of the beam at the ND280 (target contribution). . . .	74
2.11	Composition of the beam at the ND280 (non-target contribution). .	74
2.12	Composition of the beam at SK (target contribution).	75
2.13	Composition of the neutrino beam at SK (non-target contribution). .	75
3.1	Quality cuts applied to beam events for analysis.	124
3.2	Event reduction after the beam quality cuts applied for analysis. . .	124
3.3	Quality cuts applied to global rtracks for analysis.	130
3.4	Track reduction after the quality cuts applied for analysis.	130
3.5	Allowed ranges of the fitted parameters.	154
3.6	Systematic uncertainties related to the particle identification. . . .	162
3.7	Systematic uncertainties on the re-weighting factors.	176
D.1	Raw yields of positively charged pions (bin 1).	233
D.2	Raw yields of positively charged pions (bin 2).	234
D.3	Raw yields of positively charged pions (bin 3).	235
D.4	Raw yields of positively charged pions (bin 4).	236
D.5	Raw yields of positively charged pions (bin 5).	237
D.6	Raw yields of positively charged pions (bin 6).	238
E.1	Efficiencies and corrections.	240

F.1	Re-weighting factors of positively charged pions (bin 1).	242
F.2	Re-weighting factors of positively charged pions (bin 2).	243
F.3	Re-weighting factors of positively charged pions (bin 3).	244
F.4	Re-weighting factors of positively charged pions (bin 4).	245
F.5	Re-weighting factors of positively charged pions (bin 5).	246
F.6	Re-weighting factors of positively charged pions (bin 6).	247

Chapter 1

Introduction to neutrino physics

1.1 Neutrinos in the Standard Model

The Standard Model (SM) with 19 parameters, describes the electroweak and strong interactions which mediate the dynamics of 12 known fermions via 12 force carrying bosons. Because of its success in explaining a wide variety of experimental results, the SM is often regarded as a theory of almost everything. However, it is far from being a complete theory of fundamental interactions. First, it does not include the physics of gravity (general relativity, dark energy). Second, it does not have a viable dark matter particle candidate that would possess all the required properties deduced from observational cosmology. Finally, although neutrinos are included in the model, it does not account for their non-zero masses and therefore does not describe mixing in the leptonic sector.

The latter point reflects a simple fact: neutrinos are probably the least well known particles in the SM. Neutrinos have indeed a special status in the model as their existence was first postulated in 1930 by Wolfgang Pauli to preserve energy and momentum conservation in β -decay. They remained elusive and conceptual for a while, triggering major theoretical work to understand the β -decay. In particular, this led Enrico Fermi to write down the first formulation of the weak interaction. This theoretical background allowed physicists to understand if any experimental detection of the neutrinos was possible by computing the cross section of the β -process and the neutrino flux that would be required to statistically observe this process. Bruno Pontecorvo was the first one to propose a method to detect free neutrinos ([1]) from reactors using the inverse β -process. Based on the ideas developed by Bruno Pontecorvo, neutrinos were finally discovered experimentally in 1953 by Frederick Reines and Clyde Cowan [2], 23 years after they were postulated by Wolfgang Pauli. Four years later, Maurice Goldhaber's measurements [3] of the neutrino helicity were consistent with the observation of a single helicity state: all neutrinos are left-handed and all anti-neutrinos are right-handed. The mass of the neutrino being at that time consistent with zero, this last observation is the reason

why only left chiral fields were used to describe neutrinos in the SM. Actually, in the zero-mass limit, chirality eigenstates are also helicity eigenstates, thus only two fields are necessary to describe neutrinos: the left-handed neutrino field and its CPT transform the right-handed anti-neutrino field. Unlike other fermions of the SM, this treatment forbids a Dirac mass term for neutrinos, which would require to couple left-handed neutrino fields with non-existing right-handed neutrino fields.

Later on, in 1962, Leon Lederman, Melvin Schwartz and Jack Steinberger [4] experimentally showed that the neutrinos involved in the e^\pm and μ^\pm -producing reactions could not be the same particles. After the discovery of the τ lepton in a series of experiments performed between 1974 and 1977 by Martin Perl and his colleagues (e.g. [5]), this observation was in favor of the hypothesis that similar to charged leptons, neutrinos are produced in three flavors: ν_e , ν_μ and ν_τ . Only three charged-lepton mass eigenstates are known. It could well be that more than three neutrino mass eigenstates exist. In this case, the additional linear combinations ν_s^i (i running over the number of additional mass eigenstates) of these mass eigenstates would not have any charged-lepton partner, and consequently, would simply not couple to the SM W boson. The measurements of the SM Z boson decay width at LEP in 1989 [6] (see Fig. 1.1) showed that the $Z \rightarrow \nu_\alpha \bar{\nu}_\alpha$ decay yields only three distinct neutrinos ν_α of definite flavor, α . Thus, the ν_s combinations would not couple to the Z boson either. Such neutrinos, which do not have any SM weak couplings, are referred to as *sterile neutrinos*.

The SM originally describes the propagation of massless left-handed (right-handed) neutrino (anti-neutrino) fields. It also describes their interactions with ordinary matter made of nucleons and electrons. In the electroweak theory, neutrino interactions can occur both via neutral (NC) and charged (CC) currents. The neutrino-electron scattering includes the following interactions:

$$\begin{aligned} CC, NC & : \quad \nu_e + e^- \rightarrow \nu_e + e^- \\ CC, NC & : \quad \bar{\nu}_e + e^- \rightarrow \bar{\nu}_e + e^- \\ NC & : \quad \nu_{\mu,\tau} + e^- \rightarrow \nu_{\mu,\tau} + e^- \\ NC & : \quad \bar{\nu}_{\mu,\tau} + e^- \rightarrow \bar{\nu}_{\mu,\tau} + e^- \end{aligned}$$

where the processes involving ν_e , $\bar{\nu}_e$ include both NC and CC interactions. The neutrino-nucleon scattering can be summarized by four basic CC and NC reactions:

$$\begin{aligned} CC & : \quad \nu_l + \mathcal{N} \rightarrow l^- + X \\ CC & : \quad \bar{\nu}_l + \mathcal{N} \rightarrow l^+ + X \\ NC & : \quad \nu_l + \mathcal{N} \rightarrow \nu_l + X \\ NC & : \quad \bar{\nu}_l + \mathcal{N} \rightarrow \bar{\nu}_l + X \end{aligned} \tag{1.1}$$

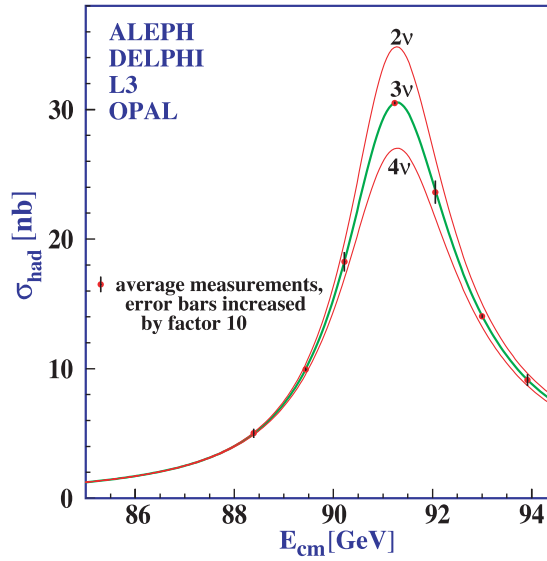


Figure 1.1: Measurements of the hadron production cross section around the Z resonance. The curves indicate the predicted cross sections for two, three and four neutrino species with SM couplings and negligible mass.

where l denotes the leptonic flavor and X stands for the hadronic final state. In the quasi-elastic regime (kinematic limit for which the Bjorken scaling variable $x = Q^2/2(p \cdot q) = 1$, where $Q^2 = -q^2$ is the transferred momentum and $p \cdot q = M(E - E') \equiv M\nu$ the energy transfer), the hadronic final state consists in a single nucleon (the invariant mass $W^2 = (p + q)^2 = M^2 - Q^2 + 2M\nu = M^2$). This applies to the two charged-current quasi-elastic processes and to the neutral current elastic reactions:

$$\begin{aligned}
 CC & : \quad \nu_l + n \rightarrow l^- + p \\
 CC & : \quad \bar{\nu}_l + p \rightarrow l^+ + n \\
 NC & : \quad \nu_l + p(n) \rightarrow \nu_l + p(n) \\
 NC & : \quad \bar{\nu}_l + p(n) \rightarrow \bar{\nu}_l + p(n)
 \end{aligned} \tag{1.2}$$

while in the inelastic regime (large Q^2), the nucleon is broken up and the final hadronic state X is composed of many hadrons. At low energy ($E < 1$ GeV) neutrino-nucleon scattering is dominated by the quasi-elastic process. The deep inelastic limit applies at large Q^2 and large ν and can be described as an incoherent sum of reactions on the point-like partons. In the intermediate region dominated by lower $Q^2 \approx 1 - 2$ GeV², the hit nucleon might only be excited into a resonance state. For example, in the case of the lightest baryonic resonance $\Delta(1232)$, one

may observe the following reactions:

$$\begin{aligned}
 \nu_l + p &\rightarrow l^- + \Delta^{++} \rightarrow l^- + p + \pi^+ & \bar{\nu}_l + p &\rightarrow l^+ + \Delta^0 \rightarrow l^+ + n + \pi^0 \\
 \nu_l + n &\rightarrow l^- + \Delta^+ \rightarrow l^- + p + \pi^0 & \bar{\nu}_l + p &\rightarrow l^+ + \Delta^0 \rightarrow l^+ + p + \pi^- \\
 \nu_l + p &\rightarrow l^- + \Delta^+ \rightarrow l^- + n + \pi^+ & \bar{\nu}_l + n &\rightarrow l^+ + \Delta^- \rightarrow l^+ + n + \pi^-
 \end{aligned} \quad (1.3)$$

All these standard model processes have been studied in numerous experiments. However, sparse measurements (especially in the quasi-elastic region) and often old low statistics and therefore inaccurate data are what gives us a global overview of the neutrino-nucleon total cross section that still suffers from large uncertainties (see Fig. 1.2).

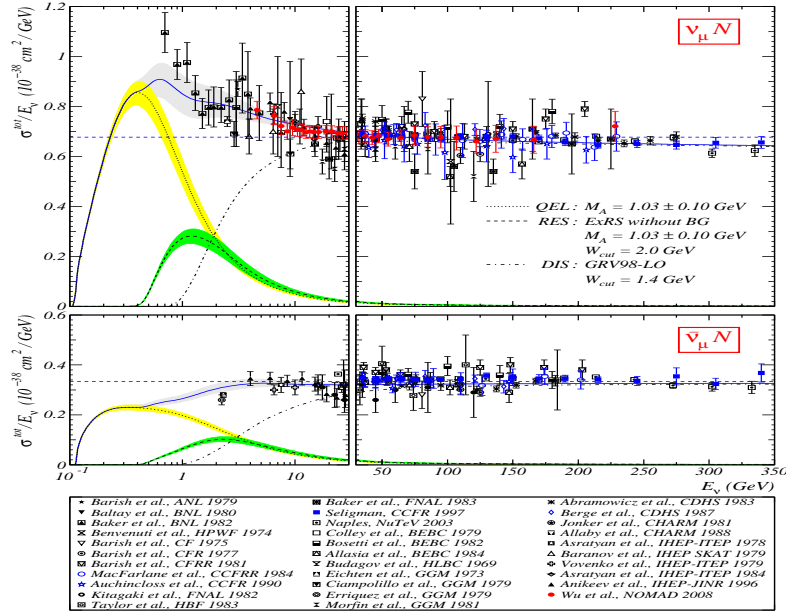


Figure 1.2: Total charged current ν_μ (top) and $\bar{\nu}_\mu$ -nucleon (bottom) inclusive cross section as a function of neutrino energy. The low energy region is dominated by the quasi-elastic (QEL) contribution (dotted), the high energy region by the deep inelastic (DIS) contribution (dashed-dotted). The intermediate regime is dominated by the resonance (RES) contribution (dashed). Points with errors bars show sparse measurements of various experiments listed in the caption. As can be seen, measurements mainly concentrate in the DIS region and measurements in the RES region suffer from larger uncertainties, while very few measurements cover the QEL region. From [7] and [8].

The neutrino properties and interactions presented in this section are all accounted for in the original formulation of the Standard Model. As we will explain in the following sections, non-zero mass neutrinos open a window over new physics

beyond the Standard Model. To understand why, let us review the main ingredients of the SM and some immediate consequences of it.

Each fermion field, f , and its anti-fermion field, \bar{f} , are described by a four-component Dirac spinor, $\psi(x)$. The evolution of free spinors satisfies the Dirac equation:

$$(i\cancel{\partial} - m)\psi = 0 \quad (1.4)$$

where $\cancel{\partial} = \gamma^\mu \partial_\mu$ (Feynman slash notation), $\partial_\mu = \partial/\partial x^\mu$ and γ^μ are the Dirac matrices. In addition we define $\gamma^5 \equiv i\gamma^0\gamma^1\gamma^2\gamma^3\gamma^4$, which in particular anti-commutes with all the other gamma matrices. There exists many representation for the gamma matrices. In the Weyl representation:

$$\gamma^0 = \begin{pmatrix} 0 & 1 \\ 1 & 0 \end{pmatrix}, \quad \vec{\gamma} = \begin{pmatrix} 0 & \vec{\sigma} \\ -\vec{\sigma} & 0 \end{pmatrix}, \quad \text{and} \quad \gamma^5 = \begin{pmatrix} -1 & 0 \\ 0 & 1 \end{pmatrix}, \quad (1.5)$$

where $\vec{\sigma}$ are the Pauli 2×2 spin matrices. In this representation, referred to as the *chiral representation*, the components of the spinors are usually explicitly written in terms of two two-component spinors ϕ and χ such that

$$\psi = \begin{pmatrix} \phi \\ \chi \end{pmatrix} \quad (1.6)$$

The projectors P_L and P_R defined as

$$P_L = \frac{1}{2}(1 - \gamma_5) \quad \text{and} \quad P_R = \frac{1}{2}(1 + \gamma_5), \quad (1.7)$$

decompose the spinors in two chirality states, a left-handed state, ψ_L (corresponding to $(\phi \ 0)$), and a right-handed state ψ_R (corresponding to $(0 \ \chi)$). As long as fermions remain massless (as originally introduced in the model), these chiral fields are completely independent and satisfy separate equations of motion. This can be seen by re-expressing the Lagrangian density leading to the Dirac equation using the projectors defined in Eq. 1.7:

$$\begin{aligned} \mathcal{L} &= \bar{\psi}(i\cancel{\partial} - m)\psi \\ &= \bar{\psi}(P_R + P_L)(i\cancel{\partial} - m)(P_R + P_L)\psi \\ &= i\bar{\psi}_L\cancel{\partial}\psi_L + i\bar{\psi}_R\cancel{\partial}\psi_R - m\bar{\psi}_L\psi_R - m\bar{\psi}_R\psi_L \end{aligned} \quad (1.8)$$

where $\bar{\psi} = \psi^\dagger \gamma^0$, with ψ^\dagger the Hermitian conjugate, is the Dirac conjugate spinor of ψ . Eq. 1.8 shows that the two chirality components of massive Dirac fields are only coupled through the mass term.

In the Weyl representation, the Dirac equation can be expressed as two coupled equations for ϕ and χ :

$$-m\phi + (p_0 - \vec{\sigma} \cdot \vec{p})\chi = 0 \quad (1.9)$$

$$(p_0 + \vec{\sigma} \cdot \vec{p})\phi - m\chi = 0 \quad (1.10)$$

which, for massless fermions, have solutions that satisfy

$$\phi = \left(-\frac{\vec{\sigma} \cdot \vec{p}}{p_0} \right) \phi \quad \text{and} \quad \chi = \left(+\frac{\vec{\sigma} \cdot \vec{p}}{p_0} \right) \chi \quad (1.11)$$

and correspond to the two helicity states described by the operator

$$h = \frac{\vec{\Sigma} \cdot \vec{p}}{|\vec{p}|} = \begin{pmatrix} \frac{\vec{\sigma} \cdot \vec{p}}{|\vec{p}|} & 0 \\ 0 & \frac{\vec{\sigma} \cdot \vec{p}}{|\vec{p}|} \end{pmatrix} \quad (1.12)$$

in the four-component notation. Thus, the chiral fields of massless fermions also describe the states of helicity for both positive and negative energy solutions of the massless Dirac equations, i.e.:

- ϕ describes a left-handed fermion for $E > 0$ and a right-handed anti-fermion for $E < 0$;
- χ describes a right-handed fermion for $E > 0$ and a left-handed anti-fermion for $E < 0$.

Since Goldhaber's measurements were consistent with a single left-handed helicity state, and since the mass of the neutrino was consistent with zero at that time, only the left-handed chiral field ν_L (and its CPT transform) was necessary to describe the neutrino and the right-handed chiral field ν_R was simply left aside from the original chiral formulation of the SM.

The SM does not only propagate fermionic fields freely, but also describes their interactions with boson fields. These fields, representing the force carriers between interacting fermions, come up as basic ingredients of gauge theories such as the SM. *Gauging* is the mechanism by which invariance under local (spacetime dependent) symmetries (e.g. $\psi(x) \rightarrow e^{i\alpha(x) \cdot \mathbf{T}} \psi(x)$) is restored. It basically consists in defining a new *covariant derivative* ∇_μ based on a *gauge field* with a proper transformation, so that $\nabla_\mu \psi(x)$ transforms as $\psi(x)$. With this mechanism, the interaction of the fermions with the gauge field appears naturally. Gauge fields have a group index i (one for each generator of the gauge group) and a spacetime vector index μ , meaning they correspond to spin-1 bosons that carry interactions from one spacetime point to another. The electroweak part of the gauge group of the SM is the group product:

$$G_{SM} = SU(2)_{I_W} \otimes U(1)_Y \quad (1.13)$$

The $SU(2)$ group is the *weak isospin* group. Its fundamental representation is two-dimensional, the three generators being proportional to the Pauli matrices. Under this representation, the left-handed fermions transform as doublets which carry a weak isospin charge $I_W = \frac{1}{2}$:

$$\Psi_{e,L}^i = \begin{pmatrix} \nu_L^i \\ l_L^i \end{pmatrix}, \quad \Psi_{q,L}^i = \begin{pmatrix} u_L^i \\ d_L^i \end{pmatrix} \quad (1.14)$$

where i labels the three generations and ν^i , l^i , u^i , d^i denote the neutrino, charged lepton, up and down-type quarks respectively. The right-handed fermions are singlets of $SU(2)$ ($I_W = 0$). They are denoted by $\psi_{e,R}^i$, $\psi_{u,R}^i$ and $\psi_{d,R}^i$. The right-handed neutrinos $\psi_{\nu,R}^i$ are simply not included in the minimal SM.

The *Higgs mechanism* allows gauge bosons and fermions to become massive, without having to insert quadratic field terms that would anyhow violate gauge invariance. The idea is to insert a new complex scalar field Φ and build the most general globally $SU(2) \otimes U(1)$ invariant Lagrangian density. The symmetry is made into a local one using a covariant derivative containing four gauge fields, one for each of the generators of the $SU(2) \otimes U(1)$ symmetry. Once this symmetry is broken, Φ acquires a non-zero *vacuum expectation value*, v . The expansion of $\Phi(x)$ around its minimum is called the *Higgs field*, $h(x)$. Inserting this expansion in the Lagrangian density, the non-zero vacuum expectation value naturally provides the mass for the Z and W gauge bosons, while the photon remains massless.

Following the same idea, the fermionic Lagrangian density $i\bar{\psi}\not{D}\psi$ is now considered without mass terms. The fermions couple to the Higgs doublet through the so-called *Yukawa coupling*. Once the symmetry is broken, the expansion in $v + h(x)$ leads to the following term:

$$\mathcal{L}_{Yukawa} = \sum_{i,j=1}^3 [\bar{u}_L^i m_{ij}^u u_R^j + \bar{d}_L^i m_{ij}^d d_R^j + \bar{l}_L^i m_{ij}^l l_R^j + h.c.] \quad (1.15)$$

where the mass matrices m_{α}^{ij} are defined from the non-zero vacuum expectation value. In this expression, the mass matrices are not necessarily diagonal and the mass of the lepton and quark fields cannot be defined. The fields present in this expression are therefore called *flavor states*. The mass matrices can be diagonalized by choosing unitary matrices such that:

$$m'_{\alpha} = (S_{\alpha,L})^{\dagger} \cdot m_{\alpha} \cdot S_{\alpha,R}$$

where $\alpha = u, d, e$. This is equivalent to re-defining spinors as:

$$\psi_{\alpha,\chi}^i = S_{\alpha,\chi} \cdot \psi_{\alpha,\chi} \quad (1.16)$$

where χ stands for the two chiralities L and R . For example, the left-handed charged lepton spinors become:

$$l_{\alpha,L}^i = \sum_{j=1}^3 S_{l,L}^{ij} l_L^j$$

The Lagrangian density in Eq. (1.15) can be re-formulated accordingly:

$$\mathcal{L}_{Yukawa} = \sum_{i=1}^3 [\bar{u}_L^i m_{ii}^u u_R^i + \bar{d}_L^i m_{ii}^d d_R^i + \bar{l}_L^i m_{ii}^l l_R^i + h.c.] \quad (1.17)$$

and the primed fields are now called *mass eigenstates*. Eq. (1.16) simply states that mass eigenstates are expressed as a linear combination of flavor eigenstates as a consequence of the change of basis used to diagonalize the mass matrices. Another important consequence that follows from the diagonalization of the mass matrices is the *flavor mixing*. The complete SM Lagrangian density is:

$$\mathcal{L} = \mathcal{L}_{f,gauge} + \mathcal{L}_{Yukawa} + \mathcal{L}_\Phi$$

where \mathcal{L}_Φ contains the kinetic and mass terms of the Higgs field, its self-interactions and the mass terms of the W and Z bosons. The first term, $\mathcal{L}_{f,gauge}$, contains the interactions of fermions with the gauge bosons and is given by:

$$\mathcal{L}_{f,gauge} = -\left(\frac{g}{\sqrt{2}}j_c^\mu W_\mu^+ + h.c.\right) - \frac{g}{\cos\theta_W}j_n^\mu Z_\mu - ej_{em}^\mu A_\mu \quad (1.18)$$

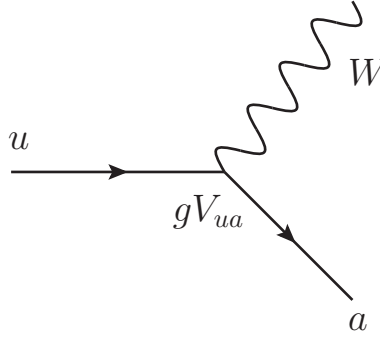
where g and e are the weak and electromagnetic coupling constants, θ_W the *weak mixing angle* and j_c^μ , j_n^μ the *charged* and *neutral vector currents* respectively. In particular, the charged vector current is given by:

$$j_c^\mu = \sum_{i=1}^3 [\bar{\nu}_{i,L} \gamma^\mu l_{i,L} + \bar{u}_{i,L} \gamma^\mu d_{i,L}] \quad (1.19)$$

Once re-formulated with the definition (1.16) and using the general notation (1.14), the Lagrangian density (1.18) includes for example terms of the form:

$$\bar{\Psi}_{u,L} \gamma^\mu \Psi_{d,L} = \bar{\Psi}_{u,L}^i \gamma^\mu [(S_{u,L})^\dagger S_{d,L}] \Psi_{d,L}^j \quad (1.20)$$

that correspond to charged-current flavor changing interactions such as:



where $a = d, s$ or b . The presence of the V matrix element modifies the SM charged current in such a way that it now couples quark fields of different families. Flavor mixing is thus a direct consequence of quarks and leptons being massive. In the previous diagram, the *quark mixing matrix* is defined as:

$$V^{ij} = [(S_{u,L})^\dagger S_{d,L}]^{ij} = \begin{pmatrix} V_{ud} & V_{us} & V_{ub} \\ V_{cd} & V_{cs} & V_{cb} \\ V_{td} & V_{ts} & V_{tb} \end{pmatrix} \quad (1.21)$$

and is known as the *Cabbibo-Kobayashi-Maskawa (CKM) matrix*. All the mixing can be placed in either the up-type or down-type quarks. By convention, the CKM matrix places all the mixing in the down-type quarks, which means that the weak eigenstates for the up-type quarks are the same as the mass eigenstates. The elements of the CKM matrix have been determined by measuring, for example, the strengths of the strangeness-changing processes, exclusive semi-leptonic decays (e.g. $B_d^0 \rightarrow \pi^- e^+ \nu_e$) and oscillations (e.g. $B_q^0 \rightarrow \bar{B}_q^0$) of neutral mesons. Let us stress that the quark flavor mixing can be observed *directly* because quarks are bound into mesons from which mass eigenstates are clearly identified.

The charged vector currents (Eq. (1.19)) being symmetric in the treatment of leptons and quarks, it is natural to suppose that leptons also mix and that flavor change occurs between the different families of leptons. Actually, if neutrinos have non-degenerate masses, after the diagonalization of the charged lepton and neutrino mass matrices, the leptonic analogue of the CKM matrix would be:

$$U^{ij} = [(S_{\nu,L})^\dagger S_{l,L}]^{ij} \quad (1.22)$$

Because neutrino masses are supposed to be degenerate (namely, zero) in the minimal SM, the unitary rotation matrix $S_{\nu,L}$ can be chosen arbitrarily. Choosing $S_{\nu,L} = S_{l,L}$ simply leads to the identity matrix for the CKM analogue in the leptonic sector. Leptonic flavor mixing is consequently absent from the minimal SM. Another natural question that arises once lepton mixing is taken into account is whether the flavor mixing in the leptonic sector can be probed similar to the mixing in the quark sector. Actually, intrinsic differences between the two sectors unavoidably distinguish the physical manifestations of mixing in these two sectors. In particular, quarks are confined, while leptons are free. As soon as particles propagate freely, *coherence* effects have to be taken into account at production, propagation and detection levels. Moreover, the way *flavor* is defined in both sectors is also somewhat dependent on the physical properties of quarks and leptons. These points will be further developed along the next section.

The overview of the SM given so far shows two major consequences of the right-handed neutrino fields not being included in the minimal version of the SM: first, neutrinos appear with degenerate (zero) masses and second, leptons do not mix. As it will be discussed in the next section, the observation of neutrino oscillations fully contradicts these two points.

1.2 Current picture of neutrino oscillations

1.2.1 The neutrino puzzles

Although Bruno Pontecorvo introduced some of the basic ideas of the phenomenology of the neutrino oscillations by considering oscillations between neutrinos and anti-neutrinos in 1957 ([9]), the phenomenology of neutrino oscillations as we know it today, was developed to solve a series of anomalies that appeared while the neutrino properties were being uncovered. The two main ones turned out into long-standing puzzles referred to as the *Solar neutrino puzzle* and the *atmospheric neutrino anomaly*.

Neutrinos are naturally produced in different sources over a large range of energies (see Tab. 1.1). Early studies of neutrinos were simply based on β -emitters. Starting from the 1950's, as precision measurements were required, artificial sources controlled in terms of time and energy distributions started to be used (e.g. nuclear reactors and secondary pion beams produced at accelerators).

Sources	Energy range
solar (fusion)	keV to MeV
atmospheric	MeV to EeV
radioactivity	MeV
reactor (fission)	MeV
accelerator	MeV to GeV

Table 1.1: Neutrino sources and corresponding energy ranges.

As soon as it was understood that the energy of the Sun is produced by proton-proton fusion (i.e. so-called *pp-chain*), it was immediately considered as a potential intense source of electron neutrinos. After about a decade of hard work (mainly to improve the accuracy of the so-called *Standard Solar Model* (SSM) expectations for the solar neutrino fluxes, shown in Fig. 1.3), the first evidence for a solar electron neutrino flux was obtained in 1964 in the experiment of the Homestake mine, led by Ray Davis. In this radiochemical experiment, electron neutrinos were detected via the inverse nuclear β -decay of Chlorine

$$\nu_e + {}^{37}\text{Cl} \rightarrow e^- + {}^{37}\text{Ar},$$

a reaction that was originally proposed by Bruno Pontecorvo [10]. The corresponding energy threshold allowed to observe neutrino energies higher than ~ 1 MeV. The published results showed that the measured neutrino flux was statistically smaller than expected from the predictions of the SSM.

The Homestake experiment ran over 30 years. It was followed by several experiments among which the Kamiokande [11] experiment (1985) in Japan and the SAGE [12] (1990) and GALLEX [13] (1991) experiments respectively in Russia

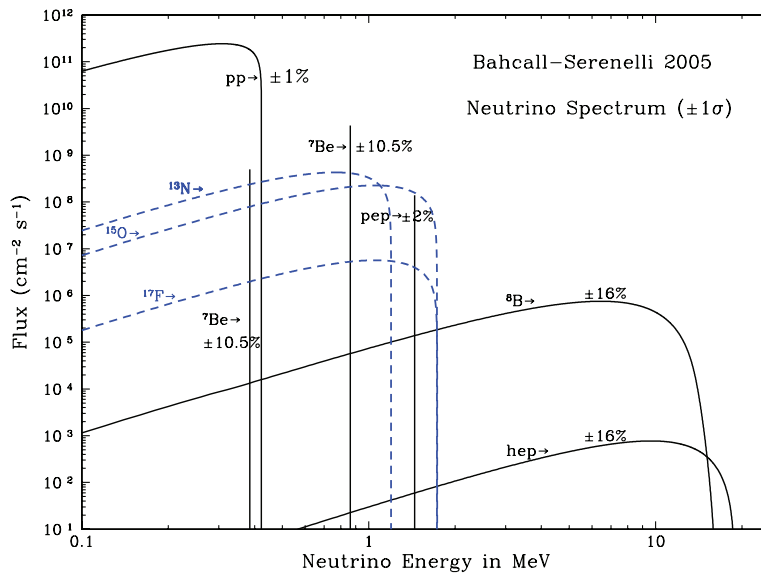


Figure 1.3: The solar neutrino spectrum predicted by the BS05(OP) standard solar model. The neutrino fluxes are given in units of $\text{cm}^{-2}\text{s}^{-1}\text{MeV}^{-1}$ for continuous spectra and $\text{cm}^{-2}\text{s}^{-1}$ for line spectra. The numbers associated with the neutrino sources show theoretical errors of the fluxes. Picture from <http://www.sns.ias.edu/~jnb/SNviewgraphs/Opacities>.

and Italy, confirmed the observed solar neutrino deficit. Fig. 1.4 shows the solar neutrino flux measured by different solar experiments compared to the SSM predictions. Although designed to search for the proton decay, the water Cherenkov based Kamiokande experiment could also detect solar neutrinos. The Cherenkov technique being sensitive to high energies (> 5 MeV), it could detect only the ^8B solar neutrinos which are the main contribution to the high energy (~ 10 MeV) part of the solar neutrino spectrum (see Fig. 1.3). Kamiokande was the first real-time experiment to correlate the neutrino direction with the position of the Sun in the sky via the elastic neutrino-electron scattering. SAGE and GALLEX were also radiochemical experiments but detecting neutrinos via the inverse β -decay of Gallium instead of Chlorine. These experiments were sensitive to the main component of the solar neutrino spectrum since the energy threshold for that reaction is at 233 keV, that is well below the end point energy of the pp -neutrinos.

Although the combined analysis of the Homestake, SAGE and GALLEX experiments ruled out most of the astrophysical solutions that could explain the observed solar neutrino deficit, evidence for neutrino oscillations did not come up before the Super-Kamiokande experiment [14] and were confirmed, beyond any reasonable doubt, by the SNO and KamLAND [15] experiments. In the meantime, from the 1980's, another source of neutrinos gained increasing interest: the atmospheric neutrinos. Cosmic rays hit the upper atmosphere of the Earth and produce hadronic showers mainly composed of pions. Muon and electron (anti-)

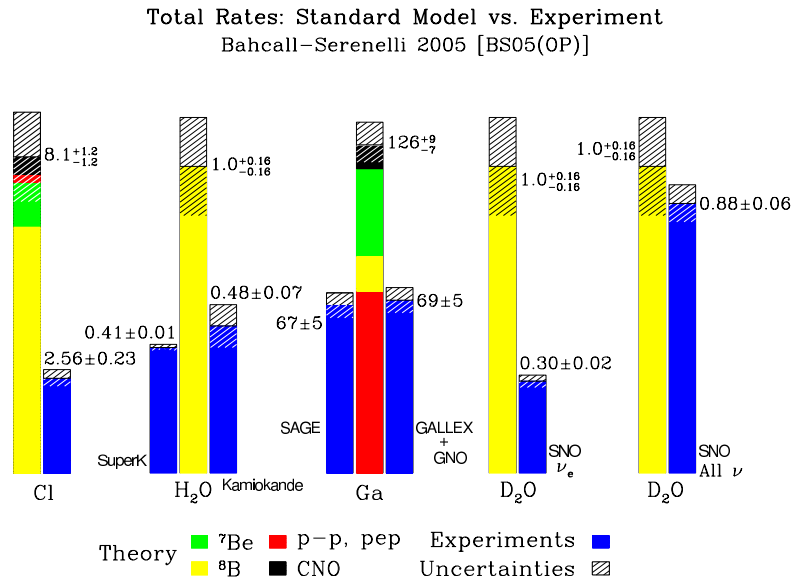


Figure 1.4: Predictions of the SSM and total observed rates in the six solar neutrino experiments: Chlorine, SuperKamiokande, Kamiokande, GALLEX, SAGE and SNO. The model predictions are color coded according to the different predicted neutrino components. The 1σ uncertainties are shown by cross hatching for both data and predictions. Picture from <http://www.sns.ias.edu/~jnb/SNviewgraphs/Nobel04>.

neutrinos are produced in the decay in flight of the pions and subsequent decay of the accompanying muons:

$$\begin{aligned}\pi^\pm &\rightarrow \mu^\pm + \nu_\mu(\bar{\nu}_\mu) \\ &\hookrightarrow e^\pm + \nu_e(\bar{\nu}_e) + \bar{\nu}_\mu(\nu_\mu)\end{aligned}$$

The flavor ratio of the atmospheric neutrino flux, $R(\mu/e) \equiv (\nu_\mu + \bar{\nu}_\mu)/(\nu_e + \bar{\nu}_e)$, which can be calculated with an uncertainty of $\sim 5\%$, is expected to be $\sim 2:1$ for low energy neutrinos ($\sim \text{GeV}$), and higher for higher energy neutrinos. Several experiments were built to study atmospheric neutrinos and measure this ratio. In particular, the NUSSEX, Frejus, Soudan and MACRO experiments were calorimeter-like detectors. The Kamiokande and IMB experiments were water Cherenkov detectors and studied the atmospheric neutrino flux as a main source of background in the search for the proton decay. The Soudan, Kamiokande and IMB experiments indicated that the muon to electron neutrino ratio was statistically smaller than the expectation. This observation was referred to as the *atmospheric neutrino anomaly*. In addition, the Kamiokande experiment also measured the muon and electron neutrino fluxes as a function of the neutrino direction. It turned out that the muon neutrino flux was larger when neutrinos entered the detector from the top than from the bottom. The electron neutrino flux was roughly independent of

the neutrino direction.

The Super-Kamiokande experiment (larger version of Kamiokande), built to improve the sensitivity to the proton decay, was also designed to investigate the two neutrino puzzles discussed so far by precise measurements of the muon and electron atmospheric neutrino fluxes and a precise measurement of the ^8B solar neutrino spectrum. The measurements provided compelling evidence that the atmospheric muon neutrinos were indeed disappearing with an up-down ratio more than 10σ away from unity. It was also established that the rate of disappearance depends on the neutrino energy and baseline (distance between the source and the detector). The angular and energy dependency of the atmospheric neutrino flux measured by Super-Kamiokande is illustrated in Fig. 1.5. As for the solar sector, Super-Kamiokande confirmed the observed deficit of electron neutrinos. In particular, the measurements showed that the deficit was energy independent in the interval $\sim 5\text{--}10$ MeV.

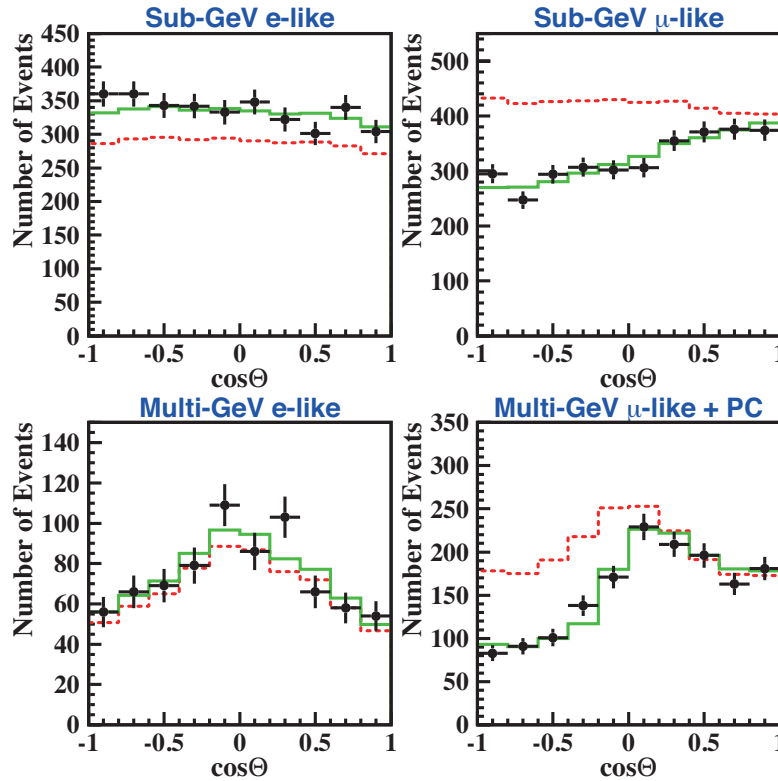


Figure 1.5: Zenith angle distribution of fully-contained single-ring e -like and μ -like events with visible energy < 1.33 GeV (sub-GeV) and > 1.33 GeV (multi-GeV). For multi-GeV μ -like events, a combined distribution with partially-contained (PC) events is shown. The dotted histograms show the non-oscillated Monte-Carlo events, and the solid histograms show the best-fit expectations for $\nu_\mu \rightarrow \nu_\tau$ oscillations. (Figure provided by the Super-Kamiokande Collab., extracted from [16]).

In 1999, a new real-time solar neutrino experiment, SNO, was built to perform independent measurements of the ^8B solar neutrino flux. Neutrinos were detected via three distinct reactions in heavy water:

$$\nu + {}^2\text{H} \rightarrow p + p + e^- \quad (1.23)$$

$$\nu + e^- \rightarrow \nu + e^- \quad (1.24)$$

$$\nu + {}^2\text{H} \rightarrow \nu + p + n \quad (1.25)$$

The key feature of the experiment was that each of these reactions is sensitive to different neutrino flavors. The CC reaction of Eq. 1.23 is sensitive to only electron neutrinos, while the NC reaction of Eq. 1.25 is flavor blind. The elastic scattering (ES) of Eq. 1.24 is mostly sensitive to electron neutrinos with a smaller cross section for muon and tau neutrinos. Using these reactions, SNO could measure simultaneously the ν_e flux and the total ($\nu_e + \nu_\mu + \nu_\tau$) flux. The fluxes measured via the reactions of Eq. 1.23 to Eq. 1.25 are respectively [17]:

$$\Phi^{CC} = (1.68 \pm 0.06(\text{stat})_{-0.09}^{+0.08}(\text{syst})) \times 10^6 \text{ cm}^{-2} \text{ s}^{-1} \quad (1.26)$$

$$\Phi^{ES} = (2.35 \pm 0.022(\text{stat}) \pm 0.15(\text{syst})) \times 10^6 \text{ cm}^{-2} \text{ s}^{-1} \quad (1.27)$$

$$\Phi^{NC} = (4.94 \pm 0.21(\text{stat})_{-0.34}^{+0.38}(\text{syst})) \times 10^6 \text{ cm}^{-2} \text{ s}^{-1} \quad (1.28)$$

Results are summarized in Fig. 1.6. Φ^{NC} being measured from the flavor blind reaction of Eq. 1.25, even in case of $\nu_e \rightarrow \nu_{\mu,\tau}$ transitions, it can be used to test the prediction of the SSM. The measurement shows indeed good agreement with the SSM expectations ($5.49_{-0.81}^{+0.95} \times 10^6 \text{ cm}^{-2} \text{ s}^{-1}$ or $4.34_{-0.61}^{+0.71} \times 10^6 \text{ cm}^{-2} \text{ s}^{-1}$, depending on assumptions about the solar heavy element abundances [18]) for the ^8B solar neutrino flux. The flux from the non- ν_e active neutrinos was deduced from the measurements of Eq. 1.26 and Eq. 1.28:

$$\Phi(\nu_{\mu,\tau}) = (3.26 \pm 0.25(\text{stat})_{-0.35}^{+0.40}(\text{syst})) \times 10^6 \text{ cm}^{-2} \text{ s}^{-1} \quad (1.29)$$

The measured ν_e suppression rate is:

$$\frac{\Phi(\nu_e)}{\Phi(\nu_{\mu,\tau}) + \Phi(\nu_e)} = 0.340 \pm 0.023(\text{stat})_{-0.031}^{+0.029}(\text{syst}) \quad (1.30)$$

The SNO measurements established without any doubt that muon and(or) tau neutrinos and(or) anti-neutrinos are coming from the Sun, and gave strong evidence for neutrino flavor conversion. However, the SNO data alone could not rule out the possibility of other solutions than flavor transitions with sufficient statistical significance to explain the solar deficit. As it will be explained in the next section, the hypothesis of flavor change in the two-neutrino model at the solar scale was finally tested by the KamLAND reactor anti-neutrino experiment. KamLAND reported the observation of the disappearance of electron anti-neutrinos with energy ~ 10 MeV at a distance larger than 100 km from the source. The survival probability measured by KamLAND is well described by the two-neutrino oscillation model, and in particular, it displays the expected oscillatory behavior.

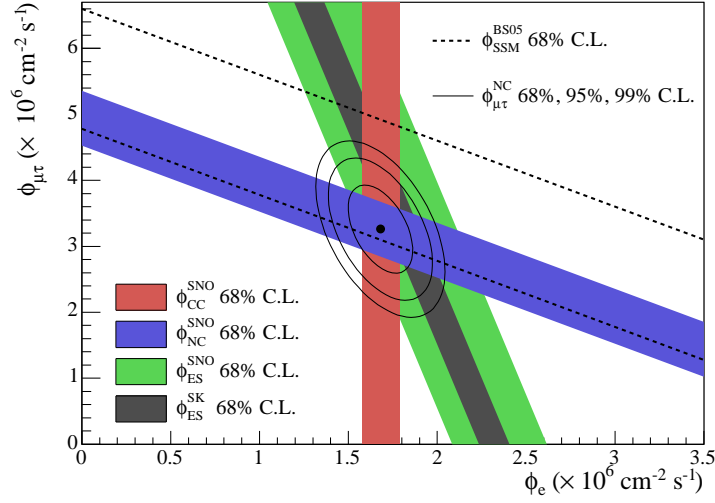


Figure 1.6: Fluxes of ^8B solar neutrinos, $\Phi(\nu_e)$ and $\Phi(\nu_{\mu,\tau})$ deduced from the SNO charged current (CC), elastic scattering (ES) and neutral current (NC) results of the salt phase measurement. The Super-Kamiokande ES flux and BS05(OP) SSM prediction are also shown. Bands represent the 1σ error. Contours show the 68%, 95% and 99% joint probability for $\Phi(\nu_e)$ and $\Phi(\nu_{\mu,\tau})$. From [17].

1.2.2 Neutrino oscillations in vacuum and matter

If neutrinos have mass, there exists a spectrum of at least three mass eigenstates ν_1, ν_2, ν_3 . As previously explained, leptons consequently mix. If leptons mix, the weak charged current interaction coupling the W boson to the lepton weak isospin doublets can couple any charged lepton mass eigenstate l_α ($\alpha = e, \mu, \tau$) to any neutrino mass eigenstate ν_i ($i = 1, 2, 3$). The amplitude for the decay of a W^+ to yield a particular combination $l_\alpha^+ + \nu_i$ is given by the matrix element $U_{\alpha i}^*$, where U is the *lepton mixing matrix* defined in Eq. (1.22). U is usually referred to as the *Pontecorvo-Maki-Nakagawa-Sakata (PMNS) matrix*. An $n \times n$ matrix has in principle n^2 complex entries, which means $2n^2$ real degrees of freedom. However, the unitarity condition on U imposes n^2 real constraints. The lepton fields can obviously be globally re-phased ($\psi \rightarrow e^{i\delta}\psi$) so that $2n - 1$ phase transformations can be applied to get rid of complex phases. The mixing matrix is thus described by $n^2 - (2n - 1) = (n - 1)^2$ real parameters: $\frac{1}{2}n(n - 1)$ Euler angles which describe the rotation between flavors and $\frac{1}{2}(n - 1)(n - 2)$ phases which cannot be removed and can lead to CP violation. For three generations, the PMNS matrix is defined as

$$\begin{pmatrix} \nu_e \\ \nu_\mu \\ \nu_\tau \end{pmatrix} = \begin{pmatrix} U_{e1} & U_{e2} & U_{e3} \\ U_{\mu1} & U_{\mu2} & U_{\mu3} \\ U_{\tau1} & U_{\tau2} & U_{\tau3} \end{pmatrix} \begin{pmatrix} \nu_1 \\ \nu_2 \\ \nu_3 \end{pmatrix} \quad (1.31)$$

and can be parametrized by the three real angles θ_{12} , θ_{13} , θ_{23} and a complex phase δ . It is commonly written as:

$$(U_{PMNS})^{ij} = \begin{pmatrix} c_{12}c_{13} & s_{12}c_{13} & s_{13}e^{-i\delta} \\ -s_{12}c_{23} - c_{12}s_{23}s_{13}e^{i\delta} & c_{12}c_{23} - s_{12}s_{23}s_{13}e^{i\delta} & s_{23}c_{13} \\ s_{12}s_{23} - c_{12}c_{23}s_{13}e^{i\delta} & -c_{12}s_{23} - s_{12}c_{23}s_{13}e^{i\delta} & c_{23}c_{13} \end{pmatrix} \quad (1.32)$$

where c_{ij} and s_{ij} denote $\cos(\theta_{ij})$ and $\sin(\theta_{ij})$ respectively. Similar to the quark sector, where by convention all the mixing is placed in the down-type quarks, the PMNS matrix places all the mixing in the neutrinos. Thus, the neutrino state created in the decay $W^+ \rightarrow l_\alpha^+ + \nu_\alpha$ is:

$$|\nu_\alpha\rangle = \sum_i U_{\alpha i}^* |\nu_i\rangle \quad (1.33)$$

Note that the notation ν_α is equivalent to the primed down-type quark notation often used to denote the weak eigenstates coupling to the up-type quarks ($d' = V_{CKM}d$, where d are the down-type quark mass eigenstates). The state described in Eq. (1.33) is the state referred to as the neutrino of *flavor* α . It is relevant to stress a difference with respect to the quark sector: here the flavor eigenstate ν_α is defined with respect to the associated charged lepton. There is no way to *measure* the flavor of a neutrino except when it interacts weakly: thus ν_α **is defined** as being the neutrino emitted together with a charged lepton l_α in the decay of the W boson. Let us stress also that this definition is however based on the assumption that the mass and flavor eigenstates of charged leptons are directly associated: if we measure for example a mass eigenstate e , we associate this state to the electron weak eigenstate in order to assign the corresponding flavor to the neutrino. This turns out to be correct due to coherence effects during production and propagation of charged leptons. As demonstrated in [19], in most practical cases (π , K and W decays) at currently available energies, charged leptons are indeed always born in charged current weak interactions as incoherent mass eigenstates, or loose their coherence practically immediately. Thus, the measurement of the neutrino flavor ν_α is provided by the decoherence of the associated charged lepton state l_α .

The mass eigenstate ν_i can be expressed as a superposition of flavor eigenstates by inverting Eq. (1.33):

$$|\nu_i\rangle = \sum_\beta U_{\beta i} |\nu_\beta\rangle \quad (1.34)$$

We consider the following case: a charged lepton l_α^+ is produced with a neutrino ν_α at a given source, the neutrino *propagates* and a charged lepton l_β^+ is created after the interaction of ν_α in the detector. Taking lepton mixing into account, the amplitude of this process is actually a sum over three amplitudes, one for each neutrino mass eigenstate ν_i . For each ν_i the amplitude is the product of three factors: the amplitude for l_α^+ to be produced with ν_i (that is the $U_{\alpha i}^*$ matrix element), the amplitude for ν_i to propagate between the source and the detector ($P(\nu_i)$) and the amplitude for ν_i to create l_β^+ (the $U_{\beta i}$ matrix element). Thus, the amplitude can be written as:

$$A[\nu_\alpha \rightarrow \nu_\beta] = \sum_i U_{\alpha i}^* P(\nu_i) U_{\beta i} \quad (1.35)$$

The propagation amplitude $P(\nu_i)$ is easily calculable in the ν_i rest frame since there:

$$i \frac{\partial}{\partial \tau_i} | \nu_i(\tau_i) \rangle = m_i | \nu_i(\tau_i) \rangle \quad (1.36)$$

where m_i is the mass eigenvalue of ν_i and τ_i is the proper time. Thus:

$$| \nu_i(\tau_i) \rangle = e^{-im_i \tau_i} | \nu_i(0) \rangle \quad (1.37)$$

and the propagation amplitude is given by:

$$P(\nu_i) \equiv \langle \nu_i(0) | \nu_i(\tau_i) \rangle = e^{-im_i \tau_i} \quad (1.38)$$

By Lorentz invariance:

$$m_i \tau_i = E_i t - p_i L \quad (1.39)$$

where L is the distance in the laboratory frame between the source and the detector, t is the time taken by the beam in the laboratory frame to traverse this distance and E_i and p_i are respectively the energy and momentum of ν_i in the laboratory frame.

When calculating the probability $P(\nu_\alpha \rightarrow \nu_\beta)$ for a neutrino of flavor α to become a neutrino of flavor β , only relative phases of the propagation amplitudes matter. Using Eq. (1.39), the relative phase of $P(\nu_i)$ and $P(\nu_j)$, $\delta\phi_{ij}$, is given by:

$$\delta\phi_{ij} = (p_i - p_j)L - (E_i - E_j)t \quad (1.40)$$

To relate this phase difference with an observation in the detector, we must choose a value for t . The rigorous expression of these relative phases is achieved with a full wave packet treatment of the emitted neutrinos (in standard weak interactions neutrinos are always produced coherently and keep their coherence while propagating, see [19]). This treatment is described in numerous papers such as [20]. Some rare papers (in particular [21]) show that the commonly seen derivation of these

relative phases is based on hand-waving approximations of neutrino energy and momentum, and in particular on wrongly employed ultra-relativistic approximations. To avoid using these approximations in the plane-wave treatment, we will follow the prescription given in e.g. [21], [22] or [23], where no *equal momentum*, *equal energy* or *equal velocity* arguments are necessary. Instead, an appropriate velocity for the center of the *corresponding* wave packet is postulated:

$$\bar{v} = \frac{p_i + p_j}{E_i + E_j} \quad (1.41)$$

which can be seen as the average of the classical velocities of the two mass eigenstates weighted by their energies:

$$\bar{v} = \frac{E_i}{E_i + E_j} v_i + \frac{E_j}{E_i + E_j} v_j \quad (1.42)$$

In [22], the author shows that, to an excellent approximation, the t in Eq. (1.40) can be replaced by L/\bar{v} and the relative phase is:

$$\delta\phi_{ij} \cong \frac{p_i^2 - p_j^2}{p_i + p_j} L - \frac{E_i^2 - E_j^2}{p_i + p_j} L \cong (m_i^2 - m_j^2) \frac{L}{2E} \quad (1.43)$$

where in the very last step, both p_i and p_j are approximated to the beam energy E , which is correct for highly relativistic neutrinos. Thus, $P(\nu_i) = \exp(-im_i^2 L/2E)$ can be used in Eq. (1.35) to calculate the amplitude of the flavor change:

$$A[\nu_\alpha \rightarrow \nu_\beta] = \sum_i U_{\alpha i}^* e^{-im_i^2 L/2E} U_{\beta i} \quad (1.44)$$

The corresponding probability is given by:

$$\begin{aligned} P(\nu_\alpha \rightarrow \nu_\beta) &= |A[\nu_\alpha \rightarrow \nu_\beta]|^2 \\ &= \delta_{\alpha\beta} \\ &\quad - 4 \sum_{i>j} \Re(U_{\alpha i}^* U_{\beta i} U_{\alpha j} U_{\beta j}^*) \sin^2(\Delta m_{ij}^2 \frac{L}{4E}) \\ &\quad + 2 \sum_{i>j} \Im(U_{\alpha i}^* U_{\beta i} U_{\alpha j} U_{\beta j}^*) \sin(\Delta m_{ij}^2 \frac{L}{2E}) \end{aligned} \quad (1.45)$$

where $\Delta m_{ij}^2 \equiv m_i^2 - m_j^2$. From this general formula, it becomes obvious that neutrinos must have non-degenerate masses and leptons mix for flavor change to occur. Actually, if all m_i have a common value, all $\Delta m_{ij}^2 = 0$ and $P(\nu_\alpha \rightarrow \nu_\beta) = \delta_{\alpha\beta}$. If there is no mixing the amplitude $U_{\alpha i} U_{\beta \neq \alpha, i}$ must be zero so that $P(\nu_\alpha \rightarrow \nu_\beta) = \delta_{\alpha\beta}$ too. Eq. (1.45) also shows how CP-violation may arise in the leptonic sector. If CPT invariance holds, $P(\bar{\nu}_\alpha \rightarrow \bar{\nu}_\beta) = P(\nu_\beta \rightarrow \nu_\alpha)$. But from Eq. (1.45),

$P(\nu_\beta \rightarrow \nu_\alpha; U) = P(\nu_\alpha \rightarrow \nu_\beta; U^*)$ and thus, $P(\bar{\nu}_\alpha \rightarrow \bar{\nu}_\beta; U) = P(\nu_\alpha \rightarrow \nu_\beta; U^*)$. This simply means that the flavor change probabilities for neutrinos and anti-neutrinos are the same, except if the matrix U is non-real, in which case probabilities can differ by having opposite signs of the last term in Eq. (1.45).

In the case of three flavors, Eq. (1.45) reduces to:

$$P(\nu_\alpha \rightarrow \nu_\beta) = 4[|U_{\alpha 3}U_{\beta 3}|^2 \sin^2(\Delta_{31}) + |U_{\alpha 2}U_{\beta 2}|^2 \sin^2(\Delta_{21}) + 2|U_{\alpha 3}U_{\beta 3}U_{\alpha 2}U_{\beta 2}|^2 \sin(\Delta_{31}) \sin(\Delta_{21}) \cos(\Delta_{32} \pm \delta_{32})]$$

where $\Delta_{ij} \equiv \Delta m_{ij}^2 \frac{L}{4E}$ and $\delta_{32} \equiv \arg(U_{\alpha 3}U_{\beta 3}^*U_{\alpha 2}^*U_{\beta 2})$ is a CP-violating phase (the “−” sign occurs for anti-neutrinos). When one big Δm^2 dominates the mass spectrum (which turns out to be the practical case), Eq. (1.45) is fairly approximated by:

$$P(\nu_\alpha \rightarrow \nu_\beta) \cong S_{\alpha\beta} \sin^2(\Delta m^2 \frac{L}{4E}) \quad (1.46)$$

where:

$$S_{\alpha\beta} \equiv 4 \left| \sum_{i \text{ gap}} U_{\alpha i}^* U_{\beta i} \right|^2 \quad (1.47)$$

In Eq. (1.47), the sum goes only over eigenstates that lie on the borders of the mass squared splitting Δm^2 . This simplification is allowed since for an experiment to be sensitive to this particular Δm^2 , the product $\Delta m^2 L/E$ must be of the order of 1 so that the \sin^2 in (1.45) is appreciable (an experiment with a given L/E is thus sensitive to a $\Delta m^2(\text{eV}^2)$ of the order of $E(\text{GeV})/L(\text{km})$). This means that all other possible mass squared splittings would simply be invisible to that experiment.

When only two mass eigenstates (and two corresponding flavor eigenstates) count, there is only a single mass squared splitting Δm^2 and one mixing angle θ . The leptonic mixing matrix can be written as:

$$U = \begin{pmatrix} U_{\alpha 1} & U_{\alpha 2} \\ U_{\beta 1} & U_{\beta 2} \end{pmatrix} = \begin{pmatrix} \cos \theta & \sin \theta \\ -\sin \theta & \cos \theta \end{pmatrix} \quad (1.48)$$

From Eq. (1.47) $S_{\alpha\beta}$ is simply given by:

$$S_{\alpha\beta} = 4 |\cos \theta \sin \theta|^2 = \sin^2 2\theta$$

and Eq. (1.46) becomes:

$$P(\nu_\alpha \rightarrow \nu_\beta) = \sin^2 2\theta \sin^2(\Delta m^2 \frac{L}{4E}) \quad (1.49)$$

Including the so far omitted \hbar and c factors gives the common two-neutrino flavor change probability:

$$P(\nu_\alpha \rightarrow \nu_\beta) = \sin^2 2\theta \sin^2(1.27 \Delta m^2 [\text{eV}^2] \frac{L[\text{km}]}{E[\text{GeV}]}) \quad (1.50)$$

and the corresponding survival probability is given by:

$$P(\nu_\alpha \rightarrow \nu_\alpha) = 1 - \sin^2 2\theta \sin^2(1.27\Delta m^2[eV^2]\frac{L[km]}{E[GeV]}) \quad (1.51)$$

As can be seen in Fig. 1.7, the flavor change probability oscillates as a function of L/E with a frequency given by the considered mass squared splitting and an amplitude given by the relevant mixing angle. Hence the term *neutrino oscillations* to describe this phenomenon which is purely quantum mechanical.

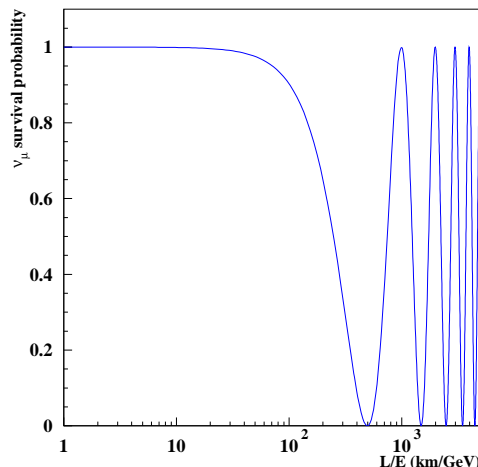


Figure 1.7: Muon neutrino survival probability as a function of L/E (km/GeV) for $\sin^2 2\theta = 1$ and $\Delta m^2 = 2.5 \times 10^{-3} \text{ eV}^2$.

The theory of neutrino oscillations formulated as such would offer a simple solution to the solar neutrino puzzle if the latter was related to oscillations in vacuum only. However, considering a neutrino energy of $\sim 10 \text{ MeV}$ and a baseline of 1 astronomical unit, the survival probability of Eq. 1.51 would require a $\Delta m^2 \sim 10^{-10} \text{ eV}^2$ and $\sin^2 2\theta \sim 1$. This possibility (referred to as the “just-so” solution) was ruled out by the combined data of Super-Kamiokande and SNO. Another ingredient was needed in the basic formulation of solar neutrino oscillations to correctly describe the data. This was related to the fact that solar neutrinos, produced at the core of the Sun, first have to propagate through matter before travelling into vacuum till their detection on Earth.

Actually, it turns out that the forward neutrino-electron scattering in matter significantly modifies the oscillation probabilities. For a detailed description of the matter effect, refer to [16, 23, 24] or [25]. When considering the charged current interaction of electron neutrinos with matter electrons, the interaction term in the

Lagrangian can be reformulated such that the corresponding Dirac equation reads

$$(i\partial^\mu\gamma_\mu - \sqrt{2}G_F N_e \gamma_0) |\nu_e\rangle = 0 \quad (1.52)$$

where N_e is the average electron number density. The solutions of Eq. 1.52 are still plane-waves and the neutrino dispersion relation is now given by

$$E \simeq |\vec{p}| \pm \sqrt{2}G_F N_e \quad (1.53)$$

where the “+” sign is for the positive energy solutions and the “−” sign for the negative energy solutions. The quantity $A = \pm\sqrt{2}G_F N_e$ is referred to as the *matter potential*, with the “+” sign for neutrinos and the “−” sign for anti-neutrinos. In the ultra-relativistic approximation, the neutrino propagation equation can be re-expressed in the mass basis as a Schrödinger-like equation:

$$i\frac{d}{dL} |\nu_i\rangle = \frac{m_i^2}{2E} |\nu_i\rangle \quad (1.54)$$

Using the unitarity of the leptonic mixing matrix defined in Eq. 1.48, the latter equation is translated in the flavor basis as

$$i\frac{d}{dL} |\nu_\beta\rangle = \sum_i U_{\beta i} \frac{m_i^2}{2E} U_{i\alpha}^\dagger |\nu_\alpha\rangle \quad (1.55)$$

which, for two neutrinos, is explicitly written as:

$$i\frac{d}{dL} \begin{pmatrix} |\nu_e\rangle \\ |\nu_\mu\rangle \end{pmatrix} = \frac{\Delta m^2}{2E} \begin{pmatrix} \sin^2 \theta & \cos \theta \sin \theta \\ \cos \theta \sin \theta & \cos^2 \theta \end{pmatrix} \begin{pmatrix} |\nu_e\rangle \\ |\nu_\mu\rangle \end{pmatrix} \quad (1.56)$$

Since the matter potential due to charged current interactions affects only the electron flavor, the matter effect will simply modify Eq. 1.56 by an additive factor on the electron flavor component:

$$i\frac{d}{dL} \begin{pmatrix} |\nu_e\rangle \\ |\nu_\mu\rangle \end{pmatrix} = \left[\frac{\Delta m^2}{2E} \begin{pmatrix} \sin^2 \theta & \cos \theta \sin \theta \\ \cos \theta \sin \theta & \cos^2 \theta \end{pmatrix} + \begin{pmatrix} A & 0 \\ 0 & 0 \end{pmatrix} \right] \begin{pmatrix} |\nu_e\rangle \\ |\nu_\mu\rangle \end{pmatrix} \quad (1.57)$$

Eq. 1.57 can be rewritten as:

$$i\frac{d}{dL} \begin{pmatrix} |\nu_e\rangle \\ |\nu_\mu\rangle \end{pmatrix} = \begin{pmatrix} A & \Delta/2 \sin 2\theta \\ \Delta/2 \sin 2\theta & \Delta \cos^2 \theta \end{pmatrix} \begin{pmatrix} |\nu_e\rangle \\ |\nu_\mu\rangle \end{pmatrix} \quad (1.58)$$

where $\Delta \equiv \Delta m^2/2E$. By comparing Eqs. 1.56 and 1.57 one can extract effective matter mixing ($\sin^2 2\theta_N$) and mass splitting parameters (Δm_N^2), related to their vacuum values by:

$$\Delta m_N^2 \sin 2\theta_N = \Delta m_0^2 \sin 2\theta_0 \quad (1.59)$$

$$\Delta m_N^2 \cos 2\theta_N = \Delta m_0^2 \cos 2\theta_0 - AE_\nu \quad (1.60)$$

where the subscripts refer to the value of the electron number density (N at the current point in matter, 0 in vacuum). From Eqs. 1.59 and 1.60, one can see that when $\text{sign}(A)$ and $\text{sign}(\cos 2\theta_0)$ agree (disagree), there is an enhancement (suppression) of the transition amplitude since $\sin^2 2\theta_N > (<) \sin^2 2\theta_0$. This is depicted in Fig. 1.8 that shows $P(\nu_e \rightarrow \nu_\mu)$ as a function of L for the two sign configurations in matter compared to the vacuum transition probability. From Eq. 1.60, one sees that the minimum value of Δm_N^2 occurs when $\Delta m_0^2 \cos 2\theta_0 = 2\sqrt{2}G_F N_e E_\nu$ and $\theta_N = \pi/4$. This is known as the Mikheyev-Smirnov resonance (see Fig. 1.9, top panel).

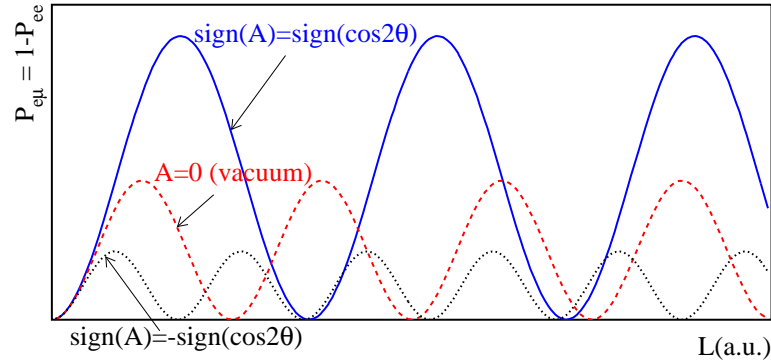


Figure 1.8: $P(\nu_e \rightarrow \nu_\mu)$ as a function of L for fixed values of E , Δm^2 , A and $\sin^2 2\theta$ in vacuum and in matter, assuming $\text{sign}(A) = \text{sign}(\cos 2\theta)$ and $\text{sign}(A) = -\text{sign}(\cos 2\theta)$. From [24].

For large values of the electron number density (i.e. inside the Sun), the mixing angle in matter approaches $\pi/2$. Thus, a ν_e produced at the core of the Sun is mostly produced in the higher matter mass eigenstate ν_2 ($\sim \sin^2 \theta_N$). This interplay between the mixing and the matter effect is illustrated in Fig. 1.9, middle panel. The key point to understand solar data is that this matter effect being energy dependent, it will affect differently the various components of the solar neutrino spectrum. In the lower region of the spectrum, pp and ${}^7\text{Be}$ neutrinos with mean energies of 0.2 MeV and 0.9 MeV respectively are little affected by the matter effect, which means that they will simply undergo quasi-vacuum oscillations. At the other end of the spectrum, ${}^8\text{B}$ solar neutrinos with a mean energy of 10 MeV are mostly produced as ν_2 mass eigenstates. To a good approximation the electron number density satisfies adiabaticity conditions, meaning in particular that the electron number density varies slowly as a function of L . Since the eigenvalues of the matter Hamiltonian of Eq. 1.58 do not cross for any L in the Sun (see Fig. 1.9, top panel), a ${}^8\text{B}$ electron neutrino born as a ν_2 mass eigenstate at the core of the Sun will remain in that state and exit the Sun as a ν_2 . Thus, high energy solar neutrinos do not undergo vacuum oscillations and the probability to observe a ν_e on Earth is simply given by the vacuum mixing parameter, $P(\nu_e \rightarrow \nu_e) = |\langle \nu_e | \nu_2 \rangle|^2 = \sin^2 \theta$. Since $\sin^2 \theta \in [0, 1]$, large suppressions of the

neutrino flux can occur for $\sin^2 \theta \ll 1$. For comparison, the energy-averaged survival probability for the two neutrino vacuum oscillations cannot be less than $1/2$ ($= 1 - \sin^2 2\theta/2$). The fact that SNO measured a ${}^8\text{B}$ neutrino suppression larger than $1/2$ (Eq. 1.30) was a direct proof that the Mikheyev-Smirnov-Wolfenstein (MSW) [26] effect contributes significantly to the solar electron neutrino suppression. The ${}^8\text{B}$ neutrino suppression does not vary with energy (as it was measured by Super-Kamiokande over the $\sim 5\text{--}10$ MeV range). This comes from the fact that the adiabaticity approximation used to derive the MSW effect, is valid over a wide range of energies for the Sun (and other astrophysical sources), and $P(\nu_e \rightarrow \nu_e) = |\langle \nu_e | \nu_2 \rangle|^2 = \sin^2 \theta$ holds accordingly.

The mean survival probability of electron solar neutrinos can thus be expressed as:

$$\langle P(\nu_e \rightarrow \nu_e) \rangle = f_1 \cos^2 \theta_\odot + f_2 \sin^2 \theta_\odot \quad (1.61)$$

where f_1 and f_2 are the fractions of neutrinos that are in the ν_1 and ν_2 mass eigenstate respectively ($f_1 + f_2 = 1$) and θ_\odot denotes the effective two-neutrino solar mixing angle. For the energies of the ${}^8\text{B}$ neutrinos, the MSW effect is large and $|\nu_e\rangle \approx |\nu_2\rangle$. The later statement can actually be quantitatively estimated from the SNO data. Actually, in the two-neutrino analysis, the charged current to neutral current ratio (CC/NC) measured by SNO is equivalent to the day-time averaged ν_e survival probability of Eq. 1.61:

$$\left. \frac{CC}{NC} \right|_{day}^{SNO} = \langle P(\nu_e \rightarrow \nu_e) \rangle = \sin^2 \theta_\odot + f_1 \cos 2\theta_\odot \quad (1.62)$$

using $f_1 = 1 - f_2$ and $\cos^2 \theta - \sin^2 \theta = \cos 2\theta$. Thus, the f_2 fraction of ${}^8\text{B}$ neutrinos differs from 1 by:

$$f_1 = \frac{\left. \frac{CC}{NC} \right|_{day}^{SNO} - \sin^2 \theta_\odot}{\cos 2\theta_\odot} = \frac{0.347 - 0.311}{0.378} \approx 10\% \quad (1.63)$$

where the value of $\sin^2 \theta_\odot$ is the best-fit value from [17]. For ${}^7\text{Be}$ neutrinos, the MSW effect is negligible and $f_1 \approx \cos^2 \theta_\odot = 0.69$, $f_2 \approx \sin^2 \theta_\odot = 0.31$. With this approximation, the average survival probability of Eq. 1.61 gives $\langle P(\nu_e \rightarrow \nu_e) \rangle = \cos^4 \theta_\odot + \sin^4 \theta_\odot \approx 0.57$, which indeed is expected from the average two-neutrino oscillation in vacuum, $\langle P(\nu_e \rightarrow \nu_e) \rangle^{vac} = 1 - \sin^2 2\theta_\odot/2$. The latter expectation is in good agreement with the measurements of the ${}^7\text{Be}$ solar neutrinos from the Borexino experiment [27].

The survival probability of Eq 1.61 is generalized to the case where electron neutrinos are produced in incoherent mixtures of ν_1 and ν_2 by introducing the *unadiabaticity* parameter P_c , that gives the probability to jump from one mass

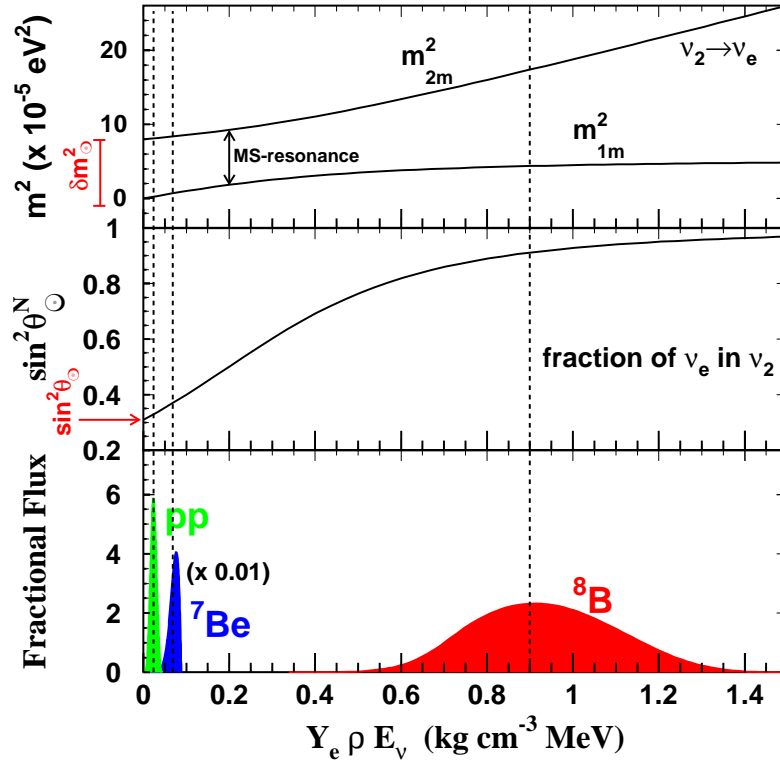


Figure 1.9: The mass spectrum (top panel), the fraction of ν_2 in ν_e 's produced, $\sin^2 \theta_{\odot}^N$ (middle panel) and the fractional flux (bottom panel) versus the product of the electron fraction Y_e ($N_e = \rho Y_e / M_n$), the matter density, ρ , and the neutrino energy, E_ν , for the best-fit values $\Delta m_{\odot}^2 = 8.0 \times 10^{-5} \text{ eV}^2$ and $\sin^2 \theta_{\odot} = 0.31$. The vertical dashed lines give the value of $Y_e \rho E_\nu$ which reproduces the average ν_2 fractions, 91, 37 and 33% for the ${}^8\text{B}$, ${}^7\text{Be}$ and pp neutrinos respectively. From [28].

eigenstate to the other during the MS resonance crossing:

$$P(\nu_e \rightarrow \nu_e) = \cos^2 \theta_{\odot} [(1 - P_c) \cos^2 \theta_N + P_c \sin^2 \theta_N] + \sin^2 \theta_{\odot} [P_c \cos^2 \theta_N + (1 - P_c) \sin^2 \theta_N] \quad (1.64)$$

This last expression of the solar neutrino survival probability explains perfectly the solar neutrino data, as long as $\sin^2 \theta_{\odot} \sim 0.31$ ($\theta_{\odot} \sim 34$ degrees) and $\Delta m_{\odot}^2 \sim 10^{-5}$ to 10^{-4} eV^2 . This solution is referred to as the Large-Mixing-Angle (LMA) solution due to the large value of the mixing parameter. The solar ν_e survival probability of Eq. 1.64 is shown in Fig. 1.10 as a function of the neutrino energy.

The LMA solution for the ${}^8\text{B}$ solar neutrinos was finally tested by the reactor based KamLAND experiment by the observation of the disappearance of reactor

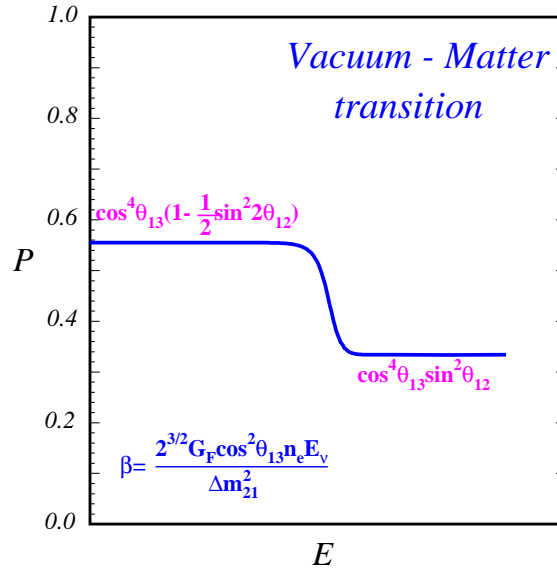


Figure 1.10: Electron neutrino survival probability as a function of neutrino energy for the LMA solution. For small values of the parameter β , the vacuum oscillation effects are dominant. For values of β greater than unity, the MSW oscillations are the most important. To properly fit the solar neutrino data, the transition between vacuum and matter oscillations should occur somewhere in the region of 2 MeV. From <http://www.sns.ias.edu/~jnb/SNviewgraphs/Roadmap>.

anti-neutrinos (with $E \sim 1 - 10$ MeV) at a distance of ~ 180 km from the sources, corresponding to the solar L/E (~ 15 km/MeV for the preferred Δm^2 region). Actually, in the two-neutrino oscillation model, CP effects (that would translate into the observation of different transition probabilities for neutrinos and anti-neutrinos) are related to the interference term between the solar and sub-leading atmospheric oscillations. For reactor experiments such as KamLAND (i.e. at the solar L/E), the atmospheric term of the oscillation probability is completely negligible. These experiments do not have the resolution to resolve the associated oscillation length which is ~ 10 times smaller than the experimental baseline. Thus, the LMA interpretation of the ^8B solar neutrino behavior implies that a substantial fraction of the reactor electron anti-neutrinos from KamLAND should disappear on their way to the detector. The survival probability measured by KamLAND (Fig. 1.11) is very well described by the two-neutrino oscillation hypothesis and almost two cycles of the expected sinusoidal structure are visible. The results of solar neutrino experiments and that of KamLAND for the oscillation parameters that are thought to be the same, perfectly overlap as depicted in Fig. 1.12.

The SNO Collaboration updated a two-neutrino oscillation analysis that includes all the solar (SNO, Super-Kamiokande, Chlorine, Gallium and Borexino) and the KamLAND data. The best-fit parameters obtained from this global solar+KamLAND analysis are $\Delta m^2 = (7.59^{+0.20}_{-0.21}) \times 10^{-5} \text{ eV}^2$ and $\theta = 34.06^{+1.16}_{-0.84}$

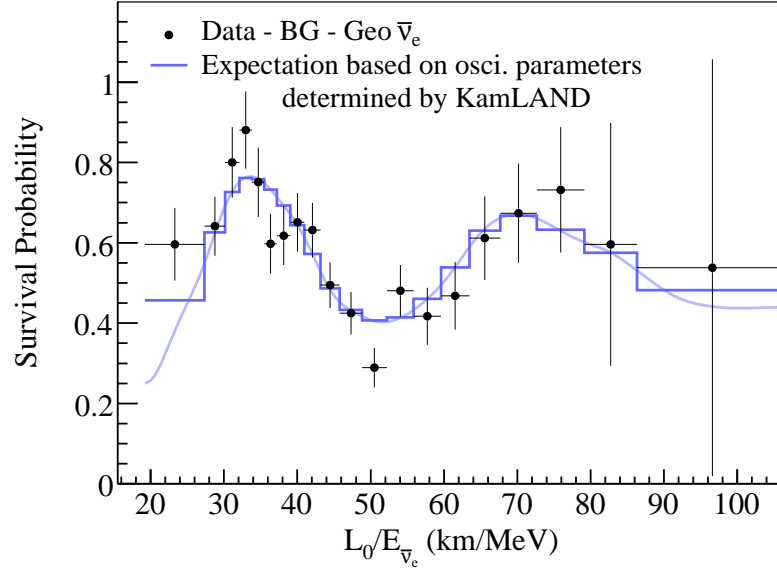


Figure 1.11: The ratio of the background and geoneutrino-subtracted $\bar{\nu}_e$ spectrum to the predicted one without oscillations as a function of L_0/E , where $L_0 = 180$ km. The curve shows the best-fit expectations for $\bar{\nu}_e$ oscillations. From [16].

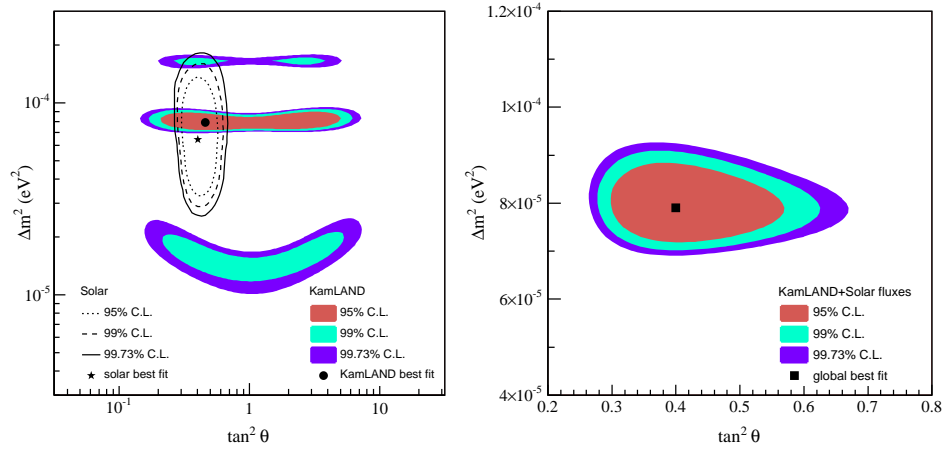


Figure 1.12: Neutrino oscillation parameter allowed region from KamLAND anti-neutrino data (shaded regions) and solar neutrino experiments (lines) (left). Result of a combined two-neutrino oscillation analysis of KamLAND and the observed solar neutrino fluxes. The fit gives $\Delta m^2 = (7.9^{+0.6}_{-0.5}) \times 10^{-5} \text{ eV}^2$ and $\tan^2 \theta = 0.4^{+0.10}_{-0.07}$ including the allowed 1σ parameter range. From [29].

degrees.

In the atmospheric sector, the zenith angle distribution of the Super-Kamiokande data alone could not completely rule out more exotic scenarios such as neutrino decay and quantum decoherence to explain the observed disappearance of the atmospheric muon neutrinos. By selecting events with a high L/E resolution though, Super-Kamiokande could confirm the characteristic sinusoidal behavior of the conversion probability and rule out other possibilities that were excluded at more than 3σ in comparison with the $\nu_\mu \rightarrow \nu_\tau$ oscillation interpretation (see Fig. 1.13). The atmospheric ν_μ disappearance was confirmed by the accelerator based K2K [30] and MINOS [31] experiments, both measuring the ν_μ flux in a near detector, before any oscillation is expected, and in a far detector at respectively ~ 250 and ~ 735 km, reproducing the atmospheric L/E ratio (~ 0.5 km/MeV for the preferred Δm^2 region). Both K2K and MINOS found that the energy spectrum of the surviving muon neutrinos in the far detector is distorted compared to the expectation without oscillation, and that the distortion is perfectly consistent with the two-neutrino oscillation hypothesis. The combined results of the atmospheric and K2K+MINOS data are depicted in Fig. 1.14.

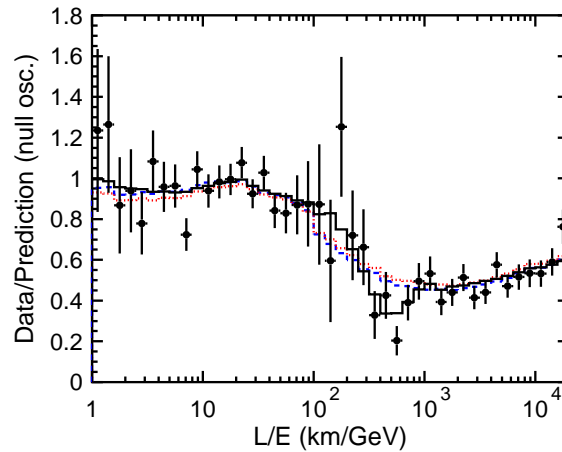


Figure 1.13: Results of the L/E analysis of the SK-I atmospheric neutrino data. The points show the ratio of the data to the Monte-Carlo prediction without oscillations as a function of the reconstructed L/E . The error bars are statistical only. The solid line shows the best-fit with two-flavor $\nu_\mu \rightarrow \nu_\tau$ oscillations. The dashed and dotted lines show the best-fit expectations for neutrino decay and neutrino decoherence hypotheses respectively. From [16].

To summarize the information reported so far, let us mention again that the understanding of neutrino oscillations was built on observations in two distinct sectors: the *solar sector* involving the suppression of solar electron neutrinos, and the *atmospheric sector* involving the suppression of atmospheric muon neutrinos:

- in the solar sector, the LMA+MSW solution describes the ν_e survival prob-

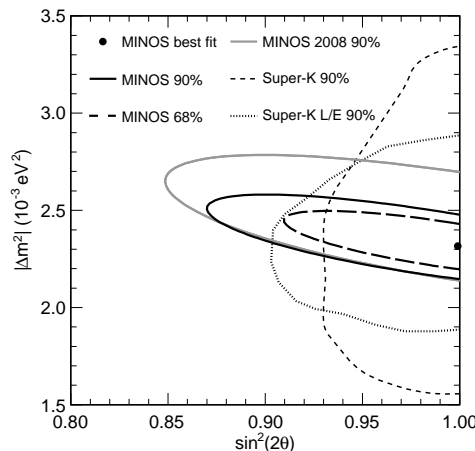


Figure 1.14: Allowed region for the $\nu_\mu \rightarrow \nu_\tau$ oscillation parameters from the MINOS results published in 2008. The 68% and 90% CL allowed regions are shown together with the SK 90% CL allowed regions. A fit to neutrino oscillations leads values of $|\Delta m^2| = 2.32^{+0.12}_{-0.08} \times 10^{-3} \text{ eV}^2$ for the mass squared splitting and $\sin^2 2\theta > 0.90$ (90% CL). From [32].

ability over the whole solar energy spectrum from ^8B down to low energy neutrinos. In the two-neutrino flavor hypothesis, the favored region for the solar parameters is $\sin^2 \theta_\odot \sim 0.3$ and $\Delta m_\odot^2 \sim 10^{-5} - 10^{-4} \text{ eV}^2$;

- the solar data clearly measures the $\nu_e \rightarrow \nu_{\mu,\tau}$ flavor change (missing electron neutrinos in SNO must have turned, at least partly, into the other active neutrino flavors to be detected);
- but it does not provide a direct proof of the oscillation hypothesis (although Super-Kamiokande did measure the ^8B solar neutrino suppression over the energy range $\sim 5 - 10 \text{ MeV}$, it turns out to be energy independent due to the validity range of the MSW effect and thus, does not show the characteristic oscillatory behavior in L/E);
- *placed* at the favored solar region, the reactor based KamLAND experiment confirms the LMA solution AND the measured survival probability as a function of L/E displays the expected sinusoidal behavior from the two-neutrino oscillation hypothesis;
- from the Super-Kamiokande atmospheric data (neutrinos with energies $\sim 1 - 10 \text{ GeV}$), the two-neutrino oscillation hypothesis, considering a baseline of $\sim 10000 \text{ km}$, favors the region $\sin^2 \theta_{\text{atm}} \sim 0.5$ and $\Delta m_{\text{atm}}^2 \sim 10^{-4} - 10^{-3} \text{ eV}^2$;

- the atmospheric data shows the characteristic sinusoidal behavior (L/E analysis of SK-I) expected from the oscillation hypothesis;
- *placed* at the favored atmospheric region, the accelerator based K2K and MINOS experiments confirm the disappearance of muon neutrinos, the measured spectral distortion of the surviving muon neutrinos being consistent with the two-neutrino oscillation hypothesis;
- the atmospheric data does not significantly measure the $\nu_\mu \rightarrow \nu_\tau$ flavor change (the no- ν_τ appearance in the Super-Kamiokande data is disfavored at only 2.4σ). The latter caveat could eventually be covered by the OPERA experiment [33] that observed so far a single event candidate for the ν_τ appearance in the CNGS muon neutrino beam in 2010.

1.3 Neutrino oscillations in the general three-flavor mixing framework

To understand the global picture of neutrino oscillations that would include solar, atmospheric, reactor and accelerator neutrino data, the two-neutrino oscillation framework is not sufficient anymore, simply because the solar (KamLAND) and atmospheric (K2K, MINOS) data point to very different values of the oscillation parameters. Almost all present data¹ can be fitted in the general three-neutrino mixing framework. Fig. 1.15 shows the region of parameter space favored or excluded by various neutrino oscillation experiments in that framework.

The parametrization of the PMNS matrix given in Eq. 1.32 can be explicitly factorized in three distinct sectors with the mixing angles θ_{12} , θ_{13} , θ_{23} and three

¹With the exception of the LSND [34] data. The LSND experiment reported an excess of $\bar{\nu}_e$ in a pure $\bar{\nu}_\mu$ beam coming from the decay of μ^+ at rest. The related KARMEN experiment [35] did not confirm the excess but it excludes only a portion of the neutrino parameter region favored by LSND. The joint analysis points to a splitting $0.2 \lesssim \Delta m_{LSND}^2 \lesssim 1 \text{ eV}^2$ ($\Delta m_{LSND}^2 \simeq 7 \text{ eV}^2$) and mixing $0.003 \lesssim \sin^2 2\theta_{LSND} \lesssim 0.03$ ($\sin^2 2\theta_{LSND} \simeq 0.004$). The MiniBooNE experiment [36] was built to check the LSND results. It studies ν_μ and $\bar{\nu}_\mu$ with an $L/E \sim 1 \text{ km/GeV}$ similar to LSND. The $\nu_\mu \rightarrow \nu_e$ analysis does not confirm LSND. The joint analysis excludes at 98% CL two-neutrino $\bar{\nu}_\mu \rightarrow \bar{\nu}_e$ oscillation as an explanation of the LSND $\bar{\nu}_e$ excess.

A recent re-evaluation of reactor $\bar{\nu}_e$ flux [37] also goes beyond the three neutrino framework. Actually, the comparison of the updated flux predictions to data measured in detectors at short baselines ($< 100 \text{ m}$) points to new oscillation parameters in the range $|\Delta m_{new}^2| > 1.5 \text{ eV}^2$ (95%) and $\sin^2 2\theta_{new} = 0.14 \pm 0.08$ (95%).

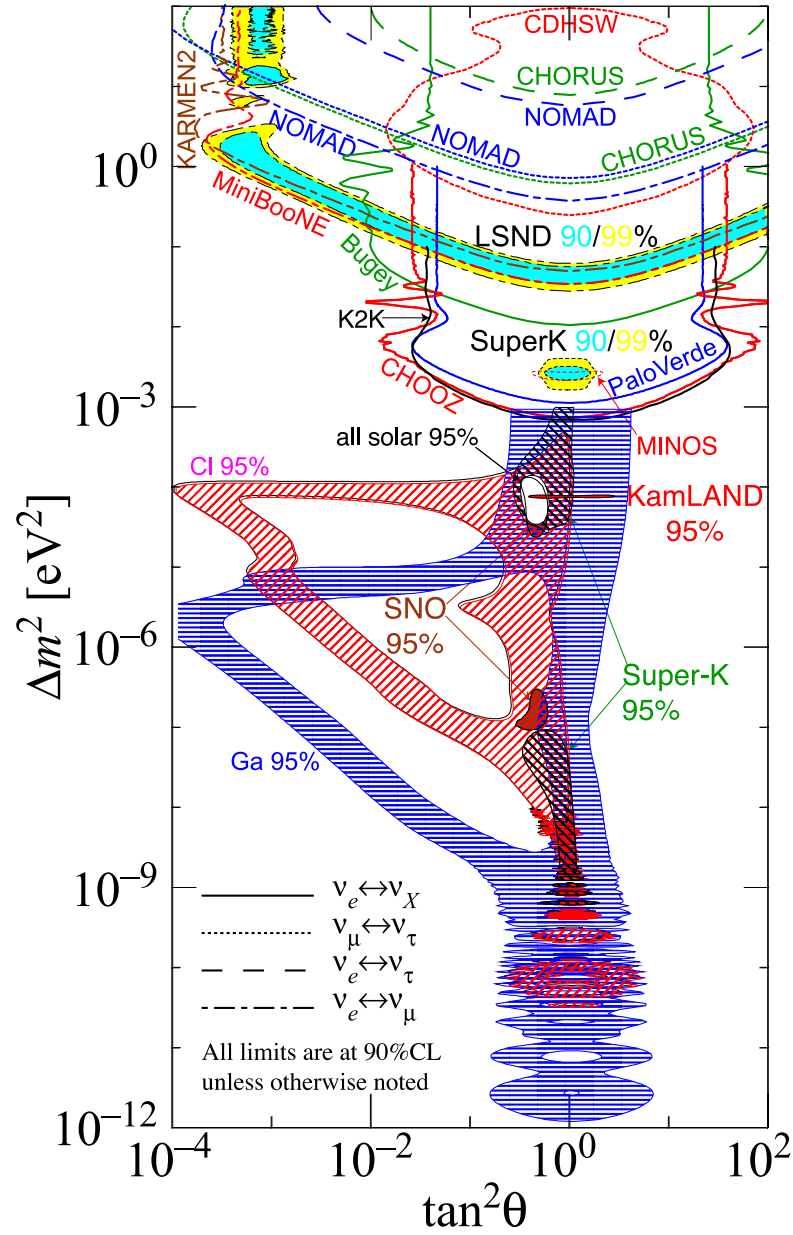


Figure 1.15: The regions of squared mass splitting and mixing angle favored or excluded by various experiments. The figure was contributed by H. Murayama (University of California, Berkeley, and IPMU, University of Tokyo). References to the data used in the figure can be found at <http://hitoshi.berkeley.edu/neutrino>. Figure extracted from [16].

complex phases, δ , ξ and η .

$$(U_{PMNS})^{ij} = \begin{pmatrix} 1 & & \\ & c_{23} & s_{23} \\ & -s_{23} & c_{23} \end{pmatrix} \begin{pmatrix} c_{13} & & s_{13}e^{-i\delta} \\ & 1 & \\ -s_{13}e^{-i\delta} & & c_{13} \end{pmatrix} \begin{pmatrix} c_{12} & s_{12} \\ -s_{23} & c_{23} \\ & & 1 \end{pmatrix} \times \begin{pmatrix} 1 & & \\ & e^{i\xi} & \\ & & e^{i\eta} \end{pmatrix} \quad (1.65)$$

For completeness, we wrote down the additional factor containing the so-called Majorana CP-odd phases, ξ and η . In the Weyl representation, the two two-component spinors ϕ and χ (Eq. 1.6) may not necessarily be independent. If they are related by $\chi = -\sigma_2\phi^*$ (σ_2 is a Pauli matrix), such spinors are referred to as *Majorana spinors*. By definition of the charge conjugation operator C ($\psi^c \stackrel{def}{=} C\gamma^0\psi^*$), using the Dirac representation of the gamma matrices, one can choose $C = \gamma^2\gamma^0$. By construction, requiring that a particle is its own anti-particle (that is $\psi = \psi^c$ with $\psi = (\phi, \chi)$) is directly related to the definition of the Majorana spinors ($\chi = -\sigma_2\phi^*$). Being the only neutral fermions, nothing prevents neutrinos from being Majorana particles. In that case, the field of any mass eigenstate ν_i is defined as its own charge conjugate up to a phase factor

$$\nu_i = \lambda_i \nu_i^c \quad (1.66)$$

As for the quarks, the leptonic mixing matrix is written in the basis where the charged lepton and (Majorana) neutrino mass matrices are real, positive and diagonal (Eqs. 1.16 and 1.21). As explained in [38], it is generically written in the form

$$U = \mathbb{E}^{i\Phi_\alpha/2} U' \mathbb{E}^{i\xi_i/2} \quad (1.67)$$

where $\mathbb{E}^{i\Phi_\alpha/2} = \text{diag}(e^{i\Phi_e/2}, e^{i\Phi_\mu/2}, \dots)$, $\mathbb{E}^{i\xi_i/2} = \text{diag}(e^{i\xi_1/2}, e^{i\xi_2/2}, \dots)$ and U' is a unitary mixing matrix. The phases contained in $\mathbb{E}^{i\Phi_\alpha/2}$ are not physical because they can be accounted for by redefining the right-handed charged lepton fields which do not participate to the charged current weak interactions. On the contrary, considering Majorana neutrino fields, the phases in $\mathbb{E}^{i\xi_i/2}$ are potentially observable (if neutrinos were Dirac particles, these phases would also be unphysical because similar to charged leptons, they would be accounted for by redefining the SM singlet right-handed neutrino fields). Thus, these phases are only physical if neutrinos are Majorana particles, but as shown in [38] they have no effect in flavor changing phenomena. The two Majorana phases ξ and η in Eq. 1.65 (only two independent phase differences are observable) affect equally all the $U_{\alpha i}$ of the PMNS matrix (they are common to all elements of a column of the PMNS matrix), while the CP-odd phase δ is not common to all elements of a column of the PMNS matrix (coming from U'). Such phases are defined as *Dirac phases*. The reason

for this definition is that on one hand, the latter phases can lead to CP violation irrespective of the nature of the neutrinos (Dirac or Majorana particles). On the other hand, if neutrinos were to be Dirac fermions, all potential Majorana phases would be unphysical due to the redefinition of the right-handed neutrino fields, and the only observable CP -odd effects would indeed come from the Dirac phases.

To understand how to reconcile all the parameters of the three-neutrino framework with the effective solar ($\theta_\odot, \Delta m_\odot^2$) and atmospheric ($\theta_{atm}, \Delta m_{atm}^2$) parameters of the simpler two-neutrino oscillation model, it is useful to relate the three mixing angles with elements of the PMNS matrix and consider the mass spectrum in more details. Actually, the elements of the PMNS matrix as defined in Eq. 1.31 are not all independent, and the parametrization of Eq. 1.32 gives

$$\frac{|U_{e2}|^2}{|U_{e1}|^2} \equiv \tan^2 \theta_{12}; \quad \frac{|U_{\mu 3}|^2}{|U_{\tau 3}|^2} \equiv \tan^2 \theta_{23}; \quad U_{e3} \equiv \sin \theta_{13} e^{-i\delta}. \quad (1.68)$$

Thus, θ_{12} relates to the fraction of ν_e in ν_1 and ν_2 , which is why the sector (12) is identified with the solar sector. Identically, θ_{23} relates to the fractions of ν_μ and ν_τ in ν_3 , and the sector (23) is identified to the atmospheric sector. The sector (13) is related to the so far unobserved ν_e flavor transitions at the atmospheric frequency that will be discussed a bit farther in this section. For the three mass eigenstates, the following convention is usually employed: $m_2^2 > m_1^2$ and $\Delta m_{12}^2 < |\Delta m_{13}^2|$. In this case, a positive sign of $|\Delta m_{13}^2|$ implies that $m_3^2 > m_2^2$, which is referred to as the *normal hierarchy*, while a negative sign yields $m_3^2 < m_1^2$, referred to as the *inverted hierarchy* (see Fig. 1.16).

Following all these definitions, the solar (reactor) and atmospheric (accelerator) observations can be formulated in the three-neutrino mixing framework. The corresponding cases of ν_e ($\bar{\nu}_e$) and ν_μ ($\bar{\nu}_\mu$) disappearance include the:

1. disappearance of solar electron neutrinos (e.g. SNO);
2. disappearance of reactor electron anti-neutrinos at the solar L/E (~ 15 km/MeV) (e.g. KamLAND);
3. disappearance of reactor electron anti-neutrinos at the atmospheric L/E (~ 0.5 km/MeV) (e.g. CHOOZ);
4. disappearance of atmospheric muon (anti-) neutrinos (e.g. Super-Kamiokande);
5. disappearance of accelerator muon (anti-) neutrinos at the atmospheric L/E (e.g. K2K, MINOS);

Let us note that there is nothing like “disappearance of accelerator muon neutrinos at the solar L/E ” mentioned in the previous list. There is actually no fundamental reason why we could not probe the neutrino oscillations with muon neutrinos at

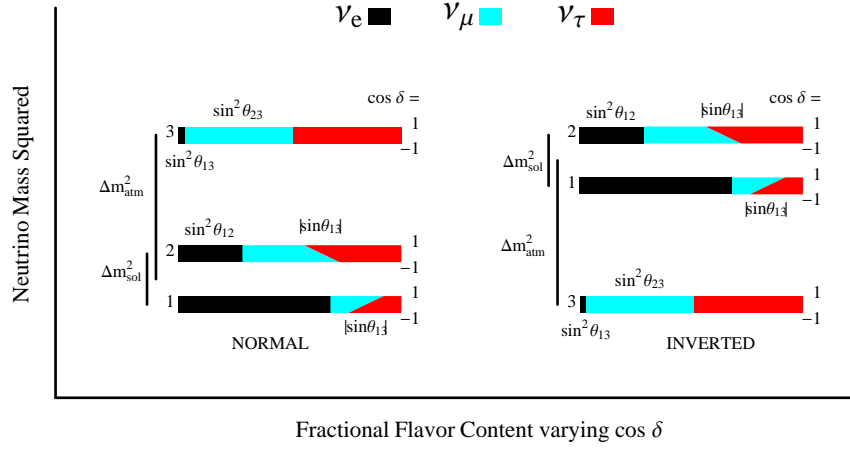


Figure 1.16: Cartoon of the two neutrino mass hierarchies that fit all the current neutrino data, for fixed values of all mixing angles and mass-squared differences, varying the CP-odd phase δ . The color coding indices the fraction $|U_{\alpha i}|^2$ of each distinct flavor ν_α , $\alpha = e, \mu, \tau$ contained in each mass eigenstate ν_i , $i = 1, 2, 3$. From [39].

the solar scale. The reason is simply technical: there is no way a reasonable accelerator ν_μ beam energy and baseline can be achieved simultaneously to be in the order of 15 km/MeV.

Using Eq. 1.45 and the unitarity of the PMNS matrix, the ν_e survival probability in the three-neutrino model is written as:

$$\begin{aligned}
 P(\nu_e \rightarrow \nu_e) = & 1 - 4 |U_{e3}|^2 |U_{e1}|^2 \sin^2 \Delta_{31} \\
 & - 4 |U_{e3}|^2 |U_{e2}|^2 \sin^2 \Delta_{32} \\
 & - 4 |U_{e2}|^2 |U_{e1}|^2 \sin^2 \Delta_{21}
 \end{aligned} \tag{1.69}$$

where $\Delta_{ij} \equiv \Delta m_{ij}^2 L / 4E$. Fig. 1.17 shows the survival probability of Eq. 1.69 as a function of L/E . For solar electron neutrinos and reactor electron anti-neutrinos at the solar L/E (points 1. and 2. of the previous list), Eq. 1.69 can be written as:

$$P_{ee} \simeq c_{13}^4 P_{ee}^{2\nu}(\Delta m_{12}^2, \sin^2 2\theta_{12}) + s_{13}^4 \tag{1.70}$$

where P_{ee} stands either for $P(\nu_e \rightarrow \nu_e)$ or $P(\bar{\nu}_e \rightarrow \bar{\nu}_e)$ and $P_{ee}^{2\nu}$ is the simple two-neutrino survival probability of Eq. 1.51. Thus, for reactor anti-neutrinos at the solar L/E , Eq. 1.70 reads:

$$P_{ee} \simeq c_{13}^4 (1 - \sin^2 2\theta_{12} \sin^2 \Delta m_{12}^2) + s_{13}^4 \tag{1.71}$$

while for solar neutrinos, the splitting and mixing parameters are the parameters in matter related to the vacuum parameters by Eqs. 1.59 and 1.60, and the matter

potential has to be modified from $A \rightarrow A \cos^2 \theta_{13}$. To derive Eq. 1.70, the subleading atmospheric oscillation has been neglected, which is fairly justified by the fact that reactor experiments such as KamLAND do not have the resolution to resolve the latter oscillation on top of the dominant solar oscillation (i.e. atmospheric effects average out since the associated oscillation length is much smaller than the experimental baseline). For solar neutrino energies ($E \lesssim 10$ MeV), the resonance density corresponding to the atmospheric scale ($|\Delta m_{13}^2|$) is by a factor of 10 larger than the electron density at the center of the Sun. In this case, the oscillations due to the atmospheric frequency occur as in vacuum. The associated oscillation length (~ 10 km) is much smaller than the production region, ΔR , of the electron neutrinos in the Sun (up to $0.2R_\odot$). Thus, the averaging over ΔR suppresses the atmospheric oscillations

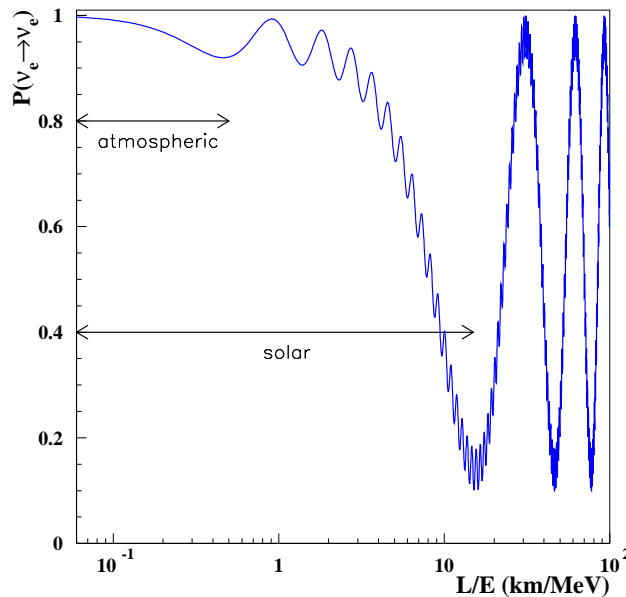


Figure 1.17: The ν_e survival probability as a function of L/E for the oscillation parameters $\sin^2 \theta_{12} = 0.31$, $\sin^2 \theta_{23} = 0.5$, $\sin^2 \theta_{13} = 0.02$, $\Delta m_{21}^2 = 8 \times 10^{-5} \text{ eV}^2$ and $|\Delta m_{32}^2| = 2.7 \times 10^{-3} \text{ eV}^2$.

Eq. 1.71 is almost an effective two-neutrino oscillation expression, all the more that θ_{13} is known to be small. This expression is used to extract the solar parameters from the data, especially Δm_{12}^2 which can be measured with high precision. In this expression, the only non-zero effect of θ_{13} is a multiplicative reduction of the survival probability. In order to measure such an effect, the neutrino flux from the reactor(s) must be predicted with great knowledge. The observation of solar

neutinos or reactor anti-neutrinos at the solar L/E is obviously not the best way to probe the sector (13) of the PMNS matrix.

That is precisely where the point 3. of our previous list makes a difference. Actually, the reactor electron anti-neutrinos have a sufficiently high flux with low energy (1-10 MeV) to be technically useful to probe both the solar and atmospheric oscillations. Within that energy range, a detector located ~ 100 km (e.g. KamLAND) from the source would probe the solar oscillation ($L/E \sim 15$ km/MeV), while a detector located at ~ 1 km would probe the atmospheric oscillation ($L/E \sim 0.5$ km/MeV). This is exactly what the CHOOZ [40] experiment aimed at, by measuring the disappearance of the electron anti-neutrinos from the Chooz nuclear reactor with a detector located at ~ 1 km. For such experiments, the survival probability of Eq. 1.69 can be written as:

$$P(\bar{\nu}_e \rightarrow \bar{\nu}_e) = 1 - \sin^2 2\theta_{13} \sin^2 \Delta_{ee} + \mathcal{O}(\Delta_{21}^2) \quad (1.72)$$

where the effects of the solar oscillation length are neglected and $\Delta_{ee} = \Delta m_{ee}^2 L/4E$. Δm_{ee}^2 is an effective atmospheric frequency defined to match the two-neutrino atmospheric oscillation:

$$\Delta m_{ee}^2 \equiv c_{12}^2 |\Delta m_{31}^2| + s_{12}^2 |\Delta m_{32}^2| \quad (1.73)$$

and corresponds to the electron flavor weighted average of Δm_{31}^2 and Δm_{32}^2 . Using $|\Delta m_{31}^2| = |\Delta m_{32}^2| \pm |\Delta m_{21}^2|$ (depending on the mass hierarchy) one can easily see that $\Delta m_{ee}^2 - |\Delta m_{13}^2| = \pm s_{12}^2 \Delta m_{12}^2$ which is a $\sim 1\%$ shift. Within these approximations Eq. 1.72 is equivalent to the simple two-neutrino oscillation expression $P_{ee}^{2\nu}(\Delta m_{13}^2, \sin^2 2\theta_{13})$ (Eq. 1.51). The CHOOZ experiment [40] did not find evidence for the $\bar{\nu}_e$ disappearance. The 90% CL upper limit was set to $\sin^2 2\theta_{13} < 0.15$ for $\Delta m^2 = 2.0 \times 10^{-3} \text{ eV}^2$. The Palo Verde reactor experiment [41] performed similar measurements and found no evidence for the $\bar{\nu}_e$ disappearance either.

Using Eq. 1.45 and the unitarity of the PMNS matrix, the ν_μ survival probability in the three-neutrino model is written as:

$$\begin{aligned} P(\nu_\mu \rightarrow \nu_\mu) = 1 - 4 & |U_{\mu 3}|^2 |U_{\mu 1}|^2 \sin^2 \Delta_{31} \\ & - 4 |U_{\mu 3}|^2 |U_{\mu 2}|^2 \sin^2 \Delta_{32} \\ & - 4 |U_{\mu 2}|^2 |U_{\mu 1}|^2 \sin^2 \Delta_{21} \end{aligned} \quad (1.74)$$

Fig. 1.18 shows the survival probability as a function of E for different fixed baselines.

For the neutrino energies considered in the atmospheric data (points 4. and 5. of our list), the effects of the solar oscillation length can fairly be neglected, the latter being much longer than the considered baselines (~ 15000 km for accelerator based neutrinos) or the diameter of the Earth (~ 150000 km for atmospheric

neutrinos). Thus for the atmospheric data, Eq. 1.74 can be written as:

$$P(\nu_\mu \rightarrow \nu_\mu) = 1 - 4 |U_{\mu 3}^2| (1 - |U_{\mu 3}^2|) \sin^2 \Delta_{\mu\mu} + \mathcal{O}(\Delta_{21}^2) \quad (1.75)$$

where $|U_{\mu 3}^2| = c_{13}^2 s_{23}^2$ and $\Delta_{\mu\mu} = \Delta m_{\mu\mu}^2 L / 4E$. $\Delta m_{\mu\mu}^2$ is an effective atmospheric frequency defined to match the two-neutrino oscillation expression:

$$\Delta m_{\mu\mu}^2 \equiv \frac{|U_{\mu 1}|^2 |\Delta m_{31}^2| + |U_{\mu 2}|^2 |\Delta m_{32}^2|}{|U_{\mu 1}|^2 + |U_{\mu 2}|^2} \quad (1.76)$$

and corresponds to the muon flavor weighted average of Δm_{31}^2 and Δm_{32}^2 .

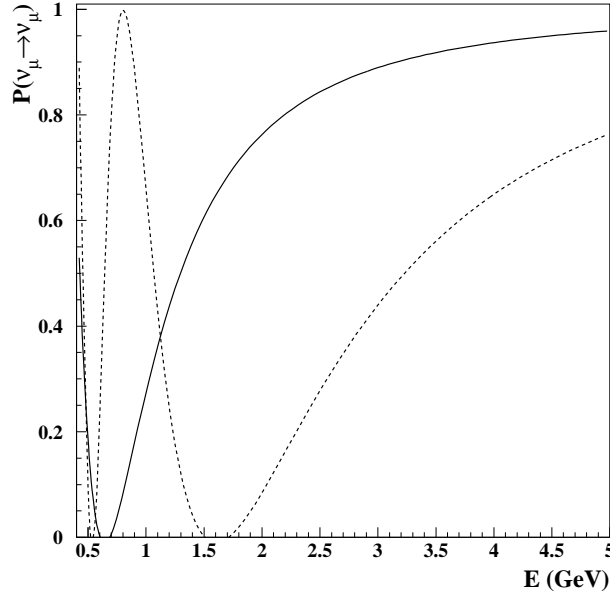


Figure 1.18: The ν_μ survival probability as a function of E for the oscillation parameters $\sin^2 \theta_{12} = 0.31$, $\sin^2 \theta_{23} = 0.5$, $\sin^2 \theta_{13} = 0.02$, $\Delta m_{21}^2 = 8 \times 10^{-5} \text{ eV}^2$ and $|\Delta m_{32}^2| = 2.7 \times 10^{-3} \text{ eV}^2$. The plain line corresponds to a baseline $L = 295 \text{ km}$ (T2K), the dashed line to $L = 735 \text{ km}$ (NOνA).

Eq. 1.75 simplifies in the limit where $\theta_{13} \rightarrow 0$ (known from the CHOOZ data). In that limit:

$$4 |U_{\mu 3}^2| (1 - |U_{\mu 3}^2|) = \sin^2 2\theta_{23} \quad (1.77)$$

$$\Delta m_{\mu\mu}^2 \equiv s_{12}^2 |\Delta m_{31}^2| + c_{12}^2 |\Delta m_{32}^2| \quad (1.78)$$

Using $\cos \theta_{13} \simeq 1$ and $|\Delta m_{31}^2| = |\Delta m_{32}^2| \pm |\Delta m_{21}^2|$ (depending on the mass hierarchy) one can easily see that $\Delta m_{\mu\mu}^2 - |\Delta m_{23}^2| = \pm s_{12}^2 \Delta m_{12}^2$ which is a $\sim 1\%$ shift. Within these approximations Eq. 1.75 is equivalent to the simple two-neutrino oscillation expression $P_{\mu\mu}^{2\nu}(\Delta m_{23}^2, \sin^2 2\theta_{23})$ (Eq. 1.51).

1.4 Unresolved questions: where do we stand ?

The three-neutrino model allows us to fit all the so far observed solar and atmospheric neutrino data within a unique framework. The current best-fit values (limits) on the oscillation parameters are:

$$\begin{aligned}
\sin^2 \theta_{12} &= 0.31 \pm 0.03, \text{ mostly solar data} \\
\sin^2 \theta_{23} &= 0.50 \pm 0.15, \text{ atmospheric and accelerator data} \\
\sin^2 \theta_{13} &< 0.04, \text{ mostly reactor (CHOOZ), accelerator data} \\
0 &\leq \delta < 2\pi \\
|\Delta m_{32}^2| &= (2.7 \pm 0.4) \times 10^{-3} \text{eV}^2, \text{ atmospheric, accelerator data} \\
|\Delta m_{21}^2| &= (8.0 \pm 0.4) \times 10^{-5} \text{eV}^2, \text{ reactor (KamLAND) data}
\end{aligned}$$

Although this gives us already a pretty complete picture of the three-neutrino model, some unresolved questions can still be addressed by oscillation experiments. In particular:

1. what is the size of $|U_{e3}|^2$, i.e. is θ_{13} different from 0 ?
2. what is the value of δ , i.e. is there CP violation in the leptonic sector ?
3. does $|U_{\mu 3}|^2 = |U_{\tau 3}|^2$, i.e. how close to maximal is the $\nu_\mu \rightarrow \nu_\tau$ mixing ?
4. what is the sign of $|\Delta m_{31}^2|$, i.e. what is the neutrino mass hierarchy ?
5. are there more than three neutrinos, i.e. are there sterile neutrinos ?

Answering the first question is what will give us a complete picture of the PMNS matrix. In the previous section we considered only the reactor $\bar{\nu}_e$ disappearance channel as a possible measure of θ_{13} at the atmospheric scale. This is indeed the purest measurement of θ_{13} , since in the very good approximation where the effects of the solar oscillation length are neglected, the suppression rate is directly given by $\sin^2 2\theta_{13}$ (Eq. 1.72). The upcoming Double CHOOZ [42], RENO [43] and Daya Bay [44] reactor experiments are designed to measure or put a limit on $\sin^2 \theta_{13}$ below the current CHOOZ limit. However, the sector (13) of the PMNS matrix can also be probed via the $\nu_\mu(\bar{\nu}_\mu) \rightarrow \nu_e(\bar{\nu}_e)$ appearance channel. Although the accelerator based K2K experiment was mainly built to confirm the atmospheric ν_μ disappearance, it was the first conventional neutrino beam experiment to probe the $\nu_\mu \rightarrow \nu_e$ oscillations. K2K did not find evidence of ν_e appearance and could set the limit $\sin^2 2\theta_{13} < 0.26$ at 90% CL at the measured $\Delta m^2 = 2.8 \times 10^{-3} \text{eV}^2$. The other conventional neutrino beam experiment, MINOS, was not only designed to be able to see a more pronounced oscillatory behavior of the muon neutrino spectrum in its far detector, and to perform a better measurement of Δm_{23}^2 than K2K, but also to achieve a better sensitivity to the $\nu_\mu \rightarrow \nu_e$ appearance. Lately, MINOS was

the first conventional beam experiment to report results with a sensitivity to θ_{13} beyond the CHOOZ limit. In the signal region, MINOS observed 62 ν_e candidates with an expected background of 50 events. Assuming $\delta = 0$ and the maximal mixing $\theta_{23} = \pi/4$, MINOS set a 90% CL upper limit of $\sin^2 2\theta_{13} < 0.12(0.19)$ and a best-fit value of $\sin^2 2\theta_{13} = 0.04(0.08)$ for the normal (inverted) hierarchy. A non-zero value of θ_{13} is excluded at 89% CL. The corresponding exclusion plots for $\sin^2 \theta_{23} \sin^2 2\theta_{13}$ as a function of δ are shown in Fig. 1.19 for both mass hierarchies.

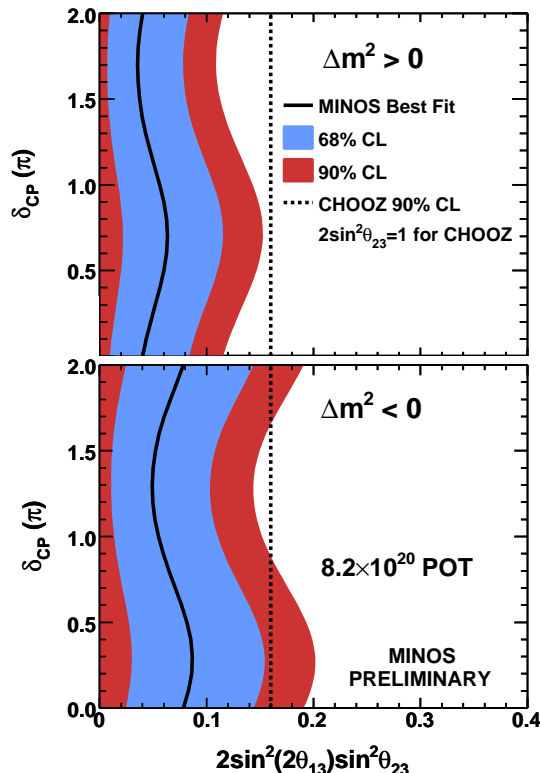


Figure 1.19: The MINOS 68% and 90% CL regions for $\sin^2 \theta_{23} \sin^2 2\theta_{13}$ for a maximal mixing $\sin^2 \theta_{23} = 1/2$ and for each value of δ_{CP} , consistent with the observed number of events in the three-flavor oscillation case for normal (top) and inverted (bottom) mass hierarchies. From <http://minos-docdb.fnal.gov/> (no 8321).

To move beyond in that direction, the $\nu_\mu \rightarrow \nu_e$ appearance (and the CP-conjugate process $\bar{\nu}_\mu \rightarrow \bar{\nu}_e$) will now be probed using much more powerful conventional beams referred to as superbeams, due to the very high intensity of the original proton beam on target. The T2K experiment [45] is the first long baseline experiment using a superbeam produced at the J-PARC accelerator complex at Tokai, Japan, with a design beam power of 0.75 MW.

Using Eqs. 1.44 and 1.45, the $\nu_\mu \rightarrow \nu_e$ oscillation probability in vacuum can be

calculated as:

$$\begin{aligned}
P(\nu_\mu \rightarrow \nu_e) &= |U_{\mu 1}^* e^{-im_1^2 L/2E} U_{e1} + U_{\mu 2}^* e^{-im_2^2 L/2E} U_{e2} + U_{\mu 3}^* e^{-im_3^2 L/2E} U_{e3}|^2 \\
&= |2U_{\mu 3}^* U_{e3} \sin \Delta_{31} e^{-i\Delta_{32}} + 2U_{\mu 2}^* U_{e2} \sin \Delta_{21}|^2 \\
&\approx |\sqrt{P_{atm}} e^{-i(\Delta_{32} + \delta)} + \sqrt{P_{sol}}|^2
\end{aligned} \tag{1.79}$$

where the unitarity relations of the PMNS matrix have been used in the second step and

$$\sqrt{P_{atm}} = \sin \theta_{23} \sin 2\theta_{13} \sin \Delta_{13} \tag{1.80}$$

$$\sqrt{P_{sol}} \approx \cos \theta_{23} \sin 2\theta_{12} \sin \Delta_{21} \tag{1.81}$$

The K2K and MINOS experiments set bounds on $\sin^2 \theta_{13}$ by using the dominant term of Eq. 1.79, which is the atmospheric driven oscillation term given in Eq. 1.80 (further approximated with $\sin^2 \theta_{23} = 1/2$ in K2K). Superbeam experiments will possibly measure or set a tighter limit on $\sin^2 \theta_{13}$ due to a much more precise measurement of the atmospheric mixing $\sin^2 2\theta_{23}$ via the ν_μ disappearance channel. Doing so, superbeams will allow us to provide answers to questions 1 and 3.

With a much higher sensitivity to θ_{13} than the conventional neutrino beam experiments, superbeams should be able to answer to the question 2 by looking at differences between $P(\nu_\mu \rightarrow \nu_e)$ and $P(\bar{\nu}_\mu \rightarrow \bar{\nu}_e)$. Actually, the interference term of the oscillation probability of Eq. 1.79 is given by

$$2\sqrt{P_{atm}}\sqrt{P_{sol}}\cos(\Delta_{32} \pm \delta) \tag{1.82}$$

where the “+” sign is for neutrinos and the “−” sign for anti-neutrinos. The expansion of $\cos(\Delta_{32} \pm \delta)$ gives rise to a CP conserving term and a CP violating term respectively given by:

$$2\sqrt{P_{atm}}\sqrt{P_{sol}}\cos \Delta_{32} \cos \delta \tag{1.83}$$

$$\mp 2\sqrt{P_{atm}}\sqrt{P_{sol}}\sin \Delta_{32} \sin \delta \tag{1.84}$$

where the “−” (“+”) sign is for neutrinos (anti-neutrinos).

When matter effects become sizable (A becomes non-negligible with respect to $\Delta m^2/2E$), the atmospheric and solar oscillation terms of Eqs. 1.80 and 1.81 are modified to

$$\sqrt{P_{atm}} = \sin \theta_{23} \sin 2\theta_{13} \frac{\sin(\Delta_{13} - AL)}{(\Delta_{13} - AL)} \Delta_{13} \tag{1.85}$$

$$\sqrt{P_{sol}} \approx \cos \theta_{23} \sin 2\theta_{12} \frac{\sin(AL)}{(AL)} \Delta_{21} \tag{1.86}$$

where $A = \pm G_F N_e \sqrt{2} \approx (4000 \text{ km})^{-1}$ in Earth, with a positive sign for neutrinos and a negative sign for anti-neutrinos. Thus, the matter effect may help answering

to question 4 and determine the type of the neutrino mass hierarchy. However, both the matter effect and the CP violating interference term would lead to a difference between $P(\nu_\mu \rightarrow \nu_e)$ and $P(\bar{\nu}_\mu \rightarrow \bar{\nu}_e)$. This is usually depicted in a bi-probability plot of $P(\bar{\nu}_\mu \rightarrow \bar{\nu}_e)$ vs $P(\nu_\mu \rightarrow \nu_e)$. The CP phase varying between 0 and 2π describes elliptical trajectories in this combined probability space. In vacuum, the ellipses corresponding to the normal and inverted hierarchies are nearly degenerate. The matter effect tends to separate these ellipses, the distance between their centers being proportional to the size of the effect. However, in the region where the ellipses for the normal and inverted hierarchies overlap, a single experiment cannot provide a value of the sign of $|\Delta m_{23}^2|$ which is not degeneracy-free for the CP phase. In order to disentangle the two contributions to the difference between the neutrino and anti-neutrino cases, the sensitivity to the matter effect must be large enough, and complementary measurements are needed. This is in particular what the combination of the T2K and NO ν A [46] experiments will be useful for (e.g. see [39]). The last question (question 5) is mainly related to the LSND puzzle ($\bar{\nu}_\mu \rightarrow \bar{\nu}_e$ transition probability driven by $\Delta m_{LSND}^2 \gg \Delta m_{atm}^2, \Delta m_{sol}^2$) and might be addressed by oscillation experiments in the sense that oscillation results can be fitted with more exotic models than the currently presented three-neutrino model. Actually, in the simplest case in which one considers only one additional sterile neutrino, only two scenarios can account for one large mass splitting and two small ones, the so-called “3+1” or “2+2” scenarios. The “2+2” scenario is ruled out by observations on solar and atmospheric data (see e.g. [24]), but other models than the “3+1” scheme, such as the “3+1+1” scenario with two additional sterile neutrinos, also allow to fit properly all the data.

Questions 1 to 5 will possibly be addressed by neutrino oscillation experiments, in particular questions 1 to 4 will be addressed by the new generation of superbeam experiments such as T2K and NO ν A via precise measurements in the $\nu_\mu \rightarrow \nu_\mu$ disappearance channel and the $\nu_\mu \rightarrow \nu_e$ appearance channel. To do better than this new era of precision measurements will require to go beyond the conventional beams which are unavoidably contaminated by intrinsic background (e.g. beam ν_e ’s from K and μ decays in a conventional ν_μ beam). Thus, future neutrino experiments will search for new facilities that can provide pure and completely flavor predictable neutrino beams. Among possible directions, the two most plausible options are the so-called *neutrino factories* and *beta-beams*. Neutrino factories actually refer to muon storage rings, where muons are stored and decay in flight producing a very well known and intense muon (anti-) neutrino and electron anti-neutrino (neutrino) beam if negative (positive) muons are stored. Beta-beams would provide pure electron (anti-) neutrino beams from the decay of β^+ (β^-) decaying nuclei stored after being accelerated to large γ factors. Possible candidates are likely to be ${}^6\text{He} \rightarrow {}^6\text{Li} + e^- + \bar{\nu}_e$ and ${}^{18}\text{Ne} \rightarrow {}^{18}\text{F} + e^+ + \nu_e$.

There are of course other unresolved questions concerning neutrinos that neutrino oscillation experiments cannot probe. Among these, the most important one deals with the true nature of neutrinos: are neutrinos Dirac or Majorana particles ? As already mentioned, the Majorana phases of the PMNS matrix do not have any effect on neutrino oscillations. Thus, whether neutrinos are their own anti-particles or not has to be addressed by another type of experiment. The most promising way of probing the Majorana nature of the neutrinos is the so-called *neutrinoless double beta decay* ($0\nu\beta\beta$). In this process, the lepton number conservation would be violated by two units since $Z \rightarrow (Z + 2) + e^-e^-$, where Z ($Z + 2$) is the atomic number of the parent (daughter) nucleus. Such a process is likely to be dominated by a mechanism in which a nucleus emits a pair of W^- bosons that exchange a neutrino mass eigenstate to produce two outgoing electrons. If CPT invariance holds, the observation of this process would demonstrate that neutrinos are Majorana particles.

From a theoretical point of view, different approaches have been considered to extend the SM in order to account for the different types of neutrino masses. A first possibility is to introduce the so far missing right-handed neutrino field ν_R , in which case the Yukawa coupling of the neutrino fields to the Higgs doublet Φ would generate a Dirac mass term (in what follows we will just consider the case of a single neutrino and omit flavors to simply illustrate the different approaches):

$$m_D(\bar{\nu}_R\nu_L + \bar{\nu}_L\nu_R) \quad (1.87)$$

where $m_D = (1/2)yv$, v being the vacuum expectation value of the Higgs field after the electroweak symmetry breaking and y the Yukawa coupling constant. To account for the value of the neutrino masses inferred from neutrino oscillations, the Yukawa coupling should satisfy $y \lesssim 10^{-12}$, that is at least six orders of magnitude smaller than the electron Yukawa coupling. Assuming that neutrinos are Majorana particles ($\nu^c = \nu$, up to a phase factor) and that the chiral components are independent, two Majorana mass terms would also be included in the Lagrangian of the new theory:

$$\mathcal{L}_\nu = m_D(\bar{\nu}_R\nu_L + \bar{\nu}_L\nu_R) + M_L(\bar{\nu}_L^c\nu_L + \bar{\nu}_L\nu_L^c) + M_R(\bar{\nu}_R^c\nu_R + \bar{\nu}_R\nu_R^c) \quad (1.88)$$

$$= \begin{pmatrix} \bar{\nu}_L^c & \bar{\nu}_R \end{pmatrix} \begin{pmatrix} M_L & m_D \\ m_D & M_R \end{pmatrix} \begin{pmatrix} \nu_L \\ \bar{\nu}_R^c \end{pmatrix} + \text{h.c.} \quad (1.89)$$

$$\equiv \bar{N}_L^c M N_L + \text{h.c.} \quad (1.90)$$

where N_L is a doublet of left-handed fields only. Each component of N_L can be written as a combination of left-handed mass eigenstates

$$\nu_L = \sum_{i=1}^2 U^{1i} \nu_L^i \quad \text{and} \quad \nu_R^c = \sum_{i=1}^2 U^{2i} \nu_L^i \quad (1.91)$$

where U is a mixing matrix written in the basis where the neutrino mass matrix is diagonal (i.e. $M' = U^t M U$ is diagonal). After diagonalization, the Lagrangian of Eq. 1.88 reads

$$\mathcal{L}_\nu \propto \sum_{i=1}^2 m_i (\bar{\nu}_L^c)^i \nu_L^i + \text{h.c.} \quad (1.92)$$

and contains only Majorana masses. The limiting case where $M_L = 0$ and $|m_D| \ll M_R$ is mostly considered. In that case, the eigenvalues of the neutrino mass matrix M , as defined in Eq. 1.89 with $M_L = 0$ are

$$m_{1,2} = \frac{M_R \pm \sqrt{M_R^2 + 4m_D^2}}{2} \simeq \frac{1}{2} [M_R \pm M_R (1 + \frac{2m_D^2}{M_R^2})] \quad (1.93)$$

that is

$$m_1 \simeq -\frac{m_D^2}{M_R} \quad \text{and} \quad m_2 \simeq M_R \quad (1.94)$$

where for m_2 the additional factor m_D^2/M_R is suppressed by the dominant term M_R . Since m_D is generated from the Yukawa coupling to the Higgs field just like for any other fermion, it is expected to be of $\mathcal{O}(m_e)$. Thus, if the Majorana mass M_R is taken to be large enough, one eigenstate acquires a mass $\ll m_e$ and the other a mass $\gg m_e$. For this reason, this mechanism is referred to as the (*type I*) *seesaw mechanism*. Another limiting case is considered when $M_L \approx 0$ is not exactly zero but very small compared to the other masses. That case leads again to two mass eigenvalues where one is proportional to M_R and the other to M_R^{-1} . It is referred to as the *type II seesaw mechanism*.

On one hand the seesaw mechanism(s) provides an explanation for the fact that neutrino masses are much smaller compared to all the other fermion masses. On the other hand, the required assumptions do not derive from any fundamental feature of the theory. The most obvious example is the type II seesaw that requires a non-zero value of M_L while this is prohibited by the gauge symmetries of the SM (the corresponding Majorana mass term in the Lagrangian, $M_L(\bar{\nu}_L^c \nu_L + \bar{\nu}_L \nu_L^c)$, is not invariant under $SU(2)$ rotations). This is not a problem in the type I seesaw where $M_L = 0$, and adding the Majorana mass term for the right-handed chirality is not forbidden since ν_R is a singlet under the SM gauge group (Eq. 1.13). This is however a problem if we suppose that neutrinos are Dirac particles. In this case, one would need to modify the symmetry structure of the SM to forbid a Majorana mass term for the right-handed neutrinos. Since such a term violates the lepton number, L , it would be forbidden by the internal global symmetry $U(1)_{B-L}$, where B is the baryon number. M_R has to be large ($M_R \gg |m_D|$) for the seesaw mechanism to work. However, it is in principle just a parameter of the model that nothing really constrains in the SM.

The previous arguments tend to disfavor the seesaw mechanism for more fundamental principles that could *naturally* explain the tiny masses of the neutrinos. In

particular, the Grand Unification Theory (GUT) considers a theory with a symmetry group larger than the current SM symmetry group, i.e. $G_{GUT} \supset G_{SM}$. This high energy theory is expected to break down to the SM at a “low” energy scale, M_{GUT} , which is generally expected to be of the order of 10^{14} GeV or higher. Since we do not observe right-handed neutrinos in our low energy experiments, it is expected that the right-handed neutrino mass is generated by some high energy processes such that $M_R \simeq M_{GUT}$. Giving up the renormalizability of the Lagrangian, such a theory could include five-dimensional operators (omitting flavors)

$$\mathcal{L}_{5d} \stackrel{def}{=} \frac{g}{M_{GUT}} ((\Psi_{e,L}^\alpha)^c \Phi^\dagger) (\Phi^\dagger \Psi_{e,L}^\beta). \quad (1.95)$$

After symmetry breaking, the Higgs field develops a non-zero vacuum expectation value and

$$m_L = \frac{gv^2}{M_{GUT}} \quad (1.96)$$

which explains the tiny neutrino masses for sufficiently large energy scales and justifies the assumption of large M_R for the seesaw mechanism.

Finally, to the question “where do we stand ?” with respect to the previously discussed and unresolved questions, the T2K experiment is without any doubt the first experiment that will allow us to bring some answers. Actually after six months of data taking, T2K is the first neutrino oscillation experiment to point to a non-zero value of the so far unknown θ_{13} mixing angle. In the near future, T2K will establish its current results more firmly and by doing so, it might also open the door to practical measurements of the CP violation in the leptonic sector. One of the main ingredients necessary to achieve these goals is the precise prediction of neutrino fluxes. The predictions of the original T2K beam simulation are presented and discussed in the next chapter.

Chapter 2

Neutrino flux predictions for the T2K experiment

2.1 Experimental setup and physics goals

The T2K long baseline neutrino oscillation experiment [45, 47] will perform a direct measurement of the *electron neutrino appearance* at the Super-Kamiokande (SK) detector in Kamioka, in a muon neutrino beam produced 295 km away at the J-PARC accelerator complex in Tokai. Doing so, it aims at measuring the so far unknown θ_{13} mixing angle, with a sensitivity down to $\sin^2 2\theta_{13} = 0.006$ at 90 % C.L. This represents an order of magnitude improvement over the current limit [40]. If θ_{13} turns out to be large enough to be measured at T2K, the search for CP violation in the leptonic sector would finally become practically possible. T2K will also perform precision measurements of the atmospheric oscillation parameters by observing the *muon neutrino disappearance*. The goal is to reach a precision of 1 % on the mixing angle, $\delta(\sin^2 2\theta_{23}) = 0.01$, and 3 % on the mass squared difference, $\delta(\Delta m_{23}^2) = 10^{-4} \text{ eV}^2$. To achieve these goals, T2K needs a high intensity neutrino beam. The J-PARC sub-GeV muon neutrino beam is a so-called *superbeam* due to the high intensity of the primary proton beam impinging on the production target. With such a proton beam, T2K will accumulate data with a 3.75 MW.yr integrated beam power, which corresponds to 5 years of running with the design beam power of 0.75 MW. The baseline of the experiment is shown in Fig. 2.1.

The T2K neutrino beam is produced by 30 GeV kinetic energy protons¹ hitting a graphite target. The primary protons are first accelerated by a LINAC, followed by a Rapid Cycle Synchrotron (RCS) up to 3 GeV and finally accelerated in the Main Ring synchrotron (MR) up to 30 GeV. The proton beam is extracted from the MR to the T2K target station through the extraction line made of normal conducting magnets and super-conducting combined-function type magnets in the

¹At later stages of the experiment the kinetic energy of incoming protons could be increased up to 50 GeV.

arc section.

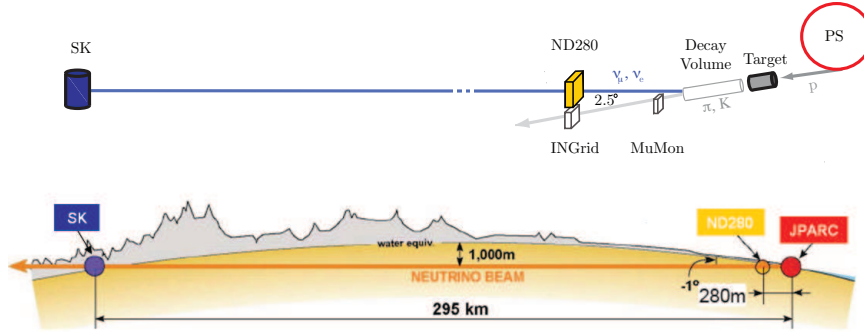


Figure 2.1: Schematic of the T2K baseline. The neutrino beam is produced at JPARC and travels the 300 km baseline towards SK. Details of the target station and near detectors are shown on top.

The production target consists in a 2.6 cm diameter and 90 cm long graphite rod with density $\rho = 1.804 \text{ g/cm}^3$. It is placed inside a cooling envelope. Details of the production target are shown in Fig. 2.2. It is important to note that the material budget around the target core (and additional material of the beam line) will contribute to the hadron production via secondary interactions. The understanding of the neutrino fluxes in terms of these different sources is mandatory for precise flux predictions. This will be further developed in the following sections. Outgoing positively charged hadrons (mainly pions, kaons and protons) are focused in the beam direction through a set of three magnetic horns operated at a pulsed current of $\sim 250 \text{ kA}$ (horns are designed for an operating current of 320 kA). Pions and kaons decay in flight along a $\sim 100 \text{ m}$ long decay pipe and produce an effective neutrino beam. Neutrinos are also generated in the decay of muons, themselves produced in the decay of pions and kaons. A beam dump is located at the end of the decay pipe, $\sim 110 \text{ m}$ away from the target. While most hadrons are absorbed in the beam dump, muons with kinetic energy greater than 5 GeV can go through. Since these muons are produced with neutrinos in the decay in flight of the focused parent pions and kaons, they reflect the beam direction and intensity. Muon monitors (MUMON) are placed right after the beam dump to measure this muon flux. It provides pulse-by-pulse information on the beam profile and intensity. The beam direction is furthermore precisely measured by the INGRID detector located 280 m away from the production target. It consists in a cross-shaped array of X-Y plastic scintillator planes interleaved with iron plates, that allow to measure the beam direction with a precision better than 1 mrad . The INGRID detector is actually associated to a detector complex located at 280 m from the target station and referred to as the ND280. The ND280 is a fine-grained spectrometer that aims at measuring the beam energy and neutrino flavor content

before oscillation. Details about the detectors that constitute the ND280 are given in [45, 48, 49].

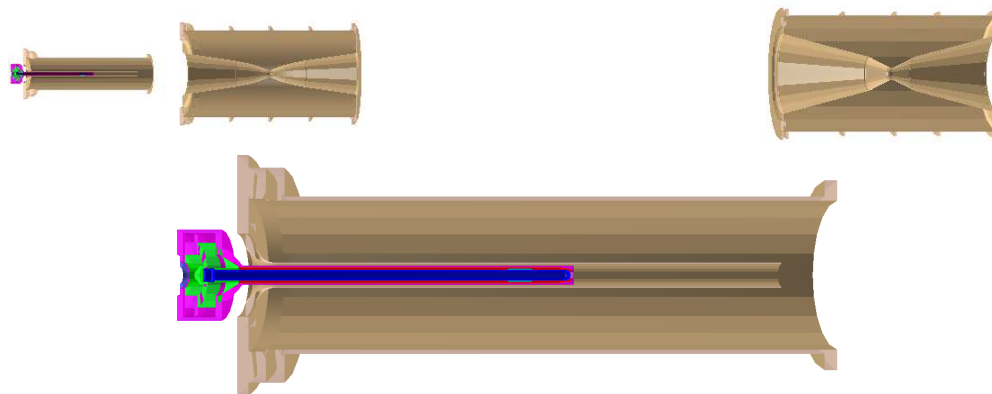


Figure 2.2: The T2K focusing system consists in a set of three magnetic horns (top). The production target (bottom) is placed in a cooling envelope (Carbon pipe shown in red) surrounded by a Titanium case (pink) which is embedded inside the first magnetic horn. The target support (green) consists of Carbon and includes the target head which is accounted for in the total length of the target. The main Carbon rod considered for our studies is shown in blue.

While the INGRID detector is located on the beam axis, the ND280 detector complex is actually placed off-axis. The most important element in the design of the T2K beam facility at J-PARC is that the beam is not pointing directly to the detector direction. Instead, it is slightly shifted off-axis with an angle of 2.5° . This tilt has immediate consequences on the shape and intensity of the neutrino flux due to simple kinematic relations. All the calculations in this section are presented in more details in Appendix A which refers to [50]. The polar axis in the laboratory system is given by the direction of the beam, while for the center-of-mass system of the decaying meson we take the meson direction as polar axis. The meson beam is considered divergence-less so that the azimuthal degree of freedom can be omitted, which reduces the problem to two dimensions. The neutrino four-momentum is expressed in the laboratory frame from the Lorentz boost applied to the four-momentum in the pion rest frame:

$$(E_\nu, E_\nu \sin \theta, 0, E_\nu \cos \theta) = (\gamma_\pi E_\nu^* (1 + \beta_\pi \cos \theta^*), E_\nu^* \sin \theta^*, 0, \gamma_\pi E_\nu^* (\cos \theta^* + \beta_\pi)) \quad (2.1)$$

from which we can deduce a relation for the angle θ between the neutrino and the pion direction in the laboratory frame as a function of the neutrino angle θ^* in the pion rest frame:

$$\sin \theta = \frac{E_\nu^* \sin \theta^*}{E_\nu} \quad (2.2)$$

Since $\sin \theta^*$ is bound by unity, this relation shows that a given neutrino energy E_ν can only be found up to a maximal laboratory angle:

$$\theta^{\max}(E_\nu) = \arcsin\left(\frac{E_\nu^*}{E_\nu}\right) \quad (2.3)$$

Conversely, at a given angle θ from the beam direction, the maximum neutrino energy is:

$$E_\nu^{\max}(\theta) = \frac{E_\nu^*}{\sin \theta} \quad (2.4)$$

The effect of the off-axis beam configuration can be understood from Eq. 2.4 if we make the simplifying assumption that all mesons are produced parallel. As can be seen in Fig. 2.3 the neutrino energy depends linearly on the pion energy for an on-axis beam. This relation becomes weaker for larger values of the off-axis angle. Around the maximum energy that can be observed for a given off-axis angle, the neutrino energy becomes almost independent of the parent pion energy. Thus, a large range of pion energies contribute to a much smaller range of neutrino energies.

To understand the effect of the off-axis configuration on the shape of the neutrino flux, we need to consider a certain energy distribution of the produced π mesons in the laboratory frame, e.g.:

$$g(E_\pi) \propto (E_p - E_\pi)^5 \quad (2.5)$$

where E_p is the proton beam energy. Even assuming a constant E_ν^* (e.g. 2-body decay), the two final state variables E_ν and $\cos \theta$ can vary independently. To derive their distribution, we need to compute the Jacobian of the transformation $(E_\pi, \cos \theta^*) \rightarrow (E_\nu, \cos \theta)$, which leads to the following expression:

$$\begin{aligned} \frac{d^2 P}{dE_\nu d\Omega} = \frac{m_\pi}{4\pi E_\nu^* \sin \theta^2 \sqrt{1 - r^2 \sin^2 \theta}} & [g(m_\pi \gamma_+) | \cos \theta - \sqrt{1 - r^2 \sin^2 \theta} | \\ & + g(m_\pi \gamma_-) | \cos \theta + \sqrt{1 - r^2 \sin^2 \theta} |] \end{aligned} \quad (2.6)$$

where $r = E_\nu/E_\nu^*$ and

$$\gamma_\pm \equiv \frac{1 - \epsilon \cos \theta \sqrt{1 - r^2 \sin^2 \theta}}{r \sin \theta^2} \quad (2.7)$$

with $\epsilon = \pm 1$ respectively (see Appendix A for details). If $r \leq 1$ only the second term is to be kept in Eq. 2.6. This distribution is plotted in Fig. 2.3 for different

values of the off-axis angle θ . The enhancement of the neutrino flux is clearly observed for values of θ different from zero. Using a lower momentum proton beam would produce the (needed) low momentum neutrino beam at the cost of intensity and large energy dispersion. By employing a higher momentum proton beam and using the off-axis configuration, a much higher intensity neutrino beam is concentrated at the required energy since a large range of meson momenta contribute to the yield of neutrinos at the energy selected through the chosen off-axis angle.

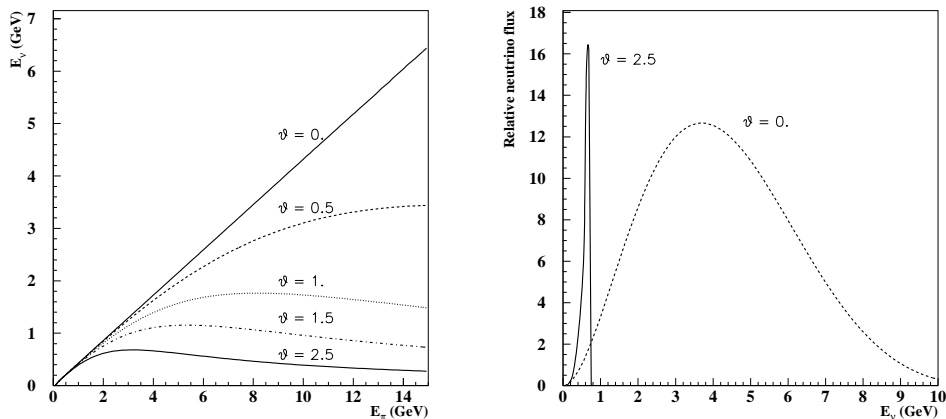


Figure 2.3: Example of the off-axis beam properties (for 30 GeV incoming protons): neutrino energy as a function of the pion energy (left) and neutrino flux (right) for different values of the off-axis angle, θ (in degrees).

After traveling the ~ 300 km baseline distance, the T2K neutrino beam is measured in the 50 kt water Cherenkov detector, Super-Kamiokande ([51],[52]), located in the Kamioka mine at a depth of 2700 m water equivalent. The total fiducial mass of the detector is 22.5 kt. The Cherenkov radiation produced by the relativistic charged particles going through the fiducial volume is detected by 11000 surrounding photo-multiplier tubes (PMTs). Their pulse height and timing information allow to reconstruct the production vertex, energy and direction of the particle. The particle identification is provided by the shape of the Cherenkov rings and yields a good e/μ separation: muon leave a clear ring in the detector, while electrons and photons, which undergo electromagnetic showers, leave fuzzy rings.

T2K will probe neutrino oscillations by using the measurements of both near (ND280 detector) and far (SK) detectors. The ν_μ and ν_e signals in the region of interest for T2K are dominated by the charged-current quasi-elastic (CCQE) contribution (see Fig. 1.2): $\nu_l + n \rightarrow p + l^-$, where $l = \mu, e$. Other contributions

come from the charged-current reaction with the production of a single charged pion (CC1 π) and the neutral-current reaction with the production of a single neutral pion (NC1 π^0), the latter being, with the intrinsic ν_e contamination in the beam, the main background for the ν_e appearance. Assuming that the neutrino direction is known (i.e. direction of the beam) and that the target nucleon is at rest (i.e. neglecting Fermi motion), the neutrino energy can be reconstructed from the measured direction, θ_l , and energy, E_l , of the charged lepton of mass, m_l , emitted in the CCQE process:

$$E_{\nu_l}^{QE} = \frac{2M_n E_l - (M_n^2 + m_l^2 - M_p^2)}{2[M_n - E_l + \sqrt{E_l^2 - m_l^2} \cos \theta_l]} \quad (2.8)$$

where M_n (M_p) is the mass of the neutron (proton).

The expected number of events (signal or background) at SK can be extrapolated from the corresponding measurements at the near detector. Among others, the *far-to-near ratio* extrapolation method can be used. In this method, the expected neutrino flux at SK, Φ_{SK}^{exp} , is given by the extrapolation of the near detector measurements, $\Phi_{SK}^{exp} = R_{F/N} \cdot \Phi_{ND}$, where $R_{F/N}$ is the so-called far-to-near ratio. The latter is determined using the beam simulation and is consequently model dependent. The expected number of events at SK as a function of the reconstructed neutrino energy, E_{ν}^r , is given by:

$$\begin{aligned} N(E_{\nu}^r)_{SK}^{exp} &= \int dE_{\nu}^t \{ \Phi_{SK}^{exp} \cdot P_{osc}(E_{\nu}^t) \cdot \sigma_{SK}(E_{\nu}^t) \cdot \epsilon_{SK}(E_{\nu}^t) \cdot r(E_{\nu}^r, E_{\nu}^t) \} \\ &= \int dE_{\nu}^t \{ \Phi_{ND} \cdot R_{F/N} \cdot P_{osc}(E_{\nu}^t) \cdot \sigma_{SK}(E_{\nu}^t) \cdot \epsilon_{SK}(E_{\nu}^t) \cdot r(E_{\nu}^r, E_{\nu}^t) \} \end{aligned} \quad (2.9)$$

where E_{ν}^t is the true neutrino energy, Φ_{SK}^{exp} the expected neutrino flux at SK, P_{osc} the oscillation probability, σ_{SK} the relevant neutrino interaction cross section, ϵ_{SK} the corresponding detection efficiency and $r(E_{\nu}^r, E_{\nu}^t)$ the detector response function. The oscillation parameters can be extracted from the comparison between the measured energy spectrum at SK and the predicted spectra with and without the oscillation hypothesis. The neutrino flux at ND is evaluated as $\Phi_{ND} = N(E_{\nu}^r)_{ND}^{obs} / (\sigma_{ND}(E_{\nu}^t) \cdot \epsilon_{ND}(E_{\nu}^t))$, where N_{ND}^{obs} is the observed number of events at ND and σ_{ND} and ϵ_{ND} are the corresponding cross section and efficiency at the near detector. The error on the expected number of events at SK comes from errors on the different terms of Eq. 2.9:

- (i) near detector measurements: to avoid complicated distortion effects of the near and far energy spectra, the energy scale at the near detector should reach a precision as good as the current 2 % resolution at SK;
- (ii) far-to-near ratio extrapolation: due to the finite extension of the production source (target + decay volume), the far-to-near ratio does not simply follow

a $1/r^2$ law, but is a complicated function of the true neutrino energy. This is the largest error contribution due to poor knowledge of the hadron production at the T2K proton beam energy. The goal is to reduce this error down to 2-3 %. This in turn implies a precision of 5 % on the absolute flux predictions (more details are given in Section 2.3.3);

- (iii) neutrino interaction cross sections: as already mentioned, neutrino-nucleon cross sections are currently known with large uncertainties in the neutrino energy range of ~ 1 GeV where T2K is operating. The near detector will perform dedicated cross section measurements with an expected precision of 5 %;
- (iv) detection efficiencies: are well measured and understood in SK. This is the smallest contribution to the total error and estimated below 1 %. A similar precision should be reached at the near detector.

To fulfill the T2K physics goals, constraining (ii) below 2-3 % is mandatory to obtain a total systematic error smaller than 10 % on the prediction of the number of background events in both appearance and disappearance channels [53].

The construction of the J-PARC accelerator complex in Japan, Tokai, was completed in 2008. The beamline of the T2K neutrino facility was finalized in March 2009 and at the end of April 2009, the first proton beam was successfully extracted from the Main Ring synchrotron to the target station. The measurements of the muon flux in the MUMON on-axis detector confirmed that the neutrino beam was effectively produced. After the commissioning of the beamline and detectors (see [49]), the stable data taking started in January 2010. Stable operation was performed at 50 kW since April 2010. By June 1st 2010, the integrated number of protons for analysis was 3.23×10^{19} . This defines the Run1 physics data taking period. During the summer shutdown starting from July 2010, new kicker magnets were installed in order to allow an operation of the beam with the designed number of 8 bunches per spill (previously 6 bunches were available). The data taking resumed mid November 2010 but unfortunately, stopped dramatically on March 11th 2011, when a powerful earthquake stroke off the northeast coast of Japan producing a tsunami that further triggered catastrophic events at the Fukushima nuclear power plant, and led Japan to suffer the considerable human and material losses that we are now aware of. The T2K experiment itself was affected by the earthquake but most damages are under control and ongoing repair work is mostly dedicated to realignment and gas tightness of the target station and decay tunnel. The goal is to get the beam back in operation by the end of 2011. These dramatic events mark the end of the Run2 data taking period of T2K, during which the beam power continually increased and reached 145 kW. The total accumulated number of protons on target for analysis (Run1 + Run2) is 1.43×10^{20} . The T2K

Parameter	Value
Beam tilt [°]	3.737
Beam momentum [GeV/c]	30.9238
Beam offset (x,y) [cm]	-
Beam width (σ_x, σ_y) [cm]	0.4243, 0.4243
Beam emittance (ϵ_x, ϵ_y) [π mm mrad]	-
Beam Twiss parameters (α_x, α_y)	-
Protons on target	10^{21}
Target length [cm]	90
Target diameter [cm]	2.6
Horn currents (1,2,3) [kA]	320, 320, 320
Detector distance (near,far) [km]	0.280, 295
Detector vertical tilt (near,far) [°]	1.733, 1.263
Detector horizontal tilt (near,far) [°]	-0.624, 0.783

Table 2.1: Main parameters of the T2K beamline simulation in the JNUBEAM 10a release.

experiment just published its very first results for the ν_e appearance channel [54], and just released results on the ν_μ disappearance, e.g. [55]. The ν_e appearance results and, in particular, the impact of the NA61 data on these results are discussed in Chapter 5.

2.2 The T2K beamline simulation program

2.2.1 Simulation of the neutrino beam

The version of the T2K beamline simulation code (JNUBEAM 10a) used in these studies was released in January 2010. The simulation code is based on GEANT 3.21 [56] for particle propagation, while primary and secondary interactions are simulated by the GCALE model [57] interfaced to GEANT 3.21. Particles are propagated through the geometry and magnetic fields of the beamline including target, cooling envelope, magnetic horns, decay pipe and beam dump (see Fig. 2.4). A precise description of the geometry and material budget of the beamline is extremely important in this respect. Protons with a kinetic energy of 30 GeV are injected into the 90 cm long carbon production target. The beam profile is assumed to be Gaussian-like and the beam is centered on the target axis with no divergence. Events are stored in the NTUPLE output format [58] for both near and far detectors. The main parameters used for the simulation are summarized in Table 2.1. In particular the beam tilt and the positions of the near and far detectors lead to the off-axis angles $\theta_{OA}^{ND} = 2^\circ$ and $\theta_{OA}^{FD} = 2.5^\circ$ respectively. No fiducial cuts are applied during simulation. For the ND280 near detector, a fiducial cut of 150×150 cm² on the transverse area is applied at the analysis level.

Typical high-energy neutrino beams are generated from decays of charged π and K mesons produced in the interaction of a primary proton beam impinging on

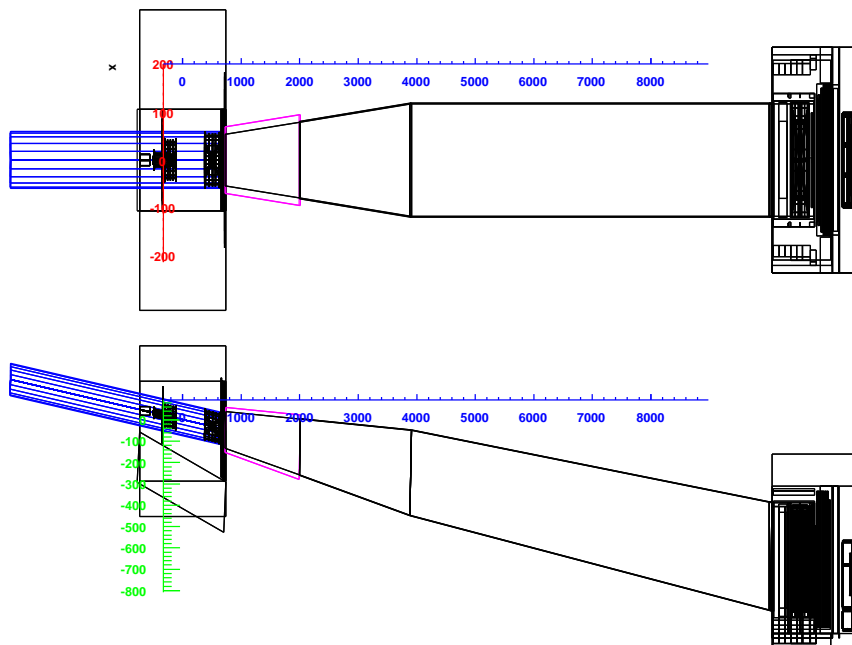


Figure 2.4: The layout of the T2K beamline geometry in horizontal (top) and vertical (bottom) projections (axis units are in [cm]). The production target and focusing system are located in the target station (left) followed by the ~ 100 m long decay tunnel. The beam dump is located at the downstream end of the decay pipe.

a thick nuclear target. Those secondary particles leave the target boosted in the forward direction but still with some divergence given by the production cross-section $d^2\sigma/dp_T dx_F$, where p_T is the transverse momentum and $x_F \equiv p_L/p_0$ is the Feynman scaling variable (which is roughly the ratio between the longitudinal momentum component of the secondary hadron p_L and the proton beam momentum p_0). It is worth mentioning here two important aspects of hadron production which are described in more details in different studies performed to characterize the properties of such neutrino beams, e.g. [59]. The first one is that the momenta of the produced hadrons scale with p_0 (e.g. similar shapes of dN/dx_F for different p_0 values), which means that the yield of hadrons with a given momentum selected to produce neutrinos of a particular energy drops with a decreasing beam momentum. The second important aspect of hadron production is that p_T does not scale much with beam momentum, which is important since transverse momentum is what controls the divergence of the secondary beam. Since the main source of transverse momentum in hadron production is the Fermi momentum of partons inside the nucleons ($\sim \hbar/1 \text{ fm} \approx 200 \text{ MeV}$), the amount of transverse momentum to be compensated for by the focusing system is of the order of the Fermi momen-

tum. This transverse momentum is small enough to get an efficient operation of magnetic horns even for high beam momenta.

The precise manipulation of π/K beams controls the energy spectrum and flavor content of the neutrino beam. Besides the ν_μ component from the pion decays, these beams will also contain intrinsic $\bar{\nu}_\mu$ and ν_e components from the subsequent muon decays. In the standard configuration of an accelerator-based neutrino experiment, pions from the production target are first focused through a set of magnetic horns before they decay in flight along a decay tunnel. A beam dump is usually placed at the end of the decay tunnel. Thus, both pion and muon decays occur along the decay pipe. From these considerations, we can estimate the beam composition that a neutrino beam simulation based on such a beamline may predict. Actually, although predictions will depend on the hadron production model chosen for the simulation of primary and secondary interactions, differences in models will affect the absolute normalization of the fluxes rather than the flux composition itself, which is mainly determined by the geometry of the beamline. From our basic description, we will assume that the relative proportion of pions and muons in the beam is roughly given by the ratio of their life time in the laboratory before they reach the beam dump. For simple estimations, we consider pions as the main source of muons that will produce the ν_e component of the beam. The muon energy in the laboratory frame is given by the Lorentz transformation from the pion rest frame:

$$E_\mu = \gamma_\pi(E_\mu^* + \beta_\pi \cos \theta^* p_\mu^*)$$

so that on average $E_\mu = \gamma_\pi E_\mu^*$ and the ratio of the pion and muon gamma factors is:

$$\frac{\gamma_\pi}{\gamma_\mu} \approx \frac{m_\mu}{E_\mu^*} = m_\mu \frac{2m_\pi}{m_\pi^2 + m_\mu^2} = 0.96$$

which leads to a life time ratio in the laboratory of:

$$\frac{\gamma_\pi \tau_\pi}{\gamma_\mu \tau_\mu} \approx 0.96 \times \frac{\tau_\pi}{\tau_\mu} = 1.14 \times 10^{-2}$$

Thus, the JNUBEAM simulation is expected to predict an integrated ν_e beam component of the order of 1% of the main ν_μ component. Other contributions to the ν_e component like that of the kaon three-body decay can also be roughly estimated. Assuming a rate of about 10% that of pions for charged kaons at the T2K proton beam energy, and a branching ratio of about 5% (see Table 2.2), yields an additional $0.1 \times 0.05 = 0.5\%$. However, such a contribution (similar to that of the pion decay to electron and neutrino) is too low to be precisely calculated from back-of-envelope estimations. The estimated 1% for the ν_e component is also valid for the $\bar{\nu}_\mu$ component since muon decays produce both species equally. But

although π^- are not focused by the system of magnetic horns (in the case of a positive focusing to produce a ν_μ beam) the production rate is still large enough to contribute dominantly to the $\bar{\nu}_\mu$ flux. The expected integrated $\bar{\nu}_\mu$ component should then be larger than that of ν_e . In these estimations, it is also worth mentioning the contribution from the so-called “prompt” neutrinos (produced in charmed meson decays). For the current configuration of the T2K neutrino beam (which is produced by 30 GeV protons) it is expected to be negligible, see e.g. [60, 61, 62].

All the previous estimations relate to the beam flavor content only. As described in Section 2.1, geometrical considerations (off-axis beam configuration) can also allow us to estimate the mean energy of the expected neutrino flux. The T2K baseline is ~ 300 km long. As illustrated in Fig. 1.7, this corresponds to the first minimum of the ν_μ survival probability for a neutrino energy of ~ 600 MeV, assuming $\Delta m^2 = 2.5 \times 10^{-3} \text{ eV}^2$. This in turn would correspond to an off-axis angle of ~ 2.86 degrees using Eq. 2.3. The T2K far detector is located at 2.5 degrees off-axis. The JNUBEAM simulation is then expected to produce ν_μ fluxes peaked around 680 MeV. Fluxes at the near detector should have a slightly higher mean energy due to the larger solid angle subtended by the detector and the finite extension of the production region.

2.2.2 Simulation of neutrino fluxes

Neutrino parent particles are propagated through the beamline geometry till they decay. To save computation time, neutrinos are not propagated but their production is forced in the direction of the near and far detectors. This is done by weighting each entry on output by the probability that neutrinos are produced at the parent decay position in the laboratory frame, in the direction of the near and far detectors. For the far detector, the distance to the source is large enough to consider the latter as point-like, and the neutrino parent decay point can be approximated to the parent production point. For the near detector, a point on the extended near detector cross section is first randomly chosen, so that the distance between the neutrino production point and the detector has to be recomputed for each neutrino to get the probability for this particular direction. In addition to the probability to reach the near and far detectors, neutrino entries on output are also weighted by a normalization factor to 10^{21} protons on target and by the normalized branching ratio corresponding to their parent decay mode. The GEANT 3.21 package treats identically different neutrino species (ν_e , ν_μ , ν_τ). Thus, a set of appropriate routines is used in the JNUBEAM code to treat neutrinos properly according to their parent particle type (taking into account branching ratio, decay kinematics and the effect of the muon polarization). The original code includes muon decay, pion and kaon 2-body decays and kaon 3-body decays $K \rightarrow \pi e \nu_e$ for charged and neutral kaons. We implemented the corresponding kaon 3-body decays to muons, as well as the $\pi \rightarrow e \nu_e$ decay (missing in GEANT 3.21 but im-

Channel	$B_r[\%]$	$B_r[\%](\text{updated})$	Normalization (updated)
$\pi^\pm \rightarrow \mu^\pm \nu_\mu(\bar{\nu}_\mu)$	100	99.9877	1
$\mu^\pm \rightarrow e^\pm \nu_e(\bar{\nu}_e)\bar{\nu}_\mu(\nu_\mu)$	100	100	1
$K^\pm \rightarrow \mu^\pm \nu_\mu(\bar{\nu}_\mu)$	63.51	63.55	71.97
$K^\pm \rightarrow \pi^0 e^\pm \nu_e(\bar{\nu}_e) (K_{e3}^\pm)$	4.82	5.07	71.97
$K_L^0 \rightarrow \pi^\pm e^\mp \nu_e(\bar{\nu}_e) (K_{e3}^0)$	38.78	40.55	67.59
$K^\pm \rightarrow \pi^0 \mu^\pm \nu_\mu(\bar{\nu}_\mu) (K_{\mu3}^\pm)$	3.27	3.35	71.97
$K_L^0 \rightarrow \pi^\pm \mu^\mp \nu_\mu(\bar{\nu}_\mu) (K_{\mu3}^0)$	27.17	27.04	67.59
$K_S^0 \rightarrow \pi^\pm e^\mp \nu_e(\bar{\nu}_e)$	neglected	–	–
$K_S^0 \rightarrow \pi^\pm \mu^\mp \nu_\mu(\bar{\nu}_\mu)$	neglected	–	–
$\pi^\pm \rightarrow e^\pm \nu_e(\bar{\nu}_e)$	–	0.0123	1

Table 2.2: Decay channels and branching ratios of neutrino parents used in JNUBEAM. The third column shows updated values of branching ratios and the fourth column shows updated normalization factors. The lower part of the table shows additional channels. Charged kaon decays are normalized to all semileptonic and leptonic modes (neglecting contributions of the order of 10^{-5} and less). K_L^0 decays are normalized to all semileptonic modes (neglecting contributions of the order of 10^{-7} and radiative modes). The K_S^0 decays are neglected. The pion decays to μ/e + neutrino are normalized to 1 neglecting other leptonic and semileptonic modes (all $< 10^{-3}$).

portant for the precise prediction of the ν_e component in the beam for the $\nu_\mu \rightarrow \nu_e$ appearance search) in the JNUBEAM 10a release. The semileptonic decays of K_S^0 are neglected. The updated JNUBEAM code finally accounts for 18 decay modes. All these contributions are summarized in Table 2.2. Updated values ([63]) of the neutrino parent branching ratios used in these studies are also quoted. In the case of positive focusing currently used in T2K, the ν_μ 's are mainly produced in π^+ decays (with the branching ratio $B_r(\pi^+ \rightarrow \mu^+ \nu_\mu) = 99.9877\%$) followed by K^+ decays (with the branching ratio $B_r(K^+ \rightarrow \mu^+ \nu_\mu) = 63.51\%$ normalized to all leptonic and semileptonic decays) and a much smaller contribution from μ^- decays (with the branching ratio $B_r(\mu^- \rightarrow e^- \bar{\nu}_e \nu_\mu) = 100\%$). The $\bar{\nu}_\mu$'s are generated from the charge-conjugated processes with major contributions from π^- and from μ^+ decays, followed by a smaller contribution from K^- decays. The ν_e 's are mainly produced in μ^+ decays (with the branching ratio $B_r(\mu^+ \rightarrow e^+ \nu_e \bar{\nu}_\mu) = 100\%$) followed by the K^+ 3-body decay called K_{e3}^+ (with the branching ratio $B_r(K^+ \rightarrow \pi^0 e^+ \nu_e) = 4.82\%$ normalized to all leptonic and semileptonic decays) and a smaller contribution from the K_L^0 3-body decay called K_{e3}^0 (with the branching ratio $B_r(K^0 \rightarrow \pi^- e^+ \nu_e) = 38.78\%$ normalized to all semileptonic decays). The $\bar{\nu}_e$'s are generated from the charge-conjugated processes with a major contribution from K_L^0 decay followed by contributions from K^- and μ^- decays. For the kaon 3-body decay the Dalitz plot density of the V-A theory is used. For the muon decay the energy and angular distributions of the ν_μ ($\bar{\nu}_\mu$) and $\bar{\nu}_e$ (ν_e) are calculated according to Michel spectra of the V-A theory and the parent muon polarization is taken into account.

When a neutrino parent decays, the neutrino energy in the parent rest frame, E_ν^* , is calculated according to the decay kinematics. For the charged pion and

kaon 2-body decays, the value of the neutrino energy is fixed by the 4-momentum conservation in the parent rest frame:

$$\begin{aligned} p_\pi &= (p_l + p_\nu) \\ p_K &= (p_\mu + p_\nu) \end{aligned} \quad (2.10)$$

which leads to:

$$\begin{aligned} E_\nu^* &= \frac{m_\pi^2 - m_l^2}{2m_\pi} \\ E_\nu^* &= \frac{m_K^2 - m_\mu^2}{2m_K} \end{aligned} \quad (2.11)$$

where p_α and m_α stand for the four-momentum and mass of particle α respectively. The subscript l for the pion decay stands for both decays to muon and electron with neutrino energies of 0.03 and 0.07 GeV in the pion rest frame respectively. For the kaon decay the neutrino has an energy of 0.236 GeV in the kaon rest frame. For both pion and kaon 2-body decays, neutrinos are produced isotropically in the parent rest frame since parents do not carry spin.

For the kaon 3-body decay the Dalitz plot density is used. Assuming that only the hadronic vector current contributes, the matrix element of the $K \rightarrow \pi l \nu_l$ decay can be described by two dimension-less form factors $f_+(t)$ and $f_-(t)$ which depend only on the squared four-momentum transfer $t = (p_K - p_\pi)^2$. The Dalitz plot density as a function of the pion and lepton energies is parametrized as follows:

$$\rho(E_\pi, E_l) \propto f_+^2(t) [A + B\xi(t) + C\xi(t)^2] \quad (2.12)$$

where

$$A = m_K(2E_l E_\nu - m_K E'_\pi) + m_l^2 \left(\frac{E'_\pi}{4} - E_\nu \right) \quad (2.13)$$

$$B = m_l^2 \left(E_\nu - \frac{E'_\pi}{2} \right) \quad (2.14)$$

$$C = \frac{E'_\pi m_l^2}{4} \quad (2.15)$$

$$E'_\pi = E_\pi^{max} - E_\pi = \frac{m_K^2 + m_\pi^2 - m_l^2}{2m_K} - E_\pi$$

$\xi(t)$ is the ratio of the form factors. The $f_+(t)$ form factor is assumed to depend linearly on the squared four-momentum transfer while $f_-(t)$ is assumed to be constant:

$$f_+(t) = f_+(0) \left[1 + \lambda_+ \frac{t}{m_\pi^2} \right] \quad (2.16)$$

$$\xi(t) = \frac{f_-(t)}{f_+(t)} \equiv \frac{\xi(0)}{f_+(t)} \quad (2.17)$$

The world average values of the λ_+ and $\xi(0)$ parameters are taken from [63] to estimate the Dalitz plot density. The current implementation in the JNUBEAM code includes the charged kaon 3-body decays K_{e3}^\pm and $K_{\mu3}^\pm$ as well as the K_L^0 3-body decays K_{e3}^0 and $K_{\mu3}^0$. The corresponding Dalitz density plots are filled at initialization. For each kaon decay, the neutrino energy is computed from the pion and lepton energies randomly chosen from these distributions. For the muon decay, the energy and angular distributions of the ν_μ ($\bar{\nu}_\mu$) and $\bar{\nu}_e$ (ν_e) are calculated according to Michel spectra, taking the muon polarization into account.

For each decay type, θ_L denotes the angle in the laboratory system between the decaying meson direction and that of the near and far detectors. The probability that neutrinos are emitted along that particular direction in the laboratory system can be computed once the relation between the angle θ_L and the corresponding angle θ^* in the meson rest frame is determined. In the simulation, the angle θ_L constrains the neutrino angle in its parent rest frame only in the case of the muon decay. Actually, in the pion 2-body decay and kaon 2-body and 3-body decays, neutrinos are emitted isotropically in the parent rest frame. For the muon decay though, θ_L is needed to account for the effect of polarization in the muon rest frame. In the following, we consider the pion 2-body decay to derive the relation between these two angles. The pion rest frame moves with a velocity $\vec{\beta}_\pi$ with respect to the laboratory frame. The neutrino energy and momentum in the pion rest frame are boosted in the laboratory frame according to:

$$\begin{aligned}\vec{p}_\nu &= \gamma_\pi(\vec{p}_\nu^* + \vec{\beta}_\pi E_\nu^*) \\ E_\nu &= \gamma_\pi(E_\nu^* + \vec{\beta}_\pi \cdot \vec{p}_\nu^*)\end{aligned}$$

where $\gamma_\pi = 1/\sqrt{1 - \beta_\pi^2}$ is the pion Lorentz boost factor and the * superscript denotes quantities in the neutrino parent rest frame. The neutrino momentum in the pion rest frame can be decomposed into transverse and longitudinal components $\vec{p}_\nu^* = \vec{p}_L^* + \vec{p}_T^*$. Since the transverse component is not affected by the Lorentz transformation, the previous relations simplify to:

$$p_L = \gamma_\pi(p_L^* + \beta_\pi E_\nu^*) = \gamma_\pi p^*(\cos \theta^* + \beta_\pi) \quad (2.18)$$

$$E_\nu = \gamma_\pi(E_\nu^* + \beta_\pi p_L^*) = \gamma_\pi E_\nu^*(1 + \beta_\pi \cos \theta^*) \quad (2.19)$$

from which relations between θ_L and θ^* can be derived:

$$\cos \theta_L = \frac{\beta_\pi + \cos \theta^*}{1 + \beta_\pi \cos \theta^*} \quad (2.20)$$

$$\cos \theta^* = \frac{\beta_\pi - \cos \theta_L}{\beta_\pi \cos \theta_L - 1} \quad (2.21)$$

Since the pion does not carry spin, it decays isotropically in its rest frame. Thus, the probability to produce a neutrino in a given solid angle, $d\Omega$, in the laboratory

frame can be expressed as:

$$\frac{dP}{d\Omega} = \frac{dP}{d\Omega^*} \frac{d\Omega^*}{d\Omega} = \frac{1}{4\pi} J_{d\Omega^* \rightarrow d\Omega} \quad (2.22)$$

where $J_{d\Omega^* \rightarrow d\Omega}$ is the Jacobian of the transformation between the rest frame and the laboratory frame:

$$d\cos\theta^* d\phi^* = \left| \begin{array}{cc} \frac{\partial \cos\theta^*}{\partial \cos\theta} & \frac{\partial \phi^*}{\partial \phi} \\ \frac{\partial \cos\theta}{\partial \cos\theta^*} & \frac{\partial \phi}{\partial \phi^*} \end{array} \right| \times d\cos\theta d\phi \quad (2.23)$$

The off-diagonal terms are null and since $\phi^* = \phi$, $\frac{\partial \phi^*}{\partial \phi} = 1$, and the Jacobian reduces to:

$$\frac{\partial \cos\theta^*}{\partial \cos\theta} = \frac{1 - \beta_\pi^2}{(1 - \beta_\pi \cos\theta)^2} \quad (2.24)$$

The probability that a neutrino is produced in the direction of the far detector in the pion 2-body decay can be expressed per unit area $ds = L^2 d\cos\theta d\phi$:

$$\frac{dP}{ds}(\pi, \beta_\pi, \theta) = \frac{1}{4\pi L^2} \frac{1 - \beta_\pi^2}{(1 - \beta_\pi \cos\theta)^2} \quad (2.25)$$

where L is the distance between the far detector and the production point (target) and θ has to be equal to θ_L . Note that for the far detector, the corresponding solid angle is small enough to consider this probability constant over the detector transverse area, A . The probability can then be given for the whole detector by integrating over the solid angle:

$$P(\pi, \beta_\pi, \theta) = \int ds \frac{dP}{ds} = \frac{A}{4\pi L^2} \frac{1 - \beta_\pi^2}{(1 - \beta_\pi \cos\theta)^2} \quad (2.26)$$

This simplification is obviously not possible in the case of the near detector.

The case of the kaon 3-body decay can be treated identically. The difference is now that the neutrino energy is not fixed but distributed over a whole spectrum dependent on the associated pion and lepton energies. Thus, we should in principle consider the probability to produce neutrinos as a function of solid angle and neutrino energy. The joint distribution in the laboratory frame is given by:

$$\frac{d^2 P}{dE_\nu d\Omega} = \frac{d^2 P}{dE_\nu^* d\Omega^*} \frac{dE_\nu^* d\Omega}{dE_\nu d\Omega} \quad (2.27)$$

Using Eq. 2.19 and Eq. 2.24, the Jacobian can be calculated:

$$\frac{dE_\nu^* d\Omega^*}{dE_\nu d\Omega} = \frac{1}{\gamma_K (1 + \beta_K \cos\theta^*)} \frac{1 - \beta_K^2}{(\beta_K \cos\theta - 1)^2} \quad (2.28)$$

This expression can be simplified by using the identity:

$$(1 + \beta_K \cos \theta^*)(1 - \beta_K \cos \theta) = 1 - \beta_K^2 \quad (2.29)$$

which is derived from Eq. 2.21. Thus

$$\frac{dE_\nu^* d\Omega^*}{dE_\nu d\Omega} = \frac{1}{\gamma_K (1 - \beta_K \cos \theta^*)} \quad (2.30)$$

and the joint probability is expressed as:

$$\frac{d^2 P}{dE_\nu d\Omega} = \frac{1}{4\pi} \frac{dP}{dE_\nu^*} \frac{1}{\gamma_K (1 - \beta_K \cos \theta^*)} \quad (2.31)$$

Replacing dP/dE_ν^* by its explicit form and E_ν^* by $\gamma_K E_\nu (1 - \beta_K \cos \theta)$ would lead to a final expression in E_ν and $\cos \theta$. As previously mentioned, the dP/dE_ν^* factor is actually sampled from the corresponding Dalitz density distributions so that, instead of considering the joint distribution in neutrino energy and solid angle, the angular distribution $dP/d\Omega$ from Eq. 2.22 can be considered independently:

$$\frac{dP}{d\Omega} = \frac{1}{4\pi} \frac{1 - \beta_K^2}{(1 - \beta_K \cos \theta)^2} \quad (2.32)$$

Expressing this probability per unit area $ds = L^2 d\cos \theta d\phi$ yields the same geometrical factor as that of the pion decay (Eq. 2.25):

$$\frac{dP}{ds}(K, \beta_K, \theta) = \frac{1}{4\pi L^2} \frac{1 - \beta_K^2}{(1 - \beta_K \cos \theta)^2} \quad (2.33)$$

2.2.3 Neutrino production history

In order to understand the different contributions to the total neutrino flux passing through the detectors of the experiment, the simulation of the neutrino beam should keep track of the full hadron production history. A storage scheme was developed and implemented in the JNUBEAM 10a release used in these studies. For a complete review of the modifications in the different releases, refer to [64]. It is important to note that the storage scheme presented here was developed within the existing framework of the JNUBEAM code. This limits the amount of information relevant for the understanding of the neutrino fluxes that can possibly be stored on output. Another important remark is that the storage scheme implemented for these studies is probably only valid for models that are directly available (interfaced) within the GEANT 3.21 simulation code. To get a model independent storage would require a totally different framework than that of JNUBEAM, and is for the moment beyond the scope of these studies. Let us note, however, that possible solutions to some of these problems could come from the Virtual Monte-Carlo (VMC) [65] concept, which is currently being developed.

The tracking information of all particles (except electrons, positrons and gammas) is stored and kept in memory till the end of each event by using the JSTACK and JKINE common blocks of GEANT 3.21. Details of the procedure can be found in [66]. In the following, the hadronic interaction of the beam proton is referred to as the *primary interaction* of the event. Daughter particles produced in the primary interaction are called *secondary particles*. Secondary particles may decay, be absorbed or produce *secondary interactions* in the target or the elements of the beamline. The generation number is counted back to the primary interaction of the event. It is set to 1 for secondary particles, 2 for daughters of secondary particles, etc. Particles are also flagged if produced in the target volume (88.8 cm long graphite rod shown in blue in Fig. 2.2). The relation between the generation number, the target production flag and the neutrino flux contributions in terms of hadron production measurements² will be developed in Section 2.3. Decay chains (referred to as *n-generation chains*, where n is the number of successive decays) are accounted for in both the generation numbering and the target production flag: the generation number remains 1 all along decay chains of secondary particles, and the target production flag remains 1 all along decay chains of any particle produced in the target volume. Table 2.3 summarizes all the n -generation chains that are taken into account. A decay chain code is associated to each chain. The longest chain corresponds to $n = 5$.

The following information is stored while tracking particles back to the primary interaction of the event:

- (i) neutrino parent: particle type (GEANT 3.21 PID code), position and momentum at starting and stopping vertex, decay chain code (set to zero if a re-interaction was found on the way);
- (ii) neutrino grand-parent: particle type, position and momentum at starting and stopping vertex, medium, production process and number of daughters at stopping vertex;
- (iii) secondary particle (daughter of the primary proton interaction): particle type, position and momentum at starting and stopping vertex, medium, production process and number of daughters at stopping vertex;
- (iv) primary proton: position at starting and stopping vertex, medium, production process and number of daughters at stopping vertex;

This set of variables was added on output to the original set (see [66]) describing the neutrino fluxes in the near and far detector ntuples. In our opinion, this scheme allows to store a minimal amount of information along the neutrino history to understand the different contributions to the neutrino fluxes. According to the generation number, the following cases may occur:

²Choice between measurements with a thin or a long target.

- (i) generation = 3: the whole information chain is stored without discontinuities;
- (ii) generation < 3: the whole information chain is stored but some of it may be redundant, since some variables overlap according to the generation number (e.g. for generation = 1, secondary particle = neutrino parent, primary proton = neutrino grand-parent, etc).
- (iii) generation > 3: whatever happens in between the stopping vertex of the secondary particle and the starting vertex of the neutrino grand-parent particle is not stored. However, whether decays or re-interactions occurred in between is known since the generation number and target production flag keep track of the decay chains. If the current neutrino is produced from a decay chain with $n > 3$, the latter can still be identified by the associated decay chain code.

In this storage scheme, a neutrino parent particle might be considered as produced in the primary interaction or in the target volume, although it is not a daughter of the primary interaction itself, nor produced in the target volume directly. For example, let us consider a simple 1-generation chain, e.g. $\pi^+ \rightarrow \mu^+ \nu_\mu$. The π^+ meson is eventually produced in the primary interaction (in the target volume) and its generation number (target production flag) is set to 1. Since positive focusing is used in the T2K beamline for the first stage of the experiment, the following μ^+ will also be focused in the beam direction, decay, and contribute to the ν_e ($\bar{\nu}_\mu$) flux. The μ^+ being part of a 1-generation chain, its generation number (target production flag) is also set to 1. Thus, if one considers the contribution of secondary particles (particles produced in the target) to the total ν_e flux, positively charged muons will be the main contributors. Were the decay chains not taken into account, the contribution of secondary particles (particles produced in the target) to the ν_e flux would be considerably reduced (only from $\pi^+ \rightarrow e^+ \nu_e$, K_{e3}^+ and K_{e3}^0 decays). Fig. 2.5 illustrates the muon contribution to the fraction of the ν_e ($\bar{\nu}_\mu$) flux coming from particles produced in the target.

In the existing framework of JNUBEAM, each entry on output corresponds to a neutrino. Thus, with the storage scheme presented in this section, different entries will sometimes partly share a common history, e.g. in the previous example of the $\pi \rightarrow \mu \nu$ 1-generation chain, one entry refers to the neutrino produced in the pion decay, the other refers to the neutrino produced in the following muon decay; for both entries, the secondary particle is the same π meson. When considering phase space distributions (e.g. in $\{p, \theta\}$) of secondary particles (or particles produced in the target) which contribute to the neutrino fluxes, keeping track of decay chains through the generation number (target production flag) allows to count particles correctly. Indeed, each secondary particle (or particle produced in the target) that generates a decay chain is automatically counted as many times as a neutrino of a given flavor is found along the chain. Each entry is however weighted by the

Chain type	Decay channel
2-generation chains	$K^\pm \rightarrow \pi^\pm \pi^0$
	$K^\pm \rightarrow \pi^\pm \pi^+ \pi^-$
	$K^\pm \rightarrow \pi^\pm \pi^0 \pi^0$
	$K_S^0 \rightarrow \pi^+ \pi^-$
	$K_L^0 \rightarrow \pi^\pm e^\mp \nu$
	$K_L^0 \rightarrow \pi^\pm \mu^\mp \nu$
	$K_L^0 \rightarrow \pi^+ \pi^- \pi^0$
	$\Omega^- \rightarrow \Xi^0 \pi^-$
	$\Omega^- \rightarrow \Lambda K^-$
	$\bar{\Omega}^+ \rightarrow \bar{\Xi}^0 \pi^+$
	$\bar{\Omega}^+ \rightarrow \bar{\Lambda} K^+$
	$\Sigma^- \rightarrow n \pi^-$
	$\Sigma^+ \rightarrow n \pi^+$
	$\bar{\Sigma}^- \rightarrow \bar{n} \pi^-$
	$\bar{\Sigma}^+ \rightarrow \bar{n} \pi^+$
	$\Xi^- \rightarrow \Lambda \pi^-$
	$\Xi^+ \rightarrow \Lambda \pi^+$
	$\Lambda \rightarrow p \pi^-$
	$\bar{\Lambda} \rightarrow \bar{p} \pi^+$
	$\eta \rightarrow \pi^+ \pi^- \pi^0$
	$\eta \rightarrow \pi^+ \pi^- \gamma$
3-generation chains	$\Omega^- \rightarrow \Xi^0 \pi^- \rightarrow \Lambda \pi^0 \mu^- \nu$
	$\Omega^- \rightarrow \Lambda K^- \rightarrow p \pi^- \mu^- \nu$
	$\Omega^- \rightarrow \Lambda K^- \rightarrow p \pi^- \pi^- \pi^0$
	$\Omega^- \rightarrow \Lambda K^- \rightarrow p \pi^- \pi^- \pi^0 \pi^0$
	$\Omega^- \rightarrow \Lambda K^- \rightarrow p \pi^- \pi^- \pi^+ \pi^-$
	$\Omega^- \rightarrow \Xi^- \pi^0 \rightarrow \Lambda \pi^- \pi^0$
	$\bar{\Omega}^+ \rightarrow \bar{\Xi}^+ \pi^0 \rightarrow \bar{\Lambda} \pi^+ \pi^0$
	$\bar{\Omega}^+ \rightarrow \bar{\Lambda} K^+ \rightarrow \bar{p} \pi^+ \mu^+ \nu$
	$\bar{\Omega}^+ \rightarrow \bar{\Lambda} K^+ \rightarrow \bar{p} \pi^+ \pi^+ \pi^0$
	$\bar{\Omega}^+ \rightarrow \bar{\Lambda} K^+ \rightarrow \bar{p} \pi^+ \pi^+ \pi^0 \pi^0$
	$\bar{\Omega}^+ \rightarrow \bar{\Lambda} K^+ \rightarrow \bar{p} \pi^+ \pi^+ \pi^+ \pi^-$
	$\bar{\Omega}^+ \rightarrow \bar{\Xi}^0 \pi^+ \rightarrow \bar{\Lambda} \pi^0 \mu^+ \nu$
	$\Xi^- \rightarrow \Lambda \pi^- \rightarrow p \pi^- \mu^- \nu$
	$\Xi^+ \rightarrow \bar{\Lambda} \pi^+ \rightarrow \bar{p} \pi^+ \mu^+ \nu$
	$\Sigma^0 \rightarrow \Lambda \gamma \rightarrow p \pi^- \gamma$
	$\bar{\Sigma}^0 \rightarrow \bar{\Lambda} \gamma \rightarrow \bar{p} \pi^+ \gamma$
	$\Xi^0 \rightarrow \Lambda \pi^0 \rightarrow p \pi^- \pi^0$
	$\bar{\Xi}^0 \rightarrow \bar{\Lambda} \pi^0 \rightarrow \bar{p} \pi^+ \pi^0$
4-generation chains	$\Omega^- \rightarrow \Xi^- \pi^0 \rightarrow \Lambda \pi^- \pi^0 \rightarrow p \pi^- \pi^- \pi^0$
	$\Omega^- \rightarrow \Xi^0 \pi^- \rightarrow \Lambda \pi^0 \pi^- \rightarrow p \pi^- \pi^0 \pi^-$
	$\bar{\Omega}^+ \rightarrow \bar{\Xi}^+ \pi^0 \rightarrow \bar{\Lambda} \pi^+ \pi^0 \rightarrow \bar{p} \pi^+ \pi^+ \pi^0$
	$\bar{\Omega}^+ \rightarrow \bar{\Xi}^0 \pi^+ \rightarrow \bar{\Lambda} \pi^0 \pi^+ \rightarrow \bar{p} \pi^+ \pi^0 \pi^+$

Table 2.3: Decay chains of secondary particles taken into account for counting the generation number of the neutrino parents. For clarity, chains that do not lead to higher generations are not mentioned (e.g. chains with only muons in the final state, which include in particular the 1-generation chains $\pi^\pm \rightarrow \mu^\pm \nu$, $\pi^\pm \rightarrow e^\pm \nu$ and $K^\pm \rightarrow \mu^\pm \nu$, and all the 5-generation chains).

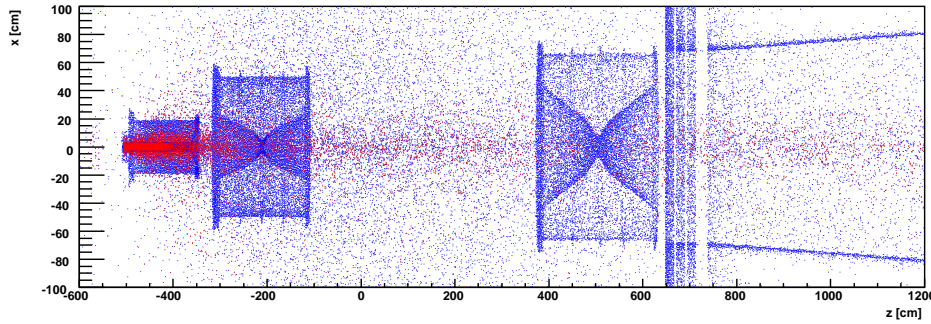


Figure 2.5: Production point of the neutrino parent particles in the XZ projection. Points displayed in red correspond to parents that are produced in the target or along decay chains of particles produced in the target. The red dots along the beamline correspond mainly to muons from the decay of particles produced in the target.

associated probability that the neutrino reaches the near and far detectors. For example, in the $K^\pm \rightarrow \pi^\pm \pi^+ \pi^-$ 2-generation chain, if the K meson is a secondary particle (or produced in the target), it will contribute twice to the ν_μ flux via the decay of the two associated positively charged pions. Were the decay chains not taken into account, the contribution of secondary particles (or particles produced in the target) could be underestimated in some $\{p, \theta\}$ bins of the relevant phase space.

2.3 Prediction of neutrino fluxes from different sources

Precise prediction of neutrino fluxes is crucial for the next generation of accelerator neutrino experiments such as T2K. Some experience (using GEANT 3.21 package [56]) has already been gained in previous experiments, e.g. in the short baseline experiment NOMAD [67] (with SPY as auxiliary hadron production experiment [68]) and in the first long baseline experiment K2K [69] (with HARP as auxiliary hadron production experiment [70]). A detailed simulation of the Fermilab booster neutrino beamline in the GEANT 4 framework [71] has also been performed recently by the MiniBooNE collaboration [72] using input from the HARP data [73]. For a review on the importance of hadron production experiments for the prediction of neutrino fluxes see e.g. [74].

In the storage scheme presented in the previous section, particles may be flagged as *secondary particles* and *particles produced in the target*. A careful definition of these two contributions is absolutely mandatory to understand to which extent the prediction of the neutrino fluxes in the T2K beamline simulation can be constrained by hadron production measurements. An auxiliary hadron production experiment may provide information about the primary interaction relevant for

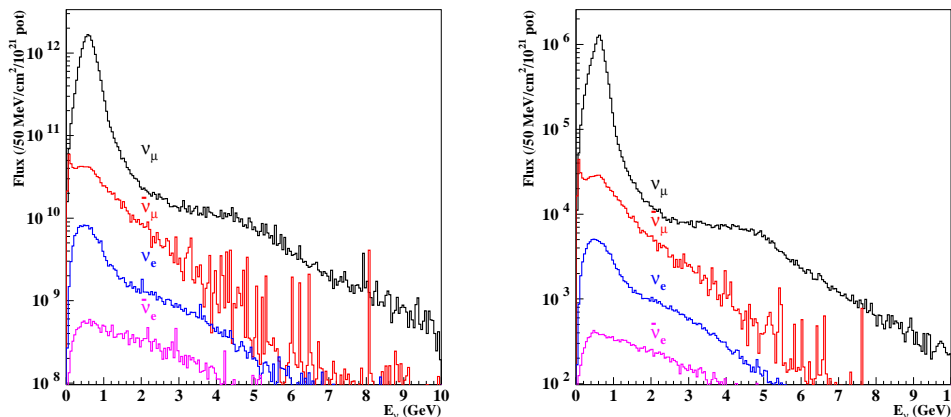


Figure 2.6: Energy spectra for ν_μ (black), $\bar{\nu}_\mu$ (red), ν_e (blue) and $\bar{\nu}_e$ (purple) at the ND280 near detector within the transverse fiducial area of $150 \times 150 \text{ cm}^2$ (left) and at the far detector (right).

the experiment, by measuring hadron production cross sections out of a thin (a few % of the interaction length) target (e.g., for T2K, hadron production cross sections in proton-Carbon interactions at 30 GeV beam kinetic energy). It may also provide information about re-interactions in the production target, by measuring hadron yields out of a long target (intermediate or full-size replica of the production target). Both types of measurements are certainly complementary. The advantage of one or the other may be based on the two following aspects:

- (i) the fraction of the neutrino fluxes that these measurements can effectively constrain;
- (ii) the degree of complexity of the associated method used to constrain the flux predictions and to propagate the corresponding systematics to the final predictions.

In this section, we try to develop further the first point. In the following, all plots correspond to a total statistics of 10.5 M events generated with the GCALOR model (default in JNUBEAM 10a). Total neutrino flux predictions at the near and far detectors for the four different neutrino species (ν_μ , $\bar{\nu}_\mu$, ν_e and $\bar{\nu}_e$) are shown in Fig. 2.6. For each of them, the contributions of the corresponding parent particles are shown in Fig. 2.7 and Fig. 2.8. The composition of the neutrino beam is summarized in Tables 2.4 and 2.5 for the near and far detectors respectively. The chosen binning has been proposed and presented in [75]. For clarity, the following flux predictions are shown only for the far detector. Fluxes are presented

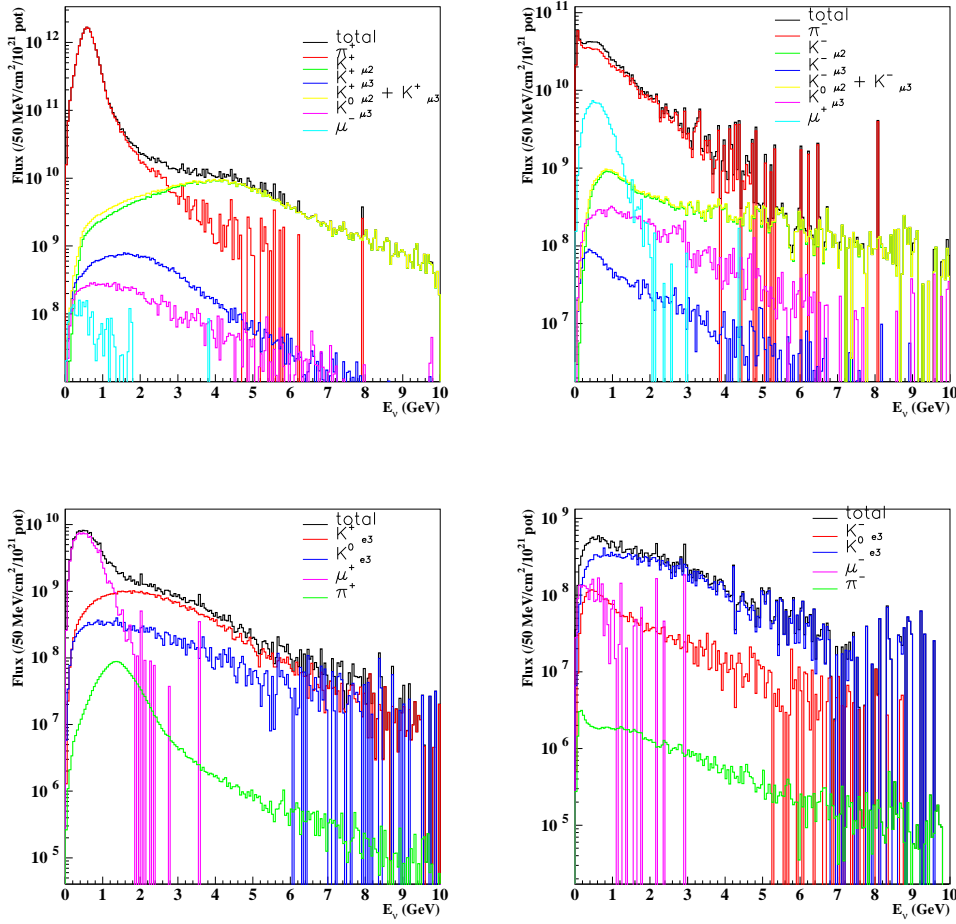


Figure 2.7: Composition of the ν_μ (top left), $\bar{\nu}_\mu$ (top right), ν_e (bottom left) and $\bar{\nu}_e$ (bottom right) energy spectra at the ND280 near detector within the transverse fiducial area of 150×150 cm².

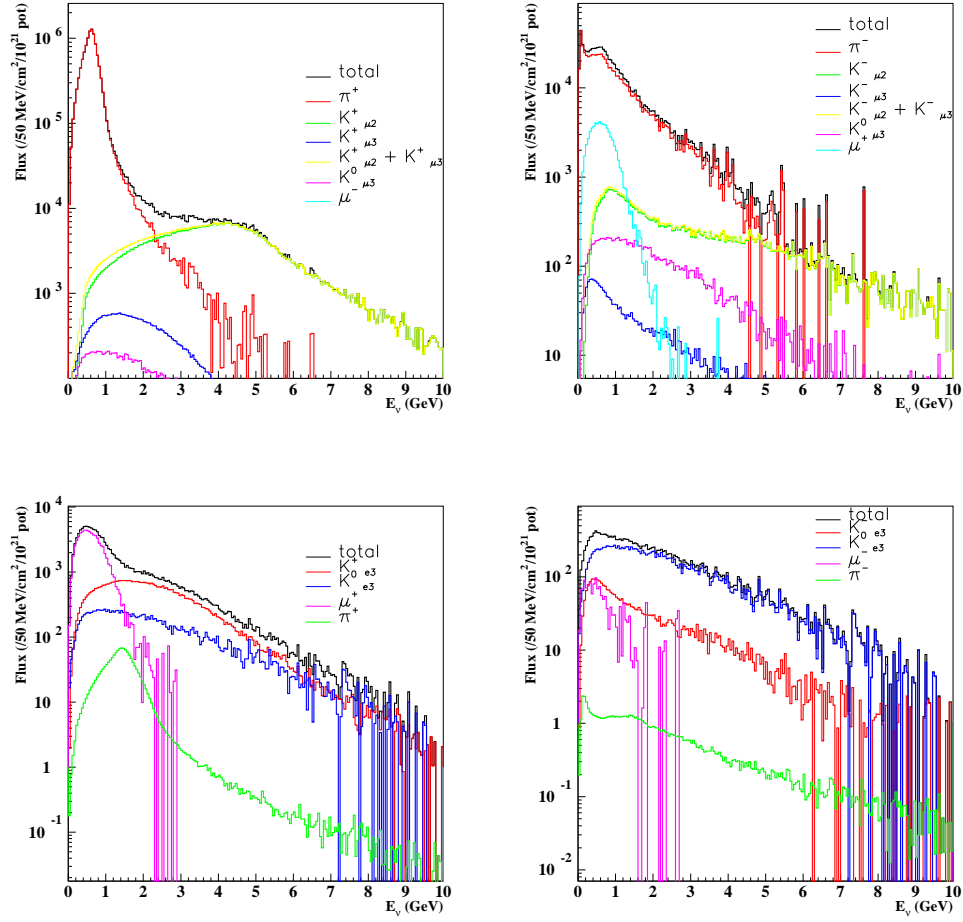


Figure 2.8: Composition of the ν_μ (top left), $\bar{\nu}_\mu$ (top right), ν_e (bottom left) and $\bar{\nu}_e$ (bottom right) energy spectra at the far detector.

ν species	Flux		Source									
			π^+ or π^-		K^+ or K^- (K2)		K^+ or K^- (K3)		K_L^0		μ^+ or μ^-	
	Abund.	$\langle E_\nu \rangle$	%	$\langle E_\nu \rangle$	%	$\langle E_\nu \rangle$	%	$\langle E_\nu \rangle$	%	$\langle E_\nu \rangle$	%	$\langle E_\nu \rangle$
ν_μ	1.0	0.84	95.5	0.69	4.2	4.15	0.2	2.13	0.1	2.10	< 0.01	0.80
$\bar{\nu}_\mu$	0.0692	1.19	85.8	1.13	4.0	3.21	0.2	1.70	1.2	2.12	8.8	0.66
ν_e	0.0110	1.41	1.0	1.58	–	–	30.7	2.48	11.1	2.52	57.2	0.62
$\bar{\nu}_e$	0.0016	2.26	0.4	2.40	–	–	13.6	1.91	76.7	2.49	9.2	0.88

Table 2.4: Composition of the neutrino beam and its various species at the ND280 near detector within the transverse fiducial area of $150 \times 150 \text{ cm}^2$. Integrated values are quoted.

ν species	Flux		Source									
			π^+ or π^-		K^+ or K^- (K2)		K^+ or K^- (K3)		K_L^0		μ^+ or μ^-	
	Abund.	$\langle E_\nu \rangle$	%	$\langle E_\nu \rangle$	%	$\langle E_\nu \rangle$	%	$\langle E_\nu \rangle$	%	$\langle E_\nu \rangle$	%	$\langle E_\nu \rangle$
ν_μ	1.0	0.79	95.1	0.64	4.5	4.0	0.24	1.93	0.1	2.05	0.01	0.75
$\bar{\nu}_\mu$	0.0701	1.14	85.8	1.05	4.6	3.1	0.2	1.56	1.3	2.05	8.0	0.68
ν_e	0.0110	1.40	1.0	1.48	–	–	33.0	2.25	12.5	2.38	53.3	0.64
$\bar{\nu}_e$	0.0017	2.18	0.4	2.32	–	–	14.7	1.84	77.6	2.38	7.2	0.75

Table 2.5: Composition of the neutrino beam and its various species at the far detector. Integrated values are quoted.

for (anti)neutrino energies up to 2 GeV in the main body of this thesis. Corresponding plots up to 10 GeV can also be found in Appendix B. Error bars refer to statistical errors of simulated data only.

In summary (the fractions quoted in the text are for the near detector case, more details can be found in Tables 2.4 and 2.5), among neutrinos produced in the T2K beam simulation:

- ν_μ 's are primarily produced via π^+ (95.5 %) and K^+ (4.2 %) two-body decays. A small fraction comes from the three-body decays of K^+ (0.2 %) and K_L^0 (0.1 %) while the μ^- contribution is negligible (< 0.01 %). Neutrinos from pion decays dominate the ν_μ spectrum up to $\sim 2 \text{ GeV}$ while those from kaon decays dominate beyond this energy.
- Similar to ν_μ 's the $\bar{\nu}_\mu$'s are primarily produced via π^- (85.8 %) and K^- (4.0 %) two-body decays but a much larger fraction of the flux comes from μ^+ (8.8 %) decays since those are not affected by the defocusing of the magnetic horns. Smaller fractions come from the K^+ (0.2 %) and K_L^0 (1.2 %) three-body decays. Anti-neutrinos from pion decays dominate the spectrum up to $\sim 4 \text{ GeV}$, followed by those from muon and kaon decays. Beyond this energy, the spectrum is dominated by the kaon decays. The $\bar{\nu}_\mu$ flux is 6.9 % that of the ν_μ .
- The main contribution to the ν_e flux is from μ^+ (57.2 %) decays, followed by the three-body decays of K^+ (30.7 %) and K_L^0 (11.1 %). A small fraction of about 1 % (but very well peaked around 1 GeV) comes from the π^+ decay.

The ν_e flux relative to ν_μ in the absence of $\nu_\mu \rightarrow \nu_e$ oscillations is expected to be about 1.1 % integrated over all energies.

- The main source of $\bar{\nu}_e$ is the three-body decay of K_L^0 (76.7 %). The other sources are K^- (13.6 %) three-body decays and a smaller contribution of μ^- (9.2 %) decays. Still a fraction of 0.4 % comes from the π^- decay. The $\bar{\nu}_e$ flux is ~ 0.16 % that of the ν_μ .

2.3.1 Direct contribution and thin target measurements

The storage scheme of Section 2.2.3 allows us to define a first set of contributions to the neutrino flux:

- (i) *direct* contribution: a neutrino parent particle contributes directly to the neutrino flux if it is a secondary particle (produced in the primary interaction) or a particle along a decay chain of a secondary particle. By extension, a secondary particle contributes directly to the neutrino flux if a neutrino is produced at any generation along its decay chain (e.g., in the $K^\pm \rightarrow \pi^\pm \pi^+ \pi^-$ 2-generation chain, the K meson is considered as a direct contributor if the pions or following muons decay);
- (ii) *indirect* contribution: a neutrino parent particle contributes indirectly to the neutrino flux if it is produced in a re-interaction (of a secondary particle or of a particle of any higher generation). By extension, a secondary particle contributes indirectly to the neutrino flux if its re-interaction leads to the production of a neutrino.

Thus, the direct contribution accounts for the neutrino production related to the secondary particles produced in the primary interaction. Neutrinos produced from re-interactions in the target or in the elements of the beamline are accounted for in the definition of the indirect contribution. The direct production includes two sources of neutrinos: neutrinos produced in the decay of secondaries and neutrinos produced along decay chains of secondaries. From comparisons of current results with previous iterations that did not include the treatment of decay chains, it was shown that the second source contributes to less than 10 % of the direct production. By measuring secondary hadron production cross sections out of a thin target, an auxiliary experiment would provide information about the first source of neutrinos. Such an experiment would measure, for example, the π meson production cross section, but not the spectrum of muons produced in the decay of these mesons. However, the previous definition accounts as well for decay chains for the following two reasons: first, if the secondary hadron spectrum is measured, the spectrum of daughters can eventually be predicted from these measurements; second, if measurements are used to constrain secondary hadron production in the beam simulation, the whole neutrino production history related to the initial

secondary hadrons has to be constrained accordingly. Thus, in order to estimate the fraction of the neutrino flux that can effectively be constrained by secondary hadron production measurements, the definition of the direct contribution accounts for the whole neutrino production that can be related (via decay chains) to secondary hadrons.

For each of the neutrino species, the flux is predicted at both near and far detectors. The direct and indirect contributions are computed according to the previous definitions. These are shown as an example for ν_μ and ν_e neutrinos in Fig. 2.9 and Fig. 2.10 respectively. The ratio of the indirect over the total contribution (direct + indirect) is also computed and shown for all species in Fig. 2.11. The beam composition for both direct and indirect contributions is summarized in Tables 2.6 and 2.7 for the near detector and in Tables 2.8 and 2.9 for the far detector.

As can be seen in Fig. 2.11, the indirect production accounts for a large fraction of the fluxes below 2 GeV neutrino energy. At peak energy (see Tab. 2.5), it represents a fraction of $\sim 42\%$ of the ν_μ flux and $\sim 44\%$ of the ν_e flux. Integrating distributions up to 10 GeV neutrino energy (see Appendix B, Fig B.6), the (direct : indirect) contributions are estimated to $\sim (56\% : 44\%)$ for the ν_μ flux and $\sim (62\% : 38\%)$ for the ν_e flux. Thus, by measuring secondary hadron production cross sections using a thin target, one would constrain a fraction of $\sim 60\%$ of the total ν_μ and ν_e fluxes. Consequently, a large fraction ($\sim 40\%$) of the flux predictions would still be completely model dependent. The uncertainty on this model dependent contribution would eventually be constrained by additional measurements (related to hadron re-interaction in the target and elements of the beamline).

2.3.2 Target contribution and long target measurements

A set of two more contributions to the neutrino flux can be defined using the storage scheme of Section 2.2.3:

- (i) *target* contribution: includes neutrino parent particles that are produced in the target volume or along decay chains of particles exiting the target;
- (ii) *non-target* contribution: includes neutrino parent particles that are produced out of the target and not along a decay chain of a particle exiting the target.

The definition of the target volume is based on the simulated target geometry shown in Fig. 2.2. It consists of a cylinder of 2.6 cm diameter and 88.8 cm length. The definition does not include the target head, which is a 2.244 cm thick piece of graphite placed 0.4 cm upstream of the main rod. In the previous section, the direct contribution was related to measurements of secondary hadron production cross sections using a thin target. An auxiliary experiment could as well measure hadron production yields out of a long target. In this case, the measured yields

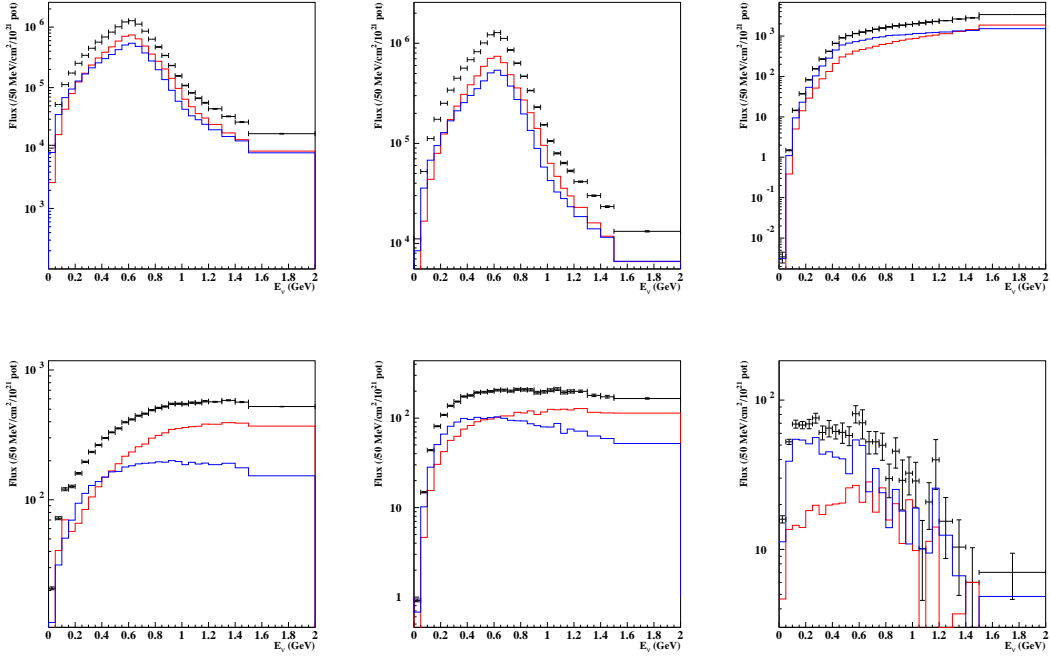


Figure 2.9: ν_μ flux in the far detector from all contributions (top left), from π^+ (top middle), from $K_{\mu 2}^+$ (top right), from $K_{\mu 3}^0$ (bottom left), from $K_{\mu 3}^0$ (bottom middle) and from μ^- (bottom right) decays. Direct (red) and indirect (blue) contributions are shown for each parent particle.

ν species	Source											
	Flux		π^+ or π^-		K^+ or K^- (K2)		K^+ or K^- (K3)		K_L^0		μ^+ or μ^-	
	Abund.	$\langle E_\nu \rangle$	%	$\langle E_\nu \rangle$	%	$\langle E_\nu \rangle$	%	$\langle E_\nu \rangle$	%	$\langle E_\nu \rangle$	%	$\langle E_\nu \rangle$
ν_μ	1.0	0.88	94.6	0.69	5.0	4.38	0.2	2.25	0.1	2.38	< 0.01	1.1
$\bar{\nu}_\mu$	0.0554	1.53	82.3	1.49	4.8	3.74	0.26	2.05	1.7	2.43	10.9	0.66
ν_e	0.0118	1.59	1.0	1.59	—	—	34.6	2.63	12.6	2.82	52.7	0.65
$\bar{\nu}_e$	0.0017	2.62	0.3	3.1	—	—	12.5	2.28	81.5	2.77	5.7	1.14

Table 2.6: Composition of the neutrino beam and its various species at the ND280 near detector within the transverse fiducial area of $150 \times 150 \text{ cm}^2$ for the direct contribution. Integrated values are quoted.

ν species	Source											
	Flux		π^+ or π^-		K^+ or K^- (K2)		K^+ or K^- (K3)		K_L^0		μ^+ or μ^-	
	Abund.	$\langle E_\nu \rangle$	%	$\langle E_\nu \rangle$	%	$\langle E_\nu \rangle$	%	$\langle E_\nu \rangle$	%	$\langle E_\nu \rangle$	%	$\langle E_\nu \rangle$
ν_μ	1.0	0.76	96.6	0.67	3.1	3.64	0.2	1.88	0.1	1.57	0.02	0.62
$\bar{\nu}_\mu$	0.0874	0.89	88.7	0.85	3.3	2.54	0.1	1.24	0.8	1.55	7.0	0.67
ν_e	0.0100	1.12	1.2	1.55	—	—	24.6	2.13	10.1	2.00	64.1	0.59
$\bar{\nu}_e$	0.0014	1.69	0.6	1.91	—	—	15.4	1.42	69.2	1.95	14.7	0.73

Table 2.7: Composition of the neutrino beam and its various species at the ND280 near detector within the transverse fiducial area of $150 \times 150 \text{ cm}^2$ for the indirect contribution. Integrated values are quoted.

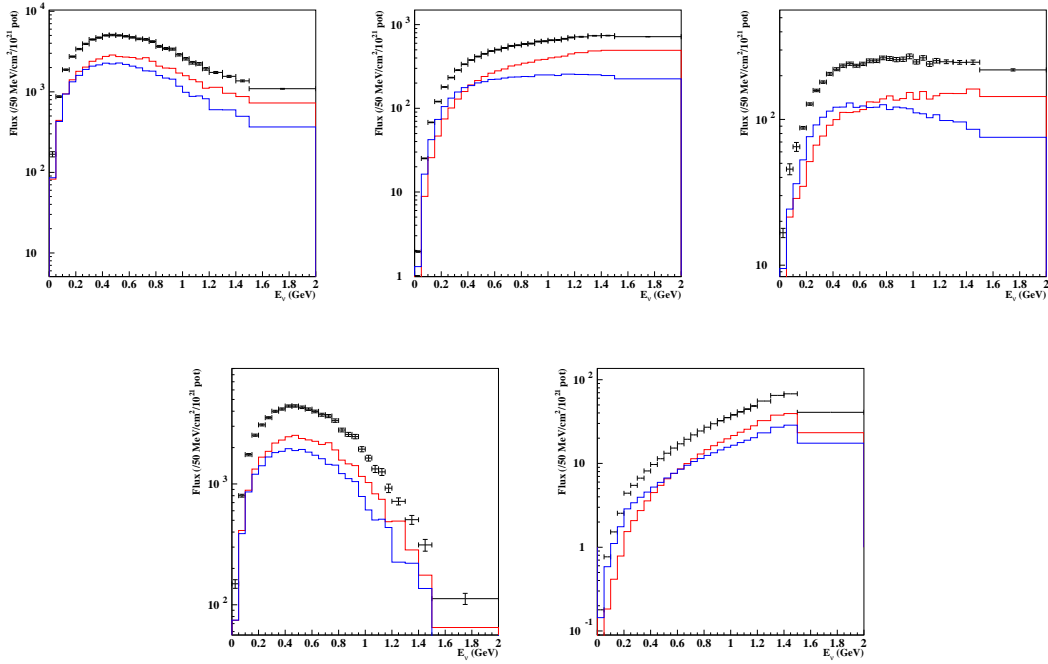


Figure 2.10: ν_e flux in the far detector from all contributions (top left), from K_{e3}^+ (top middle), from K_{e3}^0 (top right), from μ^+ (bottom left) and from π^+ (bottom right) decays. Direct (red) and indirect (blue) contributions are shown for each parent particle.

ν species	Source											
	Flux		π^+ or π^-		K^+ or K^- (K2)		K^+ or K^- (K3)		K_L^0		μ^+ or μ^-	
	Abund.	$\langle E_\nu \rangle$	%	$\langle E_\nu \rangle$	%	$\langle E_\nu \rangle$	%	$\langle E_\nu \rangle$	%	$\langle E_\nu \rangle$	%	$\langle E_\nu \rangle$
ν_μ	1.0	0.84	94.1	0.64	5.5	4.2	0.3	2.03	0.1	2.3	0.01	0.95
$\bar{\nu}_\mu$	0.0571	1.40	82.3	1.31	5.7	3.53	0.3	1.80	2.0	2.27	9.7	0.69
ν_e	0.0120	1.56	1.0	1.49	—	—	36.8	2.37	13.3	2.63	48.9	0.65
$\bar{\nu}_e$	0.0019	2.48	0.3	2.82	—	—	13.9	2.13	81.5	2.62	4.3	0.90

Table 2.8: Composition of the neutrino beam and its various species at the far detector for the direct contribution. Integrated values are quoted.

ν species	Source											
	Flux		π^+ or π^-		K^+ or K^- (K2)		K^+ or K^- (K3)		K_L^0		μ^+ or μ^-	
	Abund.	$\langle E_\nu \rangle$	%	$\langle E_\nu \rangle$	%	$\langle E_\nu \rangle$	%	$\langle E_\nu \rangle$	%	$\langle E_\nu \rangle$	%	$\langle E_\nu \rangle$
ν_μ	1.0	0.73	96.4	0.63	3.3	3.5	0.2	1.7	0.1	1.64	0.02	0.62
$\bar{\nu}_\mu$	0.0872	0.90	88.8	0.85	3.4	2.50	0.2	1.23	0.8	1.64	6.5	0.66
ν_e	0.0098	1.15	1.2	1.46	—	—	27.1	2.0	11.3	1.91	60.4	0.62
$\bar{\nu}_e$	0.0016	1.69	0.6	1.92	—	—	16.1	1.44	71.4	1.91	11.9	0.66

Table 2.9: Composition of the neutrino beam and its various species at the far detector for the indirect contribution. Integrated values are quoted.

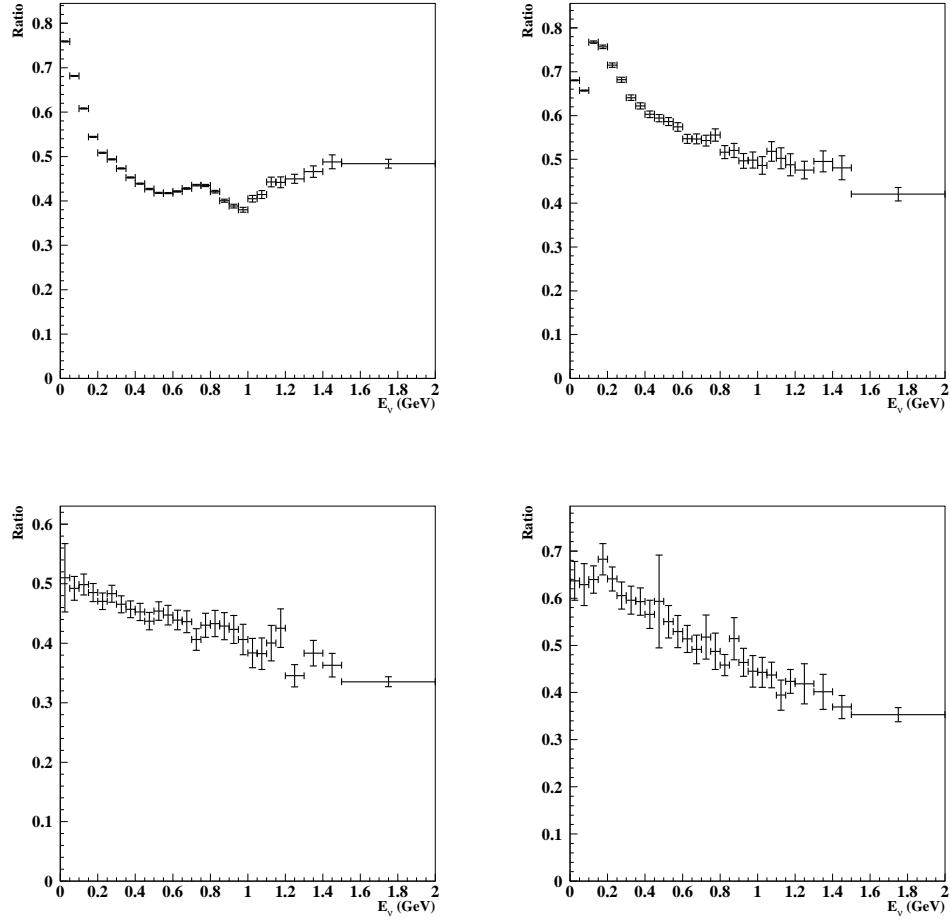


Figure 2.11: Ratio of indirect to total contribution for the far detector for ν_μ (top left), $\bar{\nu}_\mu$ (top right), ν_e (bottom left) and $\bar{\nu}_e$ (bottom right) fluxes.

would account for secondary hadrons exiting the target, as well as for hadrons produced in re-interactions in the target. For the same reasons that were developed in the previous section, decay chains are included in the definition of the target contribution to estimate which fraction of the neutrino flux could effectively be constrained by such measurements.

For each of the neutrino species, the flux is predicted at both near and far detectors. The target and non-target contributions are computed according to the previous definitions. These are shown as an example for ν_μ and ν_e neutrinos in Fig. 2.12 and Fig. 2.13 respectively. The ratio of the non-target over the total contribution (target + non-target) is also computed and shown for all species in Fig. 2.14. The beam composition for both target and non-target contributions is summarized in Tables 2.10 and 2.11 for the near detector and in Tables 2.12 and 2.13 for the far detector.

As can be seen in Fig. 2.14, the non-target production accounts for a relatively small fraction of the fluxes below 2 GeV neutrino energy. At peak energy (see Tab. 2.5), it represents a fraction of $\sim 10\%$ of both ν_μ and ν_e fluxes. Integrating distributions up to 10 GeV neutrino energy (see Appendix B, Fig B.12), the (target : non-target) contributions are estimated to $\sim (85\% : 15\%)$ for the ν_μ flux and $\sim (88\% : 12\%)$ for the ν_e flux. Thus, by measuring hadron yields out of a full-size replica of the T2K production target, one would constrain a fraction of $\sim 90\%$ of both ν_μ and ν_e fluxes at peak energy. In our opinion, these estimations stress the importance of measurements out of a long target. As shown in the previous section, the measurement of secondary hadron production cross sections would constrain up to $\sim 60\%$ of the flux predictions at peak energy. The remaining 40 % (from re-interactions) would still carry large uncertainties (with respect to the T2K requirements on absolute flux predictions) due to the model dependency of the predictions. In the case of long target measurements, uncertainties on both primary and secondary interactions are mostly constrained, since measurements account for all hadron production processes in the target volume. The fraction of the flux prediction that would still suffer from large uncertainties is reduced down to $\sim 10\text{--}15\%$.

In Section 3.2, we will further develop the arguments in favor of the long target measurements for T2K. The two following points should in particular be studied:

- (i) what is to be measured: in which phase space ? what is the best set of track parameters ?
- (ii) which statistics should be reached to fulfill the T2K requirements ?

2.3.3 Far-to-near ratio predictions

Once fluxes are predicted for both near and far detectors, the so-called far-to-near ratio can be computed accordingly. It is shown for the four neutrino species in

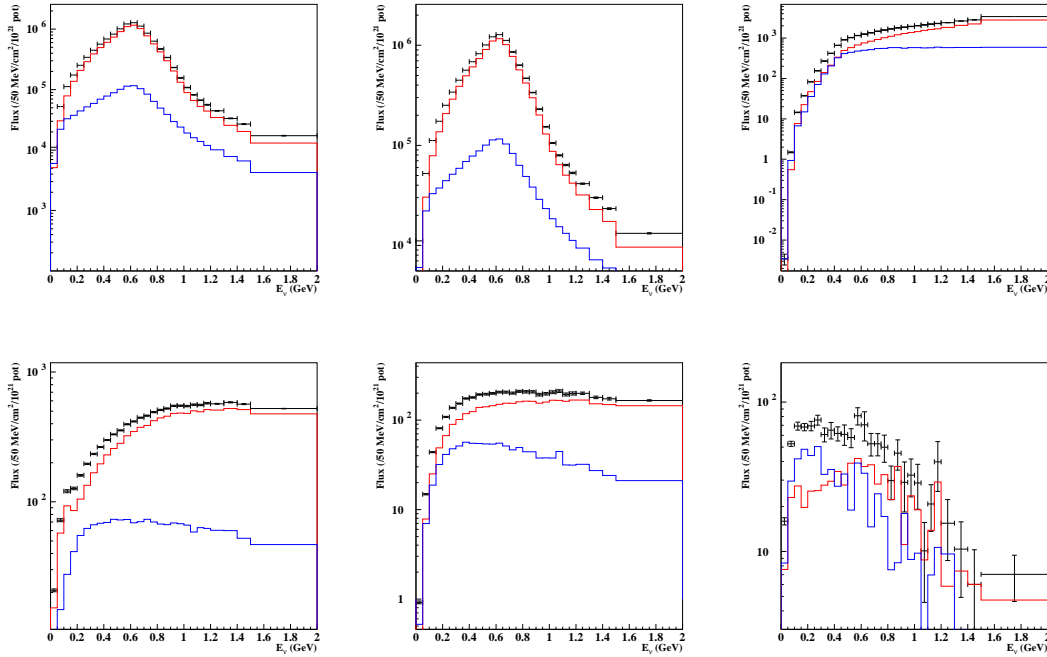


Figure 2.12: ν_μ flux in the far detector from all contributions (top left), from π^+ (top middle), from $K_{\mu 2}^+$ (top right), from $K_{\mu 3}^+$ (bottom left), from $K_{\mu 3}^0$ (bottom middle) and from μ^- (bottom right) decays. Target (red) and non-target (blue) contributions are shown for each parent particle.

ν species	Flux		Source								μ^+ or μ^-	
			π^+ or π^-		K^+ or K^- (K2)		K^+ or K^- (K3)		K_L^0			
	Abund.	$\langle E_\nu \rangle$	%	$\langle E_\nu \rangle$	%	$\langle E_\nu \rangle$	%	$\langle E_\nu \rangle$	%	$\langle E_\nu \rangle$	%	$\langle E_\nu \rangle$
ν_μ	1.0	0.84	95.5	0.68	4.2	4.27	0.2	2.19	0.1	2.25	< 0.01	0.98
$\bar{\nu}_\mu$	0.0493	1.46	81.3	1.45	4.3	3.61	0.24	1.98	1.6	2.3	12.6	0.66
ν_e	0.0111	1.44	1.0	1.57	–	–	30.8	2.55	10.2	2.73	57.9	0.63
$\bar{\nu}_e$	0.0014	2.49	0.3	3.0	–	–	12.0	2.2	80.4	2.65	7.3	1.14

Table 2.10: Composition of the neutrino beam and its various species at the ND280 near detector within the transverse fiducial area of $150 \times 150 \text{ cm}^2$ for the target contribution. Integrated values are quoted.

ν species	Flux		Source									
			π^+ or π^-		K^+ or K^- (K2)		K^+ or K^- (K3)		K_L^0		μ^+ or μ^-	
	Abund.	$\langle E_\nu \rangle$	%	$\langle E_\nu \rangle$	%	$\langle E_\nu \rangle$	%	$\langle E_\nu \rangle$	%	$\langle E_\nu \rangle$	%	$\langle E_\nu \rangle$
ν_μ	1.0	0.82	95.6	0.71	4.0	3.22	0.2	1.67	0.1	1.44	0.05	0.6
$\bar{\nu}_\mu$	0.2127	0.73	93.3	0.66	3.5	2.35	0.2	1.1	0.6	1.34	2.4	0.68
ν_e	0.0106	1.19	1.1	1.60	—	—	30.0	1.91	17.7	1.65	51.1	0.61
$\bar{\nu}_e$	0.0030	1.48	0.8	1.52	—	—	19.4	1.27	63.9	1.78	15.8	0.49

Table 2.11: Composition of the neutrino beam and its various species at the ND280 near detector within the transverse fiducial area of $150 \times 150 \text{ cm}^2$ for the non-target contribution. Integrated values are quoted.

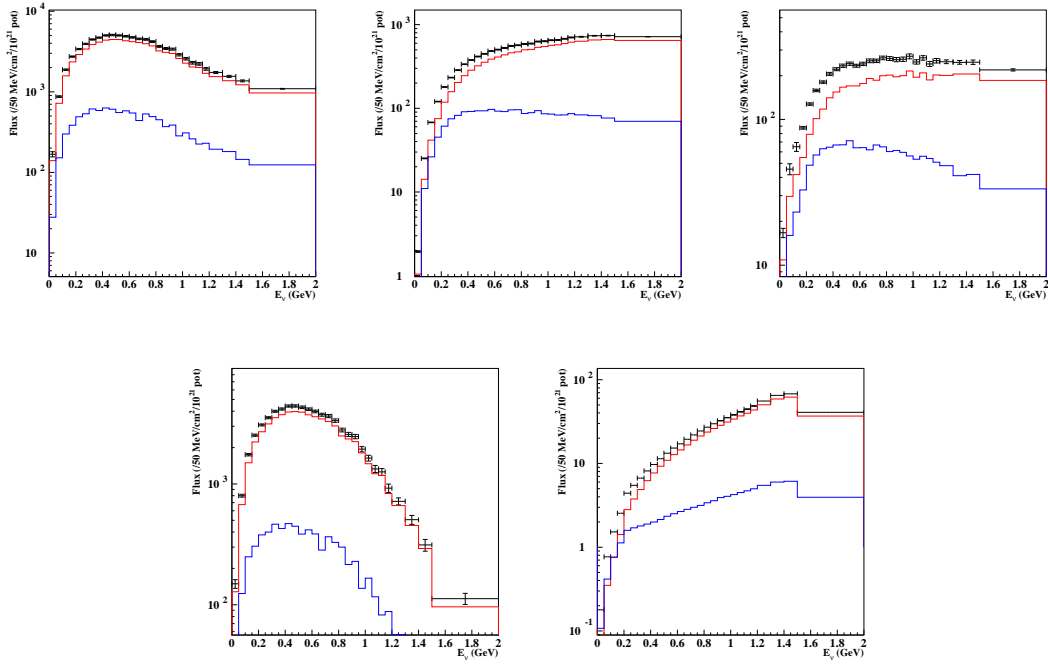


Figure 2.13: ν_e flux in the far detector from all contributions (top left), from K_{e3}^+ (top middle), from K_{e3}^0 (top right), from μ^+ (bottom left) and from π^+ (bottom right) decays. Target (red) and non-target (blue) contributions are shown for each parent particle.

ν species	Flux		Source									
			π^+ or π^-		K^+ or K^- (K2)		K^+ or K^- (K3)		K_L^0		μ^+ or μ^-	
	Abund.	$\langle E_\nu \rangle$	%	$\langle E_\nu \rangle$	%	$\langle E_\nu \rangle$	%	$\langle E_\nu \rangle$	%	$\langle E_\nu \rangle$	%	$\langle E_\nu \rangle$
ν_μ	1.0	0.79	95.1	0.63	4.6	4.06	0.2	1.97	0.1	2.15	< 0.01	0.90
$\bar{\nu}_\mu$	0.0520	1.33	81.8	1.27	5.2	3.37	0.3	1.72	1.7	2.15	10.9	0.67
ν_e	0.0111	1.42	1.0	1.47	—	—	33.2	2.3	11.8	2.50	53.9	0.64
$\bar{\nu}_e$	0.0016	2.35	0.3	2.77	—	—	13.7	2.03	80.7	2.50	5.3	0.90

Table 2.12: Composition of the neutrino beam and its various species at the far detector for the target contribution. Integrated values are quoted.

ν species	Flux		Source									
			π^+ or π^-		K^+ or K^- (K2)		K^+ or K^- (K3)		K_L^0		μ^+ or μ^-	
	Abund.	$\langle E_\nu \rangle$	%	$\langle E_\nu \rangle$	%	$\langle E_\nu \rangle$	%	$\langle E_\nu \rangle$	%	$\langle E_\nu \rangle$	%	$\langle E_\nu \rangle$
ν_μ	1.0	0.77	95.5	0.67	4.1	3.26	0.2	1.62	0.1	1.51	0.04	0.53
$\bar{\nu}_\mu$	0.2041	0.76	93.4	0.70	3.4	2.30	0.2	1.10	0.6	1.51	2.4	0.68
ν_e	0.0103	1.23	1.1	1.54	—	—	32.1	1.87	18.2	1.75	48.5	0.61
$\bar{\nu}_e$	0.0029	1.48	0.8	1.57	—	—	19.2	1.30	65.0	1.75	15.0	0.51

Table 2.13: Composition of the neutrino beam and its various species at the far detector for the non-target contribution. Integrated values are quoted.

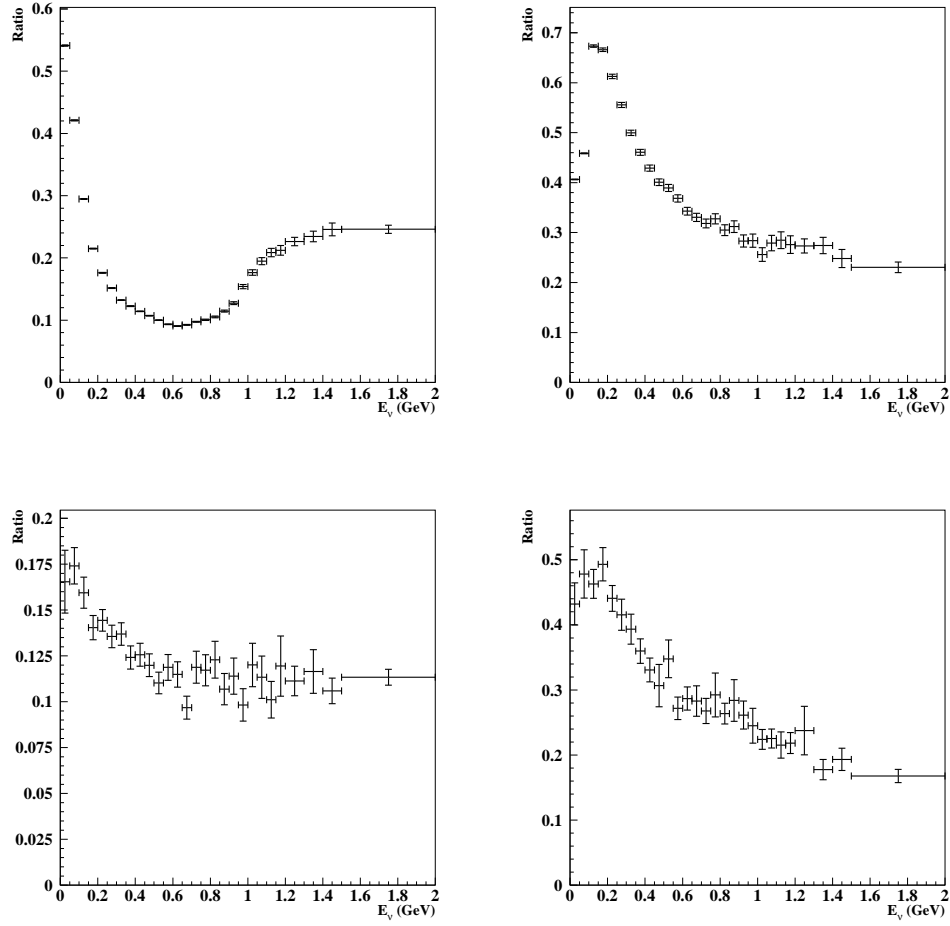


Figure 2.14: Ratio of non-target to total contribution for the far detector for ν_μ (top left), $\bar{\nu}_\mu$ (top right), ν_e (bottom left) and $\bar{\nu}_e$ (bottom right) fluxes.

Fig. 2.15 for the direct and indirect contributions, and in Fig. 2.16 for the target and non-target contributions. To build these ratios, fluxes at the near detector are normalized to the fiducial area of $150 \times 150 \text{ cm}^2$. The flux ratio is multiplied by the ratio of the squared distances L_{SK}^2/L_{ND}^2 of the far and near detectors to the target respectively.

The far-to-near ratio computed with the T2K beamline configuration does not follow a simple $1/r^2$ law, but is a complicated function of the neutrino energy. This is due to the short distance (280 m) between the target station and the near detector. At such a distance, the neutrino production cannot be considered as point-like anymore: the near detector covers a larger solid angle than that of the far detector and the neutrino production hence extends all along the decay tunnel. Pions and kaons producing neutrinos cover different regions of the $\{p, \theta\}$ phase space which are affected differently by the focusing system. Thus, as can be seen in Fig. 2.15 and Fig. 2.16, the far-to-near ratio is also dependent on the contribution type to the neutrino fluxes (direct vs indirect, target vs non-target). In order to understand to which extent hadron production measurements could constrain the far-to-near ratio predictions, it is important to understand the phase space of hadrons producing neutrinos in terms of contribution type. As an example, Fig. 2.17 and Fig. 2.18 show the phase space distributions of positively charged π and K mesons producing neutrinos reaching the far detector. It can be seen that direct (target) and indirect (non-target) contributions cover different regions of the phase space of interest. Corresponding distributions of π^- , K^- and K_L^0 for the far detector are shown in Appendix C, as well as distributions of π^\pm , K^\pm and K_L^0 for the near detector.

A particular region of the hadron production phase space is the very forward region at high momentum and low production angle. Hadrons produced in this kinematic region will mostly re-interact in the target (due to the large amount of matter they have to go through before exiting the target), while those exiting the target will not be affected by the focusing system and will eventually re-interact in the elements of the beamline. In particular, Fig. 2.19 shows the phase space distribution of secondary protons and neutrons which contribute indirectly to the neutrino production via re-interactions in the target. In our studies, we could observe a clear contribution of the elastic proton scattering in the target. We tried to apply different treatments to this process, e.g. counting the scattered proton still as a primary proton or as a secondary particle. However, all the flux predictions obtained in these studies turned out to be stable within $\sim 5\%$. Although this fraction (model dependent) is not large, the uncertainty on the identification of the underlying process in a long target is large. Depending upon the treatment of these protons the cross section to be considered may differ by $\sim 20\%$. This may have a large impact on flux predictions when considering re-weighting procedures.

Finally, it should also be stressed that the prediction of the far-to-near ratio, when used e.g. as a reference to study the requirements for the T2K physics goals,

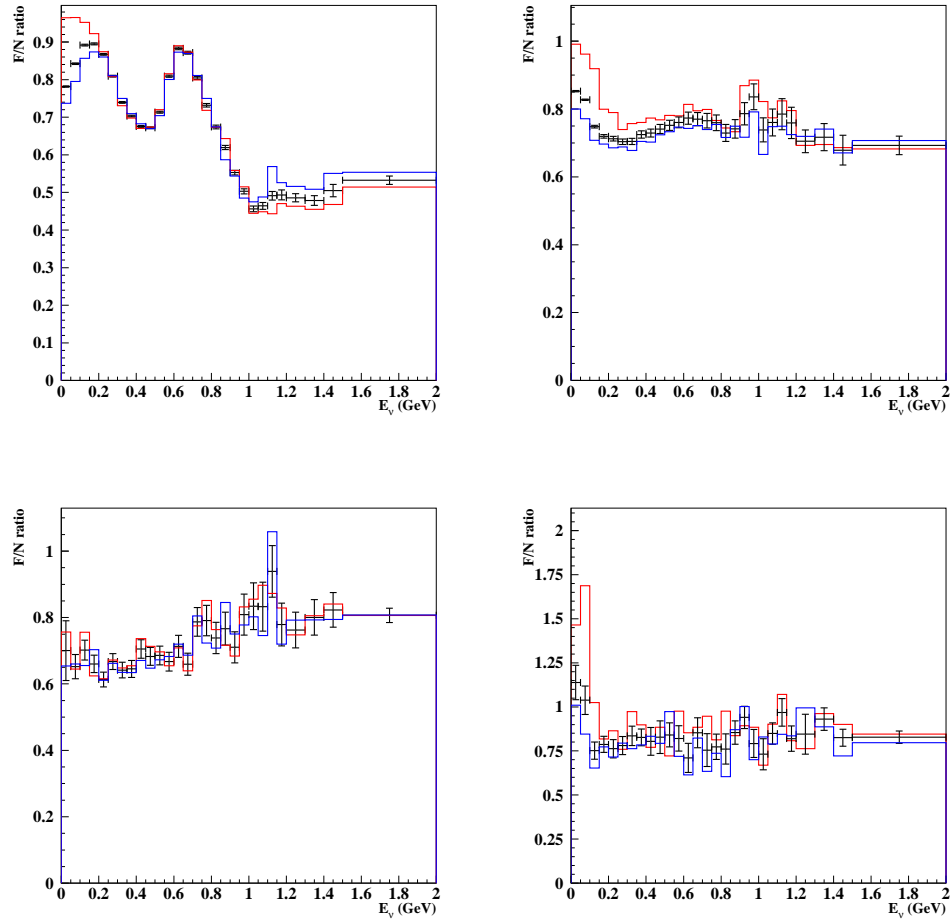


Figure 2.15: Far-to-near ratio prediction for ν_μ (top left), $\bar{\nu}_\mu$ (top right), ν_e (bottom left) and $\bar{\nu}_e$ (bottom right) fluxes. Direct (red) and indirect (blue) contributions are shown for all species.

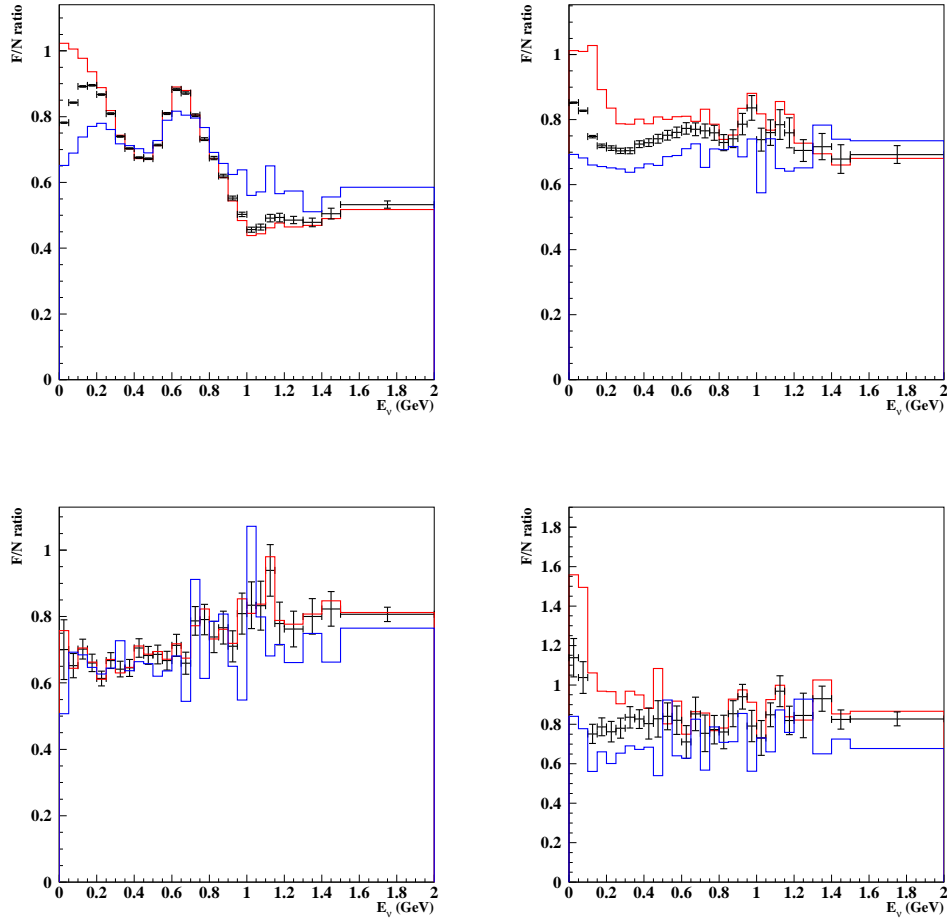


Figure 2.16: Far-to-near ratio prediction for ν_μ (top left), $\bar{\nu}_\mu$ (top right), ν_e (bottom left) and $\bar{\nu}_e$ (bottom right) fluxes. Target (red) and non-target (blue) contributions are shown for all species.

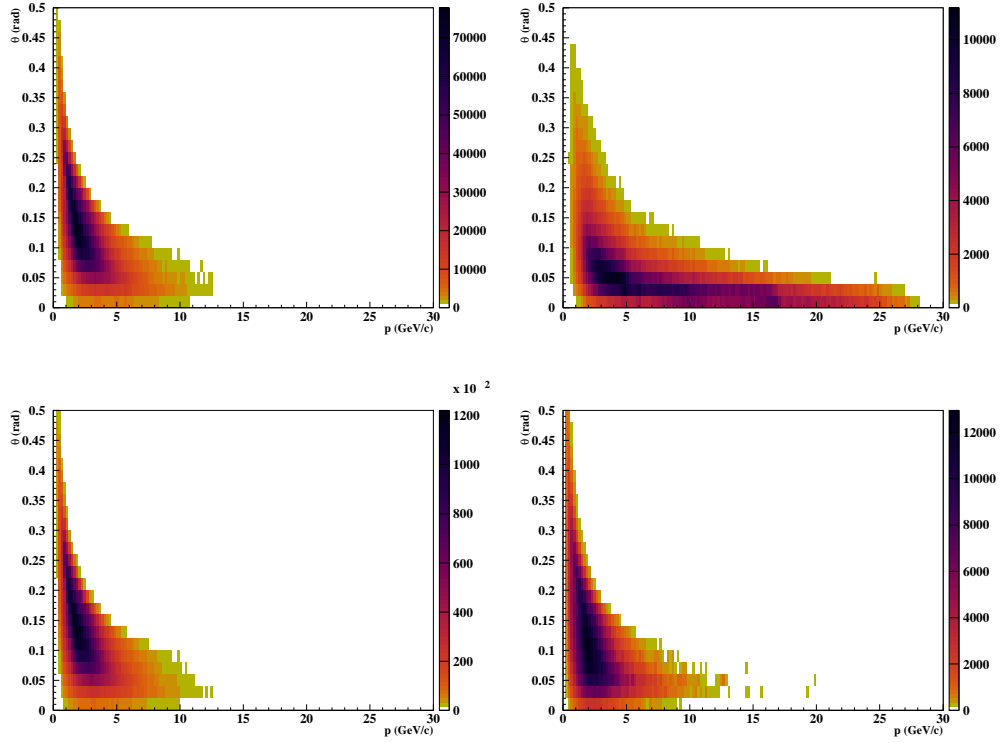


Figure 2.17: The $\{p, \theta\}$ distributions of secondary π^+ giving neutrinos in the far detector for the direct (top left) and indirect (top right) contributions, and of parent π^+ for the target (bottom left) and non-target (bottom right) contributions are shown.

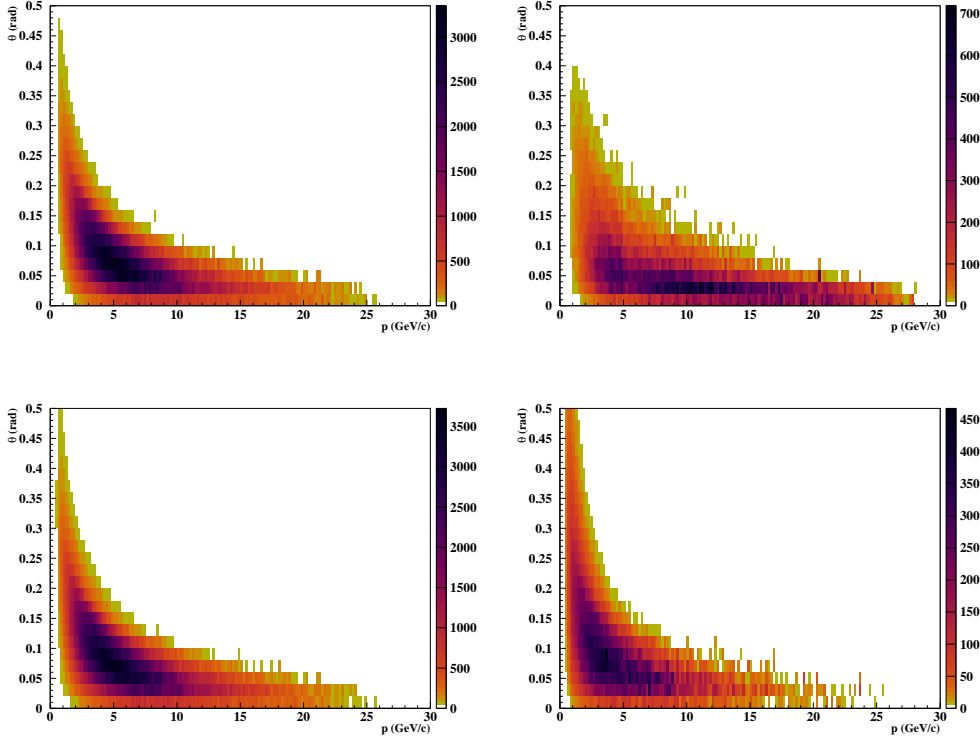


Figure 2.18: The $\{p, \theta\}$ distributions of secondary K^+ giving neutrinos in the far detector for the direct (top left) and indirect (top right) contributions, and of parent K^+ for the target (bottom left) and non-target (bottom right) contributions are shown.

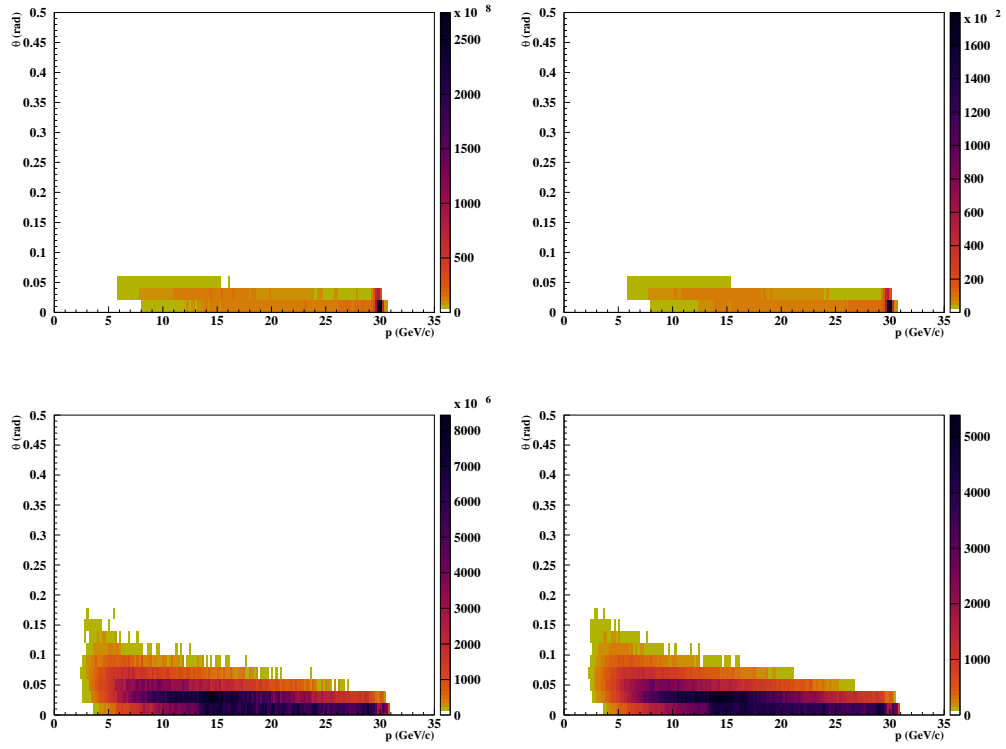


Figure 2.19: The $\{p, \theta\}$ distributions of protons (top) and neutrons (bottom) indirectly producing neutrinos in the near (left) and far detectors (right).

should be considered for all four different neutrino species (ν_μ , $\bar{\nu}_\mu$, ν_e , $\bar{\nu}_e$), not only for ν_μ 's. Actually, the far detector will measure both muon-like ($\nu_\mu + \bar{\nu}_\mu$) and electron-like ($\nu_e + \bar{\nu}_e$) events via charged current quasi-elastic (CCQE) reactions: in these processes the angle of the outgoing lepton is reconstructed but its charge is not measured, so that neutrinos and anti-neutrinos cannot be distinguished. On the contrary, the near detector has charge measurement capabilities in the reconstruction of the same reactions and will distinguish the four different neutrino species. Thus, the prediction of the number of muon-like or electron-like events in the far detector requires the extrapolation of spectra for both neutrino and anti-neutrino measured in the near detector and their convolution with the corresponding energy-dependent neutrino cross sections.

2.3.4 Model dependence of the neutrino flux predictions

Different systematics have been considered in recent studies of the T2K Beam Group, [76]. Among others, uncertainties on the proton beam parameters, neutrino beam direction, target and horn alignment, horn currents and magnetic field asymmetries are considered. In this section, we concentrate on the systematic error that can be attributed to the model dependence of the flux predictions. The T2K flux predictions depend on the choice of model used to simulate primary and secondary interactions in the JNUBEAM code.

Different Monte-Carlo samples were produced using models within the Geant 3.21 framework that were available in the JNUBEAM 10a release. These include the GHEISHA [56] (default hadronization model of Geant 3.21), GFLUKA [56] and GCALOR [57] models. The plots shown in this section correspond to the following statistics: 10.5 M events for GCALOR, 1.5 M events for GHEISHA and 1.5 M events for GFLUKA. Predictions from the three sets of events were produced using the same model for the simulation of both primary and secondary interactions. Fig. 2.20 shows flux predictions for ν_μ and ν_e species for the different models for both near and far detectors.

Model predictions may vary quite significantly over the same energy range. Thus, the maximal difference between various predictions may be considered as an estimator of the systematic error related to the use of different models. In such a case, Fig. 2.20 clearly shows that predictions of the absolute neutrino fluxes could be different by a factor of up to 2 depending upon the choice of hadronization model, e.g. ν_μ flux at peak energy for near and far detectors. Systematic uncertainties presented in [76] (updated in [54]) related to the proton beam parameters, misalignment of the elements of the beamline, horn currents and field asymmetry, already account for $\sim 2\%$ (summed in quadrature). The contribution due to the choice of model only would already be larger than the requirement of 5 % needed to fulfill the T2K physics goals.

The far-to-near ratio can be computed according the predictions of the previ-

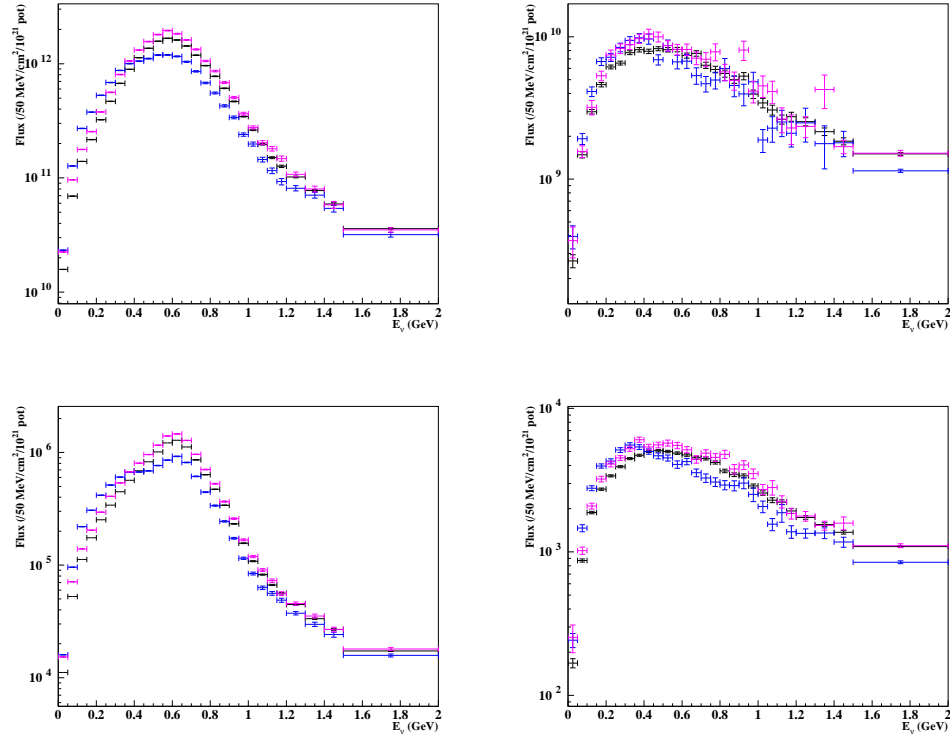


Figure 2.20: ν_μ (left) and ν_e (right) spectra at the ND280 near detector for a fiducial transverse area of $150 \times 150 \text{ cm}^2$ (top) and at the far detector (bottom). Predictions are shown for different models used for the simulation of both primary and secondary interactions: GCALOR (black), GFLUKA (purple), GHEISHA (blue).

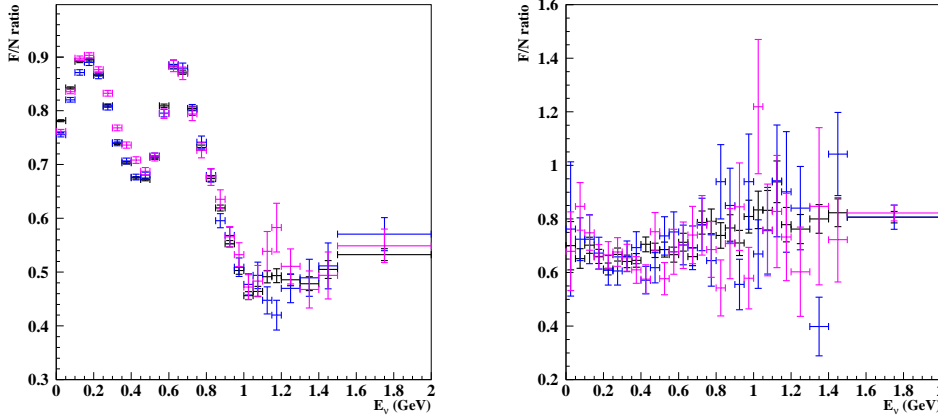


Figure 2.21: Far-to-near ratio for ν_μ (left) and ν_e (right) species. Predictions are shown for different models used for the simulation of both primary and secondary interactions: GICALOR (black), GFLUKA (purple), GHEISHA (blue).

ously discussed models. Fig. 2.21 shows the far-to-near ratio predictions for the ν_μ and ν_e species. For comparisons, we consider the predictions obtained with the GICALOR model as the reference sample. The relative fraction of the GHEISHA and GFLUKA models with respect to the GICALOR predictions are shown for the ν_μ and ν_e species in Fig. 2.22. As can be seen, the far-to-near ratio prediction for the ν_μ flux varies by more than 3 % as a function of the neutrino energy. For the other species, the available statistics of the different Monte-Carlo sets does not allow us to draw clear conclusions.

The differences between predictions based on various models is due to different treatment of primary and secondary interactions in the target and elements of the beamline (e.g. conductor of the magnetic horns). Different treatments of interactions will actually result in variations over the $\{p, \theta\}$ phase space of hadrons exiting the production target. However, the focusing system of the T2K beamline selects a particular region of this phase space. The very forward production region (very low polar angle) is also particularly important since not affected by the focusing and already in the beam direction. Thus, if these regions of the $\{p, \theta\}$ phase space are populated differently by the various models, the relative fraction of hadrons producing neutrinos over a given energy range will be different. Differences between models in terms of secondary hadron production and secondary interactions in the target are illustrated in Fig. 2.23, that shows the relative fractions of the indirect and non-target productions for the ν_μ and ν_e species.

In summary, the estimations presented in this section clearly show that, using the T2K beamline simulation without additional constraint on the hadron produc-

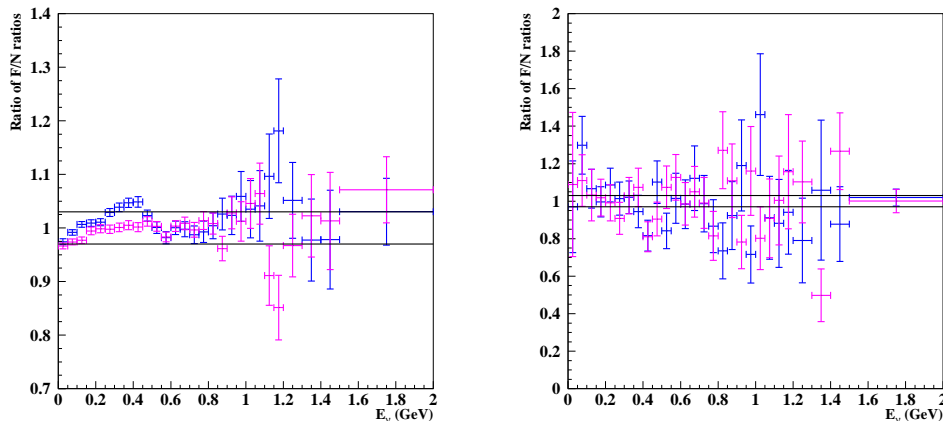


Figure 2.22: Ratios of far-to-near ratios computed with GHEISHA (blue) and GFLUKA (purple) models with respect to the reference ratio computed with the GCALOR model. The horizontal black lines show a $\pm 3\%$ band.

tion model chosen for the predictions, would not allow to fulfill the T2K physics goals. In terms of the T2K requirements:

- (i) the 5 % precision on the absolute flux prediction is not reached;
- (ii) the 2-3 % precision on the far-to-near ratio prediction is not reached either.

These conclusions are certainly justified for the ν_μ flux. Drawing conclusions for the other neutrino species obviously requires to repeat these studies over a larger statistics.

In the next chapter, the NA61/SHINE hadron production experiment is presented. In particular, in Section 3.2, requirements on the statistics of the NA61 measurements are estimated based on the T2K physics goals. In this chapter, we stressed the importance of the long target data measurements to maximize our control on the flux predictions obtained from a given hadronization model in the T2K beam simulation. However, how to use such measurements to constrain models efficiently is not that obvious. Actually, different options can be considered based on the following points:

- (i) unlike thin target data, long target measurements (unless primary and secondary interaction vertices are reconstructed in the target) cannot provide production cross sections;
- (ii) with an appropriate set of reconstructed track parameters, such measurements could eventually be used as a direct input to the simulation (on an

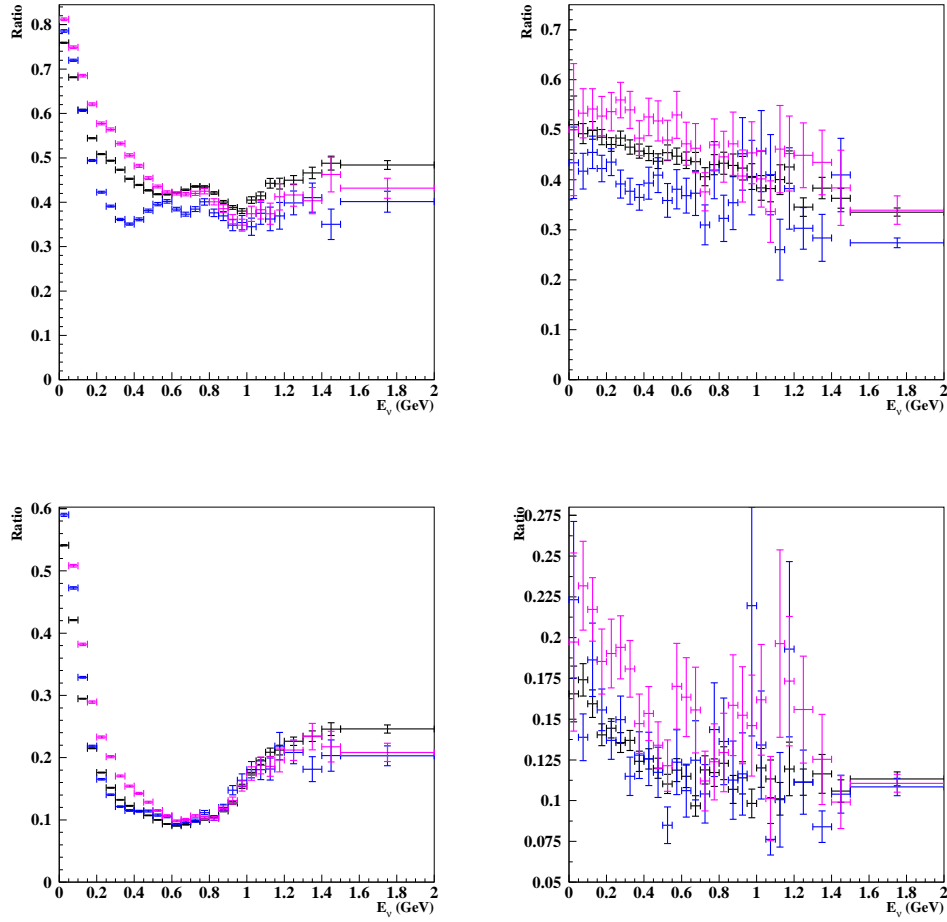


Figure 2.23: Ratio of the indirect (top) and non-target (bottom) contributions over the total contribution for the far detector for ν_μ (left) and ν_e (right) fluxes using the GICALOR (black), GHEISHA (blue) and GFLUKA (purple) models.

event-by-event basis) of the neutrino beam. This would in principle require that the measurements cover a full 4π acceptance;

- (iii) comparisons with thin target measurements may constrain secondary interactions in the long target (e.g. HARP thin and long target data comparisons [77]). However, such comparisons require that the primary interaction of the model used in the simulation is already constrained by some other data. In such a two-step approach, the full potential of the long target data might not be used in an optimal way, and systematics related to the method might be complicated to estimate and to control.

To our knowledge, there are currently no neutrino experiment for which the flux predictions are based on long target auxiliary measurements. As an example, the HARP based neutrino flux predictions for the K2K neutrino oscillation experiment were based on data taken with a thin ($5\% \lambda_I$) Aluminum target. The same is true for the MiniBooNE experiment with a thin ($5\% \lambda_I$) Beryllium target. In most cases, production cross sections are measured out of a thin target at the beam energy of the neutrino experiment and used to constrain the primary production of the hadronization model used in the beam simulation. Re-interactions in the elements of the beamline (including the target material) may also be constrained by sparse measurements of production cross sections of relevant hadrons on different nuclei at various energies below that of the beam. This general procedure is currently followed by the T2K Beam Group: the primary interaction is constrained by the NA61/SHINE cross section measurements of $p+C$ at 31 GeV/ c beam momentum, while re-interactions are constrained by re-weighting the model production cross sections with a collection of cross section measurements for p , π^\pm and K^\pm below 31 GeV/ c on Carbon and Aluminum (material of the magnetic horns) targets, [64]. Later on, a two-step procedure such as (iii) might be developed.

In the next chapter we try to go farther and present a long target based analysis for the T2K neutrino flux predictions. To our mind, long target data was not efficiently (at all) used so far in neutrino flux predictions due to the lack of compatibility between the simulation of the neutrino beam experiments and that of the auxiliary hadron production experiments. In most cases, the two experiments are completely independent while a common formulation of results should be developed between the two. On one hand, flux predictions should be computed in terms of sources relevant for a hadron production experiment, and on the other hand, the measurements of the hadron production experiment should be provided in terms of variables that make sense for the neutrino flux prediction. Thus, in the case of T2K and NA61/SHINE, we first tried to understand how to express neutrino flux predictions in terms of the NA61 possible measurements (content of this chapter). In a second stage, we tried to understand the modifications that are required in the simulations of both T2K and NA61 experiments in order to provide a consistent framework for Monte-Carlo and data comparisons. These points are

developed in Section 3.3 for NA61 and in Chapter 4 for T2K. The main idea is to constrain the hadronization model used in the T2K beam simulation directly within the simulation and reconstruction chain of the NA61/SHINE experiment. Using an appropriate set of track parameters, the aim is to re-weight the T2K model at the level of charged hadrons exiting the target, thus accounting for both primary and secondary interactions in the target at the same time. By using this common framework, the comparison of the T2K model to the NA61 data can be made at the raw reconstructed data level before any correction (carrying statistical and systematic uncertainties) is necessary to get absolute particle spectra.

Chapter 3

The NA61/SHINE auxiliary hadron production measurements

The NA61/SHINE [[78],[79],[80], [81]] experiment (SPS Heavy Ion and Neutrino Experiment) is a fixed-target experiment located at the CERN SPS. Among other physics goals, the T2K oriented physics program of NA61 aims at precise measurements of pion and kaon production yields in proton-Carbon interactions at 31 GeV/ c beam momentum. The NA61 experiment performed measurements with a thin Carbon target (4 % of the interaction length, λ_I) as well as with a full-size replica of the T2K target ($1.9 \lambda_I$). All results presented in this chapter were obtained with the 2007 pilot run data. The first NA61 results on charged pion spectra in p+C interactions at 31 GeV/ c [82] are reported in Section 3.5.

The T2K physics goals require to constrain the absolute neutrino flux predictions down to 5 % and the far-to-near ratio (possible extrapolation method of the near detector measurements for the predictions at the far detector) down to 2-3 %. How these constraints translate into statistics requirements for the NA61 long target measurements is developed in Section 3.2. As explained in Chapter 2, we think that these measurements are important to constrain significantly (up to 90 % of the flux at peak energy for both ν_μ and ν_e) the T2K flux predictions at the level of both primary and secondary interactions in the target. A first analysis of the 2007 replica target data is presented in this chapter.

NA61 took more data during longer runs in 2009 and 2010. The 2010 run period was mainly dedicated to measurements with the T2K replica target. The corresponding beam request was based on the studies presented in Section 3.2.

How the NA61 long target data can be used in T2K will be discussed in Chapter 4. The current usage of the NA61 2007 thin target data in T2K is described in Chapter 5.

3.1 The NA61 experimental setup

The NA61 experiment is a large acceptance spectrometer in the North Area H2 beamline of the CERN SPS. A schematic representation of the layout is shown in Fig. 3.1. The main components of the current detector were constructed and used by the NA49 collaboration [83]. A set of scintillation and Cherenkov counters as well as beam position detectors (BPDs) upstream of the spectrometer provide timing reference, identification and position measurements of the incoming beam particles. The main tracking devices of the spectrometer are large volume Time Projection Chambers (TPCs). Two of them, the vertex TPCs (VTPC-1 and VTPC-2 in Fig. 3.1), are located in the magnetic field of two superconducting dipole magnets with a maximum combined bending power of 9 Tm. In order to optimize the acceptance of the detector at 31 GeV/ c beam momentum, the magnetic field used during the 2007 data taking period was set to a bending power of 1.14 Tm. Two larger TPCs (MTPC-L and MTPC-R) are positioned downstream of the magnets symmetrically to the beamline. The TPCs are filled with Ar:CO₂ gas mixtures in proportions 90:10 for VTPCs and 95:5 for MTPCs. The particle identification capability of the TPCs based on measurements of the specific energy loss, dE/dx , is complemented by time-of-flight measurements using Time-of-Flight (ToF) detectors. The ToF-L and ToF-R arrays of scintillator pixels have a time resolution of better than 90 ps. Before the 2007 run, the experiment was upgraded with a new forward time-of-flight detector (ToF-F) in order to extend the acceptance for the T2K physics program. The ToF-F consists of 64 scintillator bars with photomultiplier (PMT) readout at both ends resulting in a time resolution of about 115 ps, see Fig. 3.2. In 2009, the ToF-F was extended by two modules (80 scintillator bars in total for an active area of $\sim 700 \times 120$ cm²) to enlarge further the acceptance of the detector for the neutrino physics program.

A 31 GeV/ c secondary hadron beam is produced from 400 GeV protons extracted from the SPS in slow extraction mode. The beam is transported along the H2 beamline towards the experiment. Collimators in the beamline are adjusted to get an average beam particle rate of 15 kHz. Protons from the secondary hadron beam are identified by two Cherenkov counters, a CEDAR and a threshold counter, labeled C1 and C2, respectively. The CEDAR counter, using a 6-fold coincidence, provides positive identification of protons, while the threshold Cherenkov counter, operated at a pressure lower than the proton threshold, is used in anti-coincidence in the trigger logic. The fraction of protons in the beam was about 14%. A selection based on signals from Cherenkov counters allowed to identify beam protons with a purity of about 99%. A consistent value for the purity was found by bending the beam into the TPCs with the full magnetic field and using the dE/dx identification method.

A 24 mm diameter scintillation counter, S2, positioned between BPD-1 and BPD-2, provides beam definition. Another counter, S1, located upstream of BPD-

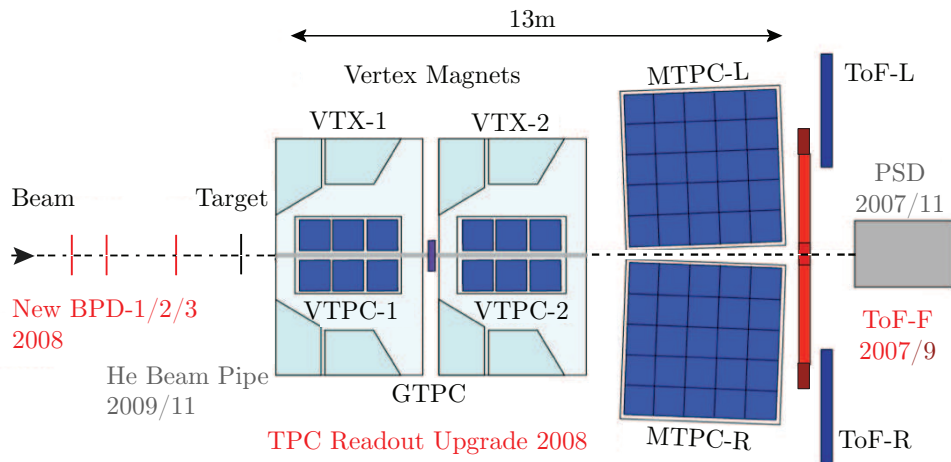


Figure 3.1: The layout of the NA61 experiment at the CERN SPS (top view, not to scale). The incoming beam direction is along the z axis. The magnetic field bends charged particle trajectories in the $x - z$ (horizontal) plane. The drift direction in the TPCs is along the y (vertical) axis.

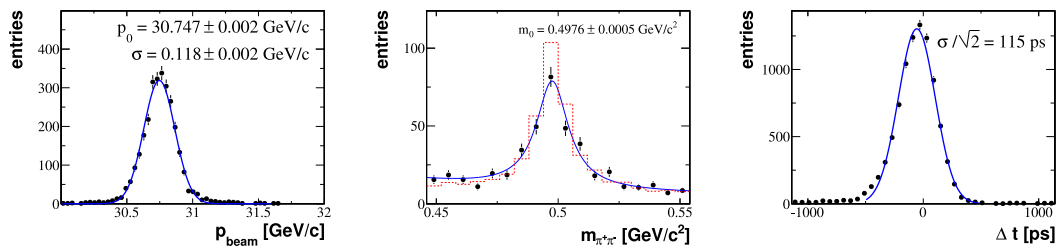


Figure 3.2: The beam momentum distribution (statistical error only) measured in the TPCs (left), invariant mass distribution of the K_S^0 candidates (middle, the dashed histogram shows the simulation normalized to data) and resolution of the ToF-F (right).

1, provides the timing information (start time for all counters). Beam protons are then selected by the coincidence $C1 \cdot \overline{C2} \cdot S1 \cdot S2$.

The overall quality of the measurements was studied by reconstructing the momentum of beam particles and masses of K_S^0 and Λ particles from their V^0 decay topology. The beam momentum was measured directly in a dedicated run by bending the incoming beam particles into the TPCs with the full magnetic field. The measured beam momentum distribution is shown in Fig. 3.2. The mean value of 30.75 GeV/c agrees with the set value of 30.92 GeV/c within the available setting precision of the beam magnet currents ($\approx 0.5\%$) in the H2 beamline. The invariant mass distribution of K_S^0 candidates is also plotted in Fig. 3.2. The peak position (0.4976 ± 0.0005 GeV/c²) agrees with the known K_S^0 mass. The widths of

the K_S^0 and Λ invariant mass peaks are reasonably reproduced by the Monte-Carlo simulation which also confirms its validity for the following studies.

In order to understand the role of primary and secondary interactions in the hadron production out of the T2K target, NA61 performed measurements with two different targets: a thin (4 % of the interaction length, λ_I) Carbon target and a full-size replica of the T2K target. The thin target results reported in this thesis are based on the analysis of 667 k events recorded in 2007 with the Carbon target inserted, 46 k events recorded with the Carbon target removed and 80 k events recorded for calibration purposes.

The replica of the T2K target consists in an isotropic graphite rod of 90 cm length, 2.6 cm diameter and a density of $\rho = 1.83 \text{ g/cm}^3$. The target thickness along the beam is equivalent to about 1.9 nuclear interaction length. The analysis of the replica target data presented in this chapter is based on the 2007 data set of 235 k events.

3.2 T2K requirements on the NA61 measurements

3.2.1 Measurement of the target contribution in NA61

Initial studies of the NA61 statistics requirements were performed [53] during the preparation of the NA61 proposal [78]. These estimations have been revisited taking into account the experience from the NA61 2007 pilot run and the progress in the corresponding data analysis. In particular, the acceptance of the NA61 apparatus is now well known and can be included in these studies. The following estimations have been computed for the T2K replica target measurements and were included in the NA61 beam request for the 2010 run period.

As explained in Section 2.3.2, the target contribution accounts for ~ 90 % of both ν_μ and ν_e fluxes at peak energy. The corresponding spectra of hadrons exiting the target includes secondary hadrons as well as hadrons produced in the re-interaction of secondaries in the target. Thus, measuring hadrons exiting the T2K replica target in NA61 will directly constrain this contribution. In this section, we will consider only the target contribution of π^+ mesons contributing to the ν_μ flux. The results presented here should of course be extended to other parent particles and to the other neutrino species.

The NA61 experiment can measure the π^+ mesons exiting the target, not those produced in decays of particles exiting the target¹. For consistency, in what follows, the target contribution (as defined in Section 2.3.2) is restricted to π^+ mesons exiting the target. This is illustrated in Fig. 3.3 that shows the contribution of decay chains to the target production for the ν_μ flux at the near and far detectors.

¹Products of the so-called $V0$ -decays, e.g. $K_S^0 \rightarrow \pi^+\pi^-$, may actually be measured if a secondary vertex is reconstructed correctly. This contribution could eventually be included in a second stage of these studies.

As can be seen, the target contribution still remains as high as 80 % in the neutrino energy peak region.

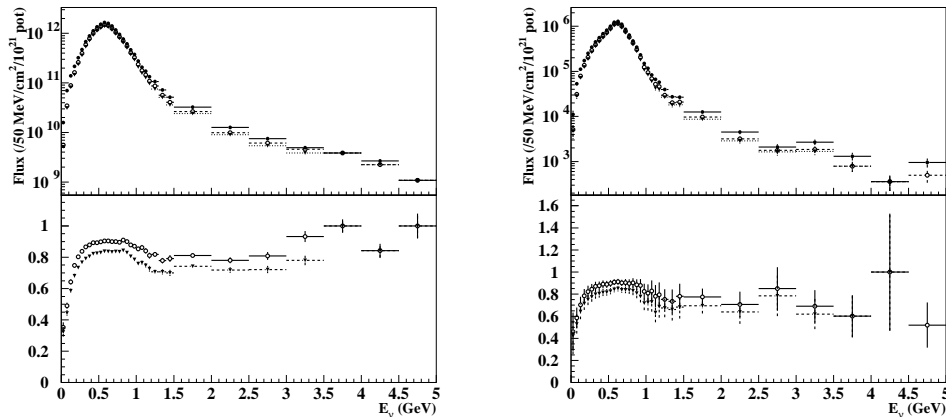


Figure 3.3: ν_μ flux from π^+ meson decays at near (left) and far (right) detectors. Upper plots show the total target contribution (full dots) and contributions with (empty dots) and without (triangles) decay chains. Lower plots show the ratio of target contributions with and without decay chains to the total contribution (same markers).

The target contribution is based on hadrons exiting the target. The reconstructed information in NA61 does not have to account for any other knowledge than that of the particle direction and momentum when exiting the target. Therefore, there is no need for a vertex constraint in the replica target (i.e. reconstruction of primary and secondary vertices). Instead, tracks reconstructed in the TPCs (so-called *global rtracks* in the NA61 terminology, see Section 3.4) can be extrapolated back in the magnetic field to the surface of the target. The spectra of hadrons exiting the target can be reconstructed in the $\{p, \theta\}$ phase space, where p is the measured momentum in the TPCs extrapolated onto the target surface, and θ is the exiting angle at the target surface.

Previous studies (e.g. [84]) have shown that the absolute neutrino fluxes and far-to-near ratio predictions are sensitive (both in shape and overall normalization) to the exit position of the neutrino parent particles on the surface of the target (along the incoming beam direction, z). Variations were also observed as a function of the beam profile used in the simulation (pencil beam, centered or shifted beam position, beam divergence, etc). To account for these effects, the replica target data in NA61 should be reconstructed in terms of longitudinal (exit point of tracks on the surface of the target) and radial (point of impact of the beam protons on the target upstream face) bins. The chosen binning for the extrapolation to the target consists in:

- (i) 6 longitudinal bins: 5 equidistant bins of 18 cm each and the last bin which represents the downstream face of the target;
- (ii) 3 to 4 radial bins (still optional, and not used in what follows).

The tracks reconstructed at the surface of the target are described by the following set of parameters:

- (i) position vector at exit point (point-of-closest-approach), \vec{q} .
- (ii) momentum vector at exit point, \vec{p} .
- (iii) angle with respect to the beam axis at exit point, θ .

Let us note, however, that track parameters at the surface of the target were not stored on output in the JNUBEAM 10a release. Instead of (ii) and (iii), momentum and polar angle at the parent production point in the target (which slightly differ from those at the surface of the target due to energy loss and multiple scattering) are used. Consequently, only five longitudinal bins are defined in the simulation in what follows (the downstream face of the target cannot be considered as a separate bin). More general modifications that should be applied to the JNUBEAM code to use the NA61 long target data consistently will be discussed in Chapter 4.

3.2.2 Statistical estimations

Different methods can be applied to propagate the NA61 statistical uncertainties in the T2K beam Monte-Carlo. In this study we developed a method that accounts for the NA61 acceptance. Acceptance maps (in the standard $\{p, \theta\}$ kinematic phase space) are computed for the 6 different longitudinal bins and using the so-called 20 GeV magnetic field configuration (corresponding to 1.14 Tm). Flat phase space distributions of *positively* charged particles are given as input to the NA61 simulation chain. Tracks are uniformly distributed over the surface of the target along the width of the longitudinal bins. In the transverse direction, the azimuthal angle is constrained above the tangent plane to the surface of the target at the exit point. The detector material is included (e.g. magnets yokes, coils, etc) in this study. More details are given in Section 3.7.

At the time this study was performed, no analysis of the replica target data had been done yet. The quality cuts used to count tracks in acceptance were based on the 2007 thin target data analysis. A better knowledge of the replica target data was gained later on and different cuts were developed for that particular analysis (see Section 3.6.2). The set of track selection cuts used for the replica target data analysis differs by an additional azimuthal cut (TRK cut(VII)), a cut on the topology (TRK cut(V)) of the extrapolated track on target and much tighter cuts on the required number of points on track. These cuts basically constrain the

acceptance above 40 mrad while the region of maximal acceptance in this study is shifted to smaller angles.

As can be seen in Fig. 3.40, the acceptance can be considered as approximately constant along the target (keeping in mind that the most downstream bin corresponding to the downstream face of the target is not considered as a separate bin in the JNUBEAM simulation). This is in particular due to the forward time-of-flight requirement that selects sharp cones in the azimuthal acceptance. For simplification, a single acceptance map is considered in the following for the whole target².

A natural way to estimate the effect of the NA61 measurement precision on the T2K flux predictions is to define a binning over the T2K $\{p, \theta\}$ phase space of interest, for which bins correspond to the same statistical accuracy of the NA61 measurements (e.g. same number of entries in acceptance). Such a binning is shown in Fig. 3.4. A default binning of the T2K phase space was proposed in former studies (e.g. [53]) and consists in bins of 200 MeV/ c in momentum and 20 mrad in polar angle. This binning is used for regions that correspond to a maximal acceptance in NA61. For regions of lower acceptance, the bin size is increased appropriately to account for the same statistical accuracy. Within this approach, uncertainties of hadron production measurements in NA61 can be translated by a uniform (in amplitude) variation of the bin content over the T2K phase space.

To do so, a variation of the content of a bin in $\{p, \theta, z\}$ has to be translated into a variation of the neutrino energy spectrum at the near and far detectors, and accordingly in a variation of the far-to-near ratio. The energy spectrum at the near and far detectors is expressed in terms of the original bin content. For each bin of neutrino energy, $\{E_\nu\}_j$, with n_j entries, the fraction of the flux, n_{ij} , coming from a given type of hadron, h , in a particular bin $\{p, \theta, z\}_i^h$ ³ is factorized in three components:

- (i) $N_i(p, \theta, z)$: number of hadrons in bin $\{p, \theta, z\}_i$
- (ii) $w_{ij}^n(E_\nu)$: normalization weight of the bin $\{p, \theta, z\}_i$ for the neutrino energy bin $\{E_\nu\}_j$
- (iii) $w_{ij}^f(E_\nu)$: fraction weight of the bin $\{p, \theta, z\}_i$ for the neutrino energy bin $\{E_\nu\}_j$

²In a second stage of these studies radial bins may also be introduced. Correlations between radial and longitudinal positions will probably require to compute different maps for the different radial bins in a given longitudinal bin.

³We will omit upper scripts labeling the hadron type since current studies are limited to π^+ mesons contributing to the ν_μ flux.

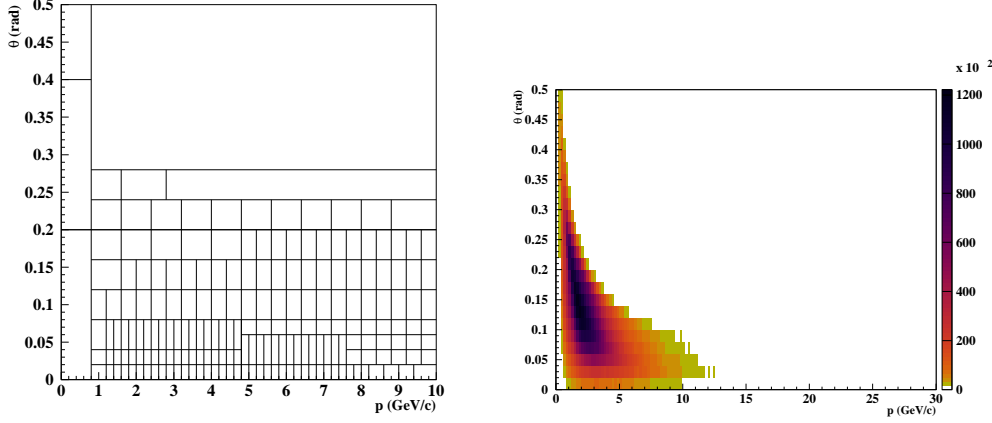


Figure 3.4: Binning template over the relevant T2K phase space which takes into account the NA61 acceptance over the measurement region (left). Different bin sizes are defined in order to get equivalent NA61 statistical accuracy in each bin. The bin size ranges from 200 MeV/c to 1200 MeV/c in momentum and from 20 mrad to 200 mrad in polar angle. Coverage of the positively charged pions from the target contribution that produce muon neutrinos in SK (right).

Normalization and fraction weights are computed as:

$$w_{ij}^n(E_\nu) = \frac{1}{N_{ij}} \sum_{k=1}^{N_{ij}} P(\pi, \beta_\pi, \theta)_k \cdot C_k \quad (3.1)$$

$$w_{ij}^f(E_\nu) = N_{ij}/N_i \quad (3.2)$$

where $P(\pi, \beta_\pi, \theta)$ are directional probabilities defined in Section 2.2.2, C_k are normalization factors for decay rates and number of protons on target, and $N_{ij}(E_\nu)$ is the number of hadrons in bin $\{p, \theta, z\}_i$ contributing to the neutrino flux in bin $\{E_\nu\}_j$. Using Eq. 3.1 and Eq. 3.2, the total flux in the neutrino energy bin $\{E_\nu\}_j$ can be re-computed as a sum over the contributions of all $\{p, \theta, z\}$ bins:

$$n_j(E_\nu) = \sum_i n_{ij}(E_\nu) = \sum_i N_i(p, \theta, z) \times w_{ij}^f(E_\nu) \times w_{ij}^n(E_\nu) \quad (3.3)$$

For a sufficiently large statistics, the fraction and normalization weights are constants that reflect the geometry and focusing properties of the beamline for each bin in $\{p, \theta, z\}$. The fraction weights represent the contribution of a given bin in $\{p, \theta, z\}$ to the flux in a particular bin of neutrino energy. The normalization weights represent the average probabilities for hadrons produced in a given $\{p, \theta, z\}$ bin to produce a neutrino in a particular energy bin in the near and far detectors. For more consistency, these weights should be computed starting from flat phase

space distributions in $\{p, \theta, z\}$. Computing them as in Eq. 3.1 and Eq. 3.2 is only exact in the limit where N_i is very large. The model dependence of these weights comes only from the treatment of re-interactions in the elements of the beamline.

Using Eq. 3.3 allows to propagate the statistical uncertainties of the NA61 measurements to the flux predictions by introducing variations of the initial number of entries in the $\{p, \theta, z\}$ bins, without any change of the corresponding fraction and normalization weights. As an illustration, Fig. 3.5 shows the re-computed spectra at the near and far detectors and corresponding far-to-near ratio for a variation of -50 % of the $\{p, \theta\}$ bin (for all z) covering the phase space region between 0.8-1.6 GeV/ c and 0.2-0.24 mrad. As can be seen in Fig. 2.17 this bin contributes significantly to the ν_μ flux from the target contribution of π^+ mesons. A clear effect is visible on the ratio plots.

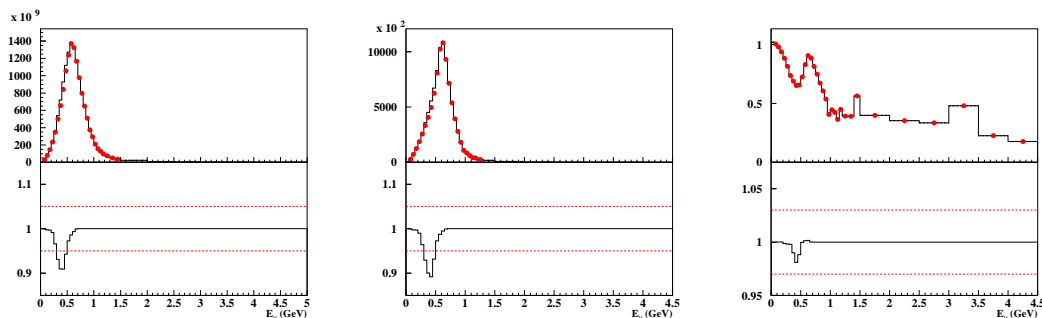


Figure 3.5: Flux predictions for the near detector (left), the far detector (middle) and the corresponding far-to-near ratio (right) over the whole target. Black histograms show the original spectra while dashed histogram with red markers show re-computed entries for a -50 % variation of the initial $\{p, \theta, z\}$ bin content of a single $\{p, \theta\}$ bin covering the phase space region between 0.8-1.6 GeV/ c and 0.2-0.24 rad. Ratios between re-computed and original spectra are shown in the bottom part of the plots. For the near and far detector spectra, dashed red horizontal lines show a ± 5 % band, and a ± 3 % band for the far-to-near ratio.

Two different approaches have been followed to introduce the NA61 measurements uncertainties. The first one simply reproduces the statistical fluctuations of the measurements by applying an independent variation of the bin contents. A 10 % uncertainty was first considered. For each $\{p, \theta, z\}$ bin, the sign of the variation is randomly chosen. Fig 3.6 shows the resulting spectra for a single experiment, while Fig. 3.7 shows results obtained by following the same procedure over 1000 different experiments. One can see that the T2K requirement of 5 % accuracy for the absolute neutrino flux predictions at the near and far detectors is not satisfied for this precision of the measurements in NA61. In a second approach, the ± 10 % bounds are considered as maximal (minimal) variations in the *shape* of the cross section over a given angular range (see Fig. 3.8). Note that this set

of variations is actually a subset of the random variations previously described. Such variations are less likely to occur but correspond more or less to what an experiment like NA61 with much more statistics would measure: data points (with much smaller error bars) would stay within the current NA61 statistical errors and the overall shape of the production cross section would vary within these bounds. Fig. 3.9 shows results obtained by following this procedure over 1000 different experiments. One can see that the T2K requirement of 5 % accuracy for the absolute neutrino flux predictions at the near and far detectors is neither satisfied for this precision of the measurements in NA61.

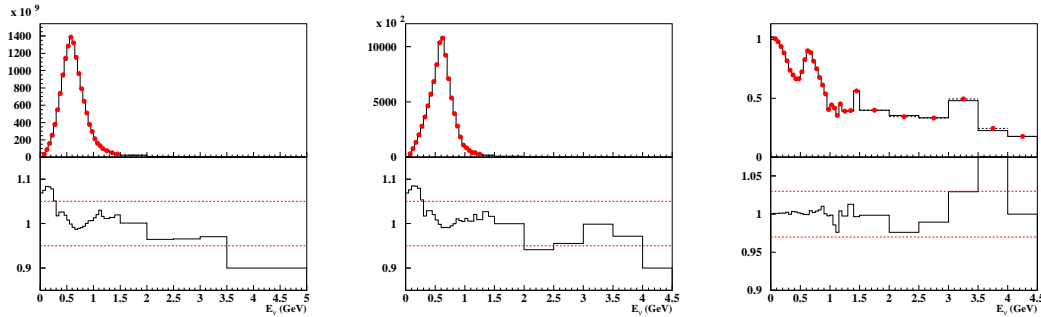


Figure 3.6: Flux predictions for the near detector (left), the far detector (middle) and the corresponding far-to-near ratio (right) over the whole target. Black histograms show the original spectra while dashed histogram with red markers show re-computed entries for a 10 % variation of the initial $\{p, \theta, z\}$ bin content. The variation is introduced independently over the bins in the different angular slices of the binning template. Ratios between re-computed and original spectra are shown in the bottom part of the plots. For the near and far detector spectra, dashed red horizontal lines show a ± 5 % band, and a ± 3 % band for the far-to-near ratio.

Fig. 3.10 and Fig. 3.11 show the same predictions over 1000 experiments considering a 5 % precision of the NA61 measurements. In this case, both requirements on the absolute flux and far-to-near ratio predictions are fulfilled at least up to 2.5 GeV neutrino energy. In terms of the NA61 measurements with the T2K replica target, a 5 % precision is obtained for 400 fully identified (with both time-of-flight and energy loss measurements) π^+ tracks in each of the $\{p, \theta, z\}$ bins of the template shown in Fig. 3.4. This number was converted into a required number of triggers (based on the efficiencies of the 2009 data taking) and included in the 2010 beam request of NA61.

3.3 The NA61 simulation chain

The NA61 simulation chain consists in four main software packages:

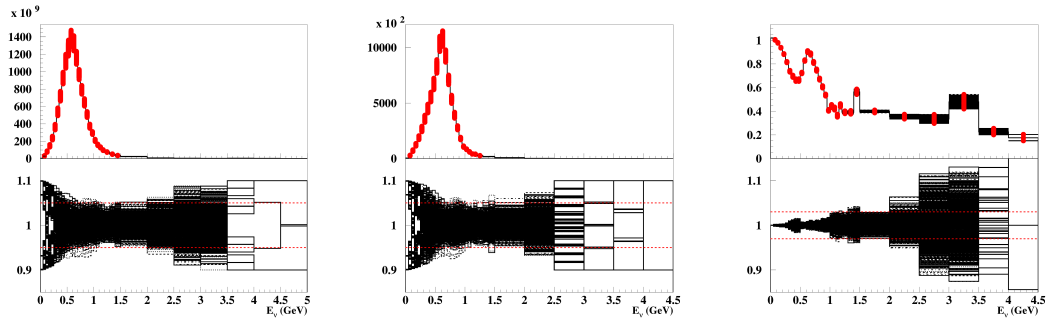


Figure 3.7: Flux predictions for the near detector (left), the far detector (middle) and the corresponding far-to-near ratio (right) over the whole target for 1000 simulated experiments with a 10 % variation of the initial $\{p, \theta, z\}$ bin contents. The variation is introduced independently over the bins in the different angular slices of the binning template. Ratios between re-computed and original spectra are shown in the bottom part of the plots. For the near and far detector spectra, dashed horizontal lines show a $\pm 5\%$ band, and a $\pm 3\%$ band for the far-to-near ratio.

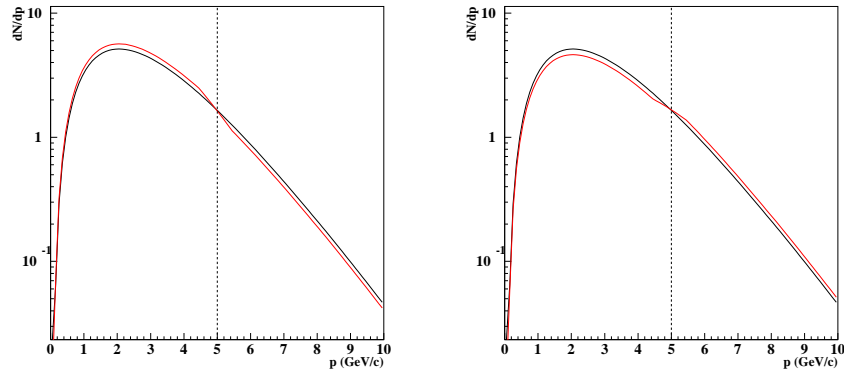


Figure 3.8: Illustration of the cross section variation for a particular angular interval. The shape of the dN/dp spectrum is modified (red curve) around a fixed point at 5 GeV/c (randomly chosen): positively shifted before and negatively shifted after (left), and opposite shifts (right). The shape is shifted at the edges of a $\pm 10\%$ band around the original (black) curve.

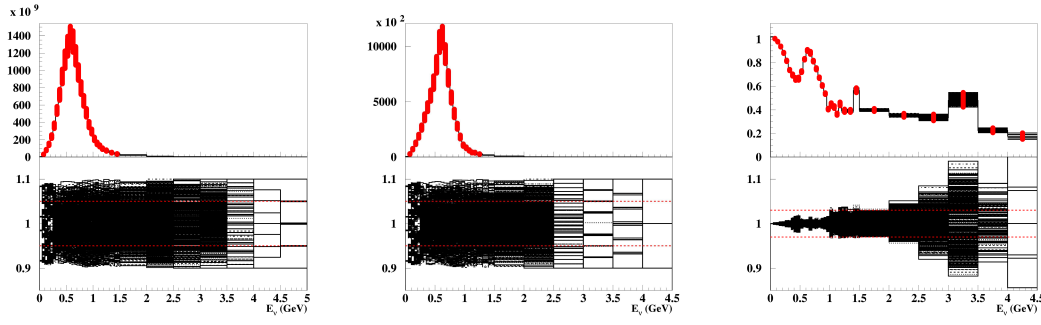


Figure 3.9: Flux predictions for the near detector (left), the far detector (middle) and the corresponding far-to-near ratio (right) over the whole target for 1000 simulated experiments with a 10 % variation of the initial $\{p, \theta, z\}$ bin contents. The variation is introduced by variations of the shape of the production cross section in the different angular slices of the binning template. Ratios between re-computed and original spectra are shown in the bottom part of the plots. For the near and far detector spectra, dashed horizontal lines show a $\pm 5\%$ band, and a $\pm 3\%$ band for the far-to-near ratio.

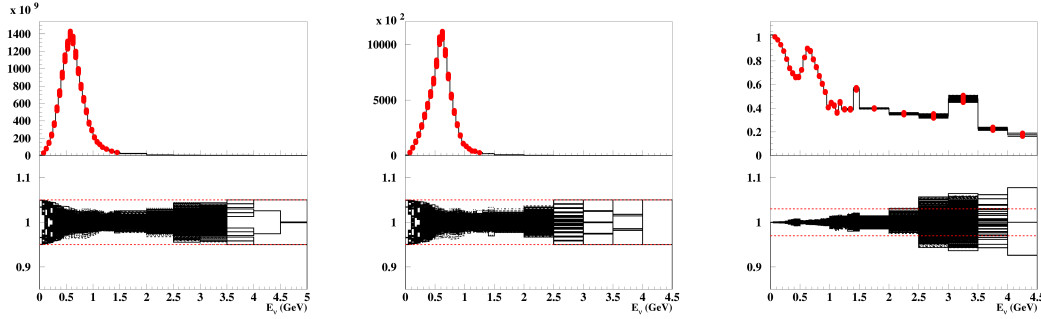


Figure 3.10: Flux predictions for the near detector (left), the far detector (middle) and the corresponding far-to-near ratio (right) over the whole target for 1000 simulated experiments with a 5 % variation of the initial $\{p, \theta, z\}$ bin contents. The variation is introduced independently over the bins in the different angular slices of the binning template. Ratios between re-computed and original spectra are shown in the bottom part of the plots. For the near and far detector spectra, dashed horizontal lines show a $\pm 5\%$ band, and a $\pm 3\%$ band for the far-to-near ratio.

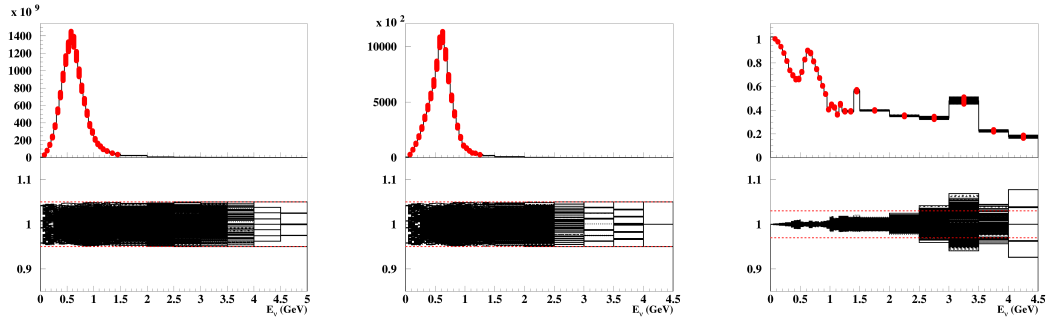


Figure 3.11: Flux predictions for the near detector (left), the far detector (middle) and the corresponding far-to-near ratio (right) over the whole target for 1000 simulated experiments with a 5 % variation of the initial $\{p, \theta, z\}$ bin contents. The variation is introduced by variations of the shape of the production cross section in the different angular slices of the binning template. Ratios between re-computed and original spectra are shown in the bottom part of the plots. For the near and far detector spectra, dashed horizontal lines show a ± 5 % band, and a ± 3 % band for the far-to-near ratio.

- (i) GEO: contains all the geometrical description of the experimental setup. Detector dimensions and positions within the NA61 coordinate system are automatically imported from the data base of the experiment using an appropriate set of keys for the compilation of the geometry source files. An overall view of the simulated geometry is shown in Fig. 3.12.

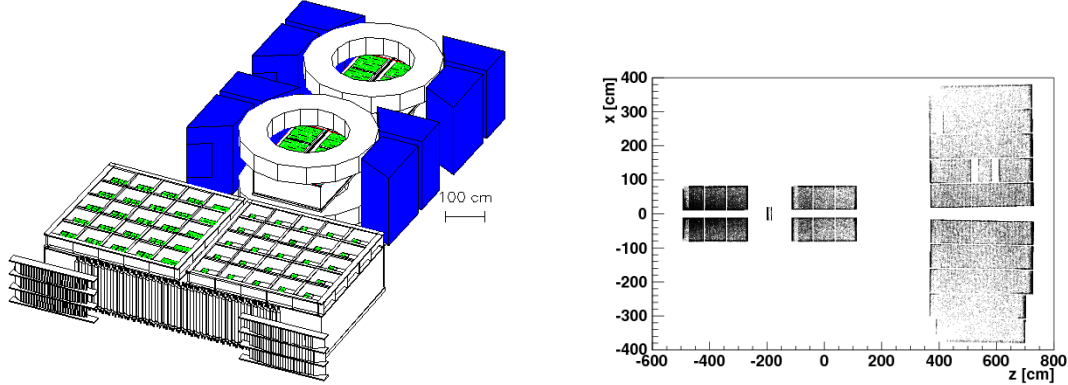


Figure 3.12: The overall simulated geometry of NA61 (left). Magnet yokes are shown in blue. The upper yokes are not displayed to show the vertex TPCs. For each TPC the cover of the readout planes are not displayed to show the structure of the readout sectors (in green). Reconstructed clusters (first and last points) of simulated tracks in the TPCs (right) are shown in the x-z projection (right). Regions without clusters in the MTPCs correspond to missing mother boards in the readout sectors during the 2007 data taking.

- (ii) GNA61: is the Geant 3.21 [56] based simulation code. It propagates particles through the detector geometry and material taking into account the magnetic field as well as relevant physics processes, such as particle interactions and decays. Hits are generated in geometrical volumes declared sensitive. No digitization is performed at this stage of the simulation.
- (iii) G2DS: fills in the NA61 standard simulated data structures from the GNA61 output. The new file format can later on be handled by DSPACK, which is the overall client manager of the reconstruction chain.
- (iv) MTSIM: performs the digitization of the TPC hits in terms of pads and time slices along the drift distance (distance between the hit position and the readout plane). The longitudinal and transverse spread of the charge along the drift length is simulated according to parametrizations of real data (e.g. cluster shape as a function of drift length). Effects of the electronics of the readout chambers such as threshold and gain are taken into account. Lots of efforts were invested to reproduce the 2007 electronics configuration of the TPC readout (see Fig. 3.12). Missing mother boards during the 2007 data taking were introduced by locally switching off simulated pad rows in the MT-PCs. Some of these boards are actually located in relevant phase space regions of the T2K measurements. The correct simulation of the number of clusters on track is of significant importance for the analysis and in this respect, a consistent treatment of the missing mother boards is required. MTSIM also applies to the simulated data all distortions which are corrected for in the real data reconstruction: effects of non-uniform electric and magnetic fields in the VT-PCs (e.g. $E \times B$ effect) and time offsets of the electronic channels are applied to the simulated clusters. Finally, MTSIM packs the simulated data in the same format used for the real data, so that both data types are reconstructed through the same chain.

The primary kinematics of the simulated events can be defined from different inputs:

- (i) external event generator for the primary interaction: an external model is used to simulate proton-Carbon primary interactions at 31 GeV/c. The outgoing particles are attached to a primary vertex, which is placed in the target according to the measured beam size in the transverse direction, and exponentially in the longitudinal direction according to the target nuclear interaction length. Secondary interactions are simulated by event generators available within Geant 3.21.
- (ii) external event generator for interactions in the target: an external model (standalone simulation) is used to simulate both primary and secondary interactions in the target material. For each event, the original position and divergence of the beam track are randomly chosen from two-dimensional prob-

ability density functions (p.d.f.s) built from the real data distributions. All particles exiting the target volume are stored on output with exiting position and momentum at the surface of the target. This information is used as input in GNA61 to propagate outgoing particles through the NA61 setup.

- (iii) internal event generator: primary and secondary interactions are simulated by available hadronization models in Geant 3.21. GNA61 includes the GHEISHA and GFLUKA generators, as well as an interface to the GCALOR model. In this mode, protons are generated upstream of target at the BPD-3 z position. The original position and divergence of the beam tracks are randomly chosen from two-dimensional p.d.f.s built from the real data distributions.
- (iv) flat phase space: a specifically formatted ASCII input generates flat phase space distributions in $\{p, \theta\}$ for detector acceptance studies. In this mode, physics processes except energy loss are switched off while distortions are still simulated.

The NA61 thin target simulated data set was produced with the VENUS 4.12 [85] model used as an external event generator for the primary proton-Carbon interactions (mode (i)). The GHEISHA model was used to simulate secondary interactions in the target and detector material.

The data set simulated for the replica target analysis was produced with the FLUKA standalone simulation for primary and secondary interactions in the target (mode (ii)). Secondary interactions in the detector material are simulated by the GCALOR model. A training set of 1 M events was used to optimize event and track quality cuts, while another statistically independent set of 1 M events was used for analysis. This Monte-Carlo production is based on major modifications of the original NA61 simulation chain. As mentioned in the previous chapter, compatibility between the NA61 and the T2K simulation chains is mandatory to use the NA61 replica target data consistently:

- (i) The T2K beam Monte-Carlo includes the simulation of the proton beam impinging on the production target according to the measured beam parameters. Since the NA61 and T2K beam profiles are different (the beam was made large enough in NA61 to cover uniformly the cross section of the target), a re-weighting in radial bins of the proton impact on the upstream face of the target might be necessary. Thus, the simulation of the proton beam on target was implemented in NA61. The beam counters and geometry of the beamline are not reproduced in the simulation. Instead, the beam is generated at the BPD-3 z position upstream of the target using data based two-dimensional p.d.f.s in the position-divergence phase space. Dedicated studies of the beam parameters have actually shown that correlations were only significant between the beam track divergence and position in BPD-3.

The original beam data distributions used to build these p.d.f.s are shown in Fig. 3.13.

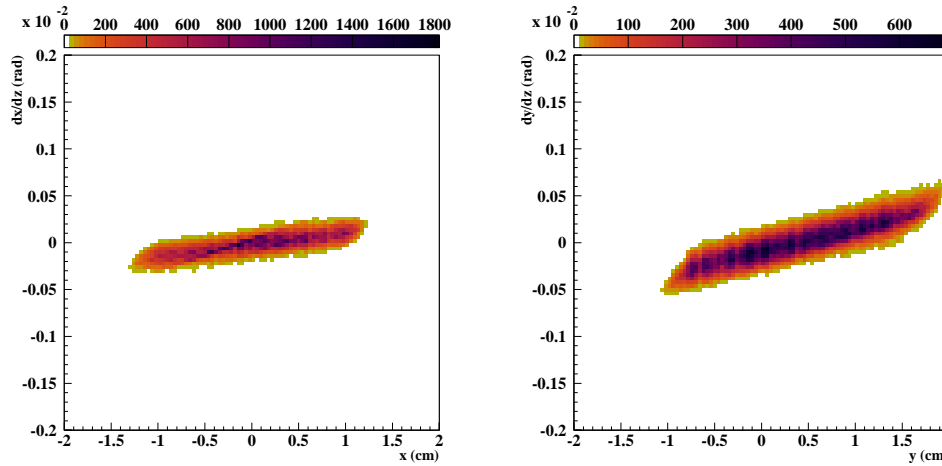


Figure 3.13: Divergence vs position of the beam in the x (left) and y (right) directions.

Inefficiencies of BPD-3 are taken into account in the p.d.f.s. by extrapolating beam tracks from BPD-2 in cases where clusters were badly reconstructed in BPD-3 (i.e. in 5 % of the events in the x direction and 15 % of the events in the y direction). The simulated beam divergence, beam profile on target and radial distribution are shown in Fig. 3.14.

To simulate correctly the impact position of protons on the upstream face of the target, dedicated studies were performed to determine the target alignment with respect to BPDs and beam axis in the NA61 reference system (see Section 3.6.1). Target tilts were estimated to +5 mrad around the y axis and -2.8 mrad around the x axis. The tilts are included in the simulated geometry of the target.

- (ii) The most important modification of the NA61 simulation chain consisted in implementing the model used for the T2K beam simulation within the NA61 framework. Studies presented in Chapter 2 are based on the JNUBEAM 10a release in which the GCALOR model was used for the simulation of both primary and secondary interactions. Later on (starting from the JNUBEAM 10d release), the standalone FLUKA model was used in the T2K beam simulation to simulate the primary and secondary interactions in the target, since a better agreement of FLUKA with the NA61 thin target data was shown in dedicated studies. Simulated tracks that exit the target are introduced in the JNUBEAM simulation on the target surface on an event-by-event basis.

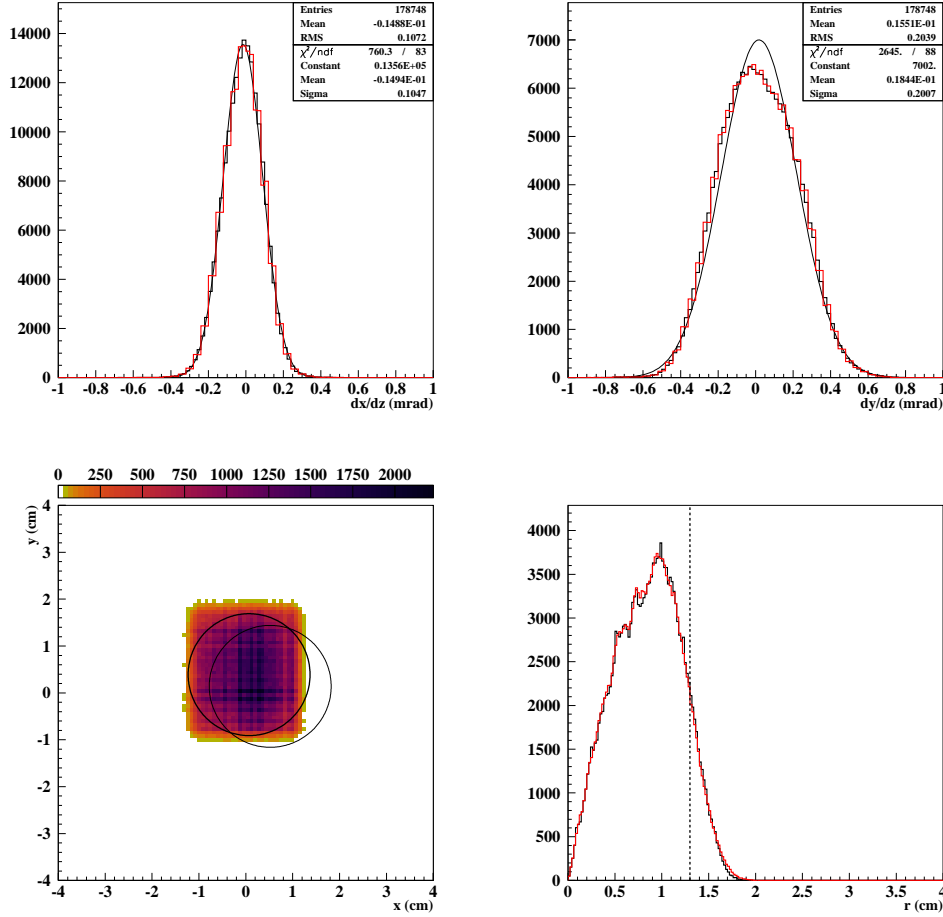


Figure 3.14: Simulated (red) beam divergence (top) given in mrad in the x (left) and y (right) directions. A gaussian fit is superimposed on real data (black). Impact distribution of protons on target (bottom left) and corresponding radial distribution (bottom right). The bold circle shows the position of the upstream face of the target, while the light one shows the position of the downstream face, corresponding to a tilt of +5 mrad in x and -2.8 mrad in y. The dashed vertical line on the radial distribution shows the target radius. Monte-Carlo distributions are normalized to the ratio of number of protons on target for the real and simulated data sets.

Secondary interactions in the elements of the beamline are still simulated by the GCALOR model (see [64] for more details).

In a first step of this work (and for consistency with the study of neutrino flux predictions presented in Chapter 2), the GCALOR model was implemented within the GNA61 framework. At the beam energy of 30 GeV, GCALOR

calls for the GFLUKA⁴ model to calculate the interaction cross section. The interpolated cross sections from GFLUKA are shown in Fig. 3.15. A fit to the longitudinal distribution of the interaction vertices in the target returns an interaction length of ~ 34.5 cm corresponding to a cross section of 290.7 mbarn (using $\rho = 1.83$ g/cm³ and $A = 12.011$ g/mol for the Carbon density and molar mass respectively). This value is in agreement with the interpolation of GFLUKA at 30 GeV for the *inelastic* interaction cross section. Since a clear contribution of protons with a momentum close to 30 GeV/ c was observed among the daughter particles of the simulated primary interactions, GFLUKA includes *quasi-elastic* scattering within the total inelastic cross-section. The recent FLUKA model, on the contrary, flags quasi-elastic scattering as *elastic* interactions.

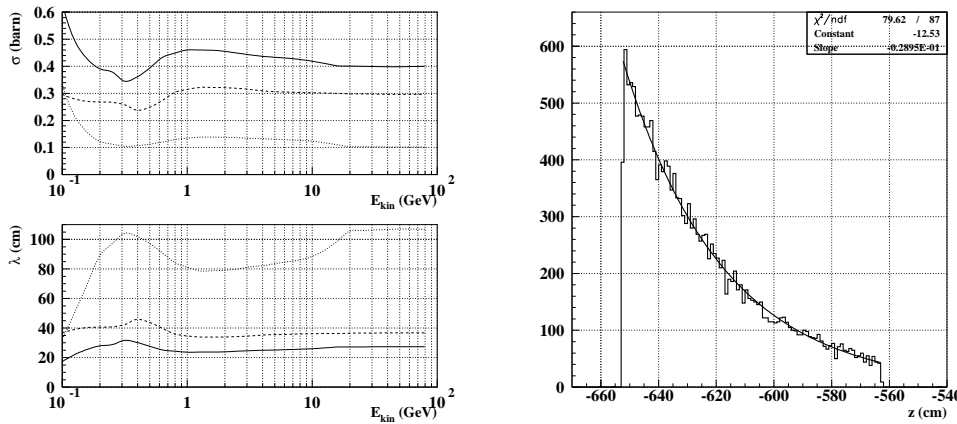


Figure 3.15: Interpolated interaction cross sections of protons on Carbon calculated by the GFLUKA (Geant3.21) model (top left) and corresponding interaction lengths (bottom left) as a function of kinetic energy. The inelastic (dashed) and elastic (dotted) contributions to the total hadronic cross section (plain) are also shown. The right plot shows a fit to the longitudinal distribution of the simulated interaction vertices in the target. The returned value gives an interaction length consistent with that of the GFLUKA inelastic contribution.

Following the latest developments of the T2K beam simulation, an interface between GNA61 and a standalone FLUKA simulation was introduced. The FLUKA based simulation includes the geometrical description of the replica target (90 cm long graphite rod and Aluminum support flanges) and the beam distribution is based on the NA61 data in order to reproduce the beam

⁴GFLUKA refers to the original implementation of FLUKA within the Geant3 framework. It has not much to see anymore with the current standalone FLUKA model.

in terms of transverse size and divergence. For each simulated event, particles exiting the target are stored on output with the corresponding position and momentum at the surface of the target. Simulated events in GNA61 consist in a given number of outgoing particles, each of them being associated with a starting vertex at the surface of the target. All secondary interactions occurring in the detector material are handled by the GCALOR model. **The code used for the FLUKA interface to GNA61 is identical to that used in JNUBEAM. The two simulation chains are thus compatible in terms of model and input for tracking.**

- (iii) As already mentioned, the re-weighting of the target contribution is based on an appropriate set of reconstructed track parameters on the surface of the target (i.e. position of the exit point, momentum and angle with respect to the beam direction at exit position). While reconstructed parameters are obtained from a dedicated extrapolation procedure, the storage of the corresponding generated quantities was implemented in GNA61 and propagated to the standard NA61 simulated data structures for the analysis. The different projections of the simulated exit points on target are shown in Fig. 3.16 for simulated tracks that have been matched to a reconstructed track extrapolated back to the target surface.
- (iv) Although the electronic response of the TPCs is simulated in the MTSIM package, the resulting particle identification (PID) capabilities in terms of truncated mean charge was not used at the time of the NA49 experiment due to a bad agreement with the data. As for the time-of-flight detectors, the detector response is not simulated at all in GNA61. In order to make comparisons between data and Monte-Carlo right after reconstruction, the variables used for particle identification must be available at the simulation level too. The full simulation of the detector response is a complex task that requires a detailed description of all possible effects and lots of tuning. Thus, it was decided not to simulate the detector response itself, but rather to associate PID variables to each reconstructed track in the simulation. In other words, a mass squared (PID variable reconstructed from the ToF information) and a truncated mean charge (PID variable reconstructed from the TPC information) are associated to each reconstructed track according to data distributions and experimental resolutions. More details are given in the next section.

3.4 The NA61 reconstruction chain

The reconstruction algorithms of NA61 are based on those developed by the NA49 collaboration [83]. The original chain was written to reconstruct tracks originating

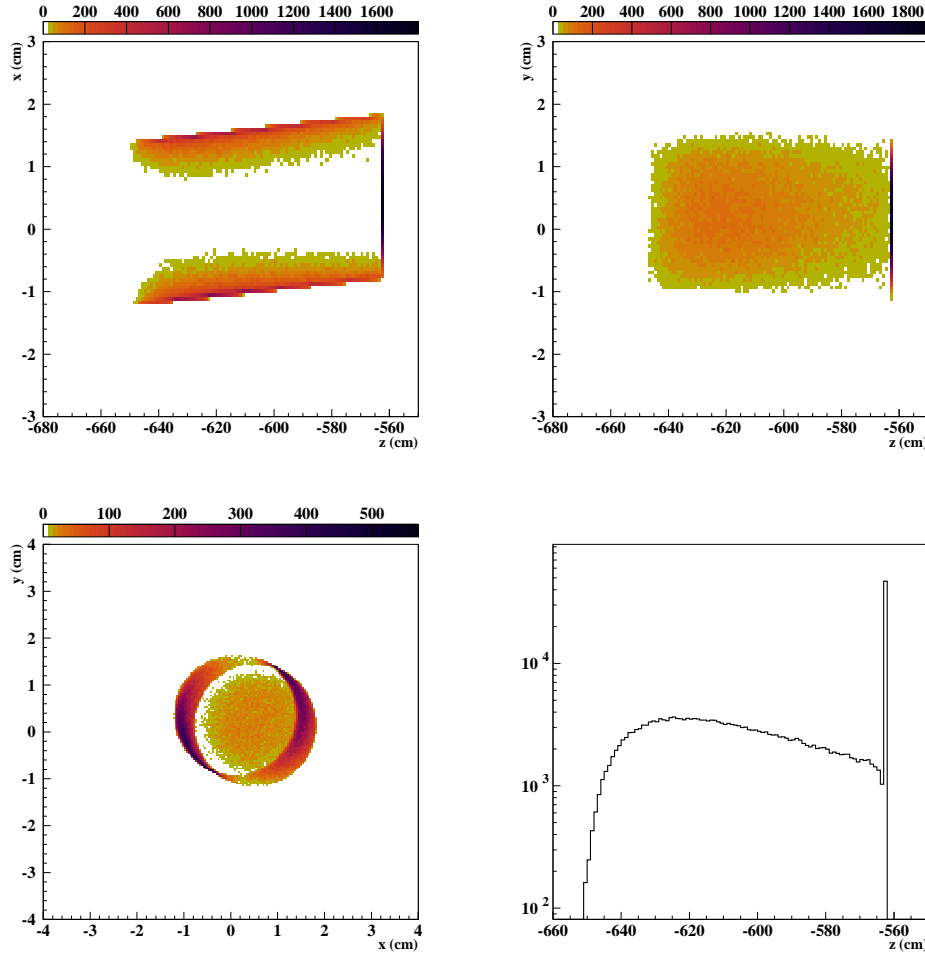


Figure 3.16: Simulated exit points on target in the x-z (top left), y-z (top right) and x-y (bottom left) projections for simulated tracks matched to reconstructed tracks. The longitudinal distribution is shown on the bottom right plot.

from a single vertex in a thin production target. The main steps of the reconstruction procedure are:

- (i) cluster finding in the TPC raw data, calculation of the center-of-gravity and total charge of clusters, and correction of cluster position due to distortions;
- (ii) reconstruction of local track segments in each TPC separately;
- (iii) matching of track segments from different TPCs into global tracks;
- (iv) track fitting through the magnetic field and determination of track parameters at the first measured TPC cluster (tracks reconstructed at this step are

referred to as *global rtracks*);

- (v) determination of the interaction vertex as the intersection point of the incoming beam particle with a plane located at the middle of the target along the beam axis;
- (vi) refitting the particle trajectory using the interaction vertex as an additional point, determining the particle momentum at the interaction vertex;
- (vii) matching of the ToF-F hits with the TPC tracks.

The analysis presented in this chapter is based on TPC tracks extrapolated back to the surface of the target. This procedure has been developed especially for the NA61 long target physics program and does not include steps (v) and (vi) of the original reconstruction chain. Instead, global rtracks, once fitted to the first measured point in the TPCs, are extrapolated back through the magnetic field and track parameters are estimated at the point-of-closest-approach on target.

It is important to stress that **since tracks are fitted without any vertex constraint, the resolution of the extrapolated track parameters at the surface of the target is driven by the achievable resolution at the global rtrack level. All the track quality cuts developed for the analysis have therefore been optimized to improve the initial resolution of the track parameters.**

The simulated data is packed in the same format as the real raw data and thus processed identically. The reconstruction chain for simulated data only differs by two additional steps:

- (viii) matching of the reconstructed tracks to the originally simulated tracks;
- (ix) simulation of time-of-flight and energy loss variables for particle identification;

Step (viii) is performed by the matching client, which associates each simulated cluster to its closest reconstructed neighbor to finally form pairs of matched simulated and reconstructed tracks. In particular, the matching procedure accounts for decays in flight for which the decay kink is small enough for the parent and daughter tracks to be reconstructed as a single global rtrack. Step (ix) is performed by the client described in the following section. This client is actually called for both real and simulated data and stores all the relevant track information for analysis in a structure common to both data types.

3.4.1 Particle identification for the simulated data

A new step was added in the reconstruction chain to implement particle identification in the simulation. The goal of the corresponding client is not to simulate

the detector response but rather to assign PID variables to the simulated tracks as they are calculated for the reconstructed data.

In NA61, the particle identification is done using the information of the track time-of-flight and energy loss in the TPCs. For the real data, the time-of-flight is used in combination with the measured track length and momentum to compute a mass squared value according to:

$$m^2 = p^2 \left(\frac{t^2 c^2}{L^2} - 1 \right) \quad (3.4)$$

where the track length, L , is computed after extrapolating the track to a plane situated at the center of the target along the beam axis, p is the fitted momentum at the primary vertex, and t is the measured time difference between the S1 signal and a hit in the ToF-F. This time-of-flight accounts for the beam time-of-flight (t_{beam}) between the S1 counter and the target, propagation of light in the scintillator, various cable lengths at the scintillator readout channels and electronics effects (grouped in t_{cable}). It can be expressed as

$$t = T_{STOP} - T_{START} - t_{beam} - t_{cable} = T_{STOP} - T_{START} + t_0 \quad (3.5)$$

The time value t has to be corrected (t_0 calibration constants for each scintillator slab) for all additional components in order to correspond to the effective time-of-flight from the center of the target to the ToF-F. The calibration procedure of the ToF-F was developed for the thin target data taking in 2007. In this case, t_{beam} is a simple constant corresponding to the time-of-flight of a beam proton between the S1 counter and the target position.

In the case of the long target measurements though, t_{beam} varies on an event-by-event basis since the beam protons may interact over the 90 cm of the target. The current calibration procedure does not account for that yet. The mass squared is computed using the momentum of the global rtracks (fitted at the first measured point). Moreover, the trigger logic is not included in the simulation and no digitization is performed for the ToF-F signal. Because of these differences, simply using Eq. 3.4 to compute a mass squared value for the reconstructed global rtracks in the Monte-Carlo does not reproduce the data mass squared distribution as a function of momentum (in particular for protons). Instead of implementing all the missing items in the simulation chain, for each reconstructed global rtrack the following steps are followed:

- (i) check if the ToF-F reconstruction client extrapolated the TPC global rtrack to the ToF-F detector;
- (ii) use the matching client information to get the mass of the originally simulated particle;

- (iii) smear the mass squared value using data based parametrizations of the width of the mass squared distribution as a function of the reconstructed momentum.

In step (ii), in case the reconstructed track is matched to more than one simulated track (e.g. decay with a very small kink), the mass of the particle with the longest track length is used. The parametrizations used in step (iii) are shown in Fig. 3.17 for pions and protons. Fig. 3.18 shows the resulting mass squared for simulated and real data. Comparisons of projections are illustrated in Fig. 3.19 for different momentum ranges.

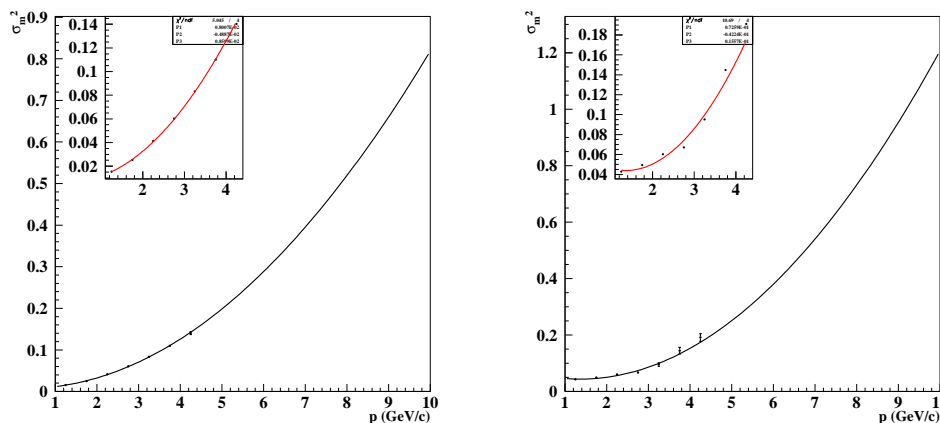


Figure 3.17: Parametrization of the width of the mass squared distributions of real data as a function of reconstructed momentum for pions (left) and protons (right). Inserts show the fitted data points.

A reasonable agreement is observed for pions while the width of the proton peak is systematically underestimated. As previously mentioned, some work is required at the calibration level for the long target to understand these discrepancies: the intrinsic uncertainty on the interaction position in the target will unavoidably affect the proton time-of-flight value if still computed assuming that tracks originate from the center of the target. Actually, secondary protons, unlike secondary pions, are not relativistic before at least 6 GeV/c ($\beta_p = 0.98$) and thus, their time-of-flight value will still be sensitive to the difference between the position of the actual production point in the target and the position of the target center ($\sim (\beta_{beam} - \beta_p)$). Although this point requires some additional work, the pion distribution and particle separation is reproduced well enough to extract pion yields from the distributions.

As for the energy loss in the TPCs, the dE/dx information is generated in the following steps:

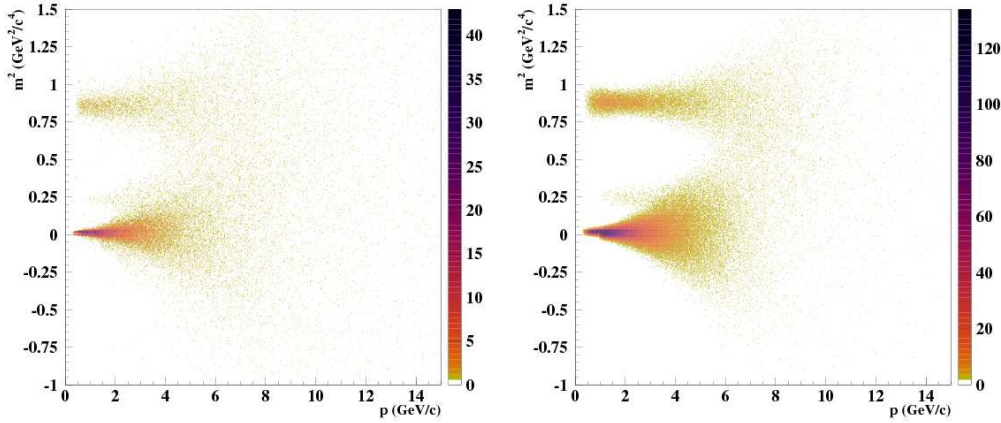


Figure 3.18: Mass squared distribution for the real (left) and simulated (right) data as a function of the reconstructed momentum in the TPCs.

- (i) get PID and momentum of the originally simulated particle from the matching client information;
- (ii) compute the $\beta\gamma$ factor to get the corresponding mean dE/dx value from the Bethe-Bloch parametrization;
- (iii) sample n dE/dx points from the Moyal distribution (analytical approximation of the Landau distribution), where n is the number of reconstructed clusters on track;
- (iv) calculate the truncated mean charge in MIP (Minimum Ionizing Particle) units using the procedure applied to real data (re-order cluster by increasing charge and keep only the lower 50 % of the distribution).

Fig. 3.20 shows the simulated energy loss for all particles (positively and negatively charged) based on a flat particle distribution (no physics). It also shows that the simulation reproduces the dependence of the dE/dx resolution on the number of points on track which goes as $\sim 38\%/\sqrt{N}$ (NA49 parametrization, see [83]). The energy loss distribution corresponding to the simulated and real data sets used for analysis are shown in Fig. 3.21. Comparisons of projections are illustrated in Fig. 3.22 for different momentum ranges. The agreement between data and Monte-Carlo is good enough to reproduce the pion peak and particle separation, while more tuning is obviously needed to get a better agreement.

Apart from assigning PID variables to the reconstructed tracks, the PID client also performs the backward extrapolation of global rtracks on the surface of the

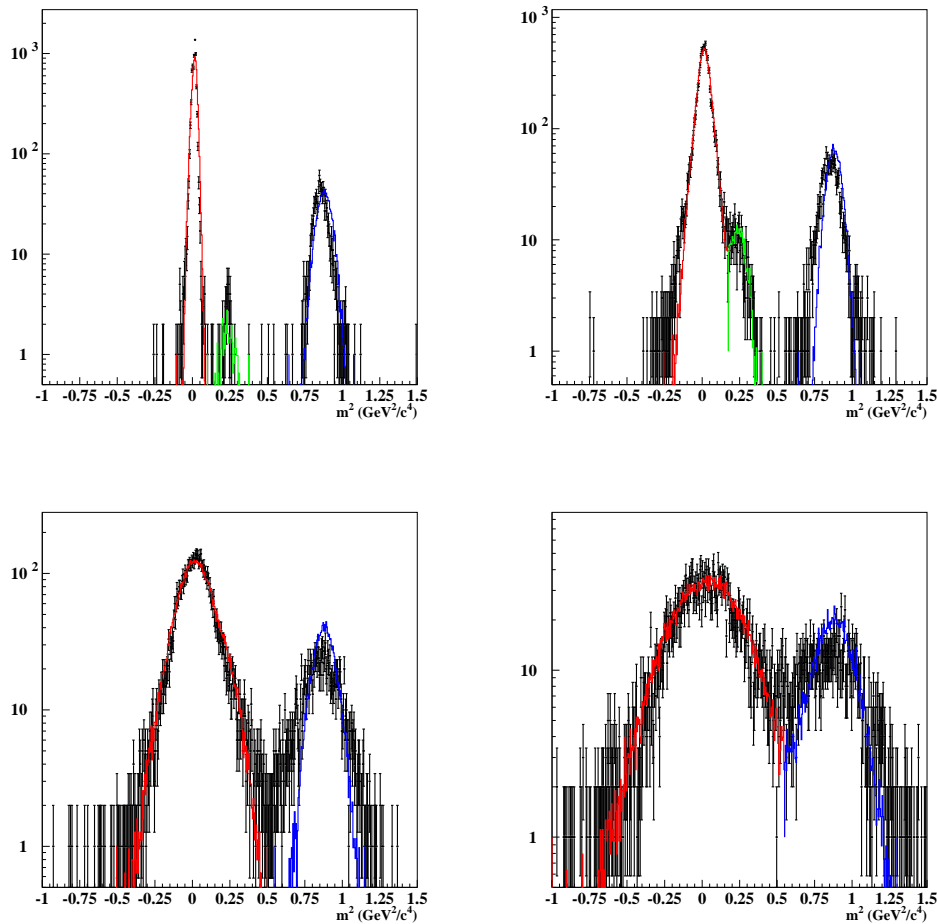


Figure 3.19: Projections of the mass squared distribution for the real (black dots with error bars) and simulated (histogram) data for the momentum ranges: $p < 1.5$ GeV/c (top left), $1.5 < p < 3$ GeV/c (top right), $3 < p < 4.5$ GeV/c (bottom left) and $4.5 < p < 6$ GeV/c (bottom right). The simulated data is normalized to the ratio of the number of p.o.t. in data and Monte-Carlo. Moreover, individual peaks in the simulation (pions (and positrons) in red, kaons in green and protons in blue) are further scaled by the relative ratio of the number of entries in data and Monte-Carlo.

target for both real and simulated data. The extrapolation function used to determine a point-of-closest-approach (p.c.a.) accounts for the estimated tilts of the target in the x-z and y-z planes (more details on the extrapolation procedure are given in Section 3.8).

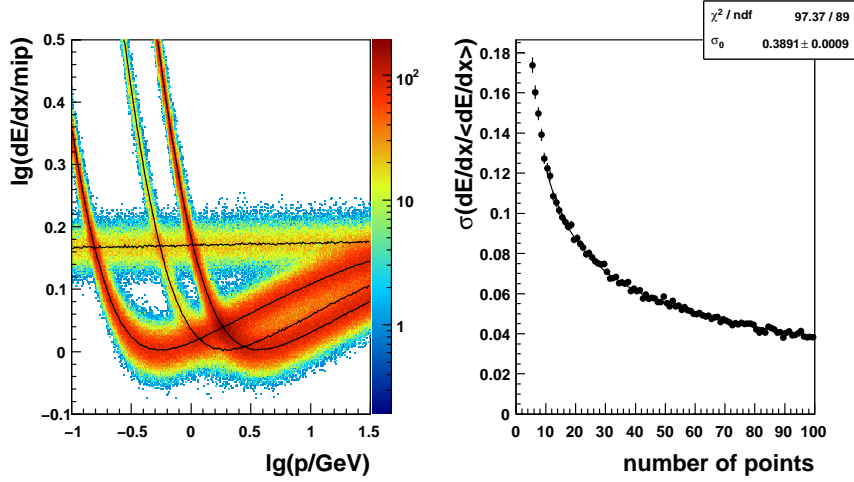


Figure 3.20: Simulated energy loss distribution for all particles (no physics distribution) as a function of momentum reconstructed at the first fitted point on global rtracks (left), and corresponding resolution (right) as a function of the number of points.

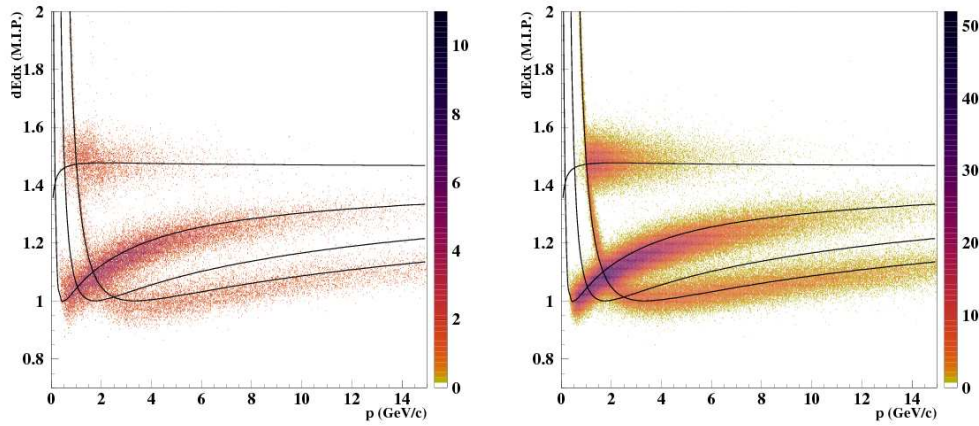


Figure 3.21: Energy loss distribution for all particles as a function of momentum reconstructed at the first fitted point on global rtracks for real (left) and simulated (right) data. The Bethe-Bloch parametrization curves from the energy loss calibration in the TPCs are superimposed on data.

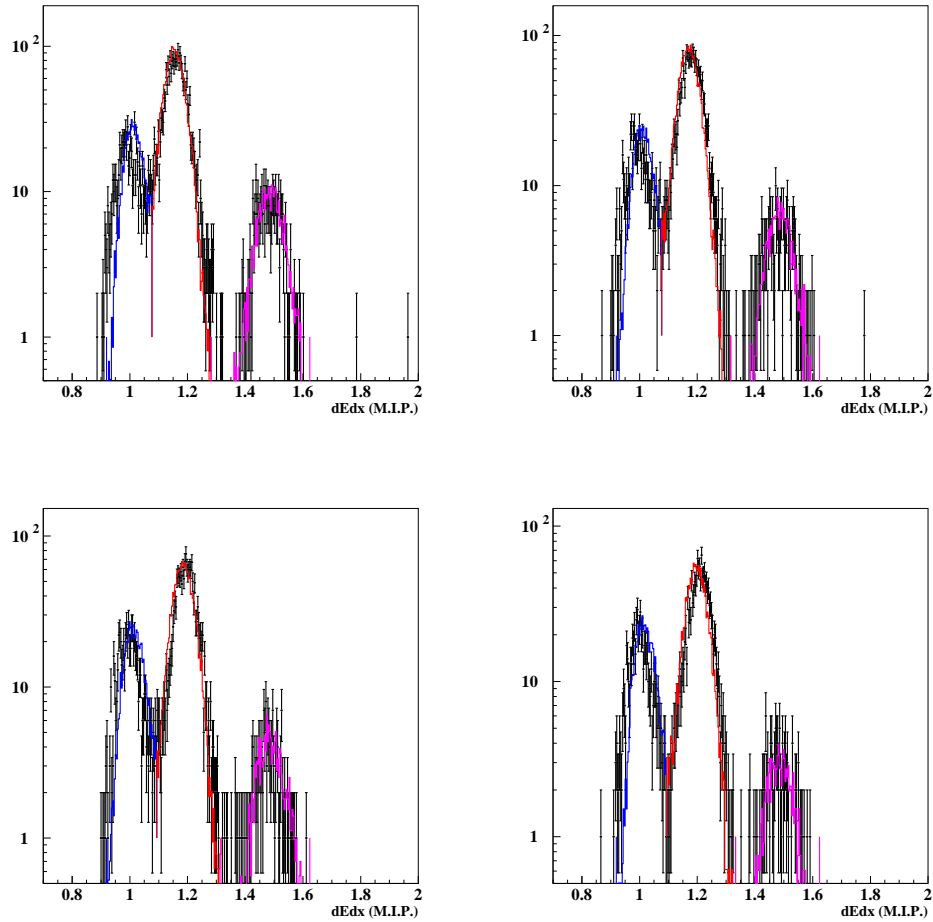


Figure 3.22: Projections of the energy loss distribution for the real (black dots with error bars) and simulated (histogram) data for the momentum ranges: $3 < p < 3.5$ GeV/c (top left), $3.5 < p < 4$ GeV/c (top right), $4 < p < 4.5$ GeV/c (bottom left) and $4.5 < p < 5$ GeV/c (bottom right). The simulated data is normalized to the ratio of the number of p.o.t. in data and Monte-Carlo. Moreover, individual peaks in the simulation (protons in blue, pions in red and positrons in purple) are further scaled by the relative ratio of the number of entries in data and Monte-Carlo.

3.5 Results from the thin target measurements

The NA61/SHINE collaboration measured differential production cross sections of positively and negatively charged pions in p+C interactions at 31 GeV/c. It also reported values of $257.2 \pm 1.9(\text{stat}) \pm 8.9(\text{syst})$ mb and $229.3 \pm 1.9(\text{stat}) \pm 9.0(\text{syst})$ mb for the corresponding total inelastic and production (corrected for the quasi-elastic contribution) cross sections respectively. The details of the analysis of the 2007 thin target data are described elsewhere [82]. In summary, three different analyses were developed:

- (i) a dE/dx analysis dedicated to the low momentum region below 3 GeV/c [86];
- (ii) a negatively charged hadron analysis without particle identification [87];
- (iii) and a combined ToF and dE/dx analysis [88].

The analysis developed for the 2007 replica target data is based on the combined ToF and dE/dx analysis of the thin target data. The measured differential spectra are shown in Fig. 3.23 and Fig. 3.24 for π^- and π^+ mesons respectively.

These results have been used by the T2K Beam Group to predict the neutrino fluxes at the near and far detectors and the expected number of background events at the far detector for the first ν_e appearance analysis recently published by the T2K collaboration [54]. How the NA61 thin target data is used in T2K is treated in more details in Chapter 5.

3.6 Measurements with the T2K replica target

3.6.1 Beam data

As mentioned in Section 3.1 the acquisition trigger is based on the combination of a particle identification signal ($C1 \cdot \overline{C2}$) that selects incoming protons and signals from two scintillation counters ($S1 \cdot S2$) that give beam definition and starting time for acquisition. The probability that more than one beam particle interacts in the target is non-negligible due to the $1.9 \lambda_I$ equivalent along the beam direction. In order to normalize data to the number of incoming protons on target (p.o.t.), events with a single proton interaction must be selected. This can be done by cutting on the number of beam particles seen in the wave form analyser (WFA) asking for $n_{beam} = 1$. The number of beam particles is counted in a $\pm 25 \mu s$ window around the beam time (original setting). The time distribution of beam particles is shown in Fig. 3.25 for events with one, two and more than two beam particles. Because the beam rate was set too high for the long target data taking (15 kHz), requiring $n_{beam} = 1$ yields a $\sim 40\%$ event reduction. The WFA cut can therefore not be used to select single proton interactions in the target.

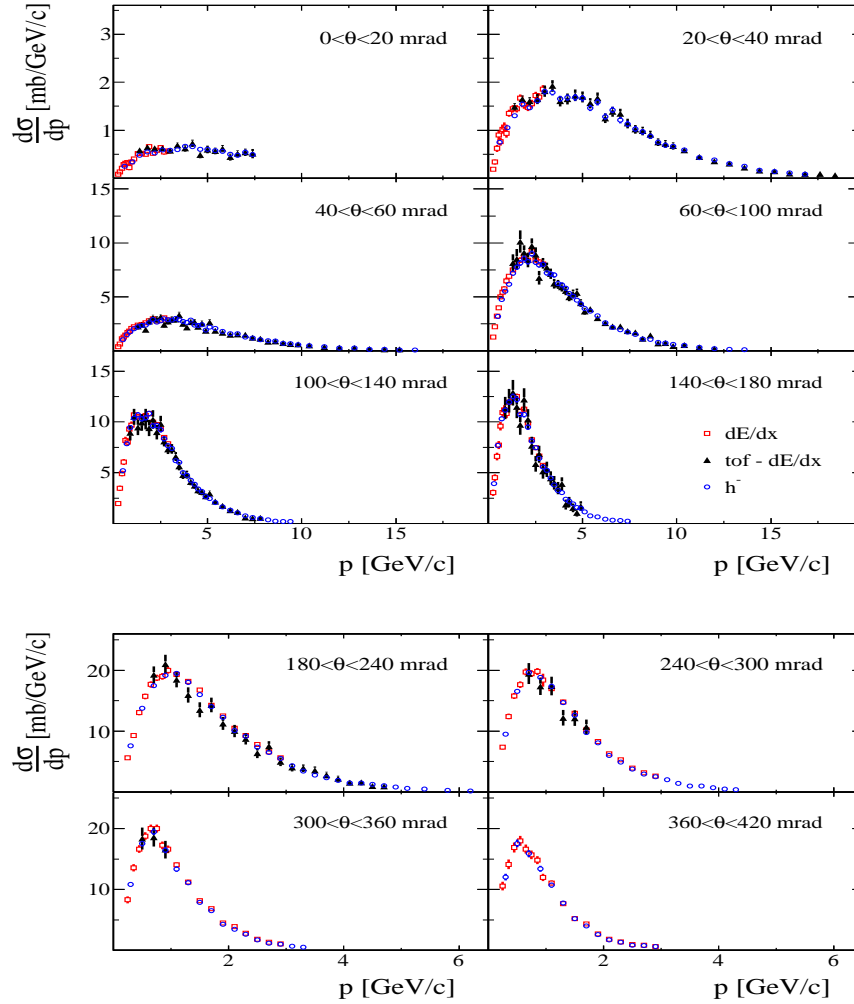


Figure 3.23: Differential cross section for π^- meson production in p+C interactions at 31 GeV/c. The spectra are presented as a function of laboratory momentum (p) and different intervals of polar angle (θ). Results obtained using three analysis methods are presented by different symbols: blue open circles - h^- analysis, red open squares - dE/dx analysis and black full triangles - $ToF - dEdx$ analysis. Error bars indicate only statistical uncertainties.

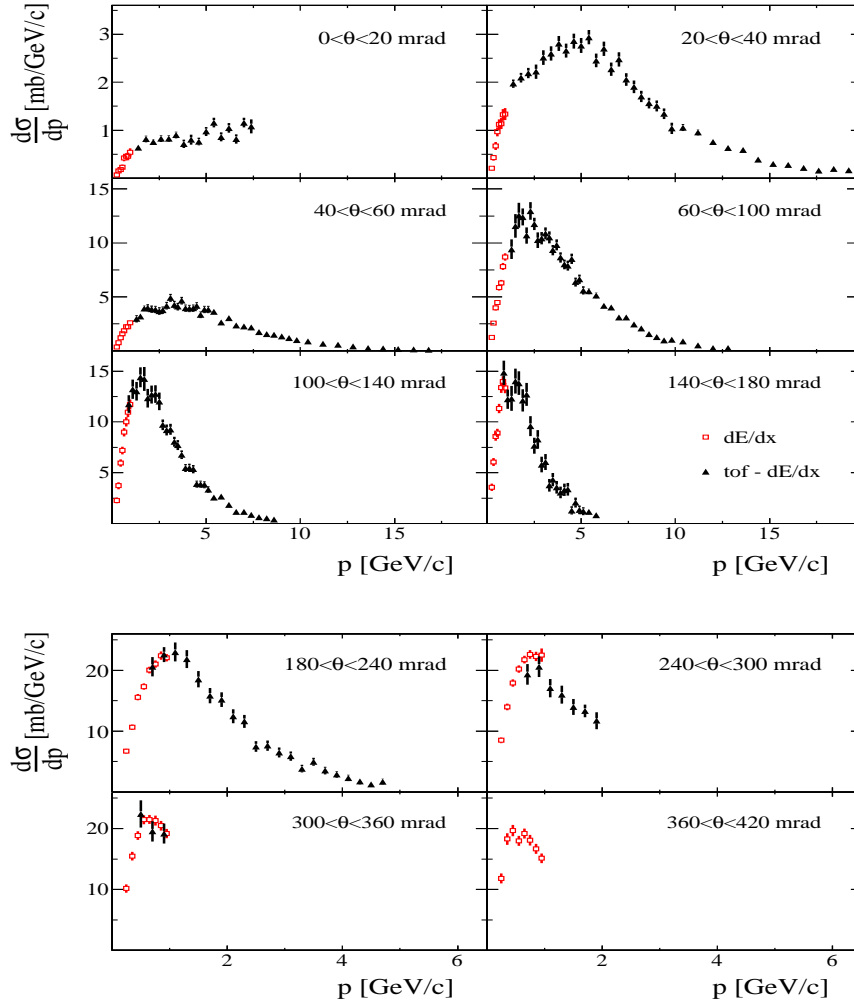


Figure 3.24: Differential cross section for π^+ meson production in p+C interactions at 31 GeV/c. The spectra are presented as a function of laboratory momentum (p) and different intervals of polar angle (θ). Results obtained using two analysis methods are presented by different symbols: red open squares - dE/dx analysis and black full triangles - $ToF - dE/dx$ analysis. Error bars indicate only statistical uncertainties.

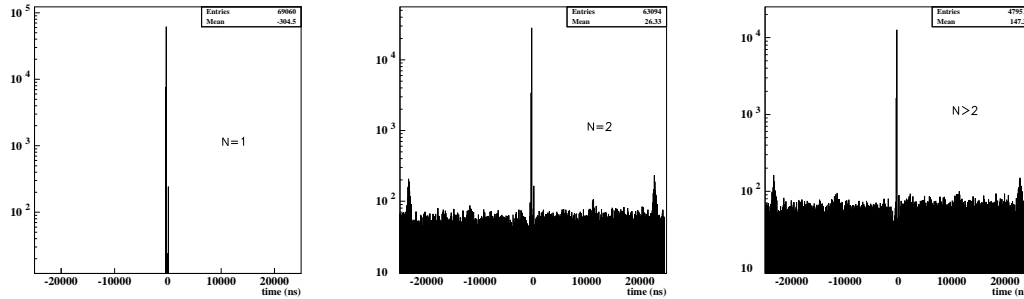


Figure 3.25: Time distribution of beam particles around the beam time (~ 300 ns) for events with one (left), two (middle) and more than two (right) beam particles in a $\pm 25 \mu\text{s}$ time window around the beam time.

However, we can take advantage of the usage of the forward time-of-flight in the analysis. Actually, the acquisition window of the time-of-flight extends over ~ 100 ns after the start signal of the $S1$ counter. With a 15 kHz mean beam rate the mean time distance between beam particles is $\sim 50 \mu\text{s}$. The ~ 100 ns dead time of the $S1$ counter yields a pile up probability of 0.2 %. For this small fraction of events, tracks coming from single or multiple interactions in the target cannot be distinguished. In all other cases, more than one proton may indeed interact in the target with a mean time distance of $50 \mu\text{s}$ between two consecutive interactions. This value also corresponds to the total drift time in the MTPCs. Consequently, off-time tracks (produced in an interaction prior to the current beam time) might still drift in the TPCs at the time the acquisition of a new event is triggered. However, requiring that TPC tracks have a signal (not overflow) in the forward time-of-flight assures that these tracks originate from a single interaction in the target due to the much shorter acquisition window of the ToF-F. This is illustrated in Fig. 3.26 that shows the track multiplicity in the TPCs as a function of the number of beam particles in the event. It can be seen that requiring that tracks hit the forward time-of-flight in events with two or more beam particles reproduces the track multiplicity distribution obtained for events with a single beam particle selected by the WFA cut $n_{beam} = 1$.

Thus, the forward time-of-flight signal is not only used for particle identification in the analysis, but also assures that results can be normalized to the number of incoming protons on target.

The trajectory of individual beam particles is measured in a telescope of beam position detectors along the beamline (BPD-1/2/3 in Fig. 3.1). These counters are small ($3 \times 3 \text{ cm}^2$) proportional chambers with cathode strip readout, providing a resolution of about $250 \mu\text{m}$ in two orthogonal directions. Beam tracks are recon-

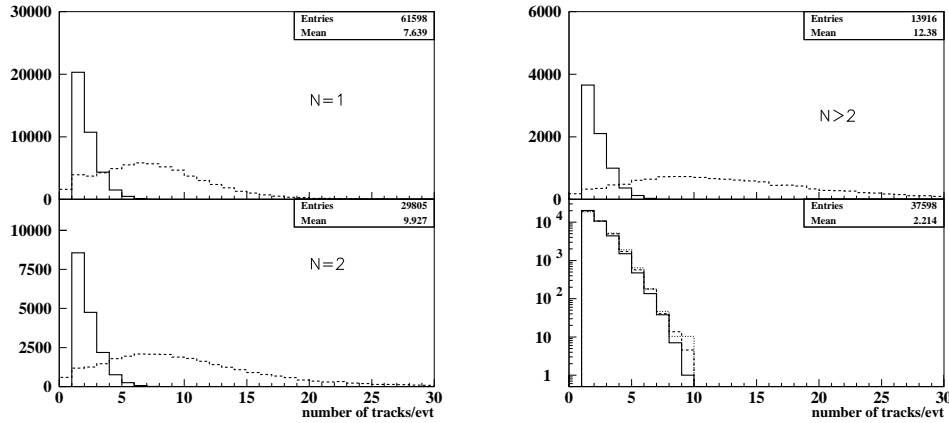


Figure 3.26: Track multiplicity in the TPCs with (plain) and without (dashed) time-of-flight requirement for one (top left), two (top right) and more than two (bottom left) beam particles in event. Two (dashed) and more than two (dotted) beam particle multiplicity distributions normalized to the single beam particle multiplicity (plain) (bottom right).

structed by fitting clusters in the three BPDs. The following set of quality cuts is applied to assure a good reconstruction of the beam tracks:

- (i) BPD cut(I): the track is fitted in both x and y directions;
- (ii) BPD cut(II): the track goes through BPD-3 (whatever the cluster quality is);
- (iii) BPD cut(III): the χ^2 of the fits are smaller than 15 (BPD residuals smaller than 1 mm).

The effect of BPD cut(III) on the BPD spatial resolution is shown as an example for BPD-2 in Fig. 3.27. The reconstructed beam spots in the three BPDs are shown in Fig. 3.28. The shadow of the S2 counter is clearly visible on BPD-2. The beam divergence computed for each beam track is shown in Fig. 3.14 with a comparison to the simulated distribution. The divergence is estimated to 100 μrad (200 μrad) in the x (y) direction.

Once beam tracks are reconstructed, they are extrapolated to the upstream face of the target from the BPD-3 z position, or BPD-2 z position in case no cluster or bad quality clusters are found in BPD-3. The BPD-3 inefficiency in 2007 (a new set of BPD detectors was used for later runs) was actually estimated to 5% (15%) in the x (y) direction. The extrapolation of the beam tracks to the upstream face of the target requires to know precisely the relative alignment of the target with respect to the BPDs and the beam axis in the NA61 reference system. The alignment of the target was determined by extrapolating TPC tracks back in the

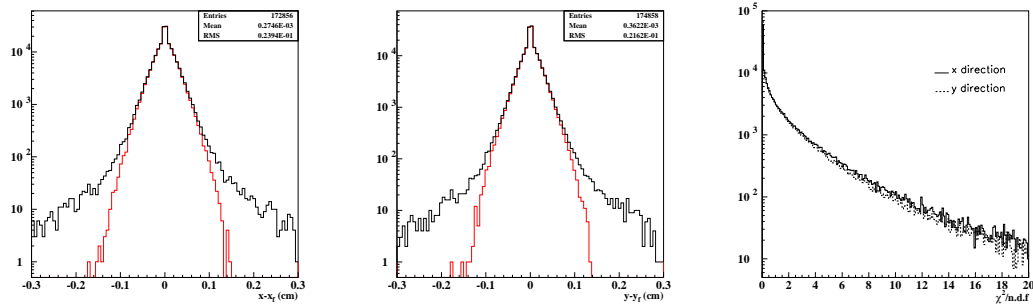


Figure 3.27: Residuals in BPD-2 in x (left) and y (middle) directions and $\chi^2/\text{n.d.f.}$ of the fit (right) in both directions. Red distributions are obtained applying BPD cut(III) ($\chi^2/\text{n.d.f.} < 15$) which basically rejects clusters with residuals larger than 1 mm.

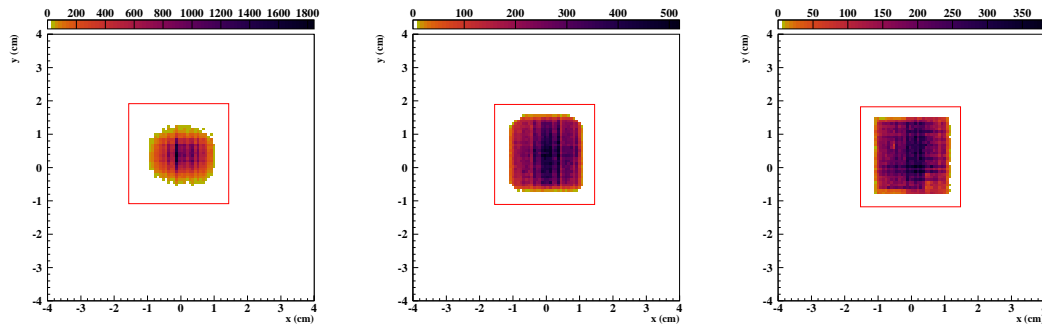


Figure 3.28: Reconstructed beam position in BPD-1 (top left), BPD-2 (top right) and BPD-3 (bottom left). Red boxes represent the BPD dimensions.

magnetic field to the surface of the target, assuming a nominal position aligned on the beam axis. The transverse distribution of the point-of-closest-approach was reconstructed in several bins along the target. For each of them, the position of the target was determined by maximizing the number of tracks extrapolated on a circle of 2.6 cm diameter. With this procedure, it was shown that **the upstream face of the target is well aligned with respect to BPD-3, while it is tilted by +5 mrad in the x-z plane and by -2.8 mrad in the y-z plane.**

The extrapolated position of the beam impact on target and the corresponding radial distribution are shown in Fig. 3.29. In addition to the BPD cuts previously described, the following cuts are applied to the extrapolation of the beam tracks:

- (i) R cut(I): the extrapolated position is within a 1.3 cm radius (target effective cross section);

- (ii) R cut(II): the extrapolation of the beam track over the full length of the target (90 cm) goes through the downstream face of the target with an additional radial cut at 1.2 cm.

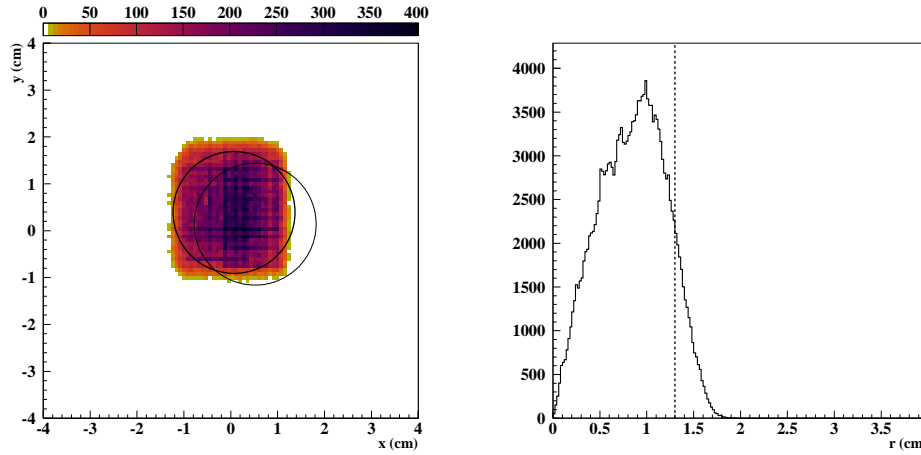


Figure 3.29: Beam profile on target (left) and corresponding radial distribution (right). The thick circle shows the position of the upstream face of the target while the light one shows the position of the downstream face, corresponding to a tilt of +5 mrad in x and -2.8 mrad in y. The dashed vertical line shows the target radius.

The first cut simply assures that the beam particles do not miss the target. The second cut assures that all selected beam protons effectively see the full length (90 cm) of the target. Actually, due to the target tilts in the x-z and y-z planes, incoming beam protons do not see the same amount of Carbon according to where they impinge on the upstream face of the target. The radial cut at 1.2 cm on the downstream face of the target is introduced to make sure that protons selected on the upstream face exit from the downstream face when taking the beam divergence and multiple scattering into account. The largest possible transverse shift due to the beam divergence (i.e. $200 \mu\text{rad}$ in the y direction) over the full length of the target is $\sim 180 \mu\text{m}$, while it reaches $\sim 490 \mu\text{m}$ for the multiple scattering (estimated with Eq. 3.6, using $X_0 = 23$ cm for the radiation length in Graphite). The effect of these radial cuts on the beam profile and radial distribution on target is illustrated in Fig. 3.30. The complete set of quality cuts applied to the beam data for the analysis is summarized in Table 3.1. The corresponding data reduction is given in Tab. 3.2.

The beam selection in the simulation is only done by the radial cuts R cut(I) and R cut(II) since the beam is generated from the data based distribution built after the BPD cuts are applied. The event reduction in the simulation is of 89.2% and 72% after R cut(I) and R cut(II) respectively, reproducing the relative fractions

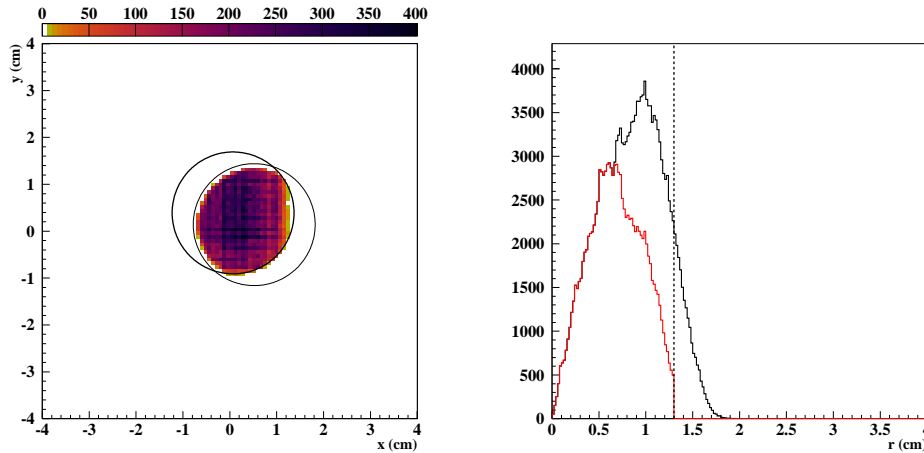


Figure 3.30: Beam profile on target (left) and corresponding radial distribution (right) after applying the cuts R cut(I) and R cut(II). For the radial distribution, the black histogram shows the original distribution while the red one shows the resulting distribution after the cuts. The thick circle shows the position of the upstream face of the target while the light one shows the position of the downstream face. The dashed vertical line shows the target radius.

Cut	Effect
BPD cut (I)	The beam track is fitted in both directions.
BPD cut (II)	The beam particle passes through BPD-3.
BPD cut(III)	$\chi^2/\text{n.d.f.} < 15$ (residuals < 1 mm).
R cut(I)	The proton impact radius on target is within 1.3 cm.
R cut(II)	The extrapolated beam track goes through the downstream face of the target.

Table 3.1: Quality cuts applied to beam events for analysis.

	Total	BPD cut(I)	BPD cut(II)	BPD cut(III)	R cut(I)	R cut(II)
Events	235046	186845	185347	178748	159377	114885
Fraction [%]		79.5	78.8 (99.2)	76 (96.4)	67.8 (89.2)	49(72.1)

Table 3.2: Event reduction after the beam quality cuts applied for analysis. Numbers in parenthesis correspond to reduction values relative to previous cuts.

given in Table 3.2 for the real data after the BPD cuts. **This shows in particular that the BPD-3 inefficiency, beam profile and relative target alignment are correctly taken into account in the simulation.**

The number of p.o.t. used in the analysis corresponds to the number of events selected after R cut(II). The systematic uncertainty on the normalization per p.o.t. is attributed to the BPD cut(III) and the radial cuts (BPD cut(I) and cut(II) are fixed requirements). The uncertainty is estimated as the maximal difference in the number of selected p.o.t. when varying the cuts independently. The χ^2 cut is

loosened to 10, R cut(I) to 1.2 cm and R cut(II) is lowered (increased) to 1.25 cm (1.15 cm) which corresponds to one (three) times the transverse deviation due to the multiple scattering over the length of the target. **The number of selected p.o.t. amounts to 114885 in the data and 639355 in the Monte-Carlo, with an estimated systematic uncertainty of 1.4%.**

3.6.2 ToF and TPC data

Global rtracks reconstructed in the TPCs are classified in terms of topology, or equivalently, in terms of momentum resolution. Four main categories of global rtracks can be identified according to the set of spectrometers the particle goes through (i.e. single or double spectrometer measurement):

- VTPC-1: momentum is determined with the first spectrometer;
- VTPC-2: momentum is determined with the second spectrometer;
- VTPC-1+VTPC-2: momentum is determined with both spectrometers;
- GTPC: momentum is determined with the GAP TPC.

The GTPC category accounts for particles going through the GAP TPC and MT-PCs only. Lots of efforts were dedicated to the implementation of the GAP TPC in the simulation and reconstruction chains. **The long target analysis presented in this Chapter is the first NA61 analysis including the GAP TPC.** Although the geometrical and drift velocity calibrations in 2007 were not optimized for the GAP TPC, we think that its usage for this analysis is fully justified by the facts that:

- (i) a good agreement is observed between data and Monte-Carlo in terms of momentum resolution;
- (ii) although the momentum resolution is worse than that of the other topologies (the readout of the GAP TPC consists only in seven consecutive pad rows along the beam direction), the resulting resolution on the extrapolated track parameters on target is still acceptable (see Section 3.8);
- (iii) the GAP TPC covers the very forward (below ~ 20 mrad) region of the kinematic phase space of interest for T2K. Actually, positively charged pions exiting the target in the very forward region are those pions which produce muons with momentum larger than 5 MeV/c. The latter are measured with the on-axis MUMON detector to monitor the beam direction on an event-by-event basis. It is therefore important to measure that forward contribution to check the agreement between the data and the beam simulation.

Fig 3.31 shows an example of reconstructed event display for the real data in which some of the previously defined track topologies can be seen. In the first three categories, the particle may also pass through the GAP TPC. These topologies can eventually be divided in two subsets according to whether they go through the MTPCs or not. Tracks that do not (non-MTPC tracks) are emitted in the very forward direction, remain mostly parallel to the beam axis and pass through the gap between the two MTPCs before hitting the ToF-F. Such tracks have a short lever arm and a very small curvature in the bending plane. This in turn impacts on the angle resolution in the VTFCs, since no additional point farther away on the lever arm can precisely constrain the track direction.

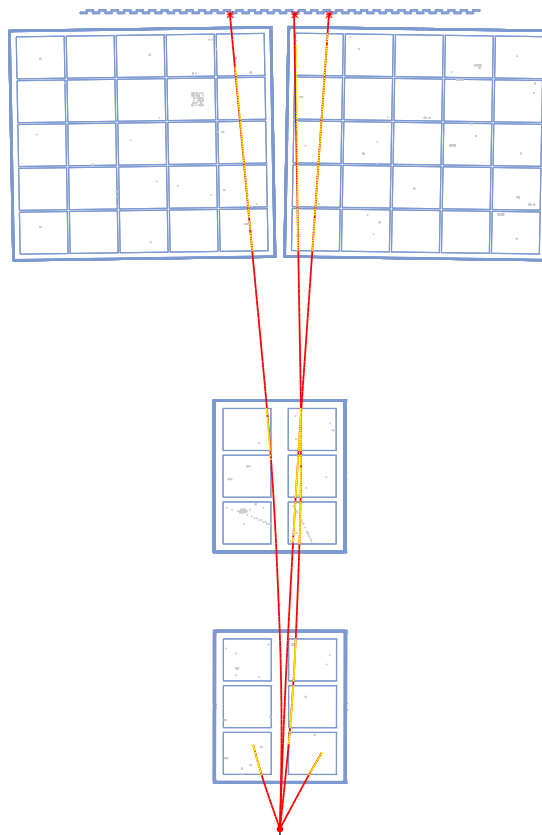


Figure 3.31: Example of reconstruction of a real data event in the NA61 2007 detector setup. Different track topologies can be observed (the GAP TPC is not displayed).

The momentum resolution of global rtracks is actually quadratic as a function of momentum since in the bending plane of the TPCs, the angle of the global rtrack, θ , is proportional to $1/p$. The error σ_θ therefore goes as σ_p/p^2 . However, in the first order, σ_θ does not depend on momentum but rather on the error on

the cluster position, which is affected by other physical effects such as multiple scattering. This implies that $\sigma_p \sim p^2$, which means that $\sigma_p/p \sim p$. These relations are illustrated in Fig. 3.32 that shows the dependence of σ_θ and σ_p/p on momentum. For non-MTPC tracks, the combination of a short lever arm and a small curvature results in a much larger error on θ . Since $\sigma_p/p \sim p \cdot \sigma_\theta$, this results in a significant increase of the slope of σ_p/p as a function of momentum. **To optimize the momentum resolution achievable after extrapolation on the target surface, the initial resolution at the global rtrack level is constrained to better than 1% by rejecting the non-MTPC tracks from the analysis** (see Fig. 3.32).

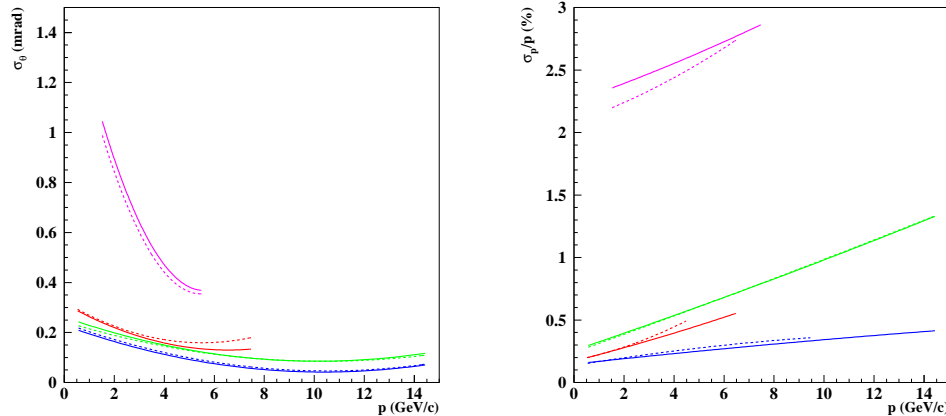


Figure 3.32: Error on polar angle (left) and momentum resolution (right) of global rtracks (in %) as a function of momentum for the real (plain lines) and simulated (dashed lines) data. The different colors correspond to the different track topologies: VTPC-1 (red), VTPC-2 (green), VTPC-1+VTPC-2 (blue) and GTPC (purple).

Different quality cuts are applied to assure a good reconstruction of the global rtracks:

- (i) TRK cut(I): the global rtrack is well fitted to its first measured point;
- (ii) TRK cut(II): the global rtrack has a time-of-flight and a dE/dx signal;
- (iii) TRK cut(III): according to the topology, a minimum number of points on track is required;
- (iv) TRK cut(IV): points are found in the MTPCs;
- (v) TRK cut(V): VTPC-2 and GTPC topologies are only selected if extrapolated on the downstream face of the target;

- (vi) TRK cut(VI): global rtracks extrapolated on the target downstream face are selected within a radius of 1.1 cm;
- (vii) TRK cut(VII): global rtracks are in the selected azimuthal region of the acceptance;
- (viii) TRK cut(VIII): the point-of-closest-approach (p.c.a.) of the extrapolated global rtracks on target is within $r < 0.6$ cm around the target.

TRK cut(I) simply assures that the angle and momentum of the global rtrack (as well as their respective errors) are well determined. TRK cut(II) selects global rtracks for which a combined particle identification based on time-of-flight and energy loss in the TPCs can be applied. TRK cut(III) requires a minimum number of points on track. For each track topology it basically selects tracks that go through at least two TPC sectors. This rejects tracks at the edges of the VTPCs where non-uniformities of the magnetic field may affect the momentum measurement. As previously mentioned, TRK cut(IV) selects global rtracks with a momentum resolution better than 1% by constraining the angular resolution in the VTPCs using points farther away on the lever arm in the MTPCs. TRK cut(V) and TRK cut(VI) are used to optimize the longitudinal resolution of the backward extrapolation for the different track topologies. As it will be further developed in Section 3.8, the longitudinal resolution of the backward extrapolation on the surface of the target is constrained by the bin size chosen for the analysis. TRK cut(V) and TRK cut(VI) assure that the resolution is good enough so that the longitudinal bin migration can be neglected.

The azimuthal acceptance of the NA61 setup in the x-y projection (transverse to the beam axis) is by construction limited to the central part of the left and right hemispheres of the phase space (see Fig. 3.33). This region is further more constrained to smaller angles by requiring that tracks hit the forward time-of-flight. TRK cut(VII) defines a subregion of the azimuthal acceptance for positively charged particles. The cut is based on the agreement between real and simulated azimuthal distributions as shown in Fig. 3.34.

Actually, the azimuthal distribution being physics independent, differences between real and simulated distributions should eventually appear in regions of the detector affected by side effects which are not, or badly, reproduced in the simulation (e.g. non-uniform magnetic or electric fields). Thus, cutting on regions of agreement assures that the acceptance correction is well understood. Details about the correction procedure are given in Section 3.7.

Finally TRK cut(VIII) is used as a criteria to decide whether a given reconstructed track is coming from the target or not. Details about the value, efficiency and purity of the cut are given in Section 3.8. The complete set of track quality cuts is summarized in Table 3.3. The corresponding data reduction is given in Tab. 3.4.

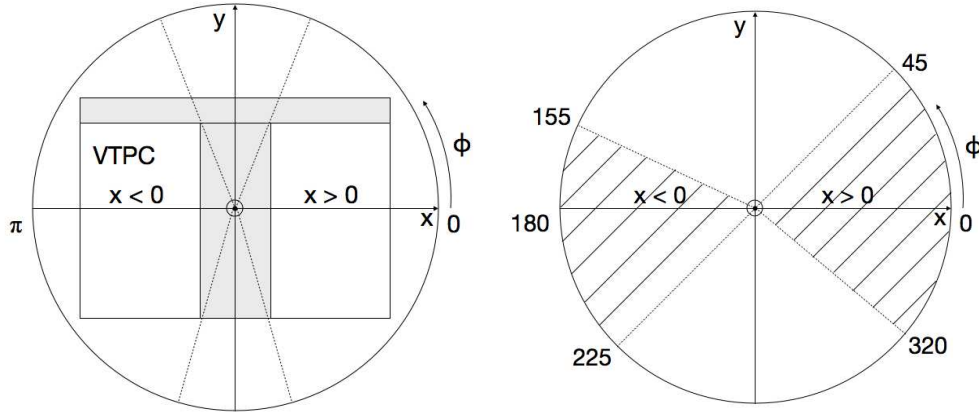


Figure 3.33: Schematic representation of the NA61 azimuthal coverage (left). The azimuthal angle, ϕ , is measured from the horizontal plane starting from the positive x side of the NA61 reference system. The dashed lines show the maximal coverage which is limited by the non-sensitive regions (shaded regions) of the VTPCs. Definition of the ϕ cut applied for analysis (right).

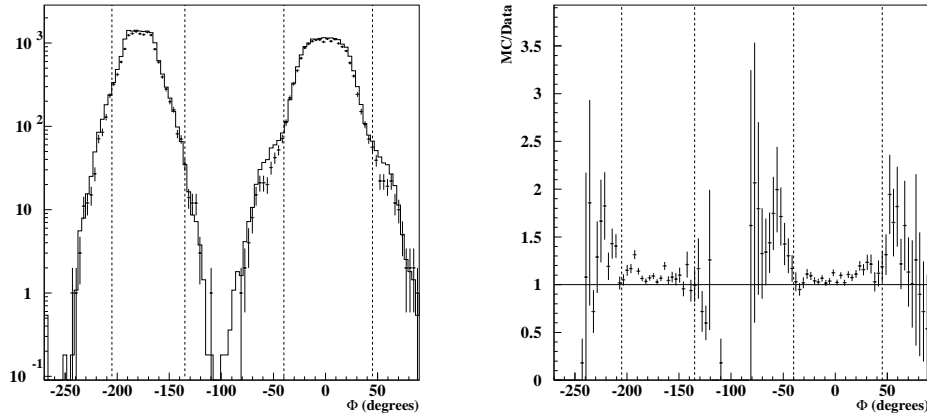


Figure 3.34: Azimuthal distribution for the real (dots with error bars) and simulated (histogram) positively charged tracks (left). The simulated data is normalized to the ratio of number of p.o.t. in data and Monte-Carlo. Ratio of the simulated over real azimuthal distribution (right). The dashed vertical lines show the ϕ cut used for analysis.

Cut	Effect
TRK cut(I)	Global rtracks are well fitted.
TRK cut(II)	Global rtracks have signals in the TPCs and the ToF-F.
TRK cut(III)	VTPC-1 global rtracks have at least 40 points. VTPC-2 global rtracks have at least 45 points. VTPC-1+VTPC-2 global rtracks have at least 50 points. GTPC global rtracks have at least 6 points in the GAP TPC.
TRK cut(IV)	Global rtracks have points in the MTPCs.
TRK cut(V)	VTPC-2 and GTPC global rtracks extrapolated on the downstream face of the target.
TRK cut(VI)	Global rtracks extrapolated within $r < 1.1$ cm on the downstream face of the target.
TRK cut(VII)	Global rtracks are in the selected azimuthal region.
TRK cut(VIII)	Global rtracks extrapolated with p.c.a. < 0.6 cm.

Table 3.3: Quality cuts applied to global rtracks for analysis.

	Total	TRK cut(I)	TRK cut(II)		
Tracks	1227268	954000	107299		
Fraction [%]		77.7	11.2		
		TRK cut(III)	TRK cut(IV)-cut(VI)	TRK cut(VII)	TRK cut(VIII)
VTPC-1	8064	6952	6394	6231	6126
Fraction [%]	7.5	86.2	79.3	77.3	76
VTPC-2	43205	22200	4559	4265	4265
Fraction [%]	40.3	51.4	10.5	10	10
VTPC-1+VTPC-2	49485	36899	34109	32413	31494
Fraction [%]	46.1	74.6	69	65.5	63.6
GTPC	6545	6060	1443	927	927
Fraction [%]	6.1	92.6	22	14.2	14.2

Table 3.4: Track reduction after the quality cuts applied for analysis.

In the following, we list some general properties of the global rtracks selected for analysis after the quality cuts summarized in Table 3.3:

- The number of points on track, momentum, polar angle and azimuthal distributions are shown in Fig. 3.35 for the different track topologies. The corresponding dE/dx and time-of-flight signals are shown in Fig. 3.36. In particular, it can be noticed that the momentum distribution in the data shows a small dip at about 1 GeV/c which affects only the VTPC-1+VTPC-2 topology. This is well understood as a consequence of the requirement on MTPC points combined with that on the forward time-of-flight. Actually for this topology, the number of points required on track is still small enough to account for tracks at the inner edge of the VTPCs (along the beam axis) that are bended back in the magnetic field and go through the gap between the two MTPCs (this type of track is referred to as *wrong-side* tracks because $p_x/q < 0$). Such tracks are rejected when asking for points in the MTPCs. The VTPC-1 and VTPC-2 topologies are not affected because the required number of points on track is large enough to exclude such wrong-

side tracks that would remain close to the beam axis and pass through the gap between the MTPCs. This purely geometrical effect is also reproduced in the simulated distribution (a step is clearly visible around 1 GeV/ c for the VTPC-1+VTPC-2 topology), although physics differences between the considered model and the data might affect the distribution as well.

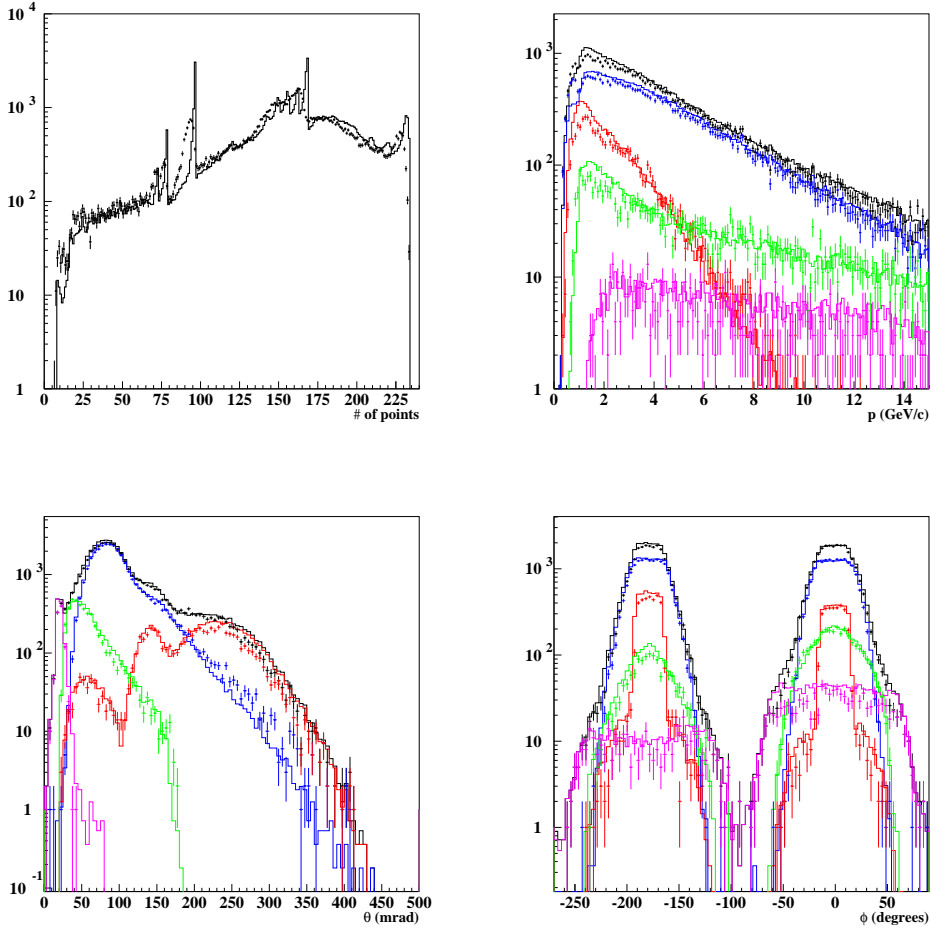


Figure 3.35: Number of points (top left), momentum (top right), polar angle (bottom left) and azimuthal (bottom right) distributions of global rtracks for the real (points with error bars) and simulated (histograms) data. The different colors correspond to the different track topologies: VTPC-1 (red), VTPC-2 (green), VTPC-1+VTPC-2 (blue) and GTPC (purple). The simulated data is normalized to the ratio of p.o.t. in data and Monte-Carlo.

- The $\{p, \theta\}$ coverage in terms of the different track topologies used in the analysis is shown in Fig. 3.36 for all global rtracks. The large angle region is

mostly covered by the VTPC-1 and VTPC-1+VTPC-2 topologies, while the small angle region is covered by the VTPC-2 topology and the very forward region by the GTPC topology.

- The $\{p, \theta\}$ coverage at the surface of the target is shown in Fig. 3.37 for positively and negatively charged particles. For positively charged particles, a contribution can be observed in the very forward direction ($\theta < 20$ mrad) at high momentum. It mainly includes protons undergoing coherent and quasi-elastic scattering. This contribution is of some interest for T2K since particles exiting the target in the very forward region are not affected by the focusing system of the T2K beamline. They will eventually interact in other elements of the beamline creating a source of neutrinos that could also be constrained by the NA61 measurements. To better measure this forward contribution, a dedicated data set was taken during the 2010 run period using the full magnetic field configuration (9 Tm bending power) in order to bend the very forward going particles through the whole length of the spectrometer. **By comparing Fig. 3.37 with Fig 2.17 to 2.19, it can be seen that positive tracks in the NA61 acceptance fully cover the phase space of relevant hadrons producing neutrinos in the T2K near and far detectors.**
- The $\{p, \theta\}$ coverage is shown for all positive tracks extrapolated back on target for the 6 longitudinal bins used in the analysis in Fig. 3.38.

3.7 The NA61 acceptance and analysis binning in $\{p, \theta, z\}$

The NA61 simulation is used to compute the detector acceptance in the 1.14 Tm bending power magnetic field configuration for positively charged particles for momenta up to 30 GeV/c and polar angles up to 300 mrad over a default binning of 0.8 GeV/c and 10 mrad bins. Acceptance maps are computed over 5 equidistant (18 cm) longitudinal bins and over the downstream face of the target for the track quality cuts defined in Table 3.3. For these calculations, GNA61 is run in the physics off mode, meaning that the main physics processes simulated in Geant 3.21 (e.g. decays) are turned off. Exception is made for energy loss in the TPCs and hadronic interaction processes that allow to account for the detector material in the calculations.

In each bin, 4 k tracks are uniformly generated in momentum and polar angle. For the first 5 longitudinal bins, tracks are uniformly distributed on the surface of the target over 2π and over the bin width (the transverse position on target at a given z position accounts for the target tilts in the x - z and y - z planes). The azimuthal angle is first constrained to the tangent plane to the surface of the target at the exit point and further limited to the region defined by the azimuthal cut

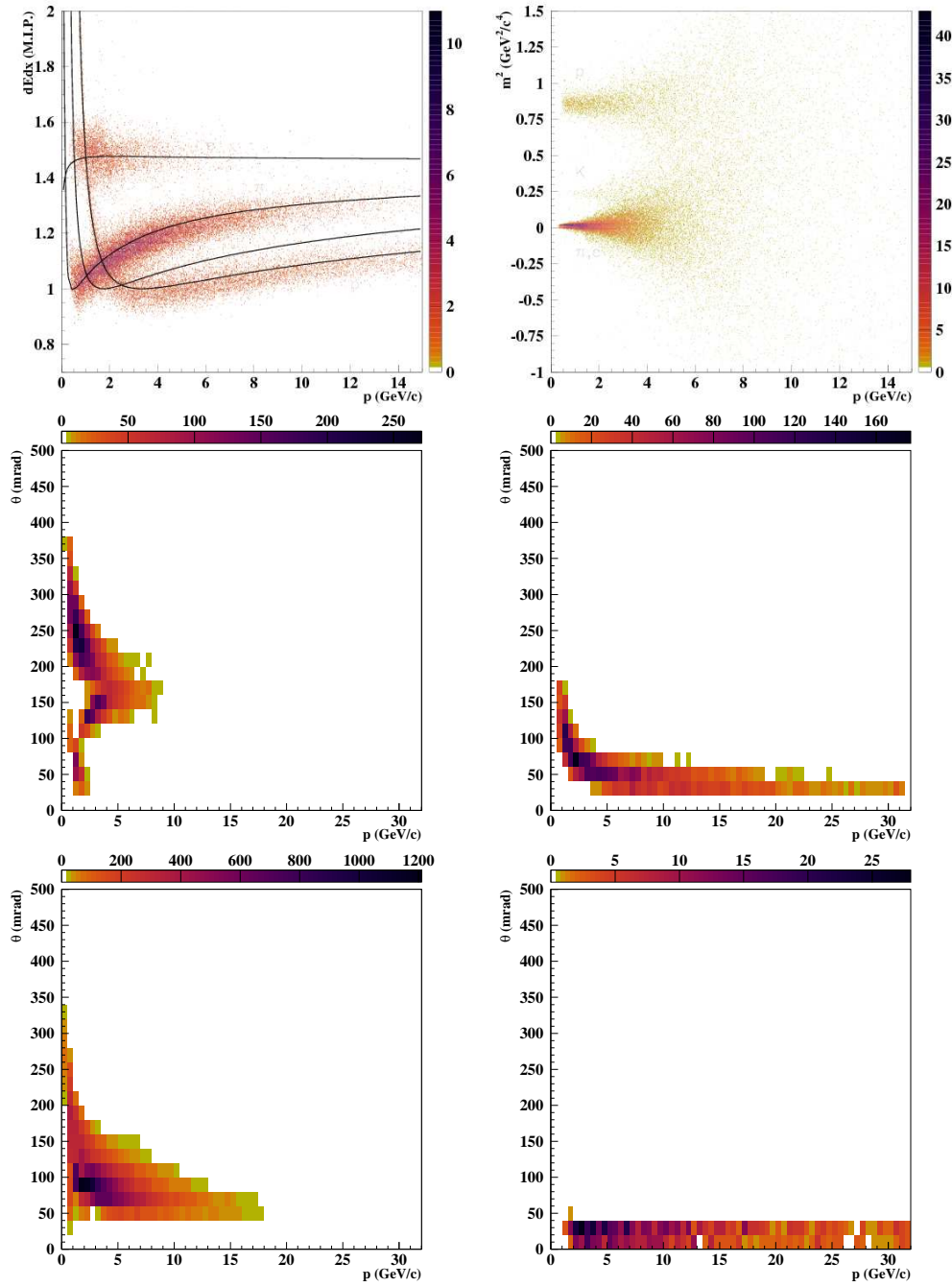


Figure 3.36: Energy loss in the TPCs (top left) and mass squared (top right) distributions as a function of momentum reconstructed at the first fitted point on global rtracks. The Bethe-Bloch parametrization curves from the energy loss calibration in the TPCs are superimposed on data $\{p, \theta\}$ coverage of the global rtracks of the VTPC-1 (middle left), VTPC-2 (middle right), VTPC-1+VTPC-2 (bottom left) and GTPC (bottom right) topologies.

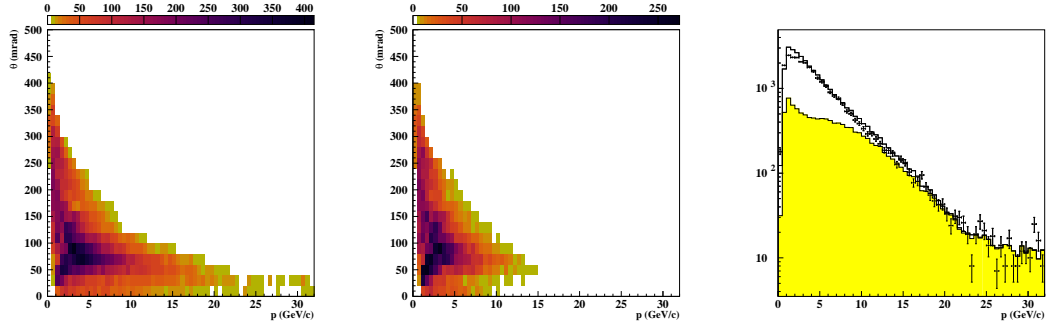


Figure 3.37: $\{p, \theta\}$ coverage at the surface of the target for positively (left) and negatively (middle) charged particles. Momentum distribution at the surface of the target for the real (dots with error bars) and simulated (histograms) positive particles. The contribution of the proton coherent and quasielastic scattering is shown in yellow. The simulated data is normalized to the ratio of the number of p.o.t. in data and Monte-Carlo.

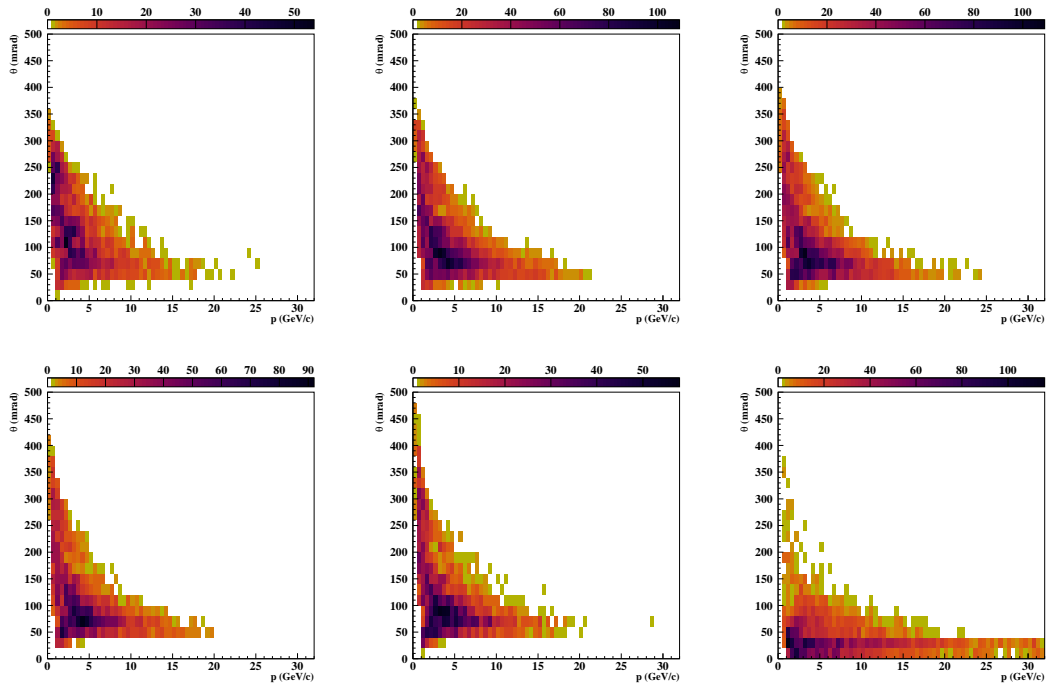


Figure 3.38: $\{p, \theta\}$ coverage at the surface of the target for positively charged particles for the different longitudinal bins. The most upstream bin is shown on the top left plot, the most downstream bin (downstream face of the target) on the bottom right plot.

used for analysis (see Fig. 3.39). For the downstream face of the target, tracks are uniformly distributed over a cross section of 1.1 cm radius and uniformly generated in the selected azimuthal region.

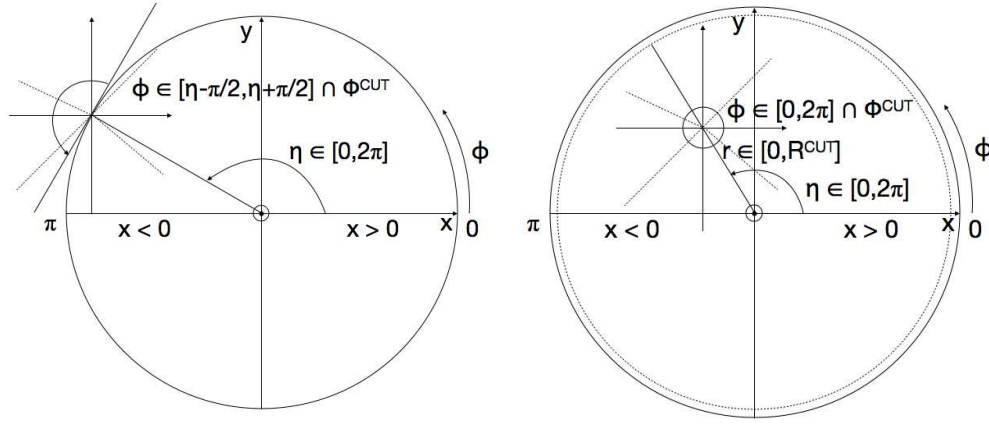


Figure 3.39: Schematic representation of the NA61 acceptance calculation for the first 5 longitudinal bins (left) and for the downstream face of the target (right). Tracks are uniformly distributed on the surface of the target using the angle η and the momentum components are calculated from the generated parameters (p, θ, ϕ) . R^{cut} and Φ^{cut} (dashed lines) refer to TRK cut(VI) and (VII) respectively.

The resulting acceptance maps are shown in Fig. 3.40. They display different characteristics that can be noted:

- starting from the low momentum region towards higher momenta, two main structures are clearly visible: a large upward going band and a downward going one with smaller acceptance. These structures correspond respectively to the so-called *right-side* ($p_x/q > 0$) and *wrong-side* ($p_x/q < 0$) tracks. The region of maximal acceptance includes the overlap of the two bands. Let us note that in the current analysis, track topologies were defined based on the spectrometer measurement rather than on right- or wrong-side tracks (as it was done in the thin target data analysis). The latter do not distinguish between different momentum resolutions (both type may pass through different sets of spectrometers), while, as already stressed, this is a parameter that matters for the long target analysis.
- The region below 30 mrad is barely covered over the first five bins. This is due to TRK cut(V) that rejects tracks of the VTPC-2 and GTPC topologies extrapolated along the target. Once included (e.g. bin corresponding to the downstream face of the target), these topologies partly cover that region. At high momenta (> 12 GeV/c) though, tracks of the GTPC topology cannot

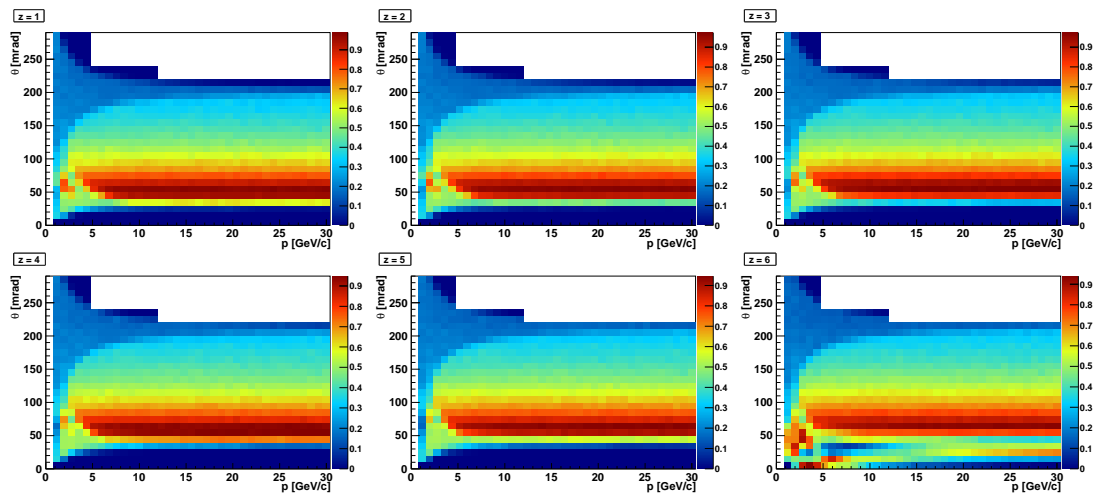


Figure 3.40: Acceptance of the NA61 apparatus for positively charged particles exiting the T2K replica target for five equidistant longitudinal bins in z along the beam direction. The most upstream bin is shown on the top left plot, the most downstream bin (downstream face of the target) on the bottom right plot.

cover the region below 10 mrad due to the requirement on MTPC points (TRK cut(IV)).

- The downward going arc-shaped region of less acceptance from 100 down to 30 mrad at low momenta is well understood as a consequence of the combination of the forward time-of-flight and MTPC point requirements. Tracks from the VTPC-2 topology partly cover that region but the coverage is limited by the requirement on the number of points on track that rejects tracks close to the beam axis. As expected, the region of maximal acceptance drifts upwards along the target (from the first to the fifth bin), since the closer tracks are emitted from VTPC-1, the larger polar angles are selected.

The analysis binning is chosen in such a way that: (i) the bin size accounts for the low statistics of the 2007 replica target data set; (ii) in particular, the size of the momentum bins should be small enough in regions of strong variations of the energy loss distribution so that the mean of the distribution does not vary too much over the bin width; (iii) bins should cover regions of uniform acceptance or at least with smooth variations and (iv) bins should eventually have the same statistical accuracy. Such a binning is schematically represented in Fig. 3.41 and shown overlaid on the data and acceptance maps in Fig. 3.42 and Fig. 3.43 respectively.

A common binning is used for the first five longitudinal bins. It covers three angular bins, [40-100], [100-160] and [160-280] mrad, although the bin size may depend on the momentum at the edges of the acceptance. For all longitudinal bins, the size of the momentum bins

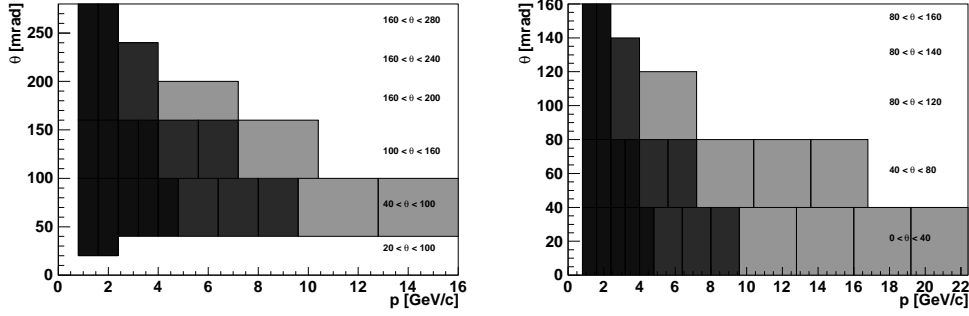


Figure 3.41: Analysis binning of the replica target data in $\{p, \theta, z\}$ for longitudinal bins 1 to 5 (left) and for bin 6 that corresponds to the downstream of the target (right). From darker to lighter gray tone, the momentum bin size corresponds to 0.8 GeV/c, 1.6 GeV/c and 3.2 GeV/c.

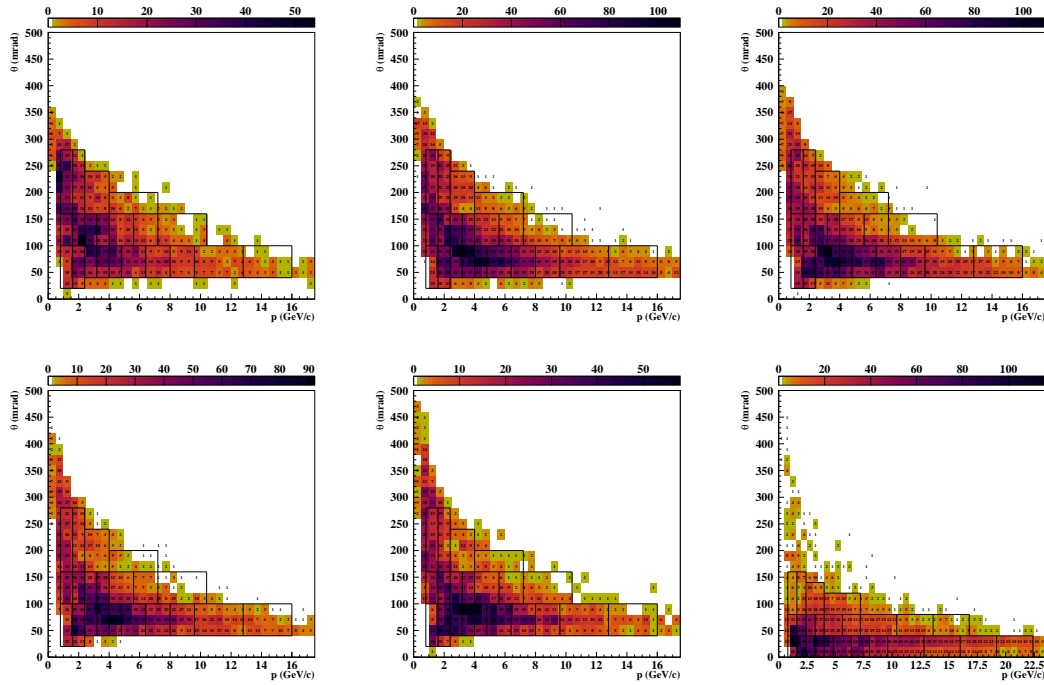


Figure 3.42: $\{p, \theta\}$ coverage at the surface of the target for positively charged particles for the different longitudinal bins. The most upstream bin is shown on the top left plot, the most downstream bin (downstream face of the target) on the bottom right plot. The binning chosen for analysis is shown on top.

is the same (0.8 GeV/c, 1.6 GeV/c and 3.2 GeV/c). The binning for the downstream face of the target extends to higher momenta. For this

last bin, the angular coverage is refined with bins of $[0-40]$, $[40-80]$ and $[80-160]$ mrad.

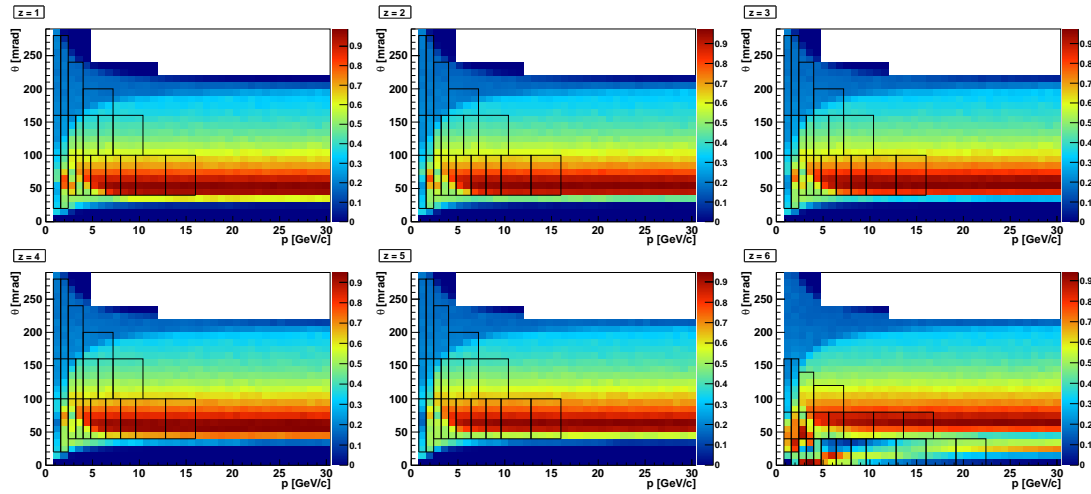


Figure 3.43: Acceptance of the NA61 apparatus for positively charged particles in $\{p, \theta, z\}$. The most upstream bin is shown on the top left plot, the most downstream bin (downstream face of the target) on the bottom right plot. The binning chosen for analysis is shown on top. A common binning is used for the first 5 longitudinal bins. For the downstream face of the target, the binning extends to larger momenta and covers smaller angles.

The statistical accuracy of all bins is illustrated in Fig. 3.44. At least 100 entries are available in most of the bins (the number of entries in bins at the edge of the analysis region may drop down to ~ 40). The low statistics is accounted for in the fitting procedure for the particle identification (i.e. likelihood technique). The statistics per bin scales with momentum in the different angular bins as a function of the longitudinal bin, which shows that the chosen binning appropriately covers regions of uniform acceptance.

The acceptance correction computed over the analysis binning is shown in Fig. 3.45.

3.8 Backward extrapolation to the surface of the target

The chosen set of reconstructed track parameters on target consists in:

- (i) $\vec{q} = \{x, y, z\}$: position of the exit point on target;
- (ii) \vec{p} : momentum at the exit point;
- (iii) θ : angle of the track with respect to the beam axis at the exit point,

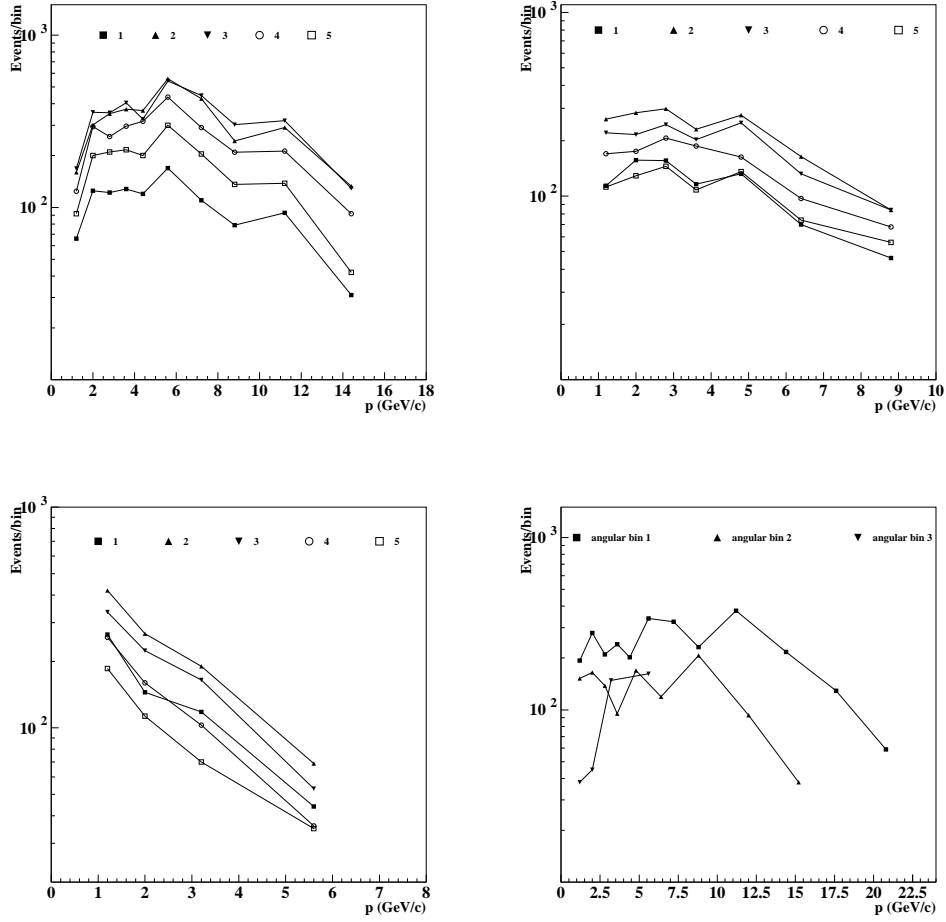


Figure 3.44: Statistics per $\{p, \theta, z\}$ bin for positive tracks over the first 5 longitudinal bins for the first (top left), second (top right) and third (bottom left) angular bins. Statistics for the downstream face of the target for the three angular bins (bottom right).

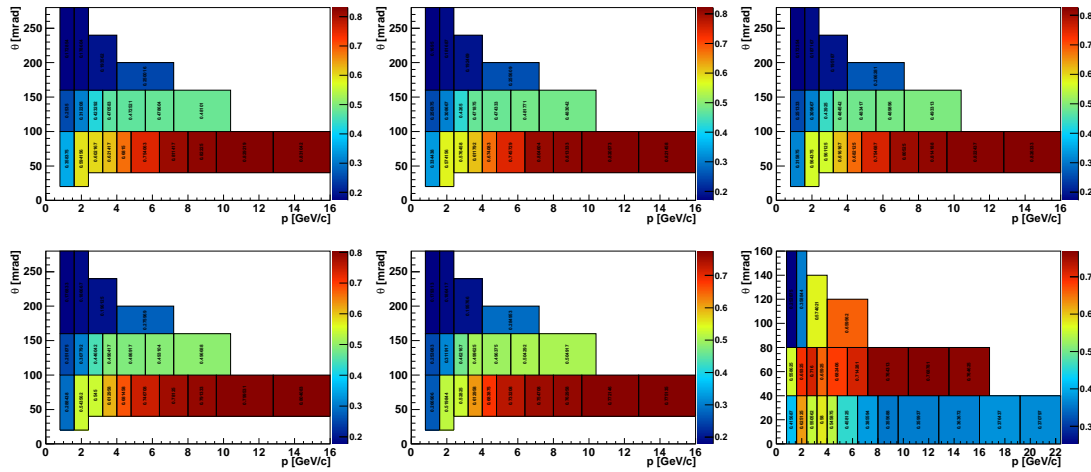


Figure 3.45: Acceptance of the NA61 apparatus for positively charged particles exiting the T2K replica target over the analysis binning for the five equidistant longitudinal bins and the downstream face of the target. The most upstream bin is shown on the top left plot, the most downstream bin (downstream face of the target) on the bottom right plot.

where the z component is stored over 5 equidistant bins of 18 cm each, plus an additional bin representing the downstream face of the target. Global rtracks are extrapolated back through the magnetic field to the surface of the target from their first measured point in the TPCs. The propagation of the error matrix is done at each extrapolation step (for details of the calculation see for example [89]). A correction factor is added at each step to take the effect of the multiple scattering in air into account. The scattering correction is given by:

$$\theta_0 = \frac{13.6 \text{ MeV}}{\beta c p} z \sqrt{x/X_0} [1 + 0.038 \ln(x/X_0)] \quad (3.6)$$

where p , βc and z are the momentum, velocity and charge number of the particle, and x/X_0 is the thickness of the scattering medium in radiation lengths (304 m in air). The extrapolation is first performed till the z position of the downstream face of the target. If the intersection of the extrapolation with the corresponding plane is within the radius of the target, the exit point and track parameters are stored at the intersection point. Otherwise, the track is further extrapolated over the whole length of the target. In a second step, a point-of-closest-approach (p.c.a.) is determined between the track trajectory and the surface of the target with a specific minimization procedure. As an illustration the p.c.a. distribution in the x - z , y - z , x - y and z projections for the real and simulated data are shown in Fig. 3.46 and Fig. 3.47.

At the analysis level, a cut on the p.c.a. at 0.6 cm is applied to select reconstructed tracks. Tracks extrapolated with a p.c.a. larger than 0.6 cm are not

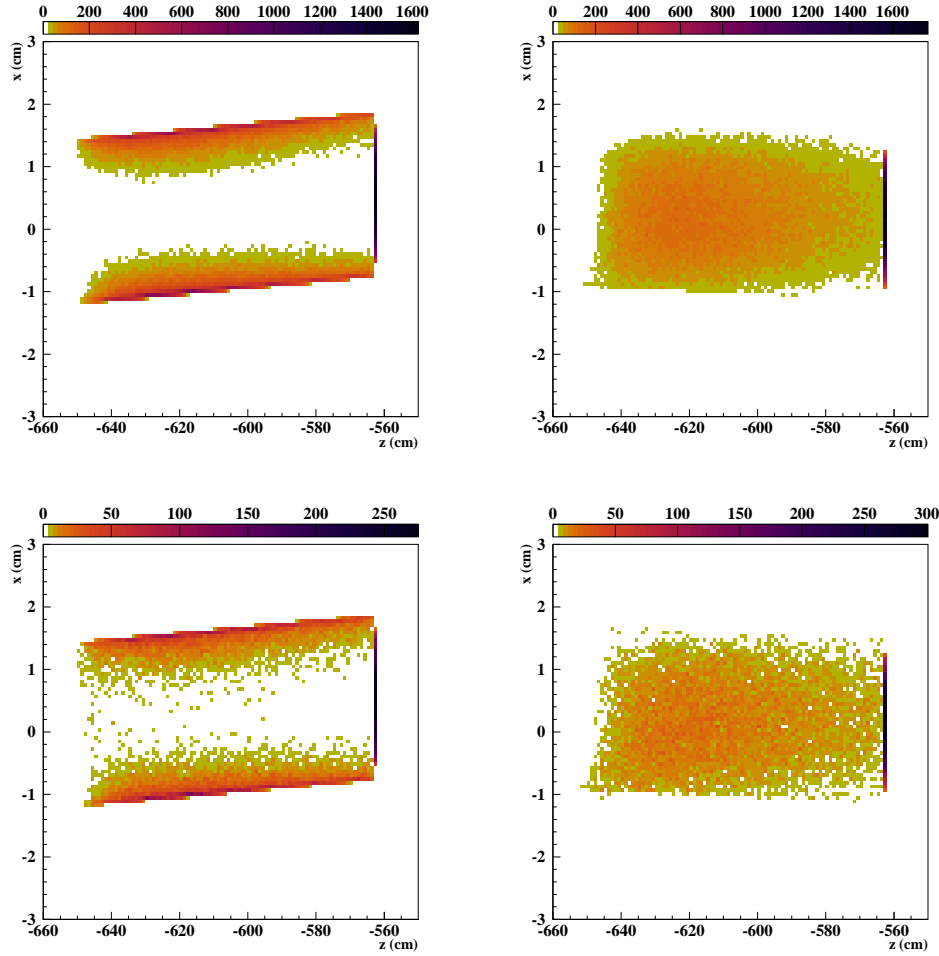


Figure 3.46: Extrapolated position on target in the x-z (left) and y-z (right) projections for the simulated (top) and real (bottom) data.

considered as coming from the target. The value chosen for the p.c.a. cut corresponds to the mean r.m.s. of the distribution of the error on the extrapolated transverse position on target as a function of the longitudinal position. The error is calculated using the covariance matrix at the p.c.a. and shown in Fig. 3.48. The error distribution in data is well reproduced by the Monte-Carlo. As can be seen in Fig. 3.49, the p.c.a. distribution as well as the effect of the p.c.a. cut on the longitudinal distribution of the exit points on target in data are also well reproduced by the Monte-Carlo: the fraction of tracks extrapolated on target is of 97.7% (98.6%) in data (Monte-Carlo), while the relative fraction of tracks extrapolated up to the end of the target (no p.c.a. found along the target) is of 0.9%

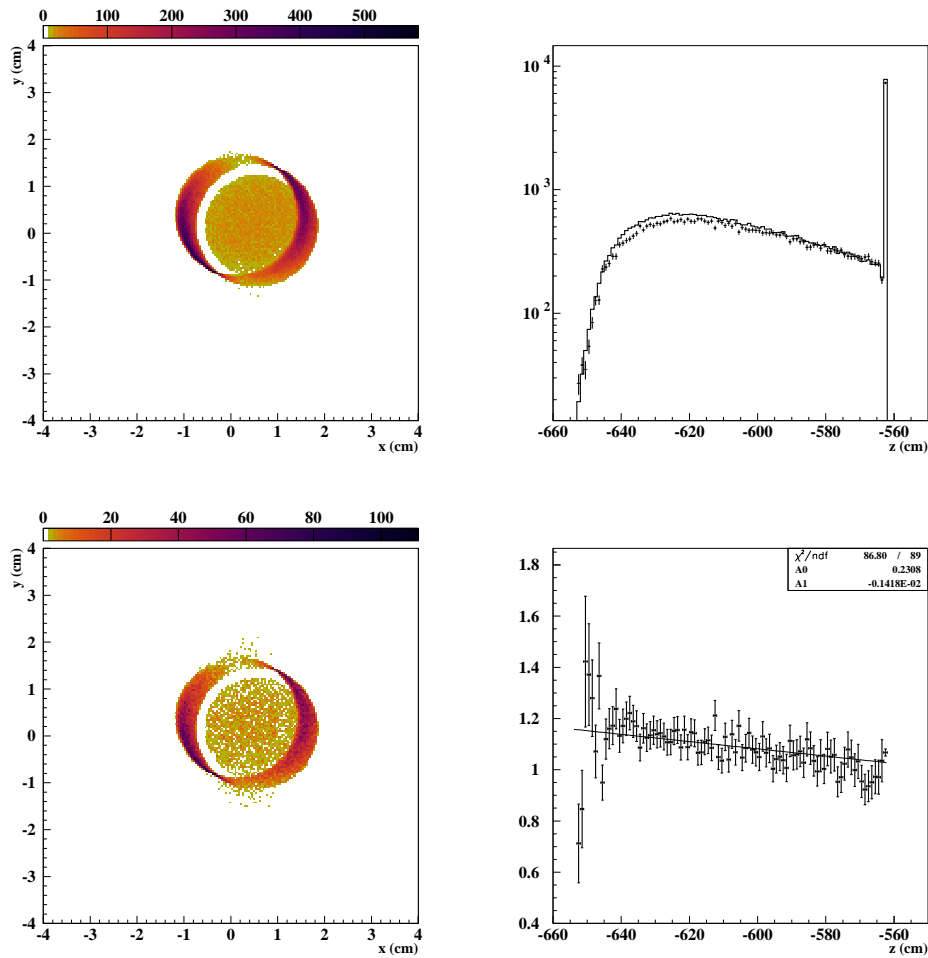


Figure 3.47: Extrapolated position on target in the x-y (left) projection for simulated (top) and real (bottom) data. Longitudinal distribution (top right) on target for the real (dots with error bars) and simulated (histogram) data, and corresponding ratio (bottom right). The simulated data is normalized to the ratio of p.o.t. in data and Monte-Carlo.

(0.6%) respectively.

The NA61 simulation is used to estimate the efficiency and purity of the selection based on the p.c.a. cut for all global rtracks (positively and negatively charged particles). Two sets of tracks are defined using the information from the matching client that associates originally simulated and reconstructed tracks:

- (i) global rtracks extrapolated within the cut with matched track in (out of) cut;
- (iii) global rtracks extrapolated out of cut with matched track in (out of) cut;

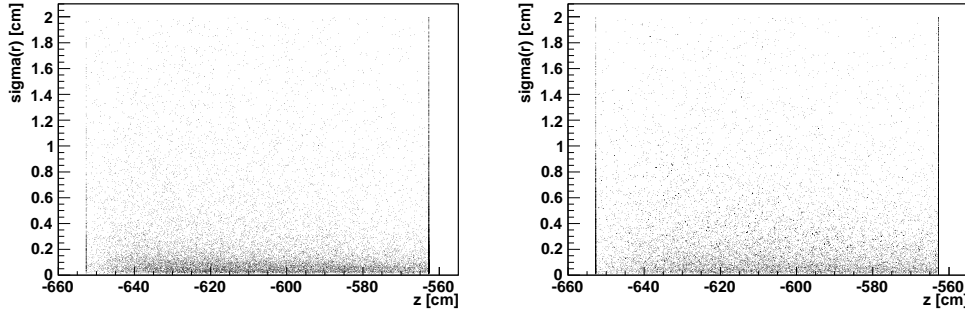


Figure 3.48: Distribution of the error on the extrapolated transverse position for real (left) and simulated (right) data.

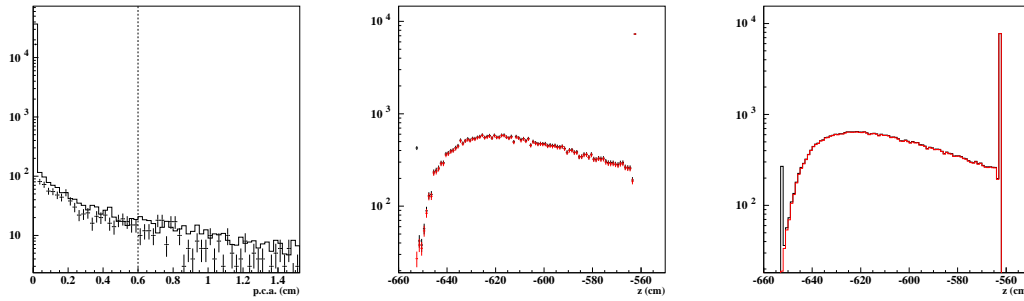


Figure 3.49: Distribution of the point-of-closest-approach on target (left) for real (dots with error bars) and simulated (histogram) data. The dashed vertical line shows the value of the p.c.a. cut. Data (middle) and simulated (right) distributions with (red) and without (black) the cut.

The efficiency of a cut is usually defined as $\epsilon = n_{true}^{sel}/n_{true}$ and the purity as $P = n_{true}^{sel}/n^{sel}$, where in the previous categories, the *true* information refers to the matched track originating from the target within the p.c.a. cut, while the *selected* information refers to the global rtrack being extrapolated within the p.c.a. cut. The efficiency and purity of the selection are defined accordingly:

$$\epsilon = \frac{\text{Number of global rtracks extrapolated within the cut with matched track in cut}}{\text{Number of global rtracks with matched track in cut}}$$

$$P = \frac{\text{Number of global rtracks extrapolated within the cut with matched track in cut}}{\text{Number of global rtracks extrapolated within the cut}}$$

The statistical error on the cut efficiency (purity) is calculated considering that the n_{true} (n^{sel}) quantity is fixed while the n_{true}^{sel} quantity varies, which allows to

treat the ratio according to the binomial statistic:

$$P(m; N, \epsilon) = \frac{N!}{m!(N-m)!} \epsilon^m (1-\epsilon)^{N-m} \quad (3.7)$$

where m (n_{true}^{sel}) is the number of *successes* among N (n^{sel}, n_{true}) events with a probability of success given by the efficiency ϵ . An estimator of the efficiency, $\hat{\epsilon}$, is given by maximizing the log-likelihood of the binomial statistic as a function of ϵ by solving:

$$\frac{\partial L(\epsilon)}{\partial \epsilon} = \frac{\partial}{\partial \epsilon} (m \ln \epsilon + (N-m) \ln(1-\epsilon) + C) = 0 \quad (3.8)$$

where C stands for constants independent of ϵ . This leads to $\hat{\epsilon} = m/N$. The variance of the binomially distributed m is given by $V[m] = N\epsilon(1-\epsilon)$ so that the variance of the estimator is given by:

$$V[\hat{\epsilon}] = V\left[\frac{m}{N}\right] = \frac{1}{N^2} V[m] = \frac{\epsilon(1-\epsilon)}{N} \quad (3.9)$$

To compute the variance numerically, we need an *estimator* of the variance of the estimator, which we can take to be the variance of the estimator with ϵ replaced by $\hat{\epsilon}$:

$$\hat{V}[\hat{\epsilon}] = \frac{\hat{\epsilon}(1-\hat{\epsilon})}{N} = \frac{m(1-m/N)}{N^2} \quad (3.10)$$

The standard deviation of the estimator of the cut efficiency is finally given by:

$$\hat{\sigma}[\hat{\epsilon}] = \frac{\sqrt{m(1-m/N)}}{N} \quad (3.11)$$

The efficiency and purity of the p.c.a. cut for the backward extrapolation on target are calculated for each $\{p, \theta, z\}$ bin. The overall efficiency and purity as a function of the three track parameters on target (p, θ and z) are shown in Fig. 3.50 for all global rtracks (positively and negatively charged particles). In particular, it can be noted that:

- **The integrated efficiency is estimated to $99.4 \pm 0.02\%$ while the purity is estimated to $97.5 \pm 0.03\%$.** The dip that we previously described in the momentum distribution for the VTPC-1+VTPC-2 topology is reflected as a drop in efficiency as a function of momentum at about 1 GeV/ c and polar angle around 20 mrad (VTPC-1+VTPC-2 tracks that pass through the MTPCs are affected, which means forward going particles).
- The drop in efficiency and purity observed at small z values (first longitudinal bin) is explained by the increase of the extrapolation error as a function of z . Actually, the longer the extrapolation is, the larger the error on the transverse position becomes (in particular due to the multiple scattering).

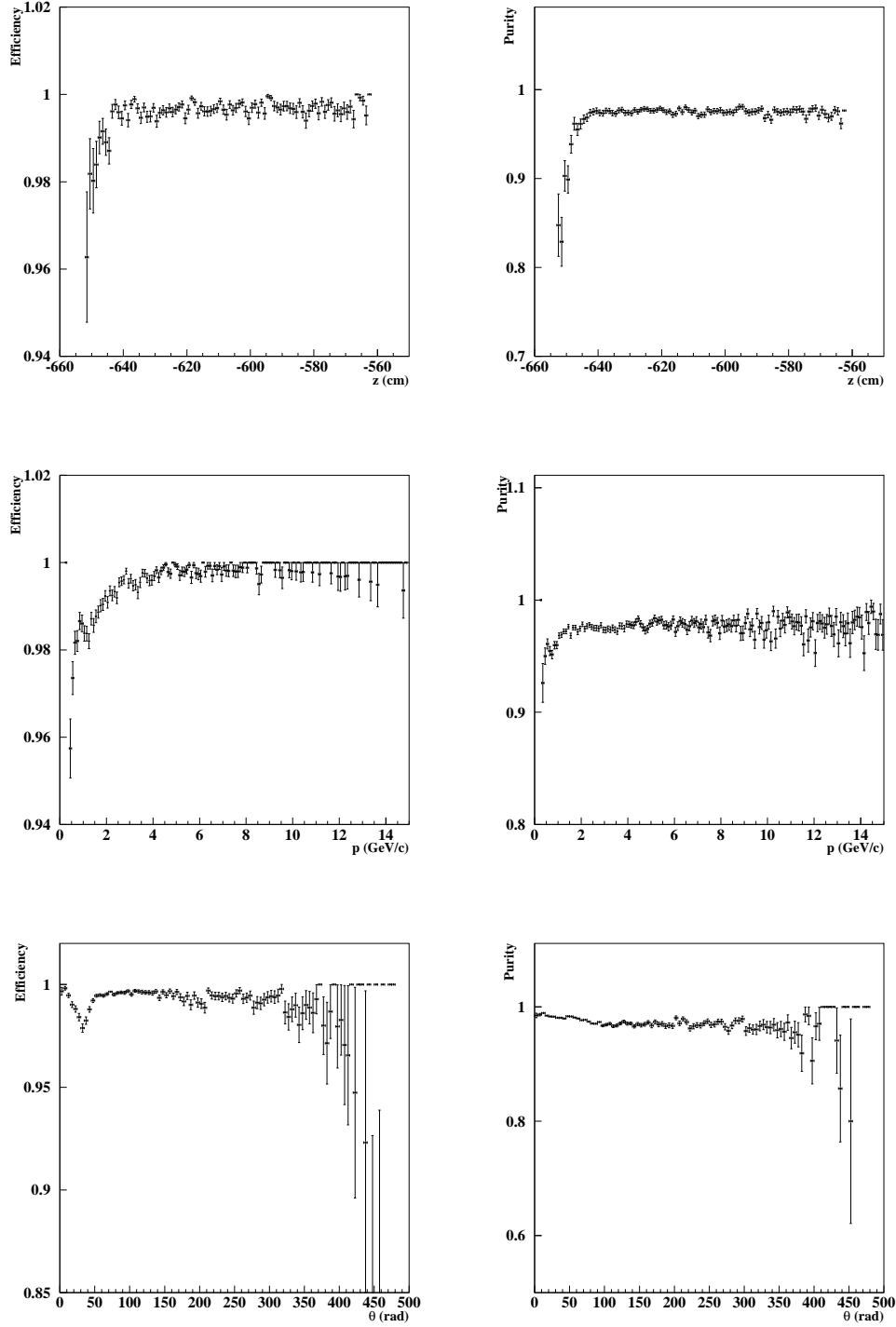


Figure 3.50: Extrapolation efficiency (left) and purity (right) for all global rtracks as a function of the track parameters on target: z (top), p (middle) and θ (bottom).

Ph.D. thesis by N. Abgrall

As we previously mentioned, the p.c.a. cut value has been fixed to the mean r.m.s. of the distribution of the error on the extrapolated transverse position along the target. This explains why less tracks are extrapolated within the cut in the upstream part of the target where the error tends to be larger than the average value over the full length of the target. In a second step of this analysis, a z -dependent cut should be applied, which in turn would probably increase the efficiency and purity in the first longitudinal bin.

- A small drop in purity can also be noticed at high z values corresponding to the downstream face of the target. The effect is not clearly visible in the very last bin due to the large number of tracks exiting from the downstream face, but it can be seen in the previous bin which corresponds to the very last section of the 5th longitudinal bin. This behavior of the purity can be understood as a consequence of the contamination from weak decays (referred to as *feed-down* contribution) which is expected to be maximal for the bin corresponding to the downstream face of the target. Actually, some neutral particles with a very short lifetime such as K_S^0 or Λ resonances, if they encounter a small amount of matter on their way, may escape the target without undergoing any re-interactions and weakly decay producing in particular π mesons (so-called V^0 -decays, e.g. $K_S^0 \rightarrow \pi^- \pi^+$, $\bar{\Lambda} \rightarrow \bar{p} \pi^+$). These pions, produced close to the downstream face of the target or close to the beam axis, are reconstructed in the TPCs, extrapolated back in the magnetic field, and associated to the target if the extrapolation falls in a radius of 1.1 cm on the downstream face of the target or within the 0.6 cm p.c.a. cut along the target. Fig. 3.51 shows the simulated distribution of the p.c.a. for all global rtracks. In particular, it can be seen that the distribution is peaked at the position of the downstream face of the target for global rtracks which are matched to simulated tracks that do not pass the p.c.a. cut. The longitudinal distribution of the starting vertex of these simulated tracks is also shown in Fig. 3.51. Some vertices are found along the target but most of them are distributed along the beamline with a clear enhancement right after the downstream end of the target. The main contribution (79.5%) comes from decays among which, in 66% of the cases, the parent particle is either a K_S^0 or a Λ resonance. A secondary contribution (19.5%) comes from re-interactions in the detector material (i.e. entrance and exit windows of the VTPC-1).
- The overall loss of purity due to the contamination from feed-down and re-interactions in the detector material is estimated to 2.5%. Previously quoted values are obviously model-dependent: the feed-down contribution mainly depends on the simulation of the strange particle production in FLUKA, while re-interactions in the detector material depend on the GCALOR model. Thus, even though the amplitude of the corresponding corrections is small, the systematic error on the corrections should reflect the uncertainty on the

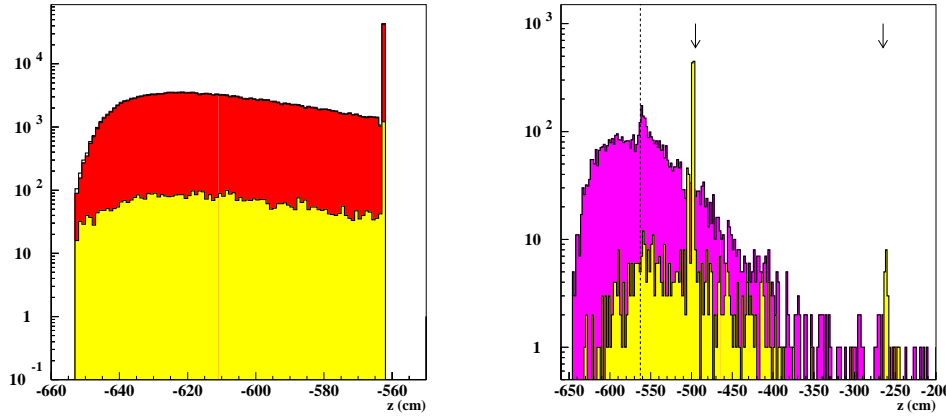


Figure 3.51: Distribution of the p.c.a. (left) for all global rtracks (black) matched to simulated tracks within the cut (red) and out of the cut (yellow). Longitudinal distribution of the starting vertex of matched simulated tracks out of the cut for the decay (purple) and re-interaction (yellow) contributions. The dashed vertical line shows the position of the downstream end of the target, while arrows show the position of the entrance and exit windows of the VTPC-1.

underlying processes which may be large (e.g. K_S^0 and Λ production).

The NA61 simulation is used to estimate the achievable resolution of the track parameters on target starting from the error on angle and momentum resolution obtained at the level of the global rtracks (Fig. 3.32) by comparing reconstructed and generated parameters on target. **The momentum (angular) resolution (shown in Fig. 3.52) is estimated to 3% (1.6%), 2.5% (6.5%), 2.8% (2%) and 7% (8.1%) for the VTPC-1, VTPC-2, VTPC-1+VTPC-2 and GTPC topologies respectively.** The angular resolution is worse for the VTPC-2 and GTPC topologies which are peaked at small angle. In order to keep the longitudinal resolution on target as small as possible compared to the longitudinal bin size (18 cm), the TRK cut(V) was introduced to select tracks from these two topologies only when extrapolated back on the downstream face of the target. Actually, from the mean angle of the VTPC-1, VTPC-2, VTPC-1+VTPC-2 and GTPC topologies (200, 60, 100 and 20 mrad respectively) and the mean error on the extrapolated transverse position (p.c.a. cut at 0.6 cm), the longitudinal resolution is expected to be of the order of 3 cm for the VTPC-1 topology and 6 cm for the VTPC-1+VTPC-2 topology, while it is expected to be of the order of 10 cm for the VTPC-2 topology and 30 cm for the GTPC topology (comparable to the bin size).

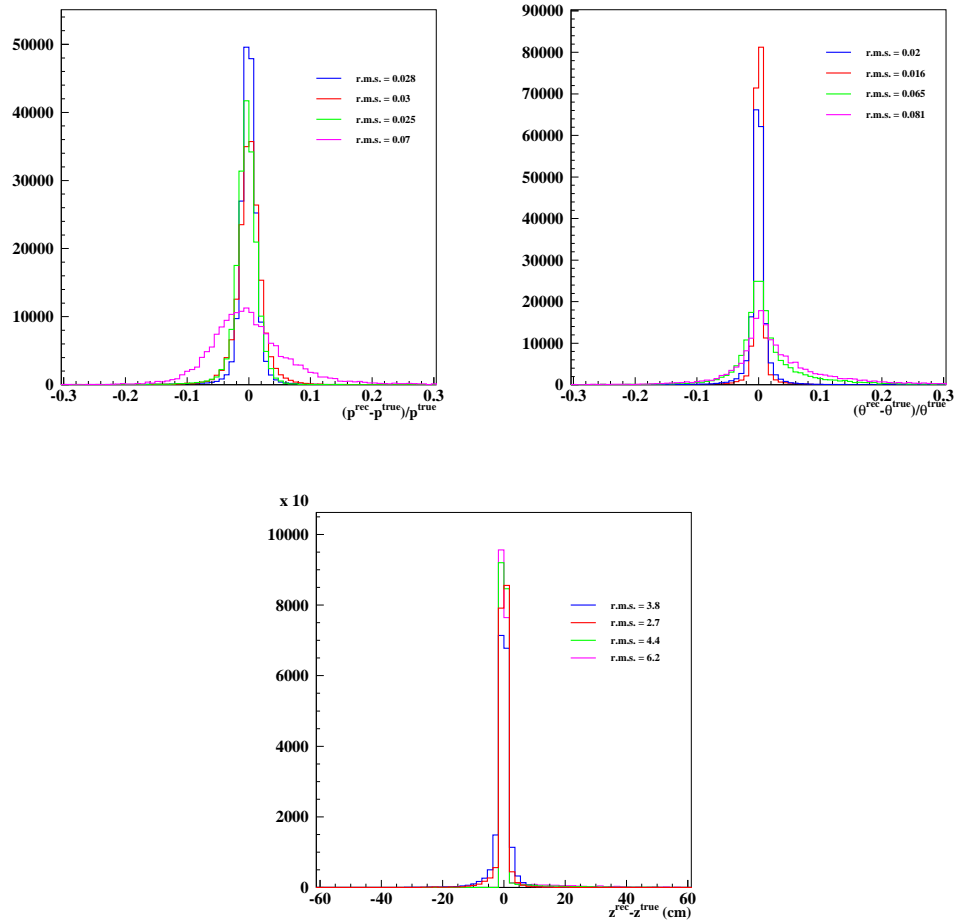


Figure 3.52: Momentum (top left), polar angle (top right) and longitudinal (bottom) resolutions on target. The different colors correspond to the different track topologies: VTPC-1 (red), VTPC-2 (green), VTPC-1+VTPC-2 (blue) and GTPC (purple). All topologies are normalized to the VTPC-1+VTPC-2 topology.

Using TRK cut(V) allows to minimize the longitudinal bin migration, defined as the relative fraction of tracks extrapolated in a given bin but generated in another one. This quantity is further more reduced by introducing TRK cut(VI) that selects tracks extrapolated within a radius of 1.1 cm on the downstream face of the target (due to the error on the extrapolated transverse position, tracks exiting along the target almost parallel to the beam direction can easily be associated to the outer region of the downstream face of the target). The bin migration is estimated to 5.8% (15%), 5.2% (9.1%), 6.1% (9.4%), 5% (9%), 3.5% (8.5%) and 1.7% (1.3%) for the VTPC-1 (VTPC-1+VTPC-2) topology over bins 1 to 6 respectively. The contribution of the first five bins to the downstream face of the target is estimated to 7.7% for the VTPC-2 topology and 5.2% for the GTPC topology.

The systematic uncertainties on the backward extrapolation efficiency are attributed to:

- (i) the choice of the p.c.a. cut: the nominal value corresponds to the mean r.m.s. of the distribution of the error on the extrapolated radial position. The corresponding systematic error is estimated by calculating efficiencies for 0.5 and 1.5 times the r.m.s. value, and retaining the maximal difference to the nominal value as the systematic error.
- (ii) the uncertainty on the real target position: the nominal target tilts in the x-z and y-z planes are used for the extrapolation on target while the nominal values are varied by ± 1 sigma (0.001 rad for both tilts) independently to define the accepted region of extrapolation based on the p.c.a. cut. Since the position of the upstream face of the target is determined from the surveyed position of BPD-3, the ± 1 sigma variation of the tilts are made with respect to the center of the upstream face of the target. This reproduces a situation where tracks would be extrapolated to a region that does not fully agree with the actual position of the target. The corresponding efficiencies are calculated and the associated systematic error is estimated as in (i).
- (iii) the stray field of VTPC-1: the stray field of the VTPC-1 magnet extends to the target region. It is extrapolated from a measured field map. As can be seen in Fig. 3.53, the mean field estimated at the center of the target along the beam axis is $\sim 0.01 \times 10^{-3}$ T and ~ 0.01 T for the B_x and B_y components respectively. The angular shift in the x and y directions for a pion track with momentum $p = 1$ GeV/c over the target length (90 cm) is given by:

$$\theta_{x,y}[rad] = 0.3 \times \frac{B_{x,y}[T] \times L[cm]}{p[GeV/c]} \quad (3.12)$$

which leads to a spatial shift of $\Delta_y \sim L \times \theta_y \sim 0.24$ cm in the vertical direction. The shift in the horizontal direction ($2.4 \mu\text{m}$) is negligible. This

value of the vertical shift corresponds to the maximal shift over the target length. To get an upper bound on the amplitude of the effect of the stray field, we consider this value as constant over the whole target and the vertical position of the extrapolated points on target is smeared with a gaussian of $\sigma = 0.24$ cm. The related systematic uncertainty is estimated by calculating the efficiency after the smearing and taking the difference with the efficiency under the nominal conditions.

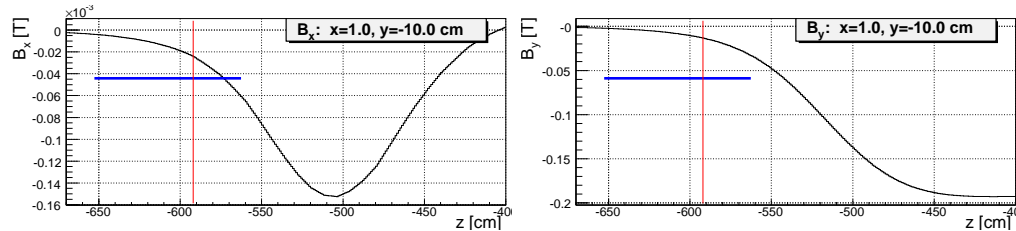


Figure 3.53: Magnetic field x (left) and y (right) components in the target (blue horizontal line) region. The red vertical line shows the limit of the measured field map. The field components are extrapolated beyond this limit.

The sources of systematics described in points (i) to (iii) are to some extent correlated due to the relations between the radial and longitudinal positions of the extrapolated points along the target. In this case, one of the systematic may already account for the others as a function of the position along the target. Thus, instead of summing the systematics in quadrature, we define the total systematic as being the largest difference with respect to the efficiency calculated with the nominal p.c.a. cut and tilt values.

3.9 Raw yields of positively charged pions on target

The particle identification in NA61 fully takes advantage of the combination of the TPC and ToF signals to achieve a particle separation that covers a large momentum range. As can be seen in Fig. 3.36, the PID capabilities of the dE/dx signal in the TPCs are pretty much limited above ~ 1 GeV/ c and below ~ 3 GeV/ c where the different particle species overlap (the region below 1 GeV/ c momentum was the topic of a dedicated dE/dx analysis of the thin target data [86]). However, beyond this limit (along the relativistic rise region), the energy loss signal can efficiently discriminate between the different particle species. The ToF signal shows as well an efficient particle discrimination up to ~ 6 GeV/ c . Combining the two signals allows a clear separation of the different species. This is illustrated in Fig. 3.54 that shows how protons, pions, kaons and positrons are separated in distinct regions of the combined $\{dE/dx, ToF\}$ phase space.

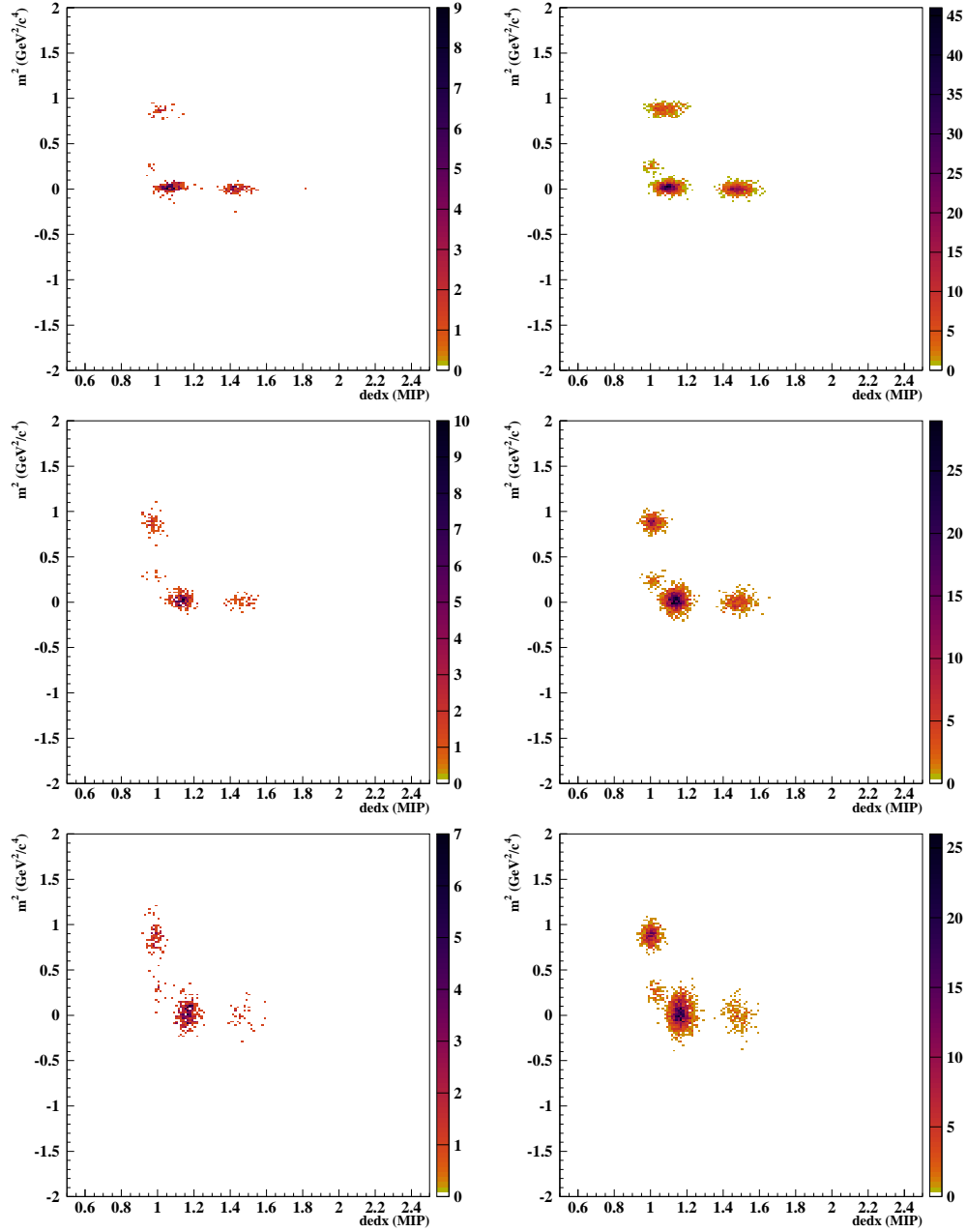


Figure 3.54: Combined $\{dE/dx, ToF\}$ distribution for the angular bin $40 < \theta < 100$ mrad, momentum bin $1.6 < p < 2.4$ GeV/c (top), $2.4 < p < 3.2$ GeV/c (middle), $3.2 < p < 4$ GeV/c (bottom) and third longitudinal bin, for real (left) and simulated (right) data.

The typical number of tracks per $\{dE/dx, ToF\}$ bin for a given $\{p, \theta\}$ bin is of the order of 10. Such a data is usually described by a Poisson statistic. It is well-known that standard χ^2 minimizations suffer from some difficulties when used to fit (*point estimation*) such distributions. They usually tend to under- or over-estimate the area under the peaks, which is related to the underlying assumption that errors are from a parent Gaussian distribution. The method of maximum likelihood is used instead for this analysis.

Particle yields can be extracted from each $\{p, \theta, z\}$ bin by fitting the corresponding $m^2 - dE/dx$ distribution with an appropriate hypothesis. We suppose that the number of events in each of the bins of the $\{dE/dx, ToF\}$ phase space, $n_i(x_{dE}, x_{m2})$, is described by the following p.d.f.:

$$f(n, \alpha) = \sum_{l=p,K,\pi,e} \frac{N_l}{2\pi\sigma_{dE}^l\sigma_{m2}^l} \exp\left[-\frac{1}{2}\left(\left(\frac{x_{dE} - \mu_{dE}^l}{\sigma_{dE}^l}\right)^2 + \left(\frac{x_{m2} - \mu_{m2}^l}{\sigma_{m2}^l}\right)^2\right)\right] \quad (3.13)$$

where $\alpha = \{N_l, \mu_{dE}^l, \sigma_{dE}^l, \mu_{m2}^l, \sigma_{m2}^l\}_{l=p,K,\pi,e}$ is a vector of 20 parameters:

- N_l : normalization factor for particle of type l ;
- μ_{dE}^l : mean energy loss of particle of type l in a given momentum bin;
- σ_{dE}^l : width of the energy loss distribution of particle of type l in a given momentum bin;
- μ_{m2}^l : mass squared of particle of type l ;
- σ_{m2}^l : width of the mass squared distribution of particle of type l in a given momentum bin.

Eq. 3.13 describes a two-dimensional Gaussian distribution. On one hand, the mass squared and truncated mean charge distributions are actually expected to be Gaussian. On the other hand, the detector resolutions may systematically affect the data and make it diverge from a purely Gaussian behavior (e.g. typically by producing tails at the edge of the distributions). These side effects should in principle be taken into account by using a more fancy expression for the p.d.f. than that of Eq. 3.13. However, the available statistics for this analysis is limited to the 2007 data set. With such a low statistics, it becomes superfluous to account for such refinements to describe side effects that cannot effectively be distinguished from simple statistical fluctuations of the data. For example, we tried to use a multi-Gaussian description (two Gaussians are used in each dimension, one to fit the main part of the peak, another with a larger sigma to fit the tails) instead of the simple expression of Eq. 3.13. This did not lead to any significant improvement neither for the convergence nor for goodness-of-fit. Concerning the different components of the fitted hypothesis:

- The normalization factors are introduced so that the parametrization allows complete freedom to adjust the overall scale of the fit. In this case, the area under the peaks is preserved ($\sum f(n_i, \alpha) = \sum n_i$). The p.d.f. being normalized, the yield of a particle of type l is directly given by the N_l parameter of the fit:

$$\int_{dE} \int_{m2} dx_{dE} dx_{m2} \frac{N_l}{2\pi\sigma_{dE}^l \sigma_{m2}^l} \exp\left[-\frac{1}{2}\left(\left(\frac{x_{dE} - \mu_{dE}^l}{\sigma_{dE}^l}\right)^2 + \left(\frac{x_{m2} - \mu_{m2}^l}{\sigma_{m2}^l}\right)^2\right)\right] = N_l \quad (3.14)$$

- The initialization of the width parameters for the energy loss and the mass squared distributions is based on the detector resolutions. For the energy loss, the track quality cuts on the number of points on track applied for analysis assure that the dE/dx resolution reaches the flat region of the $\sim 1/\sqrt{N}$ parametrization (see Fig. 3.20). Thus, a constant value of $\sigma_{dE} = 3\%$ is used to initialize the corresponding parameters of the fit. This initial value is further scaled by the derivative of the Bethe-Bloch parametrization over the width of the considered momentum bin to account for the spread of the energy loss distribution due to projections in regions of strong variations (e.g. below ~ 2 GeV/c) as a function of momentum. The width of the mass squared distributions is initialized from the parametrizations of the mass squared resolution as a function of momentum (shown in Fig. 3.19).
- The mean values (positions) of the peaks are initialized to the mass squared values of the different particle species and to the mean dE/dx values obtained from the parametrization of the calibrated Bethe-Bloch curve. It can be noted that the latter is slightly shifted above the data at lower momenta (e.g. Fig. 3.36). The allowed variation of the fitted parameters (Table 3.5) was set large enough to account for that systematic shift in a first step. A refined version of the current analysis would require to re-compute the Bethe-Bloch parametrization.

The likelihood function to maximize is constructed as the joint p.d.f. for the data. It is evaluated over N measurements in the $\{dE/dx, ToF\}$ phase space and is a function of the set of parameters α :

$$L(\alpha) = \prod_{i=1}^N f(n_i; \alpha) \quad (3.15)$$

The maximization is usually calculated for $\ln L$ (which is maximized for the same values of the parameters) and often turned into a minimization problem by considering $-\ln L$. During minimization, parameters are allowed to vary over a given range around their initial value. Allowed ranges are given in Table 3.5. No parameter is fixed at low momentum where the different particle species can clearly

be isolated. At higher momenta the distributions of the various species tend to overlap along the dE/dx direction. The overall distribution is then constrained by fixing the position of the low statistics kaon and positron peaks along that direction. Positions are fixed for $p > 6.4$ GeV/ c , $p > 5.6$ GeV/ c and $p > 4$. GeV/ c in the first, second and third angular bins respectively. Examples of fits are shown in Fig. 3.55 and Fig. 3.56 for real and simulated data respectively.

Particle	Normalization	μ_{dE}	σ_{dE}	μ_{m^2}	σ_{m^2}	Step size
p	[0, I]	[-20%, +30%]	[-20%, +50%]	[-20%, +30%]	[-20%, +50%]	10%
K^+	$[0, \frac{1}{3}I]$	$\pm 10\%$	[-10%, +20%]	$\pm 10\%$	[-10%, +20%]	10%
π^+	[0, I]	[-20%, +30%]	[-20%, +30%]	[-20%, +30%]	[-20%, +30%]	10%
e^+	[0, I]	[-20%, +30%]	[-20%, +50%]	[-20%, +30%]	[-20%, +50%]	10%

Table 3.5: Allowed ranges of the fitted parameters around their initial value. The range of the individual normalization factors varies between 0 and a given fraction of the total integral of the distribution, I . The step size is expressed in % of the range (same for all parameters).

To quantify the level of agreement between the data and the hypothesis of Eq. 3.13, we use the theorem on the likelihood ratio test that allows to convert a likelihood function into the form of a general χ^2 statistic ([90]). Let m_i be the true value (without errors) of n_i in a given bin of the $\{dE/dx, ToF\}$ phase space. One constructs the likelihood ratio λ defined as:

$$\lambda = \frac{L(y; n)}{L(m; n)} \quad (3.16)$$

where the y_i are the numbers of events predicted by the fitted hypothesis in each of the bins. The likelihood ratio test theorem states that the *likelihood* χ^2 defined by

$$\chi_\lambda^2 = -2 \ln \lambda = -2 \ln L(y; n) - 2 \ln L(m; n) \quad (3.17)$$

asymptotically obeys a general χ^2 distribution ([91],[92]). We consider a Poisson distribution for the test statistic so that

$$L(y; n) = \prod_{i=1}^N \frac{y_i^{n_i} \exp(-y_i)}{n_i!} \quad (3.18)$$

The true values m_i are then chosen to be the values that maximize the Poisson likelihood for the observed numbers of events n_i :

$$\frac{\partial L(m; n)}{\partial m} = \frac{\partial}{\partial m} (n \ln m - m - \ln n!) = \frac{n}{m} - 1 \quad (3.19)$$

which equals 0 for the condition $m = n$. Thus, the Poisson likelihood χ^2 is given by the following expression:

$$\chi_\lambda^2 = 2 \sum_{i=1}^N y_i - n_i + n_i \ln \frac{n_i}{y_i} \quad (3.20)$$

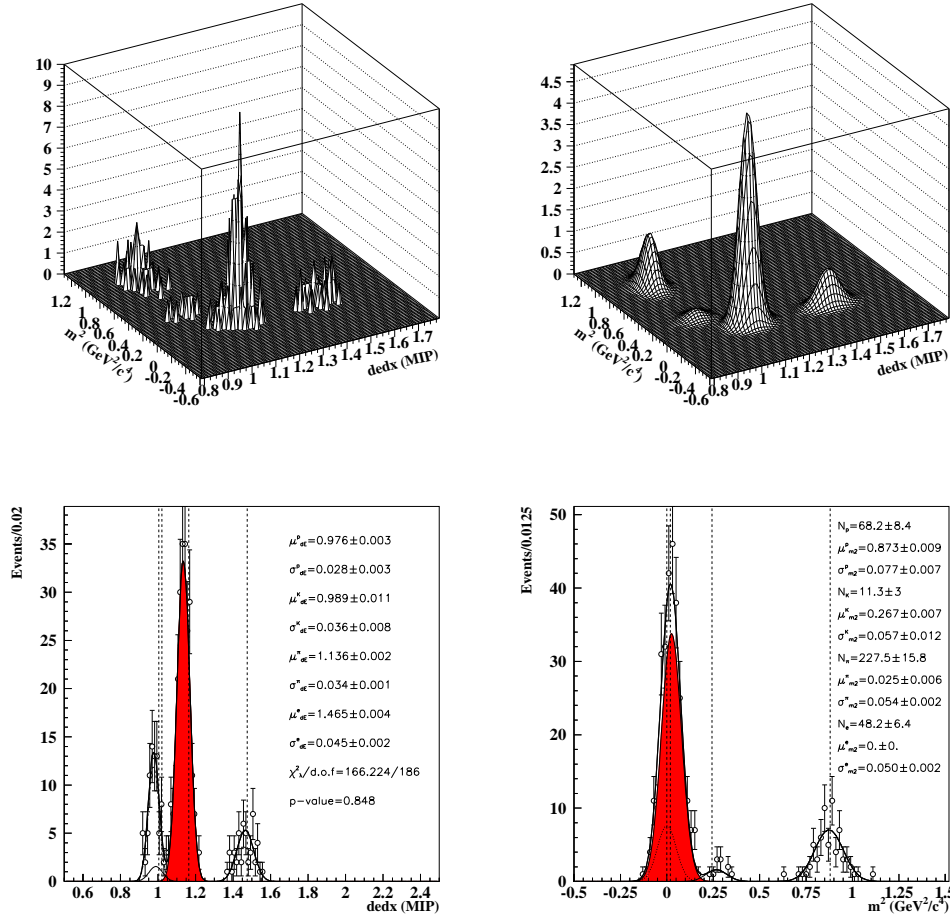


Figure 3.55: Data distribution in the angular bin $40 < \theta < 100$ mrad, momentum bin $2.4 < p < 3.2$ GeV/c and third longitudinal bin (top left), and result of the two-dimensional fit (top right). Projections of the fit (black line) are shown for the dE/dx (bottom left) and mass squared (bottom right) distributions. The pion component is shown in red, the proton component with a dashed line, the kaon component with a plain line and the positron component with a dotted line. The vertical dashed lines show the set values for the position of the peaks. Fitted parameters are given on the plots. The χ^2 (/d.o.f) value is given for χ^2_{λ} with the corresponding p-value.

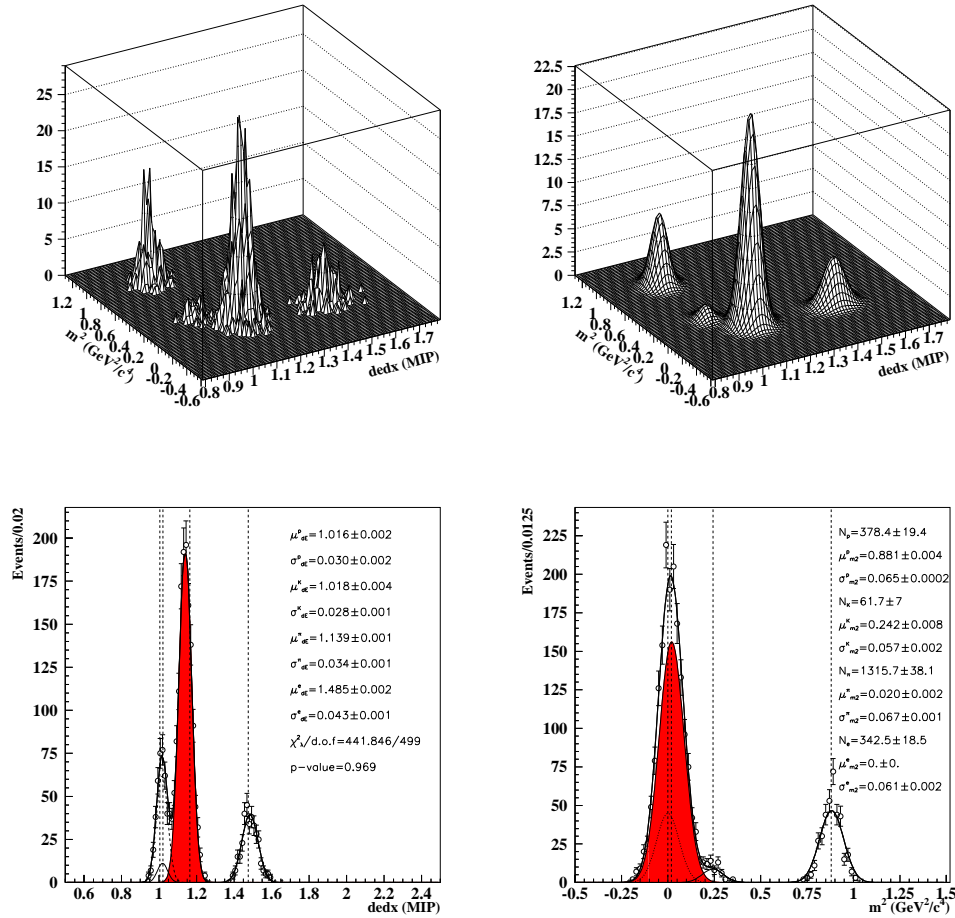


Figure 3.56: Simulated data distribution in the angular bin $40 < \theta < 100$ mrad, momentum bin $2.4 < p < 3.2$ GeV/c and third longitudinal bin (top left), and result of the two-dimensional fit (top right). Projections of the fit (black line) are shown for the dE/dx (bottom left) and mass squared (bottom right) distributions. The pion component is shown in red, the proton component with a dashed line, the kaon component with a plain line and the positron component with a dotted line. The vertical dashed lines show the set values for the position of the peaks. Fitted parameters are given on the plots. The χ^2 (/d.o.f) value is given for χ^2_{λ} with the corresponding p-value.

where the y_i are given by the hypothesis of Eq. 3.13 at their *best-fit* values. For each of the fits we compute the Poisson likelihood χ^2 , while the MINUIT [93] minimization software used for the analysis returns the standard Pearson's χ^2 defined as

$$\chi_P^2 = \sum_{i=1}^N \frac{(n_i - y_i)^2}{y_i} \quad (3.21)$$

It should be noted that this value cannot be used as a goodness-of-fit (g.o.f.) criteria since it does not correspond to the statistic that has been minimized. It simply compares data, seen as Poisson distributed numbers, with its expectation value under the assumption that it is distributed according to the Poisson distribution. Instead, the Poisson likelihood χ^2 defined in Eq. 3.20 can be used to compute a p-value for the fit. Actually, since the χ_λ^2 statistic asymptotically follows a χ^2 p.d.f., the p-value for the hypothesis is given by:

$$p = \int_{\chi_\lambda^2}^{\infty} f(z; n_d) dz \quad (3.22)$$

where n_d is the number of degrees of freedom (d.o.f.) defined as the number of measurements minus the number of fitted parameters.

Raw (uncorrected) yields of positively charged pions in bins of $\{p, \theta, z\}$ are shown in Fig. 3.57 for real data and in Fig. 3.58 for the FLUKA based simulation. The raw yields of positively charged pions and associated statistical and systematic errors normalized to the number of protons on target are summarized in Tables D.1 to D.6 of Appendix D. The distributions of the $\chi_\lambda^2/d.o.f.$ values of the fits and the distribution of the corresponding p-values in data are compared to that of the simulation in Fig. 3.60, top and middle panels. Both in real and simulated data, the $\chi_\lambda^2/d.o.f.$ values are relatively close to unity in the regions of large acceptance and high statistics. At the edge of the binning though, it significantly differs from one. The amplitude of the deviation is larger in the real data due to much lower statistics, which is reflected by the accumulation of entries at low p-value.

For the simulated data, the g.o.f. is further estimated from the difference between the fitted and the true yields in a given $\{p, \theta, z\}$ bin. The distribution of the difference between fitted and true yields, normalized to the fitted yields, is shown in Fig. 3.60, bottom panel. From this distribution, the averaged precision on the extraction of the number of positively charged pions in the simulation is estimated to $\sim 2.3\%$.

The systematic uncertainties related to the particle identification could eventually be estimated by varying different parameters of the fitting procedure (e.g., allowed variation range around initial value, fixing or releasing parameters, etc) taking into account the correlations between all the parameters. However, the 2007 replica target data set being a very low statistics sample, the results of the fit

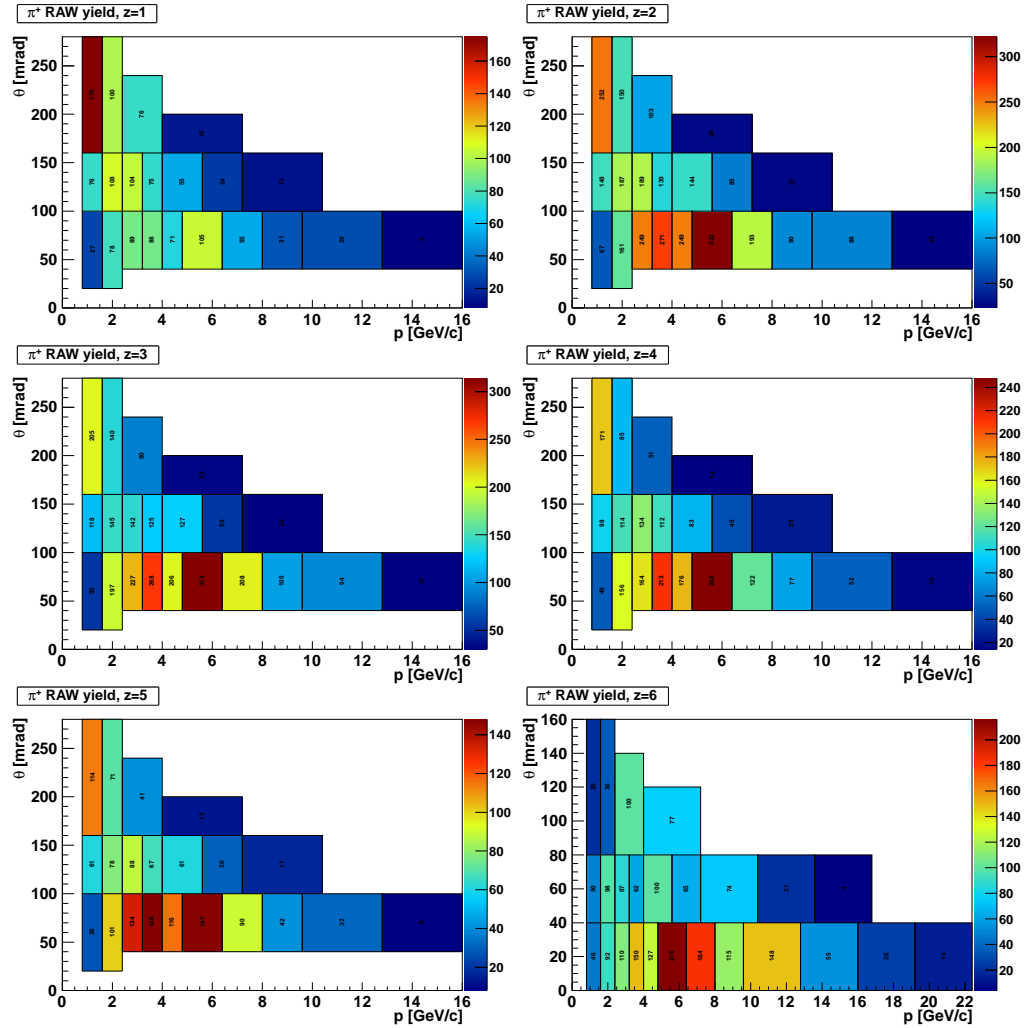


Figure 3.57: Raw π^+ yields extracted from the data in bins of $\{p, \theta\}$ for the 6 longitudinal bins along the target. The most upstream bin is shown on the top left plot, the most downstream one (corresponding to the downstream face of the target) on the bottom right plot.

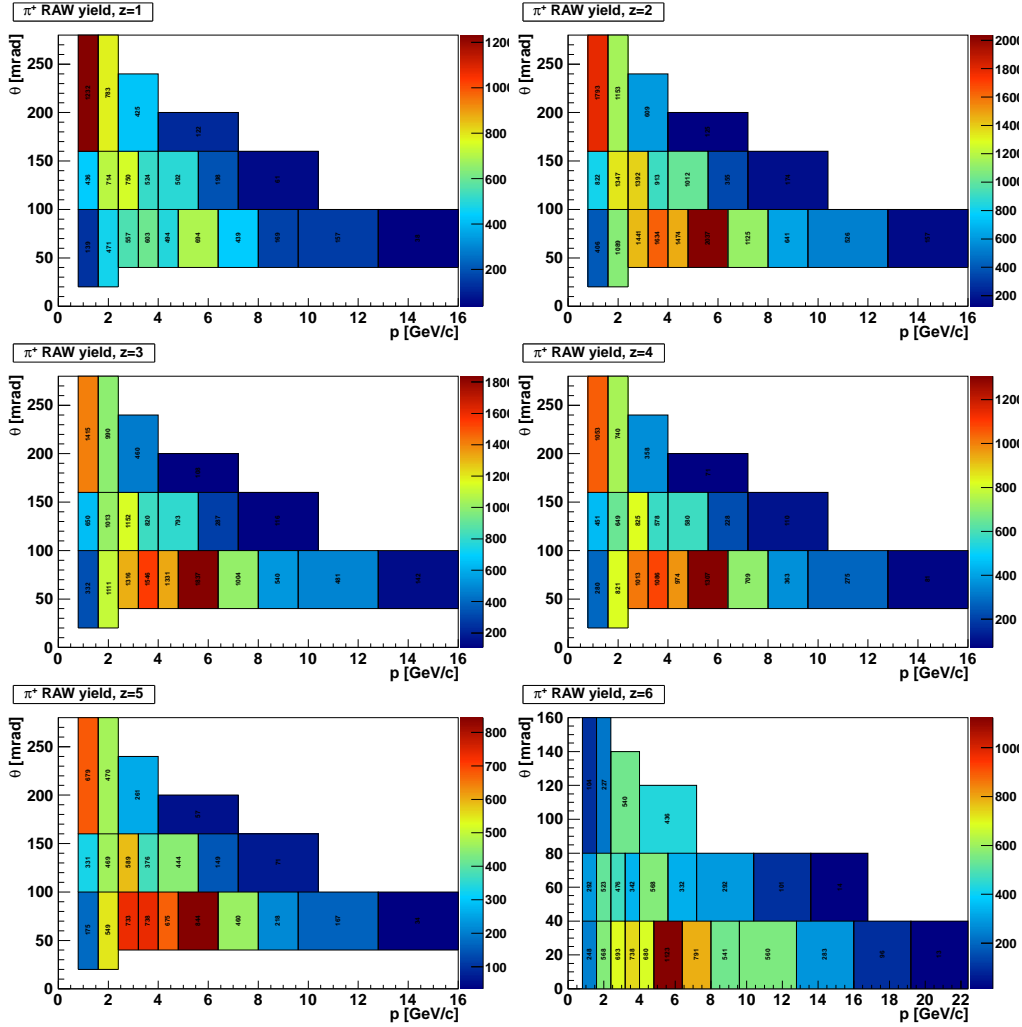


Figure 3.58: Raw π^+ yields extracted from the FLUKA based simulation in bins of $\{p, \theta\}$ for the 6 longitudinal bins along the target. The most upstream bin is shown on the top left plot, the most downstream one (corresponding to the downstream face of the target) on the bottom right plot.

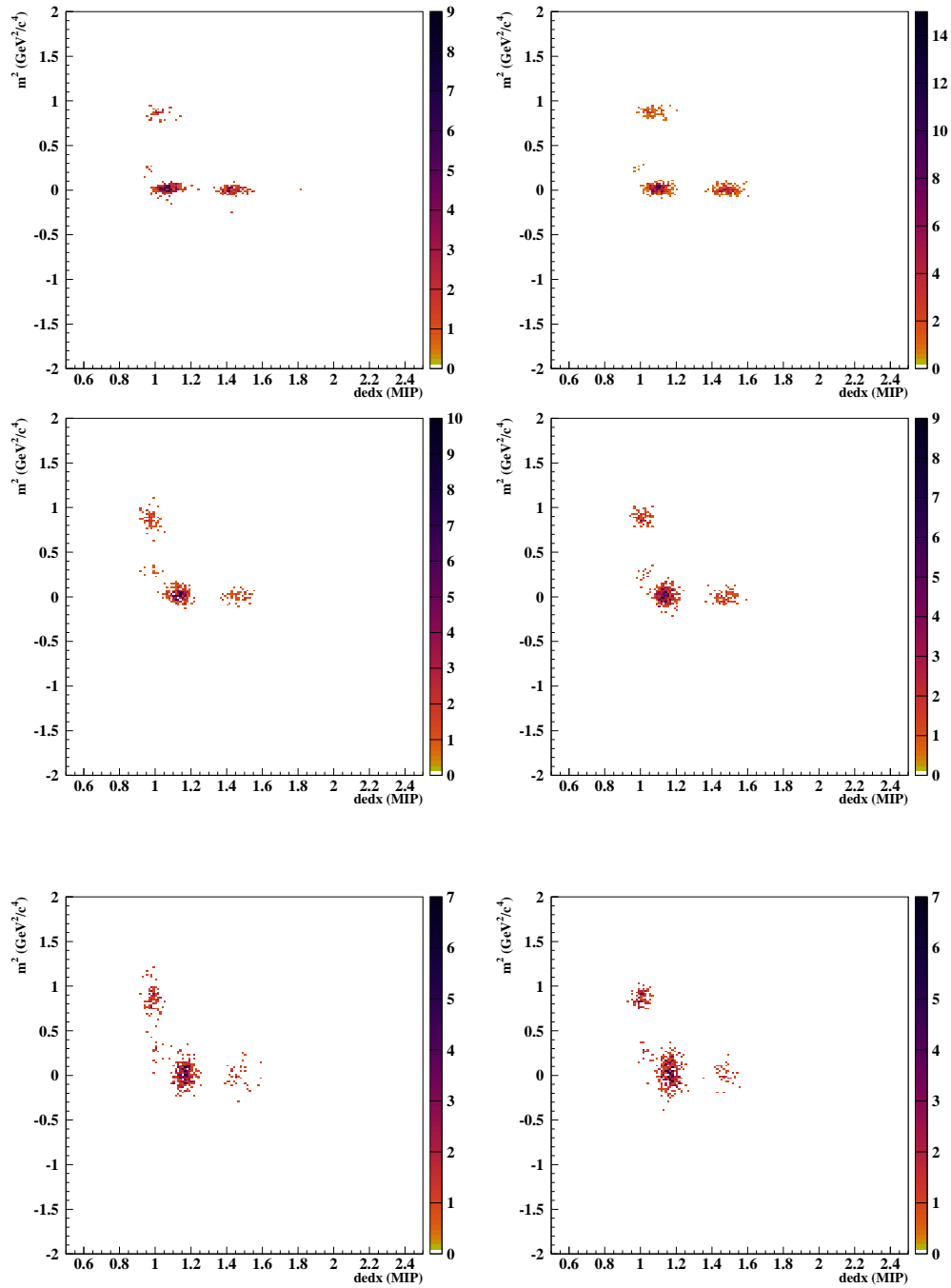


Figure 3.59: Combined $\{dE/dx, ToF\}$ distribution for the angular bin $40 < \theta < 100$ mrad, momentum bin $1.6 < p < 2.4$ GeV/c (top), $2.4 < p < 3.2$ GeV/c (middle), $3.2 < p < 4$ GeV/c (bottom) and third longitudinal bin, for real (left) and simulated (right) data. The simulated data set corresponds to a subsample of statistics comparable with that of data.

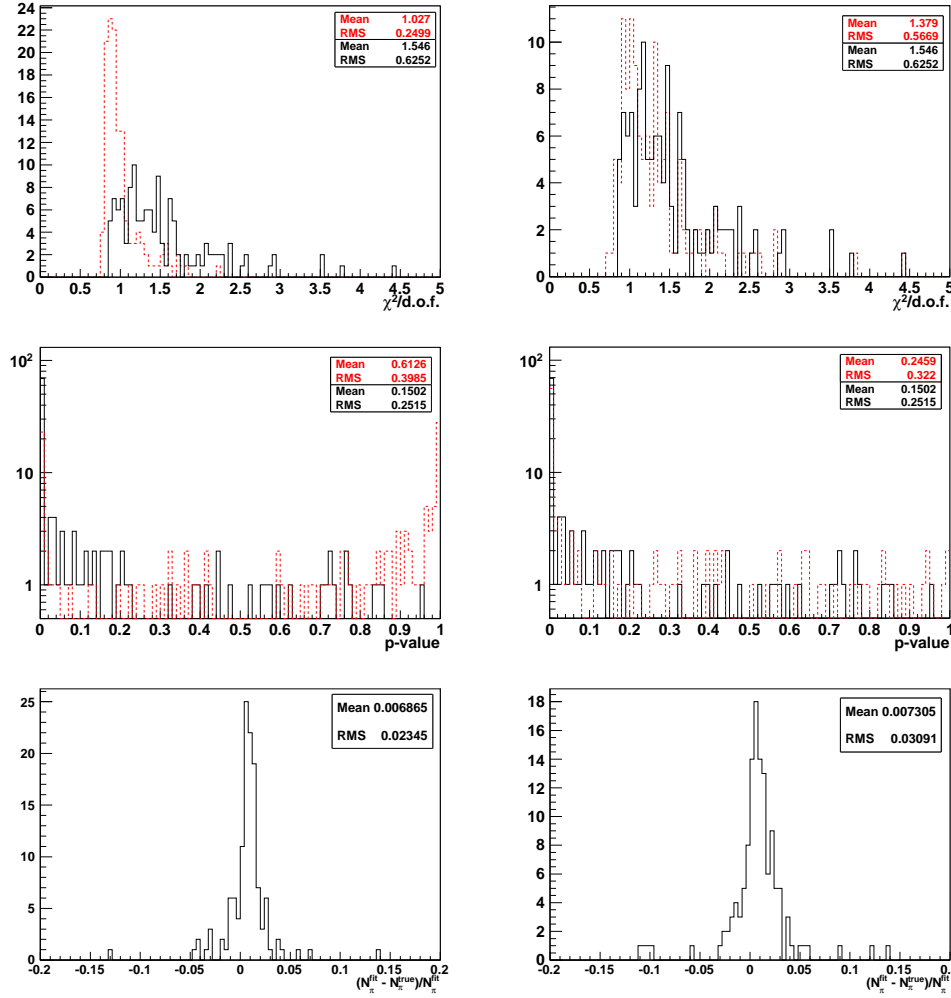


Figure 3.60: $\chi^2_{\lambda}/d.o.f.$ (top) and p-value (middle) distributions for real (plain black histogram) and simulated (dotted red histogram) data from the full statistics sample (left) and a reduced statistics sample (right). The distribution of the difference between the fitted and true positively charged pion yields normalized to the fitted yields is shown in the bottom panel for the full statistics (left) and the reduced statistics (right) samples.

is strongly dependent on the available statistics per bin. The effect of the variation of different combinations of correlated parameters (in terms of extracted pion yield) might be over-estimated due to the fact that the fitted distributions suffer from large statistical fluctuations. Instead of this approach, the systematic uncertainties are estimated from a Monte-Carlo sample with a statistic comparable to that of data. The usage of the simulation for these estimations is validated by the facts that:

- (i) the distributions simulated with low statistics reproduce well the shape of the two-dimensional distributions in real data (e.g. compare Fig. 3.54 and Fig 3.59);
- (ii) the behavior of the fit is also well reproduced, as can be seen from the $\chi^2/d.o.f.$ and p-value distributions compared to that of data in Fig. 3.60, right panels.

The systematic uncertainty attributed to the fitting procedure is defined as the Monte-Carlo based resolution on the fitted number of pions, $(N_{\pi}^{fit} - N_{\pi}^{true})/N_{\pi}^{fit}$. The error is calculated as a function of momentum only since the mass squared and dE/dx parametrizations used to initialize the fits do not depend on the polar angle. Uncertainties are summarized in Table 3.6.

Δp [GeV/c]	0.8-3.2	3.2-8	>8
Data (MC low stat.)	1.6%	2.7%	5.4%
MC (full stat.)	0.8%	1%	4.7%

Table 3.6: Systematic uncertainties related to the particle identification as a function of momentum for data and Monte-Carlo. In both cases errors are estimated from the Monte-Carlo.

In order to compare yields extracted from the data and from the simulation, the latter are normalized to the number of protons on target, N_{pot}^{NA61} for the data and N_{pot}^{FLUKA} for the simulation. In addition, the data is corrected for the time-of-flight efficiency, $\epsilon_{TOF}(p, \theta)$, which is not accounted for in the simulation (see next section). Let $N_{\pi}^{NA61}(p, \theta, z)$ be the number of positively charged pions extracted from the NA61 2007 replica target data in a given $\{p, \theta, z\}$ bin, and $N_{\pi}^{FLUKA}(p, \theta, z)$ be the number of positively charged pions extracted from the FLUKA based simulation in the same bin (these are the quantities depicted in Fig. 3.57 and Fig. 3.58 respectively). To simplify the notation we define

$$\frac{1}{\epsilon_{TOF}^{NA61}} \frac{1}{N_{pot}^{NA61}} \frac{dN_{\pi}^{NA61}}{dp} \equiv \frac{1}{\epsilon_{TOF}^{NA61}} \frac{dn_{\pi}^{NA61}}{dp} \quad \text{and} \quad \frac{1}{N_{pot}^{FLUKA}} \frac{dN_{\pi}^{FLUKA}}{dp} \equiv \frac{dn_{\pi}^{FLUKA}}{dp} \quad (3.23)$$

The dn_{π}/dp spectra from data and simulation are compared in Figs. 3.61 to 3.63 for the 6 longitudinal bins along the target. The dn_{π}^{NA61}/dp values corrected for the time-of-flight efficiency are summarized in Tables F.1 to F.6 of Appendix F. For data and Monte-Carlo, the total error in each bin is the sum in quadrature of the statistical and systematic errors. While for the Monte-Carlo this includes only the statistical and systematic errors from the normalization and the particle identification, it includes also the statistical and systematic uncertainties of the time-of-flight efficiency for the data.

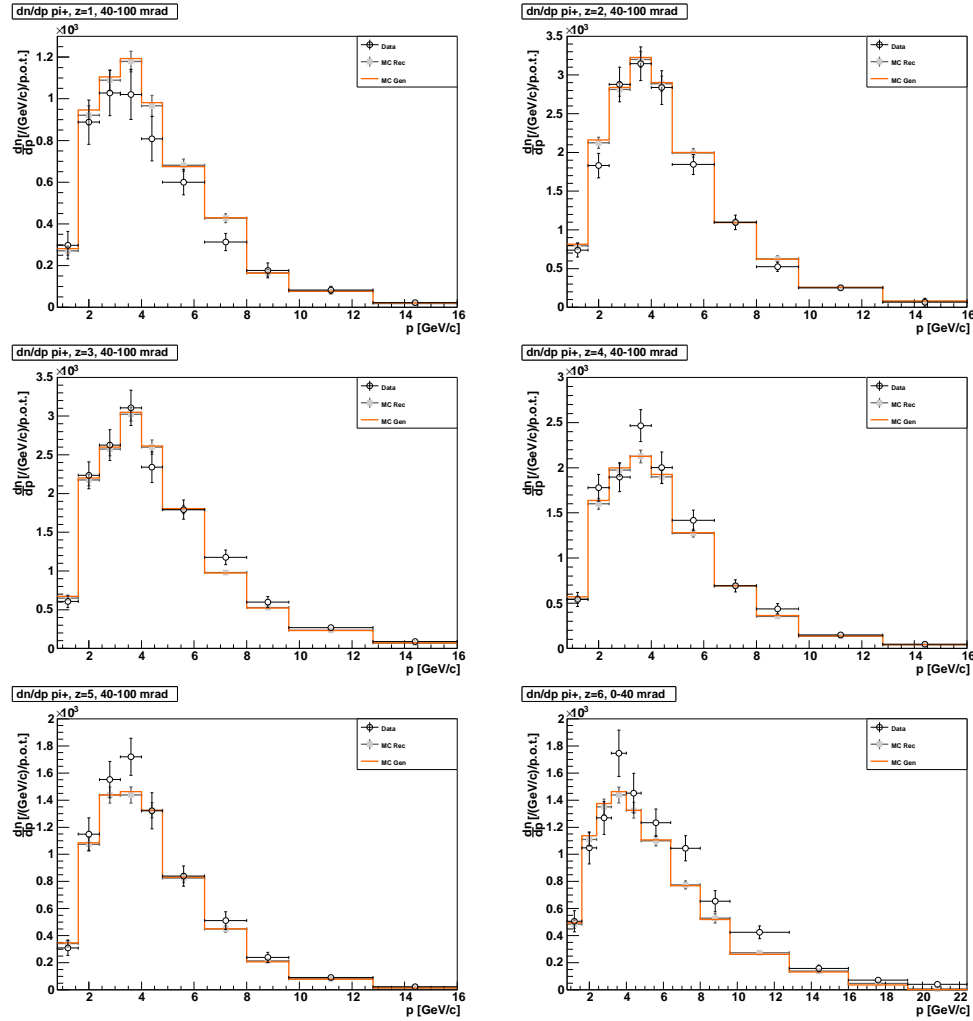


Figure 3.61: Spectra of positively charged pions normalized to the bin size and to the number of protons on target over five longitudinal bins for $[40 - 100]$ mrad, and over the downstream face of the target for $[0 - 40]$ mrad. Error bars for data and Monte-Carlo show the total errors which are the sum in quadrature of the statistical and systematic errors. The orange histograms show the true π^+ yields in acceptance (simulated tracks matched to reconstructed tracks).

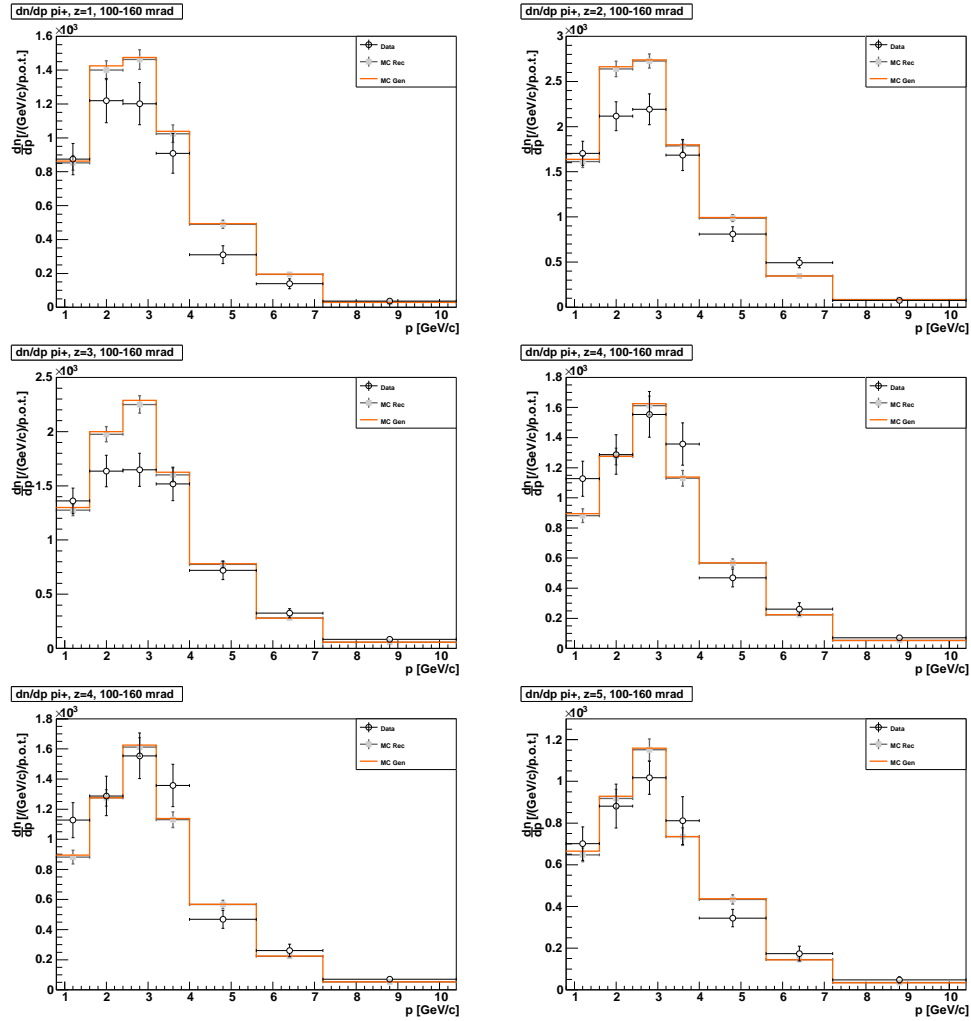


Figure 3.62: Spectra of positively charged pions normalized to the bin size and to the number of protons on target over five longitudinal bins for [100 – 160] mrad, and over the downstream face of the target [40 – 80] mrad. Error bars for data and Monte-Carlo show the total errors which are the sum in quadrature of the statistical and systematic errors. The orange histograms show the true π^+ yields in acceptance (simulated tracks matched to reconstructed tracks).

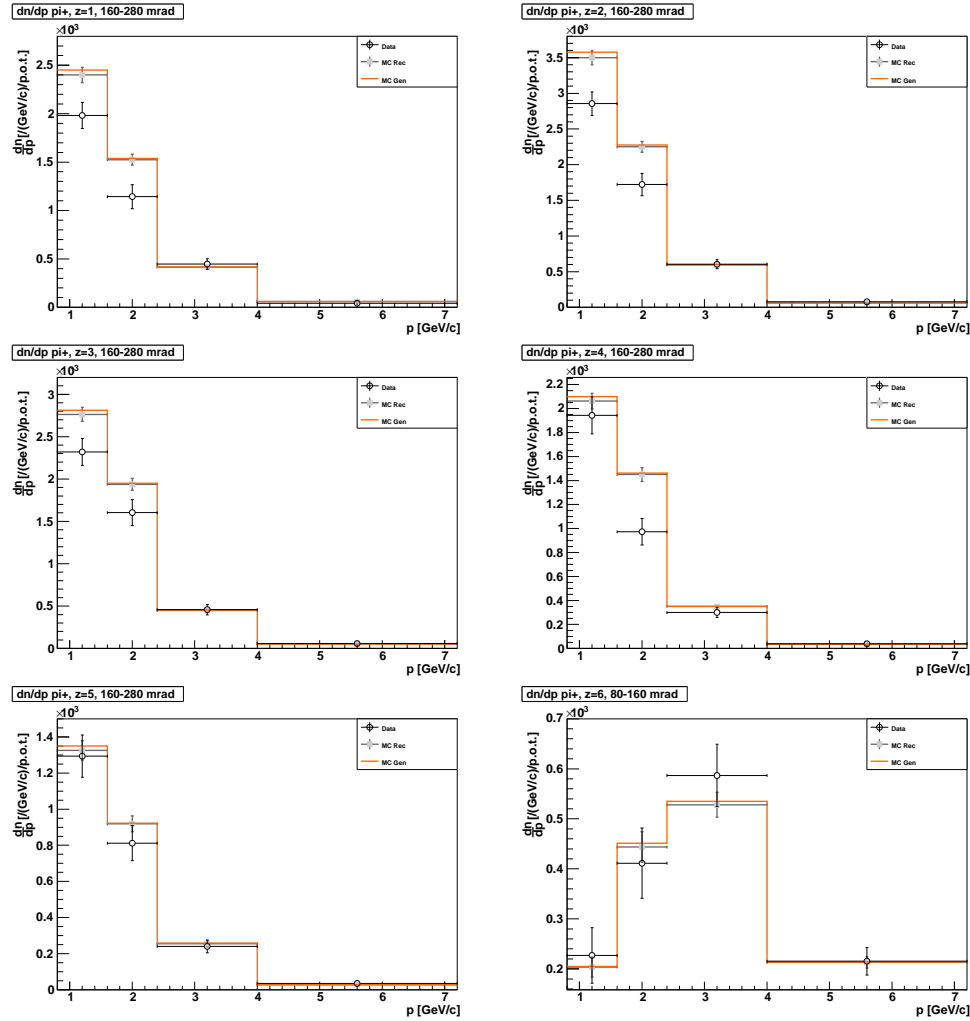


Figure 3.63: Spectra of positively charged pions normalized to the bin size and to the number of protons on target over five longitudinal bins for [160 – 280] mrad, and over the downstream face of the target for [80 – 160] mrad. Error bars for data and Monte-Carlo show the total errors which are the sum in quadrature of the statistical and systematic errors. The orange histograms show the true π^+ yields in acceptance (simulated tracks matched to reconstructed tracks).

3.10 Efficiencies and Corrections

After backward extrapolation to the surface of the target and particle identification, various corrections have to be applied to the positively charged pion spectra extracted from the replica target data. In particular, this includes:

1. acceptance correction, $C_{ACC}(p', \theta', z')$, based on MC;
2. pion loss correction, $C_{LOSS}(p', \theta', z')$, based on MC;
3. feed-down correction, $C_{FDW}(p, \theta, z)$, based on MC;
4. reconstruction efficiency, $\epsilon_{REC}(p, \theta, z)$, based on MC;
5. extrapolation efficiency, $\epsilon_{EXT}(p, \theta, z)$, based on MC;
6. ToF efficiency, $\epsilon_{TOF}(p, \theta)$, based on data;

where (p, θ, z) refers to reconstructed track parameters and (p', θ', z') to simulated track parameters on target. **All these correction and efficiency factors are relevant to extract absolute yields on target. The re-weighting being a relative approach, only corrections that differ from data to Monte-Carlo matter in the calculation of re-weighting factors.**

The acceptance correction has already been discussed in Section 3.7. The pion loss correction includes only the contribution of decays in flight before reaching the ToF-F, since the pion loss due to re-interactions in the material of the detector is already accounted for in the acceptance correction. The feed-down correction accounts for the contamination of pions which do not directly exit from the target but are produced in the decay of strange particles out of the target, or re-interactions in the material of the detector. The reconstruction efficiency is based on global rtracks in the TPCs and estimated independently of the extrapolation to the ToF-F or to the target surface. The backward extrapolation efficiency has been discussed in Section 3.8.

The time-of-flight efficiency is the only correction that is based on data. As it was mentioned in the description of the NA61 simulation chain, there is no digitization of the time-of-flight signal in the Monte-Carlo, so that the detector efficiency is by default 100% in the simulated data. Thus, in order to compare positively charged pion yields extracted from data and Monte-Carlo, the data has to be corrected for the time-of-flight efficiency first. The efficiency is calculated for positively charged global rtracks that fulfill the following requirements:

- (i) the number of points on track satisfies TRK cut(III);
- (ii) the last point in the MTPC is at $z > 680$ cm;

- (iii) the extrapolated position from the last point in the MTPC to the position of the ToF-F along the beam axis is within the transverse fiducial area of the ToF-F.

Points (ii) and (iii) assure that tracks should leave a signal in the ToF-F. For the data analysis, we have shown that the time-of-flight requirement rejects the off-time track background in the TPCs. This background consists in tracks produced from multiple beam proton interactions in the target, sufficiently close to each other in time to be included in the same acquisition window of the TPCs. The ToF-F window being only 100 ns long, all the tracks going through the TPCs and hitting the ToF-F will be off-time, except those that were produced in the interaction of the proton that actually triggered the acquisition. In order to reject this background for the calculation of the time-of-flight efficiency, events with a single beam particle in a $50 \mu\text{s}$ window centered around the beam time are selected by the WFA cut $n_{beam} = 1$. The cut assures at least $25 \mu\text{s}$ between two beam particles, which roughly corresponds to half of the drift time in the MTPCs (~ 1 m for a drift velocity of $\sim 2 \text{ cm}/\mu\text{s}$). Thus, for a given event, off-time tracks might only be present in the upper part of the MTPCs ($y > 0$). Despite the WFA cut, a small contribution of off-time tracks can still be observed at high y values in the MTPCs. To further reject this background, the time-of-flight efficiency is calculated only over the lower part of the MTPCs ($y < 0$), which does not introduce any bias since the ToF-F geometry and readout are symmetric with respect to the horizontal plane ($y = 0$). The efficiency calculated as a function of the track momentum for three angular bins is shown in Fig. 3.64.

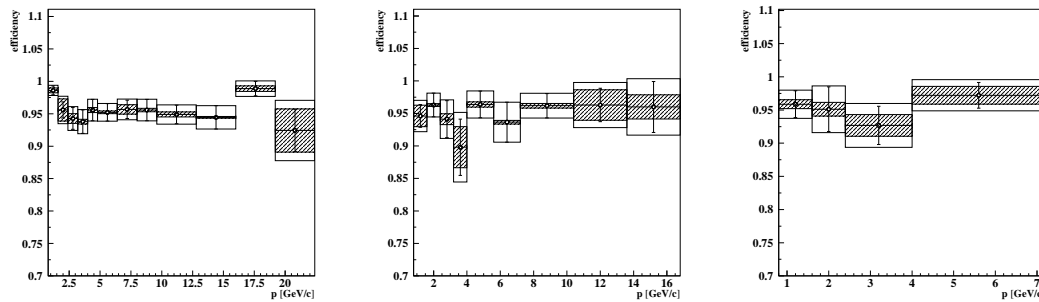


Figure 3.64: Time-of-flight efficiency as a function of momentum for the angular bins $40 < \theta < 100$ mrad (left), $100 < \theta < 160$ mrad (middle) and $160 < \theta < 280$ mrad (right). Error bars show the statistical error, hatched boxes the systematic error and empty boxes the total error (sum of statistical and systematic errors in quadrature).

The systematic uncertainty on the time-of-flight efficiency is defined as the relative variation observed when the calculation is done over the full drift length of the MTPCs or only over half of it. In this way, the systematic uncertainty reflects

the fact that off-time tracks in the MTPCs might still be accounted for in the calculation. Values of the efficiency and corresponding statistical and systematic uncertainties are summarized in Table E.1 of Appendix E.

3.11 Re-weighting factors for the T2K beam simulation

Keeping the notation previously defined for the pion yields and the various efficiencies and corrections, the NA61 re-weighting factor for the FLUKA based T2K simulation in a given $\{p, \theta, z\}$ bin is defined as:

$$w(p, \theta, z) = \frac{n_{\pi}^{NA61}}{n_{\pi}^{FLUKA}}(p, \theta, z) \times \left\{ \frac{C_{ACC}^{FLUKA}}{C_{ACC}^{NA61}}(p', \theta', z') \times \frac{C_{LOSS}^{FLUKA}}{C_{LOSS}^{NA61}}(p', \theta', z') \right. \\ \times \frac{C_{FDW}^{FLUKA}}{C_{FDW}^{NA61}}(p, \theta, z) \times \frac{\epsilon_{REC}^{FLUKA}}{\epsilon_{REC}^{NA61}}(p, \theta, z) \\ \left. \times \frac{\epsilon_{EXT}^{FLUKA}}{\epsilon_{EXT}^{NA61}}(p, \theta, z) \times \frac{\epsilon_{TOF}^{FLUKA}}{\epsilon_{TOF}^{NA61}}(p, \theta) \right\} \quad (3.24)$$

It was shown in Section 3.8 that the longitudinal resolution on target is good enough to constrain the bin migration (bias in $z' \rightarrow z$) below 10%. Resolutions on the extrapolated momentum and polar angle are also small enough compared to the bin size used in the analysis to neglect the bin migration. Thus, although some factors in Eq. 3.24 depend on simulated parameters and some others on reconstructed ones, we omitted unfolding terms (e.g. unfolding matrix $M(p, \theta, z; p', \theta', z')$) that determine the relation between simulated and reconstructed parameters when the latter is smeared by detector resolution effects.

At the exception of the time-of-flight efficiency, all correction factors are calculated from the Monte-Carlo and applied similarly to real and simulated data, i.e. $C^{FLUKA} \equiv C^{NA61}$, $\epsilon^{FLUKA} \equiv \epsilon^{NA61}$. Due to the ratios in Eq. 3.24, all corrections, henceforth all related systematic uncertainties cancel, and the re-weighting factors are simply estimated at the raw data level as

$$w(p, \theta, z) = \frac{1}{\epsilon_{TOF}^{NA61}(p, \theta)} \times \frac{n_{\pi}^{NA61}}{n_{\pi}^{FLUKA}}(p, \theta, z) \quad (3.25)$$

The systematic uncertainties on the re-weighting factors of Eq. 3.25 are attributed to:

- (i) N_{π}^{NA61} and N_{π}^{FLUKA} (fitting procedure);
- (ii) N_{pot}^{NA61} and N_{pot}^{FLUKA} (normalization);
- (iii) ϵ_{TOF}^{NA61} (time-of-flight efficiency);
- (iv) uncertainty on the beam momentum;

The estimation of the systematic errors of points (i) to (iii) has been discussed in previous sections. The systematic error attributed to the beam uncertainty in the data has been estimated from dedicated FLUKA simulations. A first simulation was produced with a beam momentum set at the nominal value of 30.92 GeV/ c and another one with a beam momentum of 30.75 GeV/ c . The latter value corresponds to the mean value of the beam momentum that was measured in the TPCs during a dedicated run. The difference with the nominal value is considered as the maximal possible deviation due to the uncertainty on the beam setting of the NA61 beamline. The positively charged pion production off the target in the two simulations is compared over the analysis binning in $\{p, \theta, z\}$. The observed bin-by-bin variations are constrained below 3%. Since this effect does not produce variations larger than the statistical precision required on the NA61 measurements (5%), the corresponding systematic error is defined as a global error of 3% on the re-weighting factors.

While the previous sources of systematic errors arise from the extraction of positively charged pion yields within the NA61 framework, other systematic uncertainties are identified for potential inconsistencies between the measurements performed in the NA61 environment and the hadron production simulated within the T2K environment. Actually, the target and beam configurations in NA61 and T2K differ with respect to several aspects, including in particular:

1. the target geometry: the NA61 replica target is a simple 90 cm long rod with an upstream mechanical support consisting in Aluminum flanges. The T2K target is a much more complex assemblage of a production rod with mechanical support and surrounding cryogenic structures. However, the NA61 geometry is to be compared to that which is implemented in the standalone FLUKA simulation for JNUBEAM. The latter consists in a bare 90 cm rod identical to that of NA61;
2. the target density: the NA61 replica target has a density of 1.83 g/cm³ while the T2K target has a density of 1.804 g/cm³;
3. the target alignment: the NA61 replica target is shifted and tilted with respect to the beam axis while the T2K target is aligned on the beam;
4. the beam profile and divergence: while the T2K and NA61 beam divergence is of the same order (~ 150 μ rad), the T2K beam profile is much narrower than that of NA61 (see Fig. 3.65).

The effects of the different target geometry, density and alignment have been studied in dedicated FLUKA simulations [94]. For the first point, it was shown that the Aluminum support flanges do not contribute to the measured pion production in NA61 since the beam protons do not diverge enough to hit the upstream mechanical support. Pions produced in re-interactions in the flanges due to backward

scattering of particles produced in the target do not contribute either to the measured yields because the reconstructed tracks are rejected either by the acceptance cuts or by the cut on the point-of-closest-approach on target.

For the second and third points, the positively charged pion production off the target in the T2K and the NA61 configurations is compared over the binning in $\{p, \theta, z\}$ used for the analysis. The bin-by-bin variations between the configurations with different densities are less than 3%. For the alignment study, a first simulation is produced with a tilted target, while a second one is produced with a target aligned on the beam axis and positioned at the center of the overlapping region between the upstream and downstream faces of the target. In both simulations, radial cuts are applied to assure that the beam protons effectively go through the full length of the target. As in the previous case, bin-by-bin variations are constrained below 3%. Moreover, this study showed that the hadron production that occurs in the missing or additional Carbon length along the proton direction due to the target tilts in the NA61 configuration is negligible (up to 1% more or 1% less). Since these two effects do not produce variations larger than the statistical precision required on the NA61 measurements either, the corresponding systematic error is also defined as a global error of 3% on the re-weighting factors.

The beam radial distribution on target was made much larger in NA61 to cover the full section of the target. The radial cuts R cut(I) and R cut(II) introduced in the analysis to deal with the misalignment of the target, actually squeeze the radial distribution. As can be seen in Fig. 3.65, the resulting distribution is much closer to that of the T2K beam. The re-weighting scheme developped in this analysis should in principle account for radial bins in addition to the current binning in $\{p, \theta, z\}$. The 2007 data set, limited in statistics, does not allow for this extra degree of freedom. **At the current stage of the analysis presented in this chapter, the beam re-weighting is not included in the model re-weighting factors as defined in Eq. 3.25.**

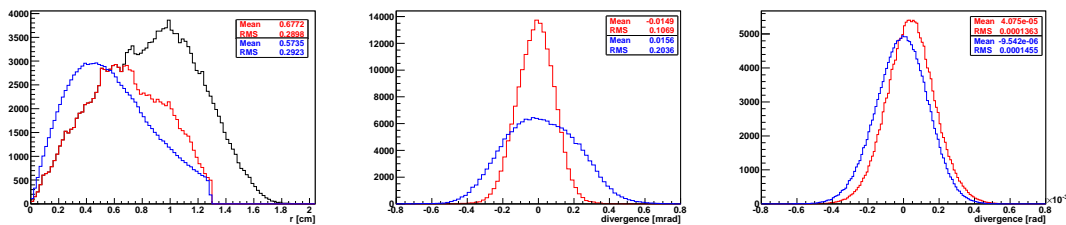


Figure 3.65: Radial distributions (left) of the simulated T2K beam (blue) and the NA61 measured beam with (red) and without (black) selection cuts. The T2K distribution is normalized to the NA61 data. The NA61 (middle) and T2K (right) beam divergence in the x (red) and y (blue) directions.

The calculated re-weighting factors are shown in Fig. 3.66 to 3.68 for the 6

longitudinal bins along the target. Values are summarized in Tables F.1 to F.6 of Appendix F.

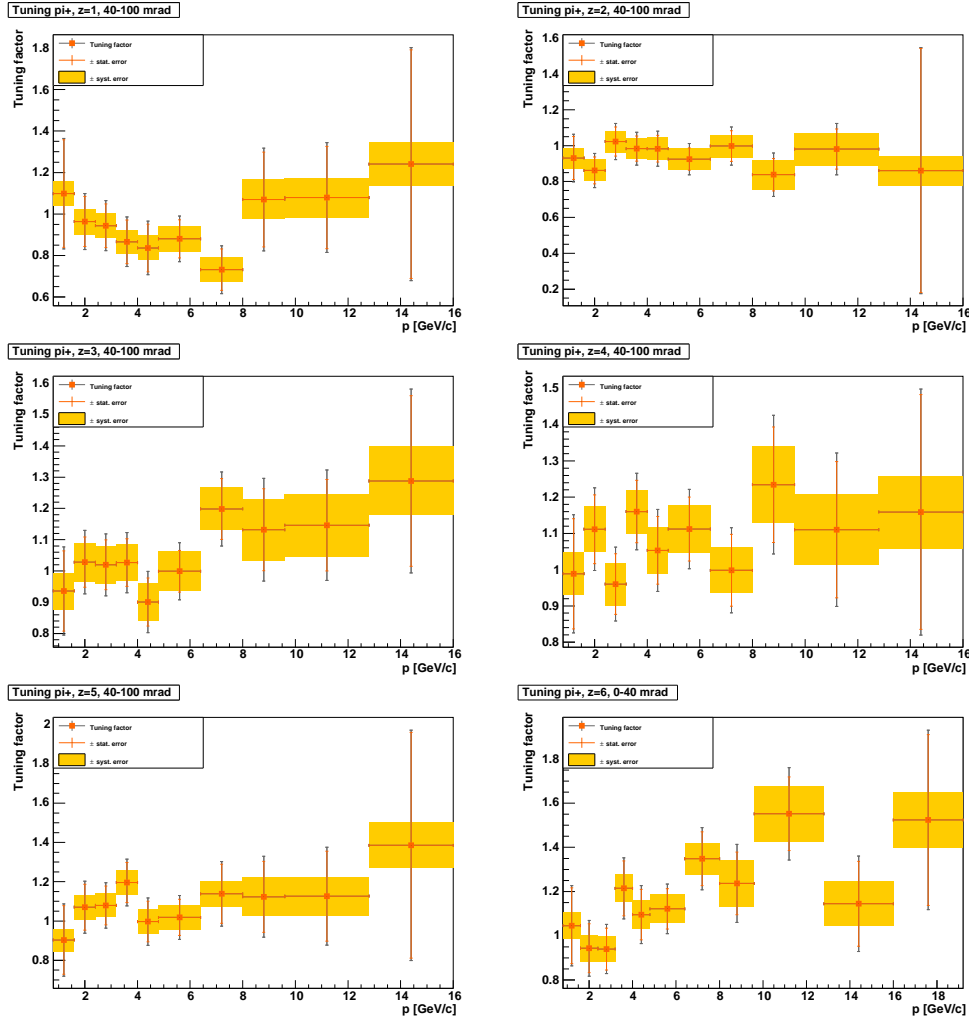


Figure 3.66: Re-weighting factors for positively charged pions over over five longitudinal bins for $[40 - 100]$ mrad, and over the downstream face of the target for $[0 - 40]$ mrad. Total (gray) and statistical uncertainties are shown by error bars, systematic uncertainties by shaded regions.

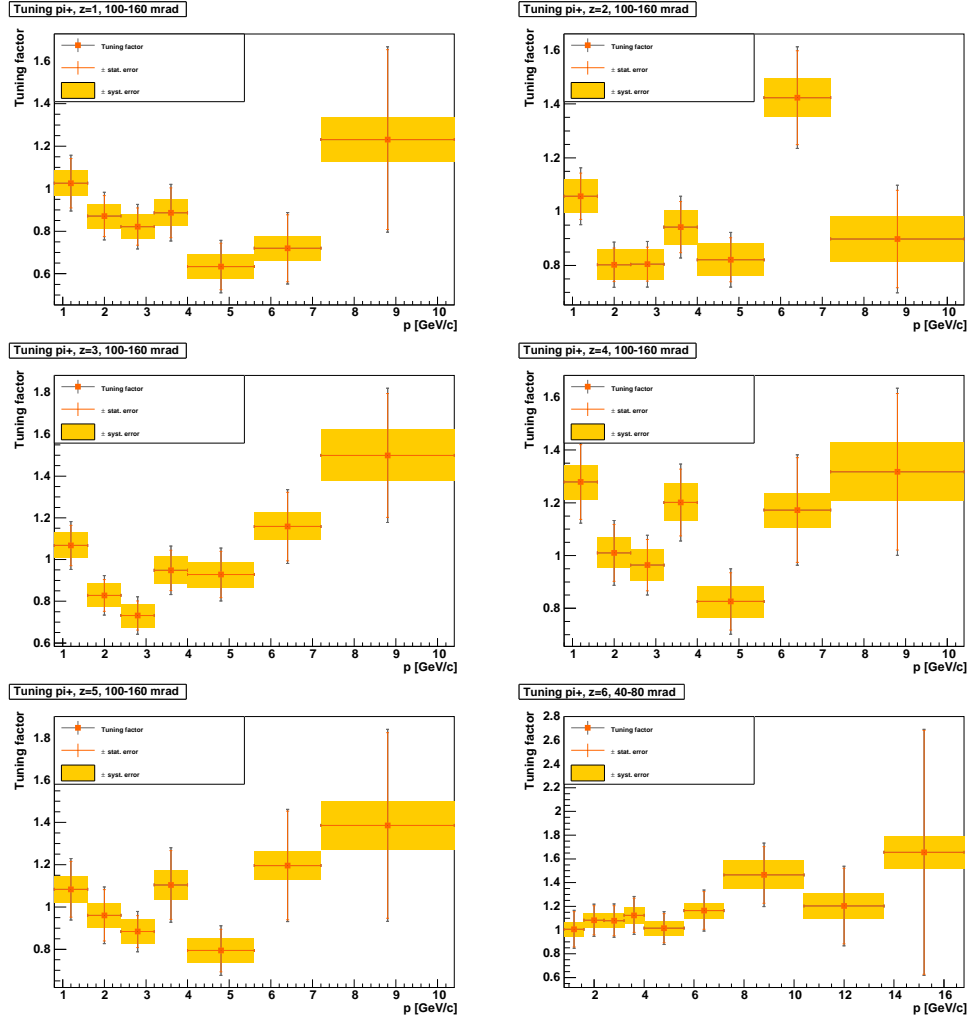


Figure 3.67: Re-weighting factors for positively charged pions over five longitudinal bins for [100 – 160] mrad, and over the downstream face of the target for [40 – 80] mrad. Total (gray) and statistical uncertainties are shown by error bars, systematic uncertainties by shaded regions.

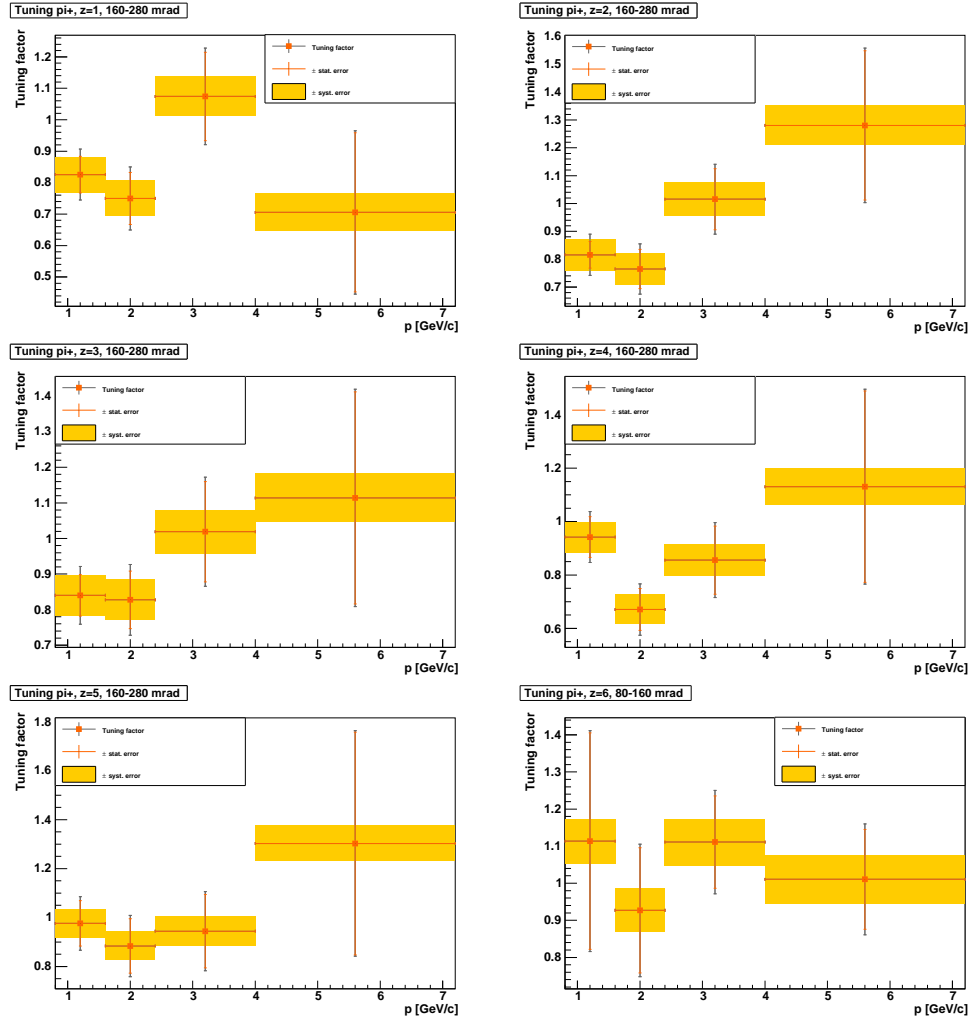


Figure 3.68: Re-weighting factors for positively charged pions over over five longitudinal bins for $[160 - 280]$ mrad, and over the downstream face of the target for $[80 - 160]$ mrad. Total (gray) and statistical uncertainties are shown by error bars, systematic uncertainties by shaded regions.

3.12 Summary of the NA61 replica target data analysis

The analysis of the NA61 replica target data presented in this chapter is based on the following steps:

1. studies of the neutrino fluxes based on the T2K beam simulation (Chapter 2) have shown that π^+ mesons contribute to 95% of the ν_μ flux at SK. About 90% of that contribution is due to pions exiting the production target, the remaining 10% being produced in re-interactions in the elements of the beamline. More than 50% of the ν_e flux comes from muons produced in the decay of the same pions. The flux prediction is sensitive to the pion phase space on target, both in $\{p, \theta\}$ and longitudinal position on target, z . **Thus, π^+ yields extracted from the NA61 replica target data in bins of $\{p, \theta, z\}$ can eventually be used to constrain the simulated pion production off the T2K target and, consequently, constrain up to 90% of the ν_μ flux prediction of the T2K beam simulation;**
2. taking the NA61 acceptance into account, estimations of the required statistics of the NA61 measurements with the long target to fulfill the T2K goals in terms of precision on the absolute neutrino flux and far-to-near ratio predictions have been made (Chapter 3, Section 3.2). **A 5% precision on the NA61 measurements constrains the flux and far-to-near ratio predictions in T2K below 5 and 3% respectively (this estimation does not include other T2K proton beam and beamline related uncertainties);**
3. long target data were taken in 2007, 2009 and 2010. The 2007 data set is used to produce the results presented in this Chapter. **This data set is very limited in statistics and results should be considered accordingly as a first attempt and proof of principle that this type of data can actually be extracted and used for flux predictions.** In a second stage, the 2009 and 2010 data sets can be used to refine the current analysis and provide more precise results;
4. **the NA61 simulation and reconstruction chains have been modified for more compatibility with the T2K beam simulation.** The main modifications include the implementation of the T2K hadronization model (based on the same interface code to the FLUKA model), the simulation of the NA61 beam on target, particle identification for simulated data and reconstruction of the TPC tracks at the surface of the replica target in bins of $\{p, \theta, z\}$ (Chapter 3, Section 3.3 and 3.4);
5. **the latter modifications allow to compare the T2K hadronization model to data directly within the NA61 simulation and reconstruction chains, i.e. reconstructed π^+ yields are compared at the raw**

data level prior to any corrections necessary to obtain absolute spectra. Doing so, on one hand, systematic uncertainties attributed to the particle identification procedure are estimated for both real and simulated data; on the other hand, all the systematic uncertainties related to the Monte-Carlo based corrections that are needed to get absolute pion spectra for comparison to simulated true yields, are avoided. The uncertainty on the data to Monte-Carlo re-weighting factors, attributed to the extraction of the pion yields within the NA61 framework, includes only statistical and systematic errors related to the normalization per p.o.t., the particle identification and the time-of-flight efficiency in the data (Chapter 3, Section 3.9 to 3.11);

6. **additional global systematic errors are estimated to account for differences in the NA61 and T2K target configurations** (Chapter 3, Section 3.11);
7. the main contributions to the systematic uncertainty of the re-weighting factors are from the particle identification in the high momentum region and the uncertainty on the target alignment with respect to the beam axis. In the 2009 and 2010 data sets, the total uncertainty will be constrained below 5% mainly because of a better control of the target alignment. The much larger statistics of these data sets will also reduce the uncertainty on the particle identification and time-of-flight efficiency in the data. For comparison, the total systematic uncertainty on the positively charged pion yields extracted from the NA61 2007 thin target data sums up to $\sim 5\text{-}10\%$ [82] depending on $\{p, \theta\}$, including uncertainties on the time-of-flight and reconstruction efficiencies, acceptance, feed-down and pion loss corrections. Computing re-weighting factors for the long target data using absolute spectra after all the necessary corrections (that account in addition for uncertainties on the backward extrapolation) are applied would yield a total uncertainty much larger than 5%. **The current uncertainties on the re-weighting factors presented in this chapter are dominated by the statistical uncertainties which are of the order of $\sim 10\text{-}15\%$, while the systematic uncertainties are typically of the order of 6%.** Systematic uncertainties are summarized in Table 3.7;
8. to use the NA61 based re-weighting factors in the T2K beam simulation, the latter is modified to be compatible with the output of the NA61 analysis (Chapter 4), i.e. neutrinos at the near and far detectors must be linked to particles exiting the production target and flux predictions weighted accordingly;
9. **the current NA61 based re-weighting factors account only for the hadronization model correction.** The re-weighting should also account for the different beam profile in T2K. The latter point is currently neglected

due to the poor statistics of the 2007 data. The 2009 and 2010 data sets have much larger statistics and, in addition, include different beam trigger configurations that allow to select a beam profile close to that of T2K.

Systematic error	dependence	estimation	value
Particle identification	p	MC	1-5%
Normalization	global	Data	1.4%
ToF efficiency	(p, θ)	Data	$< 3\%$
Beam momentum	global	MC	$< 3\%$
Target density	global	MC	$< 3\%$
Target alignment	global	MC	3%

Table 3.7: Systematic uncertainties on the re-weighting factors. Only sources of errors that do not cancel in the calculation of the re-weighting factors are listed.

Chapter 4

Re-weighting based on the NA61/SHINE replica target data

4.1 Target geometries

In this section, the target geometries in the T2K and NA61 simulations are reviewed in more details to clearly define which contribution of hadrons can be re-weighted with the results presented in the previous chapter.

The T2K target, depicted in Fig. 4.1, is a complex assemblage of Carbon pieces that form the production rod and part of its support (summing up to 90 cm), with surrounding mechanical pieces that constitute the cooling system. The material budget around the production rod includes Helium, Carbon and Titanium. The cooling envelope of the target is embedded in the first magnetic horn of the focusing system, close to the surrounding inner conductor made out of Aluminum.

Hadrons produced in the interactions of the beam protons in the Carbon rod will eventually escape the target, and some of them will interact afterward in the surrounding material before they can be focused. These re-interactions in the cooling envelope and conductor of the horns constitute secondary sources of neutrino production. In an ideal case, measurements with a perfect replica of the T2K target including the cooling envelope, would also constrain this contribution. However, mainly due to cost and time reasons, a complete full-size replica of the T2K target could not be produced for the NA61 measurements. Instead, the NA61 replica target simply consists of a bare 90 cm Carbon rod with an upstream mechanical support consisting of Aluminum flanges (see Fig. 4.1, middle panel). In terms of neutrino production, this simplified target turns out to be a fairly good approximation of the complete geometry for the two following reasons:

- as it was shown in Chapter 2, a fraction of $\sim 90\%$ of both ν_μ and ν_e fluxes is due to the decay of (daughters of) hadrons produced in the Carbon rod;

- as mentioned in Chapter 3, dedicated FLUKA simulations of the NA61 replica target including the upstream mechanical support have shown that the Aluminum flanges do not contribute to the measured production of positively charged pions.

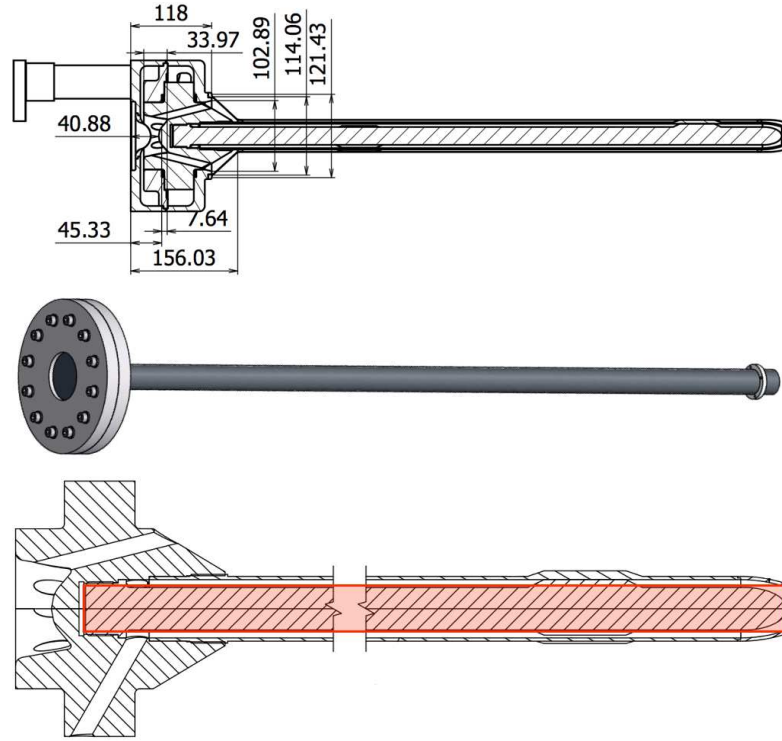


Figure 4.1: Simulated geometry of the T2K target in JNUBEAM (top), replica target in GNA61 (middle), and simplified geometry in the FLUKA simulation (bottom) for JNUBEAM (represented as a red rectangle overlaid on the complete geometry).

For consistency with the NA61 measurements, the simulated target geometry in the FLUKA simulation that provides input to JNUBEAM is limited to a simple 90 cm rod, while the full geometry is implemented in JNUBEAM. Fig. 4.1 (bottom panel) shows how the two geometries overlap. The overall Carbon budget is the same to a very good approximation. Some small local differences can be noted at the very upstream and downstream parts of the production rod due to the more sophisticated geometry of the real target (e.g. the hemisphere at the downstream end of the rod is approximated to a plane, which places Carbon where normally Helium should stand). Hadrons exiting the simplified target in the FLUKA simulation are further tracked by Geant3 in the JNUBEAM geometry. Re-interactions in the immediate surrounding material and other elements of the beamline are simulated by the GCALOR model.

The NA61 re-weighting factors calculated for the positively charged pions apply to any outgoing positively charged pion simulated by FLUKA in the coverage of the NA61 measurements, whether it decays or re-interacts in the elements of the beamline while being propagated through the JNUBEAM geometry.

4.2 Re-weighting classes

The existing framework for the tuning of the T2K neutrino fluxes with the NA61 thin target data, developed by the T2K Beam Group, is based on the information which is stored on output of the combined FLUKA and JNUBEAM simulations. For each neutrino this includes in particular:

- the neutrino energy at the near and far detectors;
- a weight that accounts for the branching ratio of the parent decay, the probability to be emitted in the LAB system in the direction of the near and far detectors, and the normalization to 10^{21} p.o.t.;
- the PID, kinematics and position of the parent at creation and decay points;
- the list of ancestors back to the outgoing track of the FLUKA simulation;
- the list of ancestors in the target simulated by FLUKA, from the outgoing track back to the beam proton track.

The lists of ancestors in the last two points include the kinematics and positions of each ancestor at creation vertex, as well as the integrated path length through the different materials the ancestor went through during propagation. This last information is needed to tune the interaction probability of p , n , π^\pm and K^\pm in Carbon and Aluminum (main materials surrounding the target) for interactions handled by the GCALOR model out of the target. Dedicated studies have shown a good agreement of the FLUKA production cross sections to existing data for p , n , π^\pm and K^\pm on Carbon at relevant momenta below 30 GeV/ c , so that no tuning of cross sections and interaction probabilities is applied inside the target, where interactions are handled by FLUKA.

The thin target based tuning is done via classes specific to each contribution:

1. the *NA61Weight.cc* class handles the tuning of secondary and tertiary charged pions with the NA61/SHINE data;
2. the *KaonWeight.cc* class handles the tuning of secondary and tertiary charged kaons based on the NA61/SHINE [82], Eichten [95] and Allaby [96] data, also using data interpolation [74] to regions out of the data coverage;

3. the *XsecWeights.cc* class handles the tuning of production cross sections and interaction probabilities out of the target.

The tuning of tertiary pions (kaons) is applied to pions (kaons) produced in the re-interaction of secondary nucleons (isospin symmetry of the pC and nC data is assumed for neutrons) in Carbon using a transformation of the original NA61/SHINE thin target weights in (p, θ) to weights in (x_F, p_T) assuming scaling of the production multiplicities with \sqrt{s} . Re-interactions of nucleons out of the target in Aluminum are tuned with the NA61/SHINE thin target weights after using an A -scaling (from Carbon to Aluminum) of the original weights based on a parametrization in x_F and p_T derived from fits to existing data. A complete description of the whole tuning procedure and its latest updates are given in [97].

In the current version of the code, errors on the kaon tuning are not propagated yet to the final flux, so that in what follows, error symbols refer to the charged pion and out-of-target tuning contributions only. The original *NA61Weight.cc* class has been slightly modified in order to restrict the tuning of secondary and tertiary pions to the forward production ($\cos\theta > 0$) and to primary proton interactions inside the target (maximal effect on the nominal tuning is of 0.4%). The tuned ν_μ flux at SK is shown in Fig. 4.2.

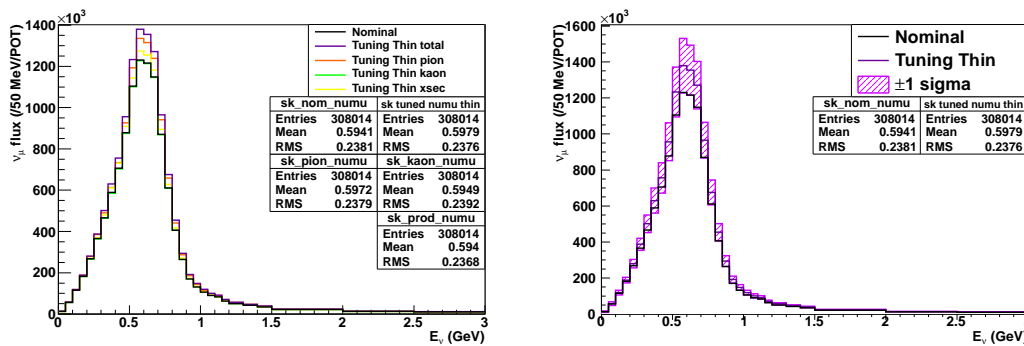


Figure 4.2: Contributions to the thin target based ν_μ flux tuning at SK up to 3 GeV (left). Tuned ν_μ flux at SK (right). The black histogram shows the nominal ν_μ flux at SK. The hatched area around the tuned flux (violet) shows a $\pm 1\sigma$ uncertainty band.

The comparison of the thin target based tuning to that based on the NA61/SHINE long target data can be done at two levels:

- (i) at the level of the neutrino flux at the near and far detectors in JNUBEAM;
- (ii) at the level of the yields of hadrons exiting the target in the FLUKA standalone simulation used as input to JNUBEAM.

In order to apply the re-weighting factors calculated from the replica target data to the flux prediction in JNUBEAM, the following set of information has been included on output of the simulation:

- the PID of the ancestor exiting the target;
- the exit position on target and corresponding longitudinal bin number of the NA61/SHINE long target analysis;
- the momentum of the ancestor on target;
- the angle between the direction of the ancestor and the beam axis on target.

The *ReplicaWeight.cc* class has been implemented on top of the current tuning framework to propagate the NA61/SHINE long target re-weighting factors to the neutrino fluxes. For each neutrino event, the tuning is applied in the following steps:

- (i) check that the outgoing ancestor is a positively charged pion;
- (ii) check that the corresponding $\{p, \theta, z\}$ parameters on target are within the NA61 long target analysis coverage;
- (iii) if the outgoing ancestor is a positively charged pion and is out of coverage, assign a tuning factor of 1. and an error of 15% (roughly in the order of the error assigned in coverage);
- (iv) if the outgoing ancestor is not a positively charged pion, assign a tuning factor of 1. and an error of 0.

The corresponding tuned ν_μ flux at SK is shown in Fig. 4.3. The tuning factor as a function of the neutrino energy is compared to that of the thin target based tuning in Fig. 4.4. **From these current and preliminary comparisons, it can be seen that both tunings are consistent within the current uncertainties.**

Let us note that the current comparison does not include the re-weighting of the NA61/SHINE beam profile on target to that of T2K (for statistics reasons, the NA61/SHINE long target data were not binned according to the beam parameters on target). However, we do not expect a significant effect from the different beam profiles on target: the beam cuts developed for the long target analysis constrain the beam distribution on target in NA61/SHINE to a profile that does not differ significantly in shape from that of T2K (see Fig. 3.65).

We also checked that the observed differences with the thin target based tuning cannot be attributed to a different phase space coverage of the NA61/SHINE thin target and long target data analyses. Actually, while the thin target data analysis fully covers the phase space of secondary pions producing neutrinos in the

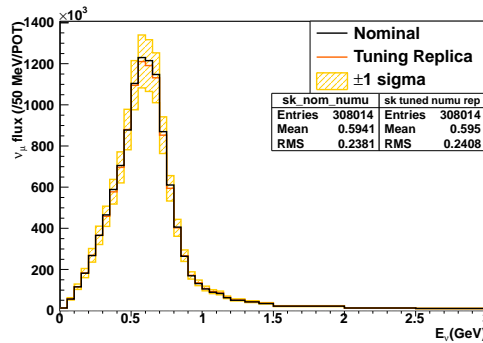


Figure 4.3: Tuned ν_μ flux at SK based on the NA61 replica target data up to 3 GeV. The Black histogram shows the nominal ν_μ flux and the hatched area around the tuned flux (orange) shows a $\pm 1\sigma$ uncertainty band.

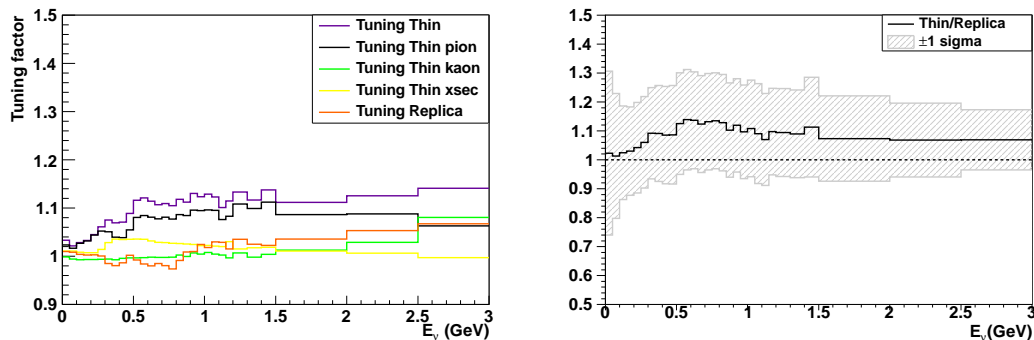


Figure 4.4: Thin and replica target tuning factors as a function of neutrino energy for the ν_μ flux at SK (left) and corresponding ratio (right). The hatched area around the tuning ratio shows the uncertainty band that corresponds to $\pm 1\sigma$ uncertainty on both tunings. No beam re-weighting is included in these comparisons.

direction of SK, the long target analysis coverage might still miss corners of the phase space of interest for outgoing pions that produce neutrinos at SK. As shown in Fig. 4.5, positively charged pions exiting the target within the following regions of the kinematical phase space are not re-weighted:

- $2.4 < p < 16$ GeV/ c , $\theta < 40$ mrad and $z \leq 5$;
- $0.8 < p < 1$. GeV/ c , $280 < \theta < 400$ mrad for $z \leq 5$ and $160 < \theta < 400$ mrad for $z = 6$.

Below 40 mrad, Fig. 4.5 shows as well that most of the outgoing pions exit the target from the downstream face so that this contribution is actually largely covered in the long target analysis. To check the impact of the currently uncovered

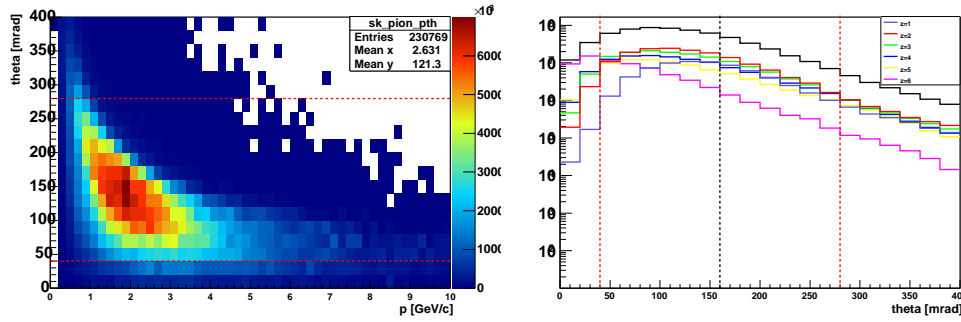


Figure 4.5: $\{p, \theta\}$ phase space of positively charged pions exiting the target and producing neutrinos at SK (left), and corresponding angular distribution (right) as a function of the outgoing position on target. Red dashed lines show the current angular coverage of the NA61 long target analysis for the first 5 longitudinal bins. The dashed black line shows the upper of the analysis coverage for the downstream face of the target.

regions of the phase space, the nominal unit weight of the corresponding outgoing pions was increased (decreased) by $+(-)20\%$. As a result (see Fig. 4.6), the long target tuning varies only within 1% below 3.5 GeV neutrino energy. Thus, the contribution of positively charged pions exiting the target out of the current analysis coverage of the NA61/SHINE long target data cannot explain the differences observed between the thin and long target based tunings.

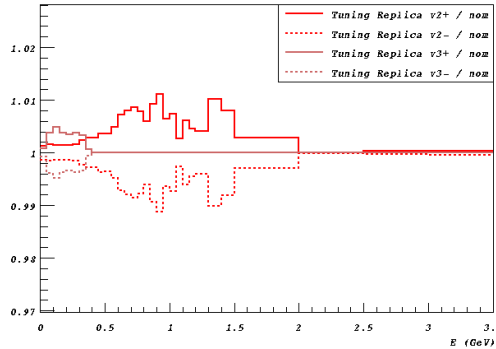


Figure 4.6: Ratio of modified long target π^+ tuning below 40 mrad (red) and at large angle below 1 GeV/c (light red) to nominal tuning shown up to 3.5 GeV neutrino energy. Plain (dashed) histograms correspond to a re-weighting increased (decreased) by $+(-)20\%$.

As mentioned previously, the effect of the hadron production tuning based on either the NA61/SHINE thin or long target data can also be estimated at the level of the FLUKA standalone simulation. The advantage is that at this level the effect on the different regions of the kinematical phase space in (p, θ) becomes obvious, while it is somewhat averaged out in terms of neutrino energy due to

the kinematical properties of the off-axis beam configuration. A dedicated class was developed to re-weight the yields of positively charged pions exiting the target following the exact procedure developed for the thin target and that developed for the long target. An example is shown in Fig. 4.7 that depicts how the nominal FLUKA prediction is changed in both cases.

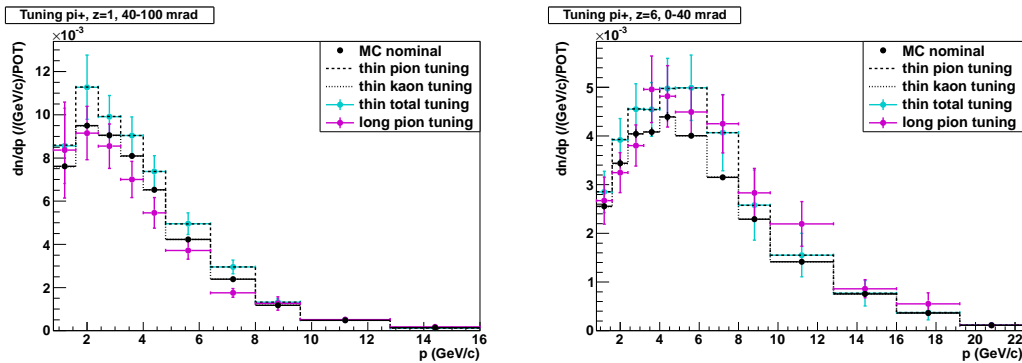


Figure 4.7: Nominal FLUKA prediction for yields of positively charged pions exiting the target along the first longitudinal bin for $40 < \theta < 100$ mrad (left), and through the downstream face of the target for $0 < \theta < 40$ mrad. Cyan points show the prediction tuned with the NA61/SHINE thin target data, purple points the prediction tuned with the NA61/SHINE long target data.

Within this new re-weighting class, we further developed methods that allow to compare both thin and long target based tunings to the NA61/SHINE long target data directly. The goals are to understand if the current thin target based procedure correctly accounts for secondary interactions within the target, and if the current long target tuning reproduces the original data.

The comparison procedure is based on a *mask* that reproduces the acceptance of NA61/SHINE (at the reconstruction level) in the FLUKA standalone simulation. Actually, as already stressed in the previous chapter, the long target data consists of raw spectra that do not account for any common correction to data and Monte-Carlo, in particular acceptance and feed-down corrections. Rather than estimating corrections to provide absolute spectra (with potential over or under-estimation of the corrections), the nominal FLUKA predictions are masked to reproduce the effect of the NA61/SHINE acceptance. The re-weighted predictions are compared to the full long target data coverage in Figs. 4.8, 4.9 and 4.10.

A few comments can be made about these comparison plots:

1. the fact that the NA61/SHINE Monte-Carlo (FLUKA input + GCALOR out of target) agrees with the reconstructed Monte-Carlo simply shows that the number of pions extracted after reconstruction and PID is correct (uncertainty on the PID is about 2-3%);
2. the agreement between the NA61/SHINE Monte-Carlo and the nominal FLUKA

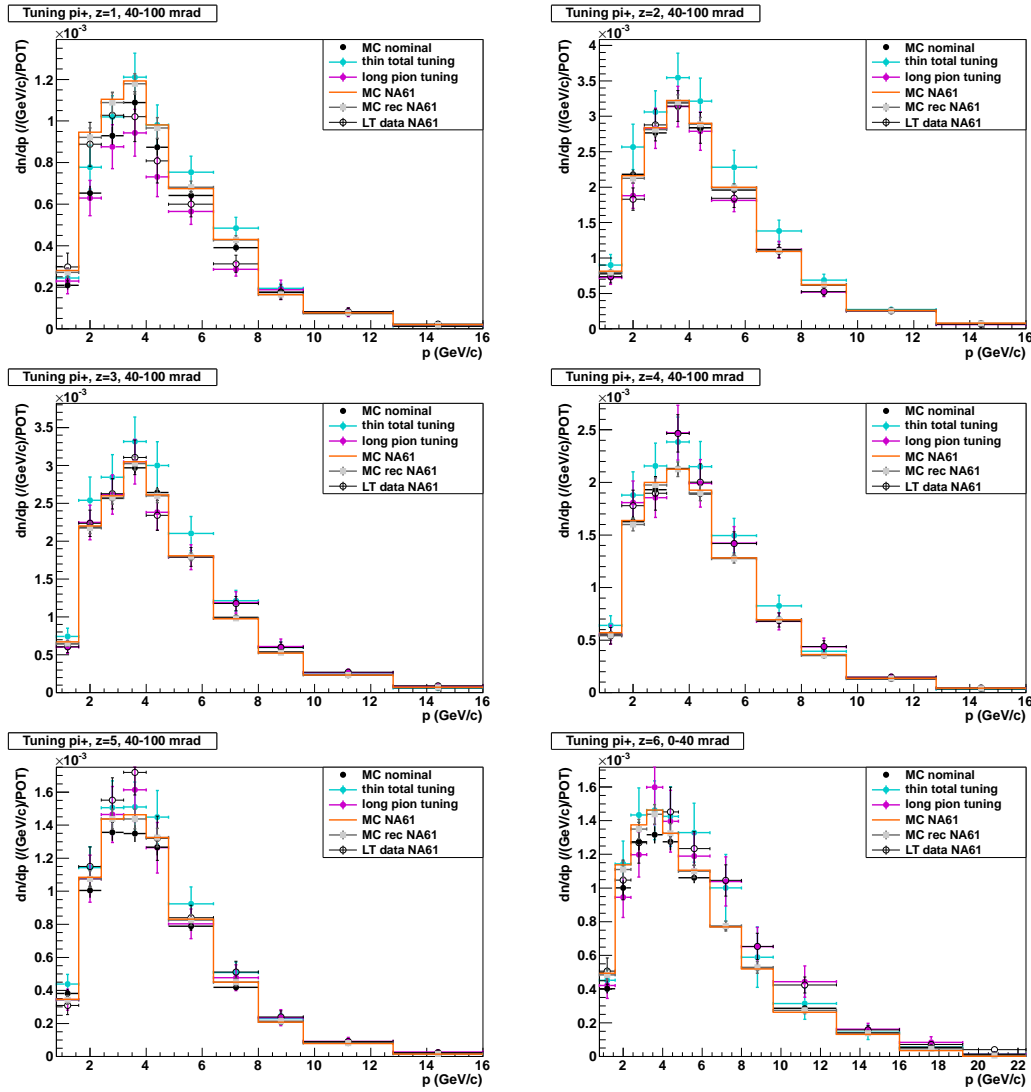


Figure 4.8: Spectra of positively charged pions normalized to the bin size and to the number of protons on target over five longitudinal bins for $[40 - 100]$ mrad, and over the downstream face of the target for $[0 - 40]$ mrad. Error bars for data and Monte-Carlo show the total errors which are the sum in quadrature of the statistical and systematic errors. The orange histograms show the true π^+ yields in acceptance (simulated tracks matched to reconstructed tracks), while black dots are the predictions of the FLUKA standalone simulation weighted for the NA61/SHINE acceptance.

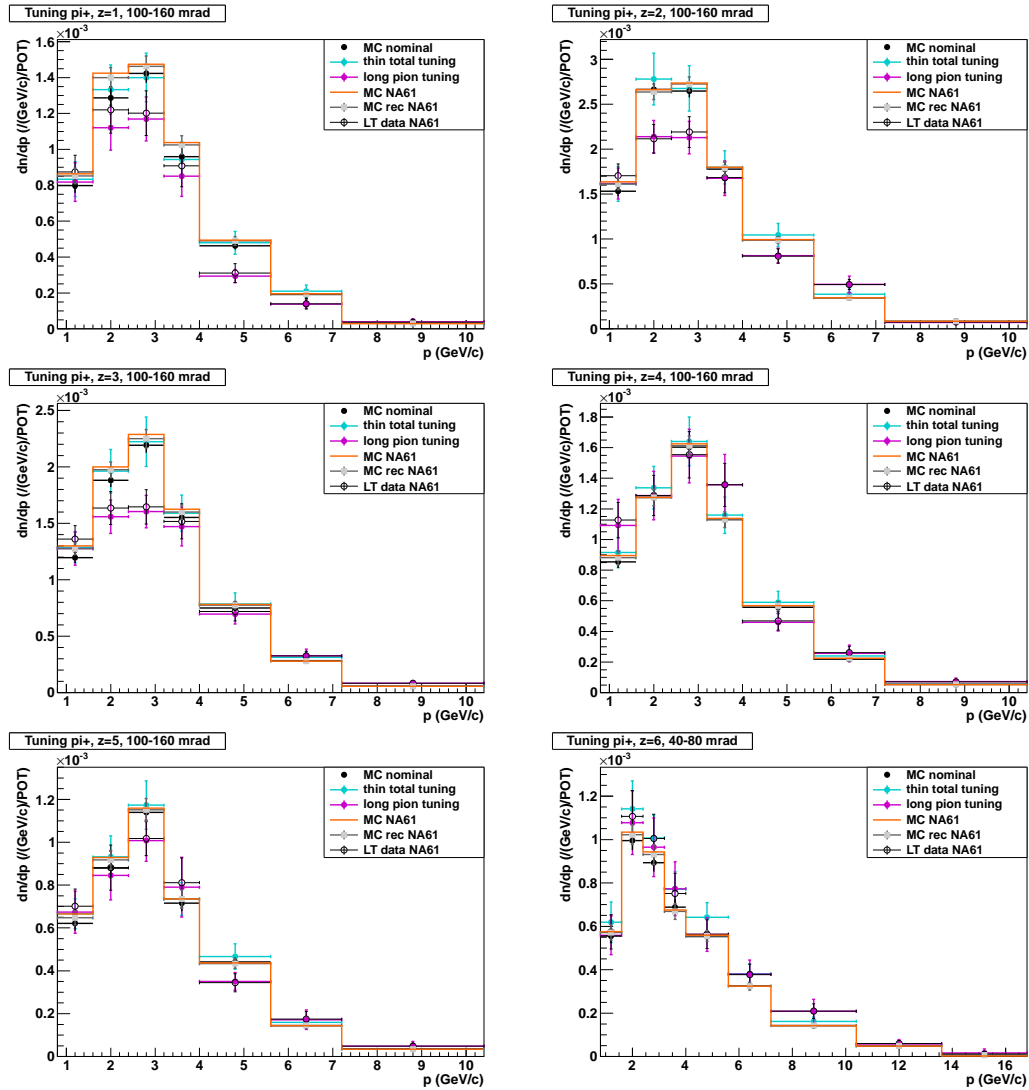


Figure 4.9: Spectra of positively charged pions normalized to the bin size and to the number of protons on target over five longitudinal bins for $[100 - 160]$ mrad, and over the downstream face of the target for $[40 - 80]$ mrad. Error bars for data and Monte-Carlo show the total errors which are the sum in quadrature of the statistical and systematic errors. The orange histograms show the true π^+ yields in acceptance (simulated tracks matched to reconstructed tracks), while black dots are the predictions of the FLUKA standalone simulation weighted for the NA61/SHINE acceptance.

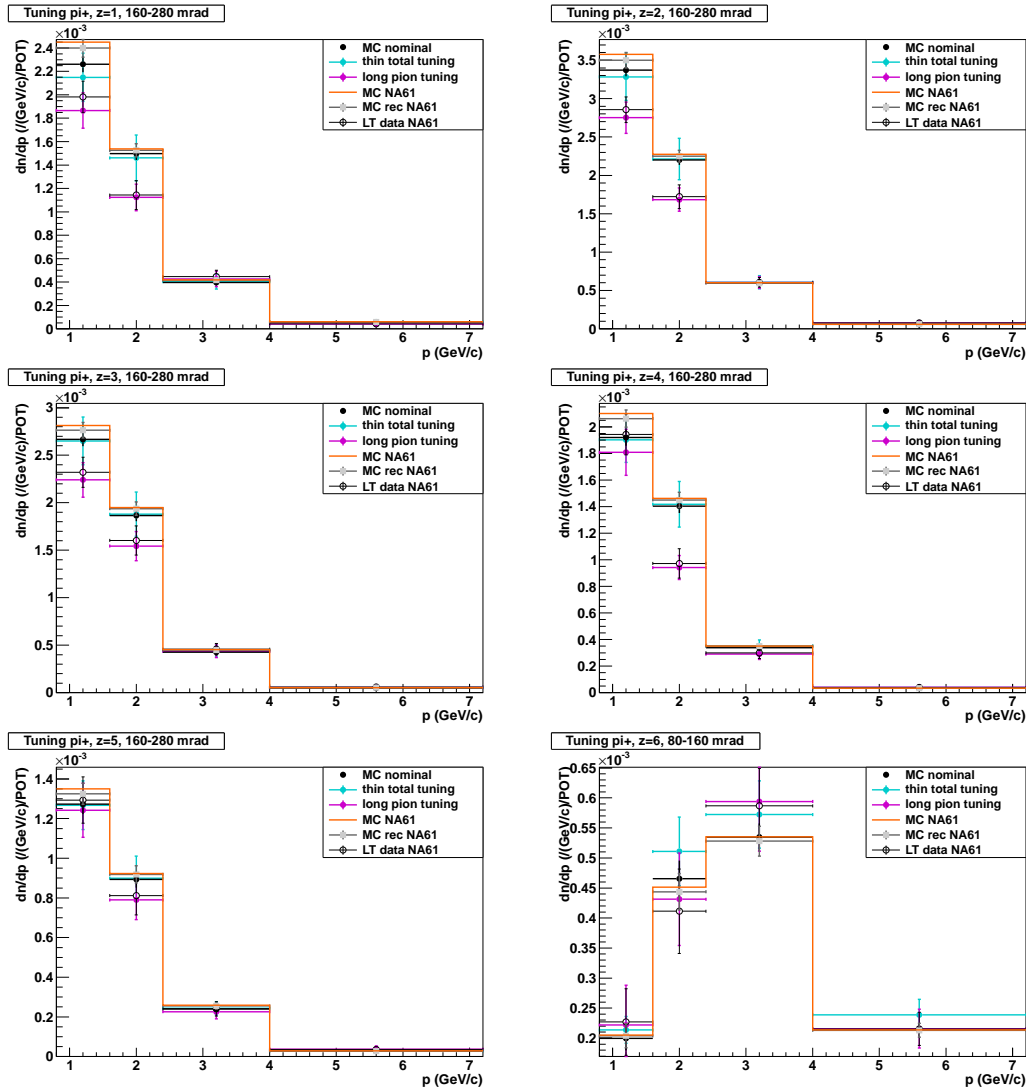


Figure 4.10: Spectra of positively charged pions normalized to the bin size and to the number of protons on target over five longitudinal bins for $[160 - 280]$ mrad, and over the downstream face of the target for $[80 - 160]$ mrad. Error bars for data and Monte-Carlo show the total errors which are the sum in quadrature of the statistical and systematic errors. The orange histograms show the true π^+ yields in acceptance (simulated tracks matched to reconstructed tracks), while black dots are the predictions of the FLUKA standalone simulation weighted for the NA61/SHINE acceptance.

predictions in acceptance (i.e. after the acceptance mask is applied) is expected within 5% due to feed-down contamination in the NA61/SHINE Monte-Carlo (i.e. all simulated pions produced out of the target and matched to a track reconstructed at the surface of the target);

3. the fact that the agreement between the FLUKA prediction tuned with the long target data and the long target data themselves follows the agreement between the nominal FLUKA predictions in acceptance and the NA61/SHINE Monte-Carlo shows that **a)** the long target re-weighting factors are correctly propagated, and that **b)** the masking procedure works correctly.

From Figs. 4.8 to 4.10 one can see that the thin target based tuning seems to globally overshoot the NA61/SHINE long target data. It can also be noted that there is a systematic mismatch between the NA61/SHINE Monte-Carlo and the nominal FLUKA predictions in the first longitudinal bin at low momenta ($< 5 \text{ GeV}/c$). The discrepancy is too large to be attributed to the feed-down contamination in the NA61/SHINE Monte-Carlo as suggested in point 2. Instead, we think that this reflects a reconstruction issue at the level of the backward extrapolation that translates into bin migration (by construction, a point-of-closest approach is always found along the first longitudinal bin if it was not found in the previous bins). This is obviously a point to take care of for the analysis of the 2009/2010 long target data sets, but in the mean time it should be kept in mind that such a problem should not affect the re-weighting factors since in principle the reconstruction treats identically the backward extrapolation of global rtracks from the TPCs whether these are from real or simulated data.

To conclude this section, let us review the arguments we developed in favor of the long target based approach for the re-weighting of the neutrino flux prediction in T2K:

- The current error envelopes of the neutrino flux predictions used for the first T2K ν_e appearance analysis presented in [54] are shown in Fig. 4.11. The total fractional error on the T2K ν_μ flux prediction [97] at the far detector is $\sim 15\%$ at the beam peak energy. Uncertainties account for two main contributions: uncertainties related to the beamline setting (e.g. beam optics, beam direction, alignment and currents of the focusing horns) and those related to the re-weighting of the neutrino flux based on the NA61/SHINE thin target data [82]. The fractional error at the beam peak energy is largely dominated by uncertainties from the second contribution (i.e. pion/kaon multiplicity, secondary nucleon multiplicity and production cross sections). The uncertainty on the NA61/SHINE thin target data is about 5%, which shows that most of the error on the flux prediction actually comes from the fact that corrections have to be estimated for secondary interactions, and

this applies to $\sim 40\%$ of the neutrino flux. To our mind this clearly shows the limitations of the thin target based procedure. More precision on the NA61/SHINE measurements (e.g. possibly down to 3%) will not reduce sufficiently the overall error to get a final 3% uncertainty on the far-to-near ratio prediction.

- In the case of the long target based approach, all these contributions are taken into account at once and there is no need for error prone estimates of secondary interactions.
- The long target data constrains up to $\sim 90\%$ of the neutrino flux **directly** (without additional interpolation), which assures a good control on the overall systematics. The current uncertainty on the long target based re-weighting factors presented in Chapter 3 is dominated by the statistical error (of the order of 10%), while systematic errors are of the order of 5-7% and expected to be reduced down to 5% or better with the analysis of the 2009/2010 NA61/SHINE long target data sets.

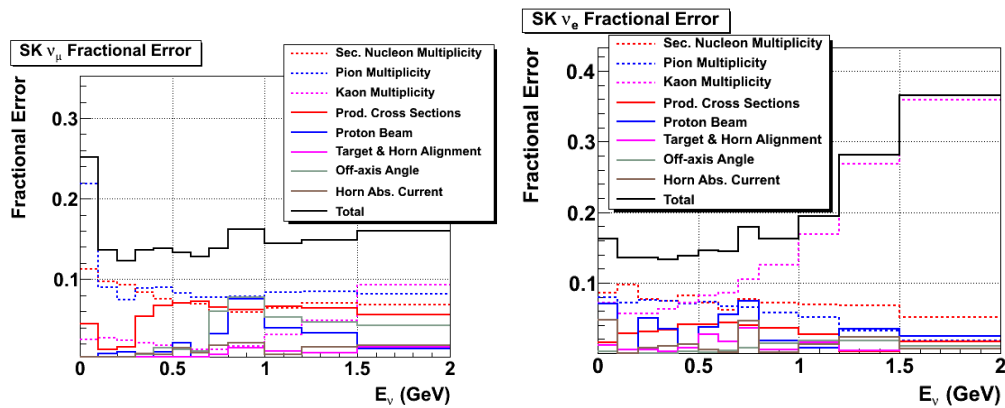


Figure 4.11: Current error envelopes of the analysis presented in [54] for the ν_μ (left) and ν_e (right) fluxes at SK.

4.3 Potential modifications of the T2K simulation

In this section, we review some aspects of the current versions of the FLUKA and JNUBEAM simulations that, to our mind, should be modified or implemented for more consistency (see [98]).

In the FLUKA simulation:

- (i) the PEANUT model should be activated for precise hadron production calculations above 5 GeV/c;

- (ii) particles that are back-scattered and exit the target from the upstream face are not stored on output. In particular these particles may re-interact in the elements of the beamline upstream of the target and indirectly produce neutrinos;
- (iii) by default in FLUKA, the simulation of neutrinos is not activated. However, some neutrinos are produced in the decay of parents inside the target. While most of these decays occur at rest, some of them occur in flight and give neutrinos with energies comparable to that of neutrinos produced out of the target. The necessary modifications have been implemented in JNUBEAM to store the relevant information associated to these target neutrinos on output.

In the JNUBEAM simulation:

the procedure that leads to neutrinos in the near and far detectors includes the following steps:

- (i) wait for leptonic and semi-leptonic decays in flight of parents (100% for π and μ , $\sim 70\%$ for K and K_L^0) propagated by Geant3 through the JNUBEAM geometry;
comment: a tracking cut at 10 MeV/c momentum discards decays at rest.
- (ii) when a neutrino is produced, keep accompanying daughters for further tracking and re-compute the neutrino energy in the LAB system with the constraint on the direction of the near and far detectors;
comment: the kinematics of the accompanying daughters should also be re-computed constrained by the neutrino direction in the LAB system, so that the following history related to these particles is fully consistent.
- (iii) in addition, repeat point (ii) for all possible decays to neutrinos of the current parent and weight neutrinos according to corresponding branching ratios;
comment: daughters of the additional decays are not generated at all.

In the current Geant3 framework of JNUBEAM, these points could be treated more generally by introducing a cut on the time-of-flight and boosting the branching ratios of semi-leptonic decays to neutrinos. Actually, by introducing a cut on the maximal time-of-flight that would reproduce the acquisition time windows at the near and far detectors, one would avoid discarding decays at rest by a cut on the parent momentum. These decays significantly contribute to the neutrino fluxes at low energy, as depicted in Fig. 4.12. Although the neutrino-nucleon cross section is low at such energies, a sharp cut on the parent momentum completely discards any possible effects of that contribution, while a cut on the time-of-flight

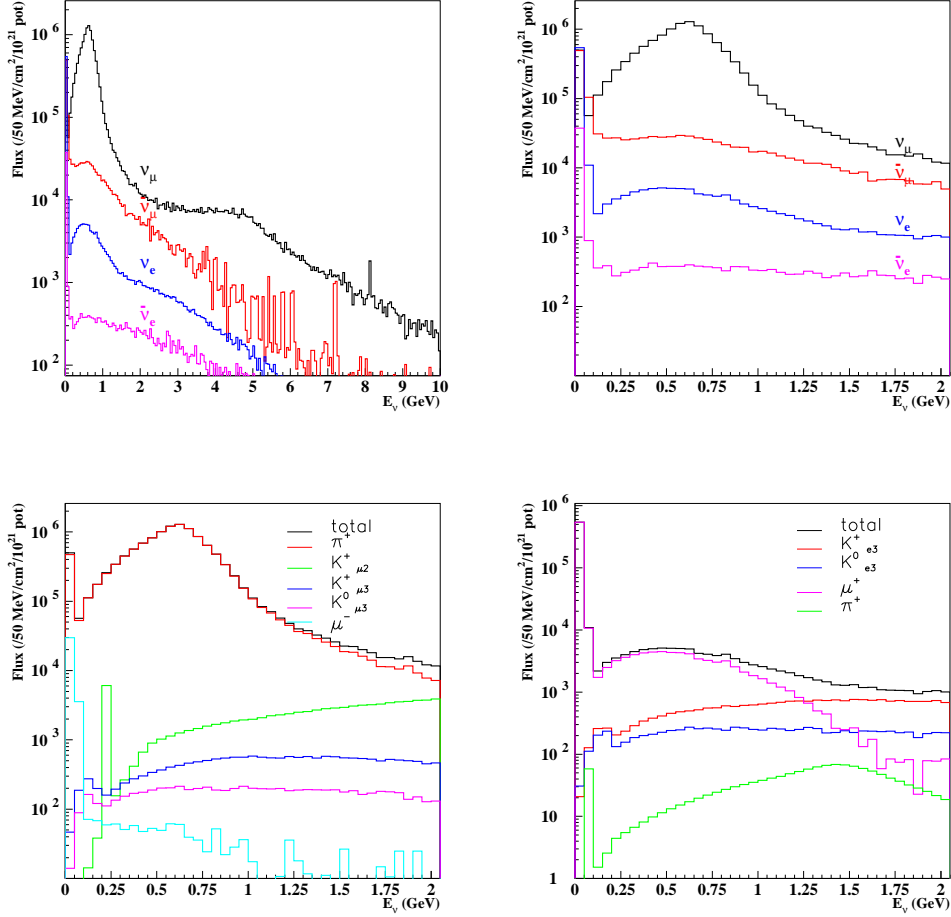


Figure 4.12: Neutrino fluxes at the far detector for all species up to 10 GeV neutrino energy (top left) and zoomed over 2 GeV (top right). Detailed contributions of neutrino parents are shown up to 2 GeV for the ν_μ (bottom left) and ν_e (bottom right) fluxes. Peaks on the distributions correspond to decays at rest.

would still account for a fraction of that contribution.

Boosting the branching ratios of semi-leptonic decays producing neutrinos would allow us to treat the kinematics of accompanying daughters consistently. Actually, if such decays occur equiprobably, there is no need to fake all possible decays at once. In such a case, single decays are generated and the original kinematics of daughters can be re-computed according to the constrained neutrino direction in the LAB before further tracking. Related to the same point, potential bias of the event history could be avoided by constraining randomly neutrinos to the near and far detectors (e.g. half of the neutrinos) instead of forcing every decays to these directions.

These potential modifications could be implemented directly in the existing Geant3 framework of JNUBEAM. However, we think important to mention that a completely independent framework may be provided by the Virtual Monte-Carlo (VMC) project [65], which is currently being developed as a category of classes within the ROOT framework. Apart from the fact that VMC is C++ based (which would allow to treat the overall neutrino production procedure more generally than the current Geant3/FORTRAN version) and provides a simple interface to import any geometry (e.g. the current JNUBEAM geometry has already been imported to VMC), its main advantage is to decouple completely the Monte-Carlo transport code from the user code. The latter point allows for simple and practical model comparisons within the same framework. VMC currently supports the Geant3 and Geant4 transport codes. It originally also supported the FLUKA transport code. The latter implementation has been discontinued by the FLUKA team in 2010.

Chapter 5

The first T2K results

5.1 Results from the ν_e appearance analysis

The first ν_e appearance results of T2K are based on the study of single e -like ring events at SK. The analysis is based on a somewhat simpler analysis flow than that required for the ν_e signal shape analysis presented in Chapter 2. In summary, it goes through the following steps:

1. extract from the SK data an enhanced sample of ν_e CCQE event candidates arising from $\nu_\mu \rightarrow \nu_e$ oscillations;
2. simulate the expected number of events at SK;
3. adjust the overall normalization using the near detector measurements;
4. compare the observed number of events to the signal and background expectations;
5. estimate systematic errors which are accounted for in the evaluation of confidence intervals for the selected data sample.

The ν_e CCQE event candidates are obtained after applying a set of pre-defined, optimized selection cuts based on Monte-Carlo studies. The selection basically cuts on the beam time window at SK, the fiducial volume of the detector, and the visible and reconstructed neutrino energy to remove low and high energy backgrounds respectively. An additional cut on the two-ring invariant mass, obtained under the assumption that the light pattern in SK is produced by two electromagnetic showers, is applied to reject misidentified π^0 mesons from the NC1 π^0 background. Details of the selection are reported in [54]. The ν_e appearance signal efficiency is estimated from the Monte-Carlo to 66%, while the background rejection is $> 77\%$ and $> 99\%$ for the intrinsic ν_e contamination in the beam and for neutral-current events respectively.

The signal and background expectations at SK are based on neutrino flux and cross section predictions (see Eq. 2.9). Fluxes are initially predicted using the FLUKA 2008.3d simulation code for the proton interactions inside the Carbon target. The GCALOR model handles hadronic interactions while outgoing particles are transported through the magnetic horns, target hall, decay volume and beam dump. The studies presented in Chapter 2 showed that, relying on model predictions only, the systematic error coming from the comparison of different models is larger than the required precision on the absolute fluxes in T2K (see Fig. 2.20). Moreover, it was shown that the target contribution to the ν_μ and ν_e fluxes (that is the FLUKA based contribution of the T2K beam simulation) is as high as $\sim 90\%$ at the beam peak energy, the remaining 10% coming from re-interactions along the beamline (the GCALOR based contribution). The same studies pointed out that the contribution to the neutrino fluxes from parents produced in the proton primary interaction in the target was $\sim 60\%$ at the beam peak energy. Approximately that fraction of the predicted ν_μ and ν_e fluxes in the T2K beam simulation was directly tuned with the NA61/SHINE pion production data from the thin target measurements. Both fluxes actually depend on the π^+ meson production, the ν_μ flux from the direct decay of pions, the ν_e flux from the subsequent decay of muons. As can be seen in Fig. 5.1, measuring the π^+ meson production phase space indirectly measures as well the phase space of π^+ mesons producing ν_e 's in the near and far detectors via the subsequent muon decay.

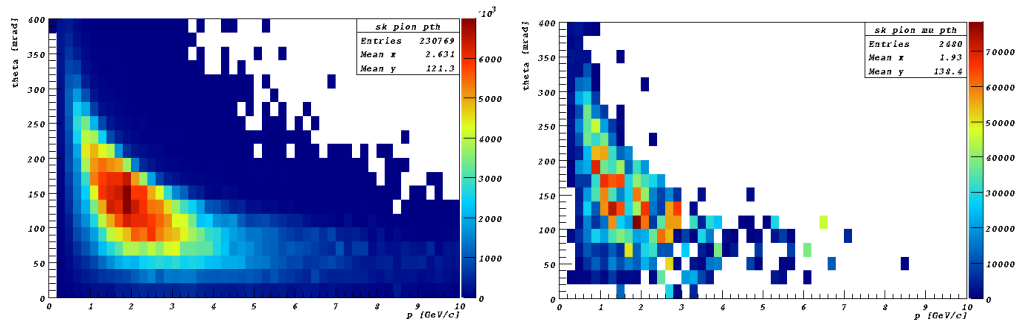


Figure 5.1: $\{p, \theta\}$ phase space of positively charged pions exiting the target and producing neutrinos at SK (left), and phase space of those producing muons that decay to ν_e passing through SK (top right).

The tuning procedure, described in details in [64], is done in three steps:

- (i) tuning of the secondary π^\pm/K^\pm multiplicity to the NA61/SHINE pion/kaon production cross sections for interactions handled by FLUKA in the target;
- (ii) tuning of the tertiary π^\pm/K^\pm (pions produced in the re-interaction of secondary protons) multiplicity to the NA61/SHINE pion/kaon production cross sections for interactions handled by FLUKA in the target;

- (iii) tuning of the interaction rate of p , π^\pm and K^\pm in different materials for interactions handled by GCALOR out of the target;

In the first step, the FLUKA pion multiplicity, $d^2n/dpd\Omega = 1/\sigma_{prod}d^2\sigma_\pi/dpd\Omega$, is normalized to the model production cross section of 231.3 mb, and compared to the NA61/SHINE pion multiplicity in bins of $\{p, \theta\}$. Each simulated secondary pion in the phase space region covered by the NA61/SHINE measurements is weighted accordingly. The NA61/SHINE systematic error for each $\{p, \theta\}$ bin (typically 5 to 10%) and the overall NA61/SHINE normalization error (2.3%) are propagated to the oscillation analysis. Outside of the NA61/SHINE coverage, the pion production is assigned a conservative 50% error.

The second step is based on the approximate Feynman scaling of the single particle invariant inclusive cross section expressed in terms of the transverse momentum, p_T , and the Feynman scaling variable, x_F . The scaling suggests that the multiplicity of the secondary pions from the primary proton interaction can be scaled with \sqrt{s} to obtain the multiplicity of pions produced in the re-interaction of secondary protons. The tuning of tertiary pions is performed similarly to that of secondary pions, using weights converted from the $\{p, \theta\}$ to the $\{p_T, x_F\}$ phase space.

The last step is not based on the NA61/SHINE data. The FLUKA and GCALOR cross sections for p , π^\pm and K^\pm on Carbon and Aluminum (material of the magnetic horns) as a function of the laboratory momentum were compared to external data. A good agreement was observed with FLUKA so that the tuning is done only for interactions handled by GCALOR out of the target. For the considered hadrons, the model interaction probability and the probability to escape from a given material are weighted according to the data production cross sections.

The predicted beam fluxes at SK for the four neutrino species are shown in Fig. 5.2. The systematic uncertainties on these predictions arise from:

- (i) the hadron production;
- (ii) the hadron interaction probabilities;
- (iii) the proton beam uncertainty;
- (iv) the neutrino beam direction, beamline alignment, horn currents and field asymmetry;

In point (i), the secondary pion production errors are taken from the NA61/SHINE thin target results, the latter being also used with appropriate re-scaling for the tertiary pion production errors. The kaon production errors are for the moment estimated from comparisons of FLUKA to data [95]. The uncertainty on the secondary nucleon production is also constrained by comparisons of FLUKA to the same data. In point (ii), the uncertainty on the interaction rates of p , π^\pm and K^\pm comes from the uncertainty on the production cross section in the different

data sets used for correction. The size of the uncertainty is estimated from the size of the corresponding quasi-elastic cross sections.

The proton beam uncertainty in point (iii) is based on the measurement errors of the beam monitors used to determine the proton beam position, width and divergence at the target position. In point (iv), uncertainties on the neutrino beam direction are based on the INGRID measurement, alignment uncertainties on survey measurements, and horn currents and field asymmetry on dedicated measurements.

In the oscillation region (below 1 GeV), for $\theta_{13} = 0$, the estimated uncertainties of the intrinsic ν_μ and ν_e fluxes is $\sim 14\%$. The main contribution is that of the hadron production uncertainty (the contribution of points (iii) and (iv) is $\sim 2\%$). Above 1 GeV (2 GeV), the ν_e (ν_μ) flux error is dominated by the uncertainty on the kaon production rate with resulting errors of 20-50%. This contribution will be reduced by the NA61/SHINE kaon production cross section results based on the 2007 thin target data (to be submitted for publication soon).

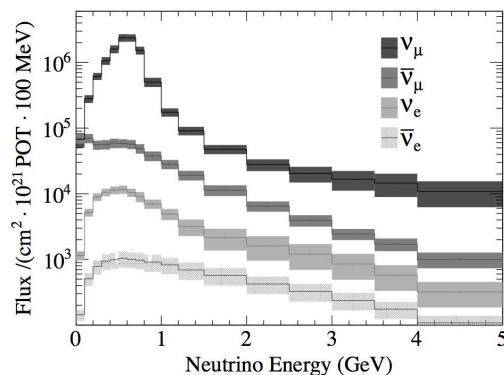


Figure 5.2: Predicted neutrino fluxes at the far detector, in absence of oscillation. The shaded boxes indicate the total systematic uncertainties for each energy bin.

The nominal cross section predictions of the NEUT event generator [99] are used to compute the background and signal expectations at SK. The uncertainty on the cross sections comes from comparisons of model to data (e.g. MiniBooNE for the $CC1\pi$ cross section, SciBooNE for the CC coherent π and NC coherent π cross sections), variation of model parameters such as the axial mass (M_A), and comparisons between models. In particular, the NEUT model was recently compared to the MiniBooNE data [100] for the $NC1\pi^0$ cross section. The dominant uncertainty on the expectations at SK comes from the pion final state interactions (FSI) which adds up to 10.1% over the neutrino energy spectrum.

The last source of uncertainty on the expected number of events at SK is due to the detector efficiency. The systematic errors due to the event selection cuts in SK were studied with cosmic-ray muons, Michel electrons and atmospheric neu-

trino events. The total contribution to the uncertainty on the expected number of signal events is of 7.6%, and 15% on the expected number of background events.

The overall normalization of the predictions at SK is adjusted to the data to Monte-Carlo ratio of the ν_μ CC interaction rate measurement at the near detector. This inclusive ν_μ CC measurement in the off-axis near detector is extracted from a data sample collected in the Run1 period, which corresponds to 2.88×10^{19} p.o.t. after detector quality cuts. The expected number of events at SK is expressed as

$$N_{SK}^{exp} = (R_{ND}^{\mu,Data} / R_{ND}^{\mu,MC}) \cdot N_{SK}^{MC} \quad (5.1)$$

where N_{SK}^{MC} is the previously discussed Monte-Carlo number of events expected at SK, and $R_{ND}^{\mu,Data}$ ($R_{ND}^{\mu,MC}$) is the ν_μ CC interaction rate normalized to p.o.t. in the data (Monte-Carlo). The measured ratio of data to Monte-Carlo is

$$R_{ND}^{\mu,Data} / R_{ND}^{\mu,MC} = 1.036 \pm 0.028(stat)^{+0.044}_{-0.037}(\text{det.syst}) \pm 0.038(\text{phys.syst}) \quad (5.2)$$

which shows a good agreement of the neutrino flux (based on the NA61/SHINE thin target data and FLUKA predictions) and interaction (NEUT) models with data. The reconstructed momentum of the ν_μ CC candidates at the near detector is shown in Fig. 5.3 with a comparison to the Monte-Carlo prediction. The detector uncertainties at the near detector are dominated by the tracking and particle identification efficiencies. The physics uncertainties are dominated by the interaction model. Errors that cancel due to correlations between the near and far detectors (i.e. flux uncertainties) are omitted.

The signal and background event rates at SK are calculated in the three-neutrino oscillation framework including oscillation probabilities and matter effects (see Section 1.4) with $\Delta m_{12}^2 = 7.6 \times 10^{-5} \text{ eV}^2$, $\Delta m_{23}^2 = 2.4 \times 10^{-3} \text{ eV}^2$, $\sin^2 2\theta_{12} = 0.8704$, a maximal mixing $\sin^2 2\theta_{23} = 1$, an average Earth density $\rho = 3.2 \text{ g/cm}^3$ and $\delta_{CP} = 0$. The expected number of events at SK are 0.03(0.03) $\nu_\mu + \bar{\nu}_\mu$ CC, 0.8(0.7) intrinsic ν_e CC, 0.1(4.1) $\nu_\mu \rightarrow \nu_e$ oscillation events for $\sin^2 2\theta_{13} = 0(0.1)$, and 0.6 NC events. The systematic uncertainties on these expectations are summarized in Table 5.1 for the different sources and $\sin^2 2\theta_{13} = 0$ and 0.1.

In the signal region, T2K observed 6 ν_e candidates with an expected background from Eq. 5.1 of 1.5 ± 0.34 events, including the contributions of NC background (0.61), intrinsic beam ν_e contamination (0.76), $\nu_\mu \rightarrow \nu_e$ oscillation through the solar mixing θ_{12} (0.09) and ν_μ CC background (0.03). Assuming a maximal mixing $\sin^2 2\theta_{23} = 1/2$, this result converted into a confidence interval yields $0.03(0.04) < \sin^2 2\theta_{13} < 0.28(0.34)$ at 90% CL for $|\Delta m_{23}^2| = 2.4 \times 10^{-3} \text{ eV}^2$ and $\delta_{CP} = 0$, and a best-fit value of $\sin^2 2\theta_{13} = 0.11(0.14)$ for the normal (inverted) neutrino mass hierarchy. The corresponding inclusion plots in the $\{|\Delta m_{23}^2|, \sin^2 2\theta_{13}\}$ and $\{\delta_{CP}, \sin^2 2\theta_{13}\}$ parameter spaces are shown in Fig. 5.4 and Fig. 5.5 respectively.

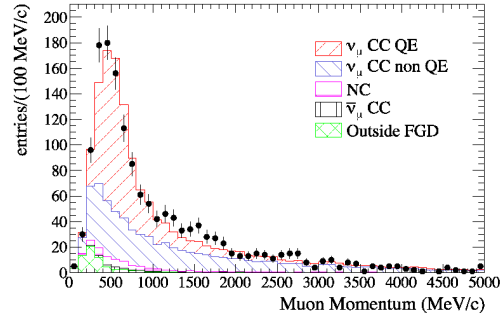


Figure 5.3: Measured momentum of ν_μ CC candidates in the fine grain detector (FGD) target of the near detector. The data is shown using points with error bars (statistical only) and the Monte-Carlo predictions are in histograms shaded according to their type.

Source	$\sin^2 2\theta_{13} = 0$	$\sin^2 2\theta_{13} = 0.1$
neutrino flux	$\pm 8.5\%$	$\pm 8.5\%$
near detector	$+5.6\%$ -5.2%	$+5.6\%$ -5.2%
near det. statistics	$\pm 2.7\%$	$\pm 2.7\%$
cross section	$\pm 14.0\%$	$\pm 10.5\%$
far detector	$\pm 14.7\%$	$\pm 9.4\%$
Total $\delta N_{SK}^{exp}/N_{SK}^{exp}$	$+22.8\%$ -22.7%	$+17.6\%$ -17.5%

Table 5.1: Contributions from various sources and the total relative uncertainty for $\sin^2 2\theta_{13}=0$ and 0.1, and $\delta_{CP} = 0$.

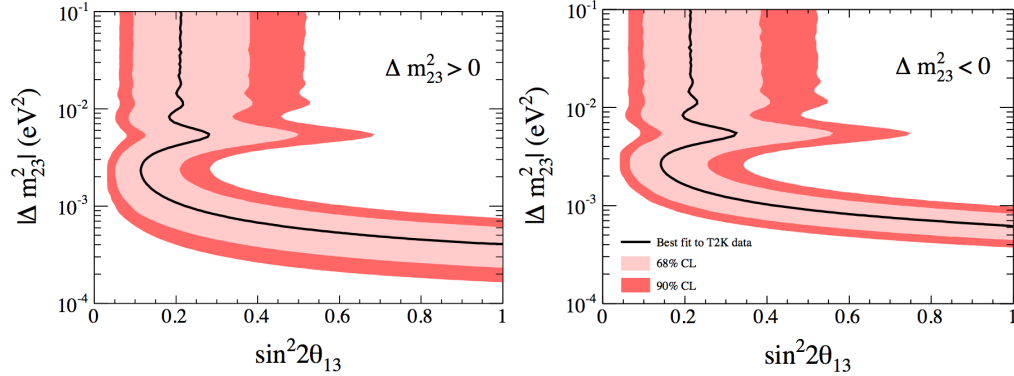


Figure 5.4: The 68% and 90% CL regions for $\sin^2 2\theta_{13}$ as a function of $|\Delta m_{23}^2|$, assuming maximal mixing $\sin^2 \theta_{23} = 1/2$ and $\delta_{CP} = 0$, consistent with the observed number of events in the three-flavor oscillation case for normal (left) and inverted (right) mass hierarchies.

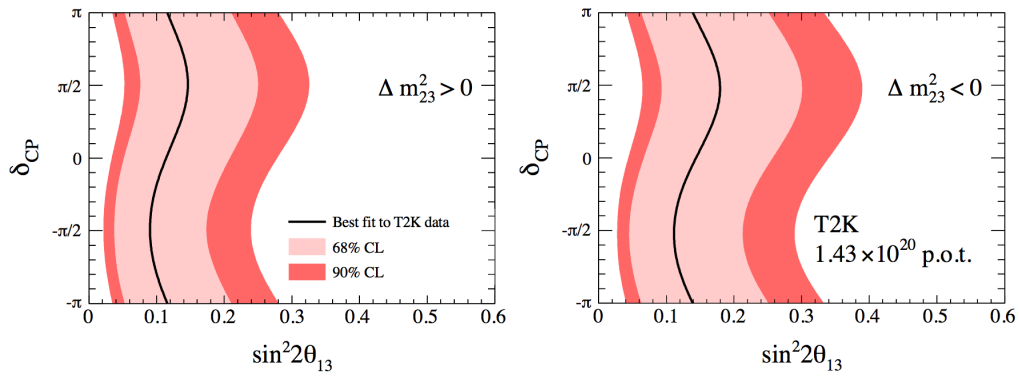


Figure 5.5: The 68% and 90% CL regions for $\sin^2 2\theta_{13}$ for each value of δ_{CP} for a maximal mixing $\sin^2 \theta_{23} = 1/2$ and $|\Delta m_{23}^2| = 2.4 \times 10^{-3} \text{ eV}^2$, consistent with the observed number of events in the three-flavor oscillation case for normal (left) and inverted (right) mass hierarchies.

The T2K best-fit value is just at the limit of the region excluded by the MINOS collaboration. **T2K is the first experiment to point to a non-zero value of θ_{13} by excluding $\sin^2 2\theta_{13} = 0$ at 2.5σ .** The aim of T2K is now to firmly establish the ν_e appearance result and better determine the θ_{13} mixing angle. To do so, analysis methods based on the ν_e signal shape are under development, and measurements at the near detector of the ν_μ CCQE and beam ν_e spectra are underway to better constrain neutrino fluxes and cross sections. The recovery work at J-PARC is in progress and activity will resume by December 2011, including accelerator complex and neutrino facility.

Conclusion

The different topics reported in this thesis cover the work that I realized while participating to the NA61/SHINE and T2K experiments.

Following the order of presentation, I performed studies of the neutrino flux predictions with the T2K beam simulation. In particular, these studies allowed us to understand which fraction of the ν_μ and ν_e fluxes could be constrained by hadron production measurements off thin and long targets. In that respect, the results presented in Chapter 2 clearly stress the importance and advantages of the long target measurements. The first long target measurements in NA61/SHINE were taken in 2007 and during part of the 2009 data taking. Related to my work on the neutrino flux studies, I performed estimations of the required statistics of the long target measurements in order to fulfill the T2K goals in terms of precision on the absolute flux and far-to-near ratio predictions. These estimations were included in the NA61/SHINE 2010 beam time request at CERN.

My analysis work in NA61/SHINE, presented in Chapter 3, is dedicated to the 2007 long target data. The product of this work consists in spectra of positively charged pions reconstructed at the surface of the T2K replica target in the $\{p, \theta\}$ phase space over six longitudinal bins, for both data and Monte-Carlo simulations based on the FLUKA model used in JNUBEAM. These spectra are used to calculate re-weighting factors for the multiplicity of positively charged pions exiting the target simulated by the FLUKA model. For this analysis, I implemented the necessary modifications to the NA61/SHINE simulation and reconstruction chains to make them compatible with the T2K simulation. I think that the latter point is a key ingredient for the successful usage of the NA61/SHINE long target data in the T2K beam simulation. In particular, a major advantage of this compatibility is the possibility to constrain the T2K model directly within the NA61/SHINE simulation and reconstruction framework, which allows for a better control of systematic uncertainties.

To complete my analysis work, I am currently working on the implementation of the NA61/SHINE long target data in the existing framework developed by the T2K Beam Group for the tuning of the neutrino flux predictions with the

NA61/SHINE thin target data. The latter was briefly described in Chapter 5, while the first stage of my work on the long target based re-weighting is presented in Chapter 4. Results obtained from a first implementation of the tuning of the ν_μ flux at SK based on the replica target data are presented and compared to the flux tuning based on the thin target data. More work is obviously necessary to understand these preliminary comparisons, but the fact that we can now produce such comparisons demonstrates that the T2K neutrino flux predictions can effectively be constrained by the NA61/SHINE long target measurements.

To my mind, the work presented in this thesis is important for our common understanding of neutrino flux predictions. As I pointed out, this is really **the first time that we try to constrain such predictions with hadron production measurements off a long target**. This type of measurements is ultimately the best source of information since it constrains the hadron production model predictions at both primary and secondary interaction levels at once. Secondary interactions contribute significantly to the neutrino flux (e.g. $\sim 40\%$ in T2K). Unfortunately, the simulation of these interactions is difficult to constrain due to the complex hadronization processes that are involved. In addition, due to the lack of data for production cross sections of secondary hadrons on materials and at energies relevant for the experiment, interpolation of existing data to the right energy or momentum and scaling to the right nucleus is usually the only way to constrain that contribution, at the price of large systematic uncertainties. The current systematic uncertainty of the T2K neutrino flux prediction is $\sim 14\%$ below 1 GeV neutrino energy, out of which the hadron production is the main contribution. The corresponding uncertainty on the expected number of events at SK is reduced to $\sim 8\%$ due to partial error cancelation with the normalization to the near detector measurements. **We hope that, in a second stage, the work carried out for the long target data analysis in NA61/SHINE will significantly reduce this contribution and allow us to determine the θ_{13} mixing angle with an increased precision.**

All the results that I am reporting in this thesis are based on the NA61/SHINE 2007 long target data set. Significant efforts were invested to optimize the analysis to compensate for the very low statistics of this data set. In that respect, I would consider this work as a *proof-of-principle*: actually, using the NA61/SHINE setup, this work showed that hadron production measurements off the T2K replica target were successfully performed and that positively charged pion yields could effectively be reconstructed at the surface of the target. Work on the NA61/SHINE simulation and reconstruction chains allowed us to calculate re-weighting factors for the pion multiplicity simulated by the T2K model directly within the NA61/SHINE framework. Finally, these results are consistently being implemented in T2K for the tuning of the neutrino flux predictions. In the next stage

of this work, several improvements are expected, in particular:

- the statistics of the 2009 and 2010 long target data sets is much larger than that of the 2007 data. This will allow us to refine the analysis procedure and get a better control of related systematic uncertainties;
- the target alignment with respect to the beam axis was better controlled for the 2009 and 2010 data taking;
- the current re-weighting factors account only for the model correction; the larger statistics of the 2009 and 2010 data sets will allow us to include the correction for different beam profiles in NA61/SHINE and T2K (part of the data was taken with a trigger configuration that approximately reproduces the T2K beam profile on target, which might even be sufficient);
- the current re-weighting factors have been calculated for positively charged pions; some more work will be carried out in the near future to extract corrections for negatively charged pions out of the same data set. In particular, this will provide a possible internal cross check with the π^- results that can be extracted in parallel with the h^- analysis of the long target data;
- the procedure developed for particle identification is also suitable for the extraction of proton and kaon yields (as it was demonstrated with the thin target data) out of the long target data. Long target based re-weighting factors for kaons would significantly constrain the intrinsic beam ν_e component, while re-weighting factors for protons would in particular constrain the flux contribution coming from the re-interactions in the elements of the beamline of protons exiting from the downstream face of the target in the very forward direction (measured in a dedicated run during the 2010 data taking).

To conclude, I review the different activities that were part of my work as a PhD student for the NA61/SHINE and T2K collaborations. As a member of the NA61/SHINE collaboration, I actively participated in:

- the construction and operation of the forward time-of-flight detector;
- the gas simulation needed for the dE/dx calibration;
- the development and maintenance of the whole NA61/SHINE simulation and related reconstruction chains;
- the large scale Monte-Carlo productions for the different analyses of the 2007 thin target data and that of the 2007 long target data;
- the analysis of the 2007 long target data;

- the statistical estimations for the long target measurements of the 2010 beam request;
- the acceptance studies for the high magnetic field measurements of the very forward hadron production in 2010.

As a member of the T2K collaboration, my participation was related to:

- the R&D effort on the readout system of the TPCs of the near detector based on the Gas Electron Multiplier (GEM) and Micromegas technologies ([101, 102, 103]);
- the tests of the second magnetic horn of the focusing system of the T2K beamline;
- the development of the T2K beam simulation;
- the development of the tuning of the neutrino flux predictions based on the NA61/SHINE thin target results presented in Chapter 3 and that was used to produce the first T2K results presented in Chapter 5;
- the development of the tuning of the neutrino flux predictions based for the first time on the NA61/SHINE long target data.

Appendix A

Kinematics of an off-axis neutrino beam

Considered decays

The pion two-body decay, $\pi^\pm \rightarrow l^\pm + \nu_l(\bar{\nu}_l)$, and the kaon three-body decay, $K \rightarrow \pi + l(\bar{l}) + \nu_l(\bar{\nu}_l)$ are considered in this appendix. For the pion two-body decay in the center-of-mass (COM) system, the neutrino energy is given by $E^* = (m_\pi^2 - m_\mu^2)/2m_\pi$ and $p^* = E^* = 29.8 \text{ MeV} \approx 30 \text{ MeV}$. In the case of the kaon three-body decay, E^* is not fixed by the conservation laws, but it makes little difference in what follows, except that the lab energy is not rigidly related to the lab angle and meson velocity.

Lorentz transformation

We take the decaying meson direction as polar axis in the following, and consider provisionally the meson beam as divergence-less. Consequently we shall not make use of the azimuthal degree of freedom and reduce the problem to two dimensions. The neutrino energy-momentum vector in the COM system is therefore $E^*(1, \cos \theta^*, \sin \theta^*)$.

Let $\gamma = \frac{E_\pi}{m_\pi}$ be the π Lorentz factor and $\beta = \frac{p_\pi}{E_\pi}$ its velocity for $c = 1$. The lab neutrino energy-momentum vector is given by:

$$E = \gamma E^*(1 + \beta \cos \theta^*) \tag{A.1}$$

$$E \cos \theta = \gamma E^*(\cos \theta^* + \beta) \tag{A.2}$$

$$E \sin \theta = E^* \sin \theta^* \tag{A.3}$$

(where we set $p = E$ since neutrinos are considered mass-less). This gives:

$$\cos \theta = \frac{\cos \theta^* + \beta}{1 + \beta \cos \theta^*} \quad (\text{A.4})$$

$$\sin \theta = \frac{\sin \theta^*}{\gamma(1 + \beta \cos \theta^*)} \quad (\text{A.5})$$

All these equations are inverted by the substitution $\beta \rightarrow -\beta$. Also, it is readily seen that

$$(1 - \beta \cos \theta)(1 + \beta \cos \theta^*)\gamma^2 = 1 \quad (\text{A.6})$$

Kinematic limits

From equation (A.5) one sees that $\sin \theta = \frac{E^*}{E} \sin \theta^*$ and therefore

$$\sin \theta \leq \frac{E^*}{E}$$

which shows that a given neutrino energy E can only be found up to a maximum lab angle

$$\theta_{max}(E) = \arcsin \frac{E^*}{E} \approx \frac{30 \text{ MeV}}{E} \quad (\text{A.7})$$

which is small for all useful neutrinos.

Conversely, at a given angle θ from the (supposedly divergence-less) beam, the maximum neutrino energy is:

$$E_{max}(\theta) = \frac{E^*}{\sin \theta} \quad (\text{A.8})$$

Probability distributions

Fixed meson energy

In this subsection we consider that the decaying meson velocity is fixed. Therefore there is only one final state variable for 2 body decay (not counting the azimuth) and the lab angular distribution is completely determined even in the case of 3-body decay of the parent meson.

Angular distribution

By differentiating the reciprocal of (A.4) with respect to $\cos \theta$, we find

$$\frac{\partial \cos \theta^*}{\partial \cos \theta} = \frac{1 - \beta^2}{(1 - \beta \cos \theta)^2} \quad (\text{A.9})$$

Since the meson is spin-less it decays isotropically in COM and the $\cos \theta^*$ distribution is flat in $[-1, 1]$. Therefore the lab distribution of the cosine for a given meson energy is:

$$\frac{\partial P}{\partial \cos \theta} = \frac{1}{2} \frac{1 - \beta^2}{(1 - \beta \cos \theta)^2} \quad (\text{A.10})$$

$$(\text{A.11})$$

or, re-establishing the azimuthal degree of freedom:

$$\frac{\partial P}{\partial \Omega} = \frac{1}{4\pi\gamma^2(1 - \beta \cos \theta)^2} \quad (\text{A.12})$$

This distribution is valid without change for the 3-body decays.

Energy-angle distribution

Equations (A.1) and (A.4) allow to calculate all the necessary partial derivatives:

$$\begin{aligned} \frac{\partial E}{\partial E^*} &= \gamma(1 + \beta \cos \theta^*) & \frac{\partial \cos \theta}{\partial E^*} &= 0 \\ \frac{\partial E}{\partial \cos \theta^*} &= \gamma\beta E^* & \frac{\partial \cos \theta}{\partial \cos \theta^*} &= \frac{1}{\gamma^2(1 + \beta \cos \theta^*)^2} \end{aligned}$$

from which we get the Jacobian:

$$\frac{D(E^*, \cos \theta^*)}{D(E, \cos \theta)} = \gamma(1 + \beta \cos \theta^*) = \frac{1}{\gamma(1 - \beta \cos \theta)}$$

So assuming some energy distribution $F(E^*)$ for E^* (independent of the angles by isotropy) we get:

$$\frac{\partial P}{\partial E \partial \Omega} = \frac{\partial P}{\partial E^* \partial \Omega^*} \frac{1}{\gamma(1 - \beta \cos \theta)} = F(\gamma E(1 - \beta \cos \theta)) \frac{1}{4\pi\gamma(1 - \beta \cos \theta)} \quad (\text{A.13})$$

For 2-body meson decay, there is only one variable (F is a Dirac δ) and this reduces to the angular distribution given above ¹, which can alternatively be expressed as

¹Pay attention to the different powers of the denominators in expression (A.12) and this one.

a distribution in energy.

For 3-body meson decay, F must be found from the decay dynamics. From (A.1) and (A.6) E_{max} for a given angle is given by $\frac{E_{max}^*}{\gamma(1-\beta \cos \theta)}$ with $E_{max}^* = \frac{M_K^2 - (m_\pi + m_l)^2}{2M_K}$ obtained when the mass of the system recoiling against the neutrino in the COM system is minimal.

Introducing a meson spectrum

We no longer consider that the energy of the parent meson is fixed. We assume an energy distribution, say $g(E_\pi)$ for the π meson in the lab. Note that we use π for definiteness. But when it comes to 3-body decays, this must be understood as K .

Even assuming constant E^* (2-body decay), the two final state variables E and $\cos \theta$ can vary separately. To derive their distribution, we need the Jacobian of the transformation $E_\pi, \cos \theta^* \rightarrow E, \cos \theta$.

Transforming $E_\pi, \cos \theta^* \rightarrow E, \cos \theta$

When doing this transformation, E^* must be considered as a fixed parameter. In the case of 3-body decay, the $E, \cos \theta$ distribution found below will be simply multiplied by the E^* COM distribution and integrated over this variable.

It is much simpler to calculate the partial derivatives of the final variables with respect to E_π and $\cos \theta^*$ than the contrary. All we need is again in the two relations (A.1) and (A.4) and the relation

$$\frac{d\beta}{d\gamma} = \frac{1}{\beta\gamma^3} \quad (\text{A.14})$$

The necessary derivatives are as follows:

$$\begin{aligned} \frac{\partial E}{\partial E_\pi} &= \frac{E^*}{m_\pi} (1 + 1/\beta \cos \theta^*) & \frac{\partial E}{\partial \cos \theta^*} &= E^* \gamma \beta \\ \frac{\partial \cos \theta}{\partial E_\pi} &= \frac{(\sin \theta^*)^2}{(1 + \beta \cos \theta^*)^2} \frac{1}{m_\pi \beta \gamma^3} & \frac{\partial \cos \theta}{\partial \cos \theta^*} &= \frac{1}{\gamma^2 (1 + \beta \cos \theta^*)^2} \end{aligned}$$

Therefore we get:

$$\frac{D(E, \cos \theta)}{D(E_\pi, \cos \theta^*)} = \frac{E^*}{m_\pi \gamma^2 \beta} \frac{\cos \theta^*}{1 + \beta \cos \theta^*}$$

Using the relations established above, the inverse Jacobian reduces to:

$$\frac{D(E_\pi, \cos \theta^*)}{D(E, \cos \theta)} = \frac{m_\pi \beta}{E^*} \frac{1}{(\cos \theta - \beta)}$$

which is singular when $\cos \theta = \beta$, corresponding to $\cos \theta^* = 0$.

Inverse transformation

To get the final $E, \cos \theta$ distribution for a given E^* , we must invert the relations yielding $E, \cos \theta$ as functions of $E_\pi, \cos \theta^*$. This is done as follows:

From (A.4) and (A.5) one easily deduce the following equations:

$$\gamma = \frac{1 - \cos \theta \cos \theta^*}{\sin \theta \sin \theta^*} \quad (\text{A.15})$$

$$\beta = \frac{\cos \theta - \cos \theta^*}{1 - \cos \theta \cos \theta^*} \quad (\text{A.16})$$

We further define: $r = \frac{E}{E^*}$ so that (A.5) becomes $\sin \theta^* = r \sin \theta$.

Hence (A.15) and (A.16) become:

$$\gamma = \frac{1 - \cos \theta \epsilon \sqrt{1 - r^2 \sin^2 \theta}}{r \sin \theta^2} \quad (\text{A.17})$$

$$\beta = \frac{\cos \theta - \epsilon \sqrt{1 - r^2 \sin^2 \theta}}{1 - \cos \theta \epsilon \sqrt{1 - r^2 \sin^2 \theta}} \quad (\text{A.18})$$

with $\epsilon = \pm 1$ according to whether $\cos \theta^* > 0$ or $\cos \theta^* < 0$, that is, $\cos \theta > \beta$ or $\cos \theta < \beta$.

Observe that (A.16) implies that $\cos \theta^*$ is always smaller than $\cos \theta$. We also get from (A.18)

$$\frac{\cos \theta - \beta}{\beta} = \frac{\sin \theta^2 \epsilon \sqrt{1 - r^2 \sin^2 \theta}}{\cos \theta - \epsilon \sqrt{1 - r^2 \sin^2 \theta}} \quad (\text{A.19})$$

This allows us to rewrite the Jacobian in terms of final state variables as:

$$\frac{D(E_\pi, \cos \theta^*)}{D(E, \cos \theta)} = \frac{m_\pi}{E^*} \frac{\cos \theta - \epsilon \sqrt{1 - r^2 \sin^2 \theta}}{\sin \theta^2 \sqrt{1 - r^2 \sin^2 \theta}} \quad (\text{A.20})$$

So for every $(\cos \theta, E)$ there are two possible $(\cos \theta^*, E_\pi)$ corresponding to the two choices of ϵ .

The solution with $\epsilon = 1$ corresponds to a lower E_π and $\cos \theta^* > 0$ while the solution with $\epsilon = -1$ corresponds to a larger E_π required by the backward ($\cos \theta^* < 0$) projection of the neutrino in the decaying meson frame.

Therefore to get the joint distribution for $(\cos \theta, E)$ we must add the contributions of these two solutions. The joint distribution for E_π and Ω^* which is simply $\frac{g(E_\pi)}{4\pi}$ is transformed to:

$$\frac{\partial^2 P}{\partial E \partial \Omega} = \frac{m_\pi}{4\pi E^* \sin \theta^2 \sqrt{1 - r^2 \sin^2 \theta^2}} \left[g(m_\pi \gamma_+) |\cos \theta - \sqrt{1 - r^2 \sin^2 \theta^2}| + g(m_\pi \gamma_-) |\cos \theta + \sqrt{1 - r^2 \sin^2 \theta^2}| \right] \quad (\text{A.21})$$

where γ_\pm means (A.17) with $\epsilon = \pm 1$ and as before, $r = E/E^*$. In case $r \leq 1$, only the second term is to be kept.

This must be multiplied by the probability density of E^* and integrated over it to get the final distribution in $(\cos \theta, E)$. In the case of a 2-body decay, this E^* density is simply $\delta(E^* - E_0^*)$ where E_0^* is a constant given by the conservation laws in the decay as seen above and the integration results in the mere replacement $E^* \rightarrow E_0^*$ in (A.21).

Appendix B

Neutrino fluxes up to 10 GeV neutrino energy

Neutrino fluxes shown up to 2 GeV neutrino energy in Chapter 2 are presented up to 10 GeV in this appendix for both near and far detectors and all four contributions described in Section 2.3.1 and Section 2.3.2. The neutrino energy binning suggested in [75] is used.

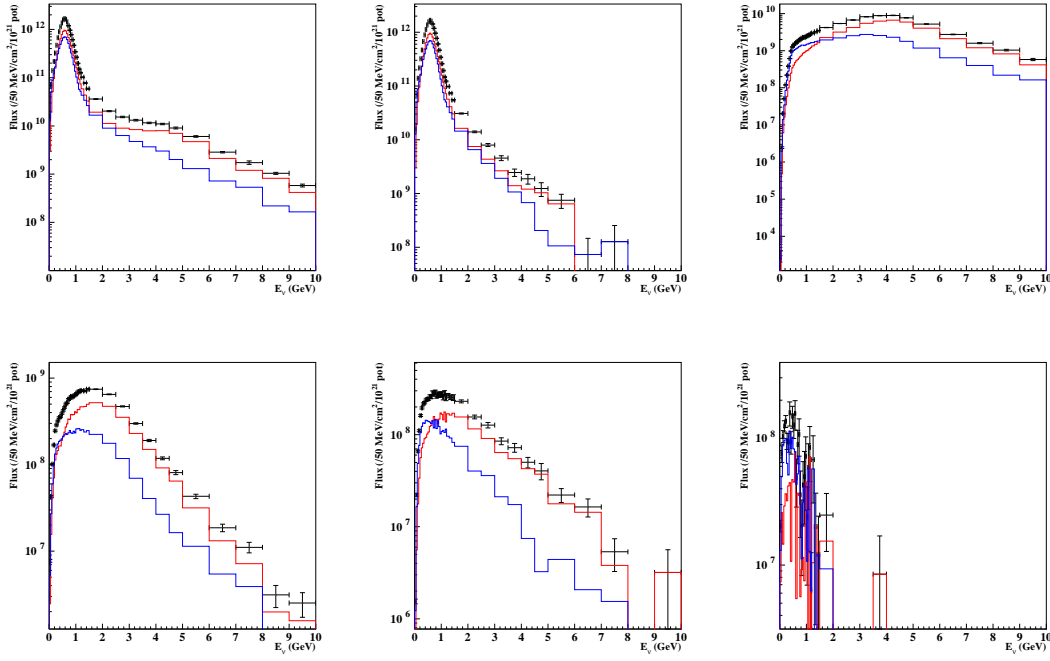


Figure B.1: ν_μ flux from all contributions (top left), from π^+ (top middle), from $K_{\mu 2}^+$ (top right), from $K_{\mu 3}^+$ (bottom left), from $K_{\mu 3}^0$ (bottom middle) and from μ^- (bottom right) decays at the near detector. Direct (red) and indirect (blue) contributions are shown for each parent particle.

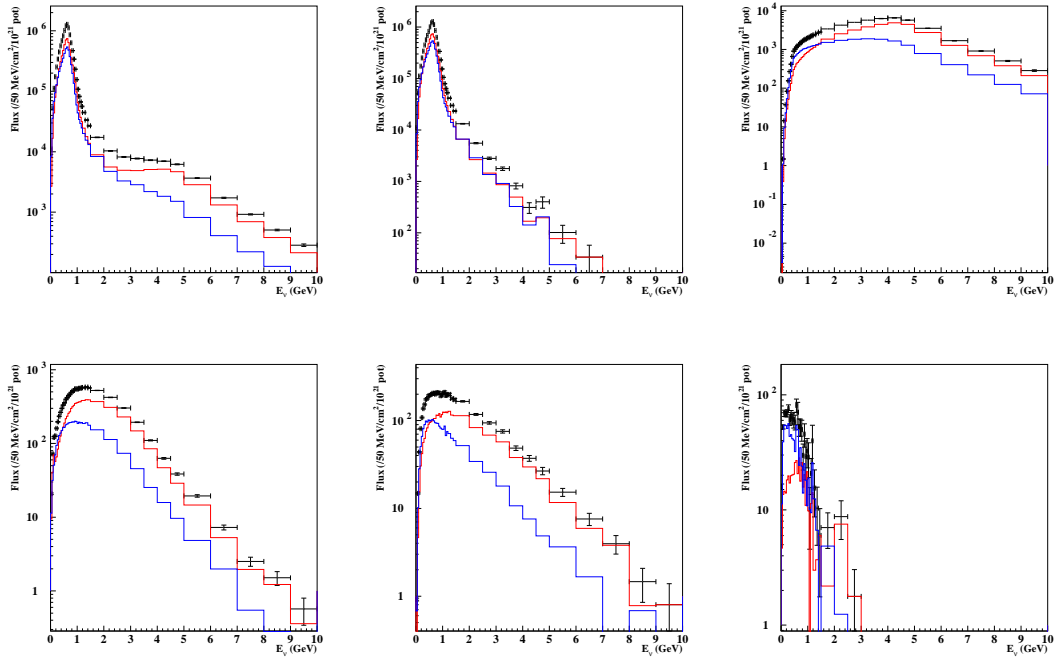


Figure B.2: ν_μ flux from all contributions (top left), from π^+ (top middle), from $K_{\mu 2}^+$ (top right), from $K_{\mu 3}^+$ (bottom left), from $K_{\mu 3}^0$ (bottom middle) and from μ^- (bottom right) decays at the far detector. Direct (red) and indirect (blue) contributions are shown for each parent particle.

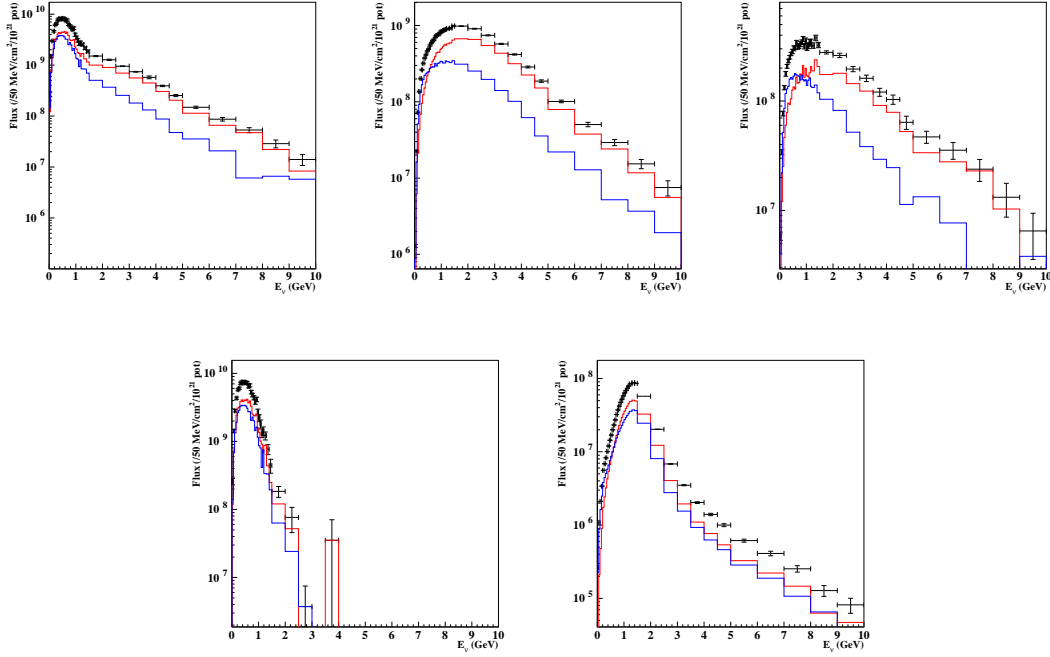


Figure B.3: ν_e flux from all contributions (top left), from K_{e3}^+ (top middle), from K_{e3}^0 (top right), from μ^+ (bottom left) and from π^+ (bottom right) decays at the near detector. Direct (red) and indirect (blue) contributions are shown for each parent particle.

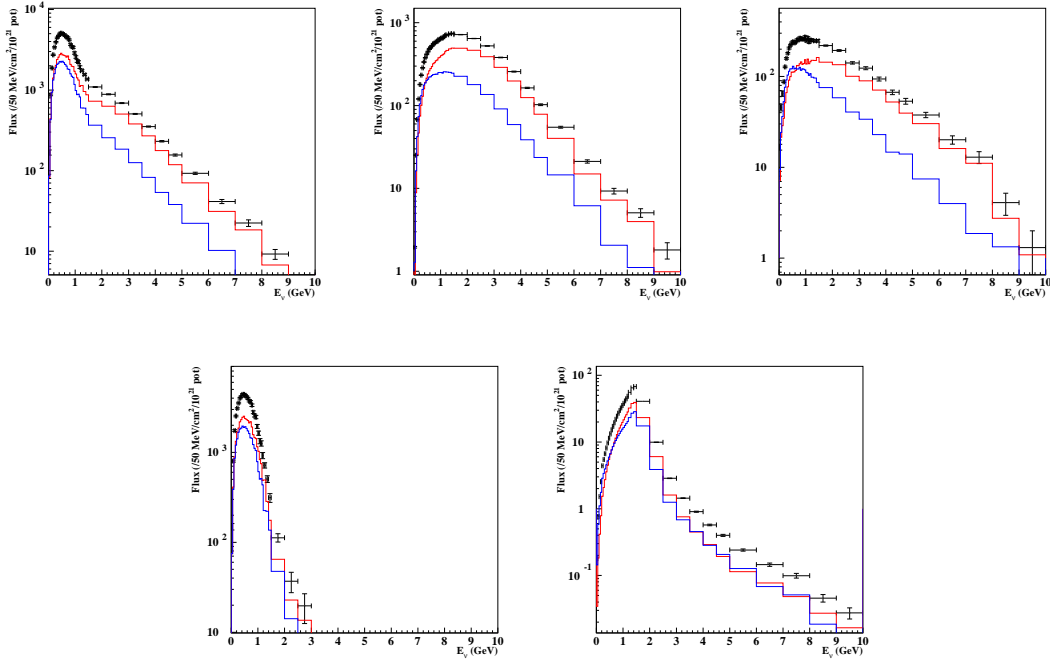


Figure B.4: ν_e flux from all contributions (top left), from K_{e3}^+ (top middle), from K_{e3}^0 (top right), from μ^+ (bottom left) and from π^+ (bottom right) decays at the far detector. Direct (red) and indirect (blue) contributions are shown for each parent particle.

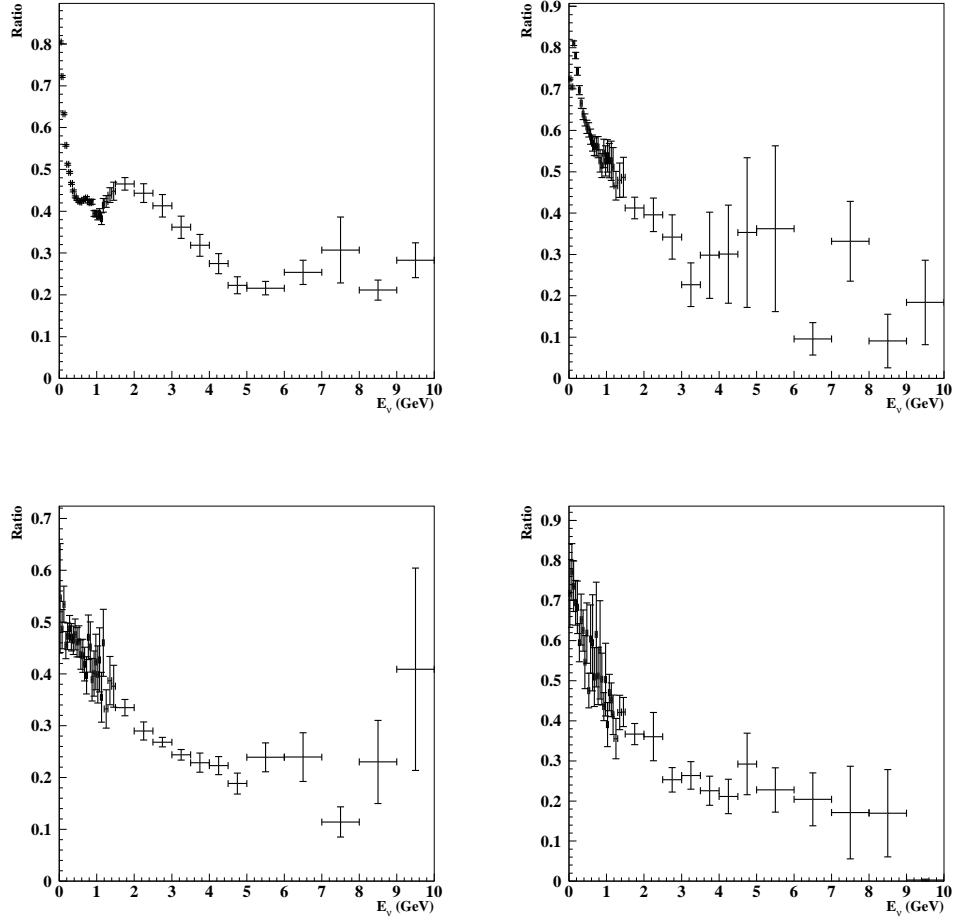


Figure B.5: Ratio of indirect contribution over total contribution for ν_μ (top left), $\bar{\nu}_\mu$ (top right), ν_e (bottom left) and $\bar{\nu}_e$ (bottom right) fluxes at the near detector.

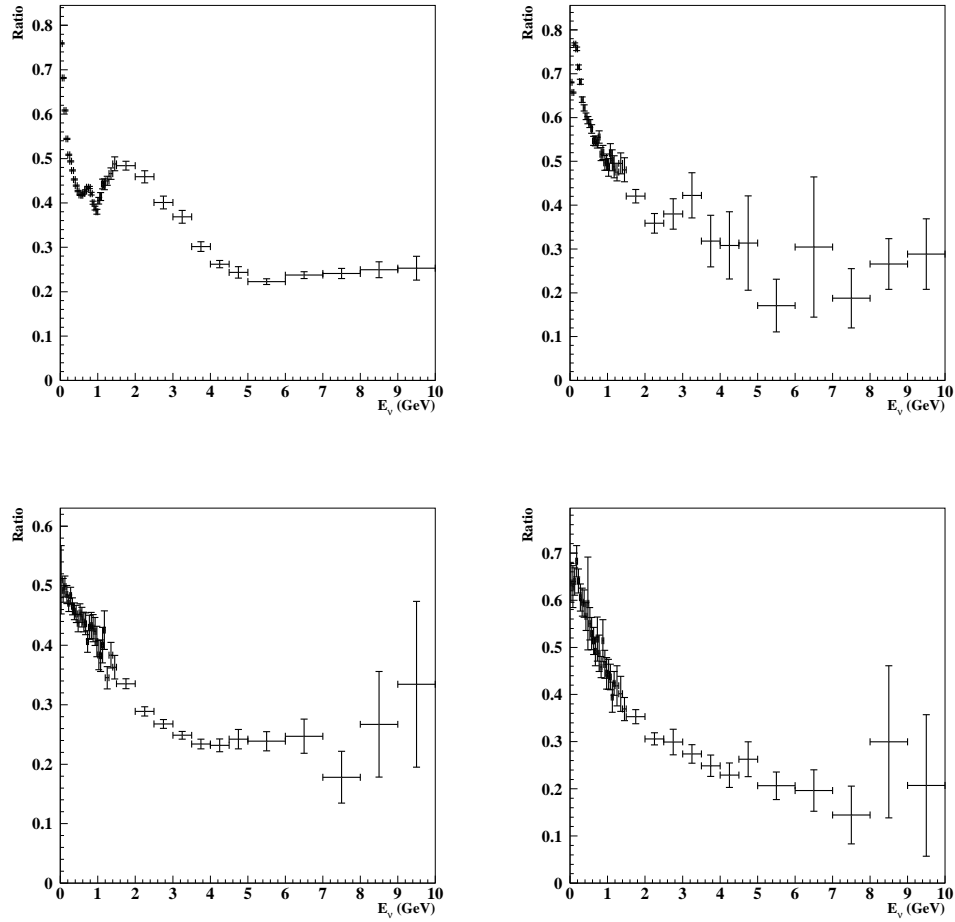


Figure B.6: Ratio of indirect contribution over total contribution for ν_μ (top left), $\bar{\nu}_\mu$ (top right), ν_e (bottom left) and $\bar{\nu}_e$ (bottom right) fluxes at the near detector.

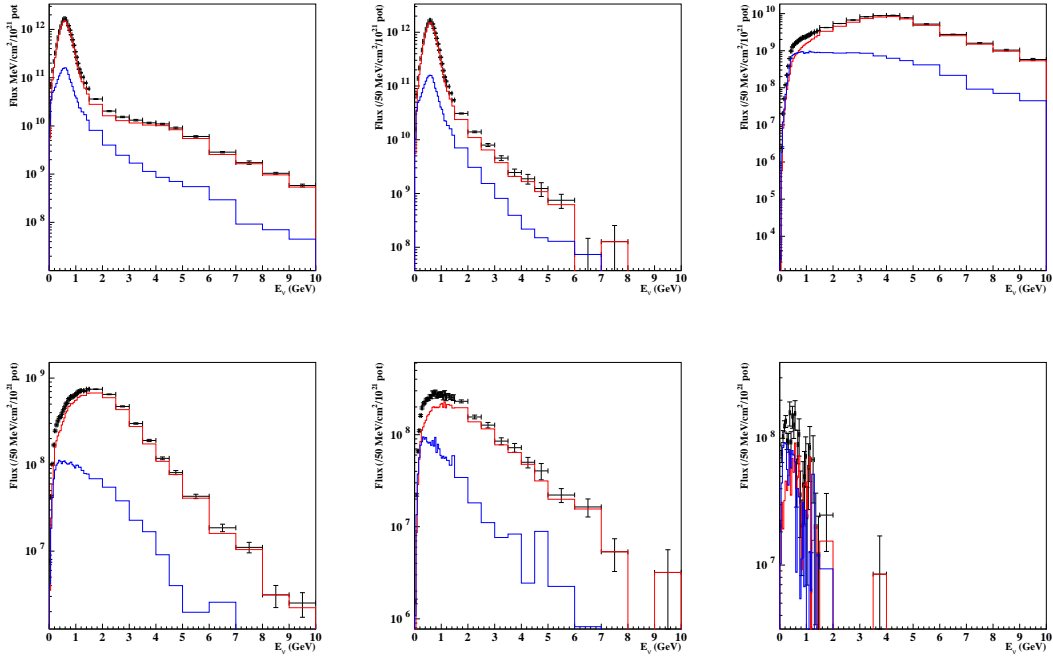


Figure B.7: ν_μ flux from all contributions (top left), from π^+ (top middle), from $K_{\mu 2}^+$ (top right), from $K_{\mu 3}^+$ (bottom left), from $K_{\mu 3}^0$ (bottom middle) and from μ^- (bottom right) decays at the near detector. Target (red) and non-target (blue) contributions are shown for each parent particle.

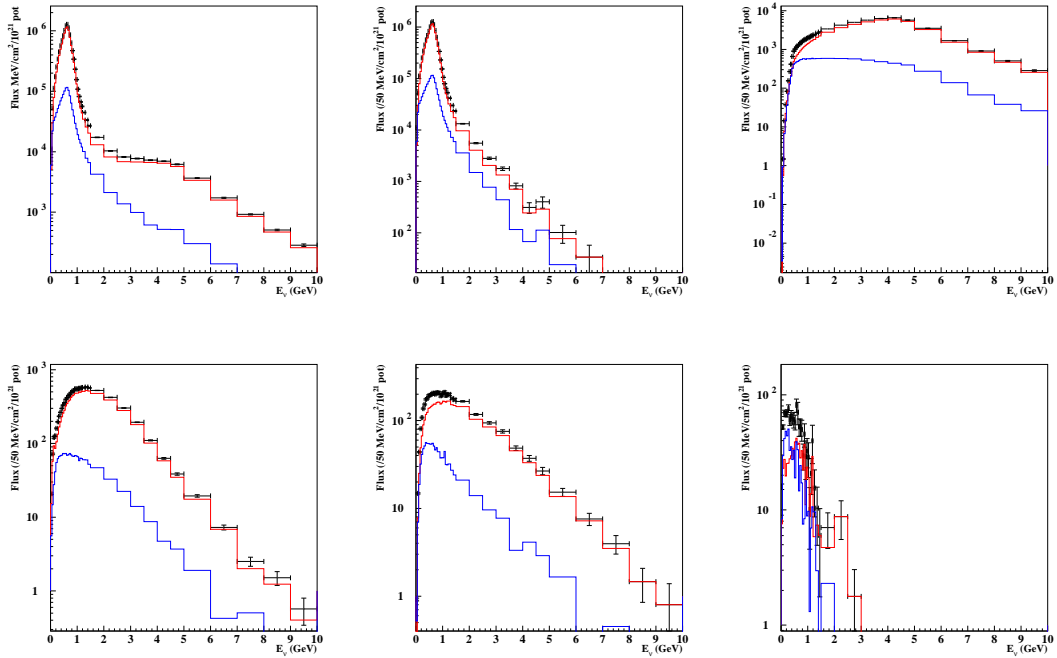


Figure B.8: ν_μ flux from all contributions (top left), from π^+ (top middle), from $K_{\mu 2}^+$ (top right), from $K_{\mu 3}^+$ (bottom left), from $K_{\mu 3}^0$ (bottom middle) and from μ^- (bottom right) decays at the far detector. Target (red) and non-target (blue) contributions are shown for each parent particle.

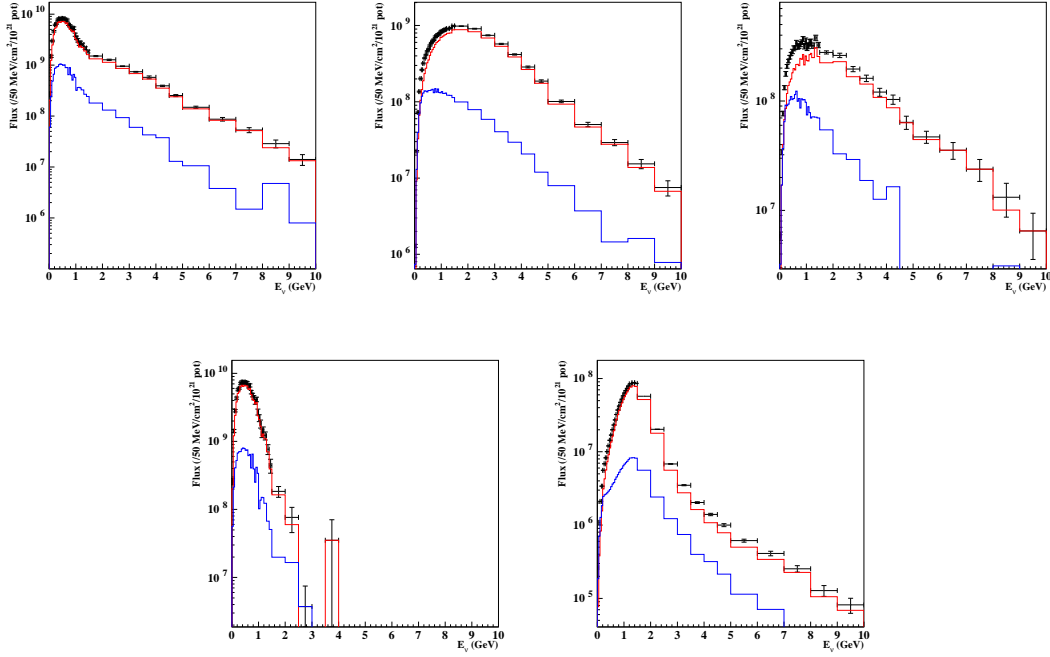


Figure B.9: ν_e flux from all contributions (top left), from K_{e3}^+ (top middle), from K_{e3}^0 (top right), from μ^+ (bottom left) and from π^+ (bottom right) decays at the near detector. Target (red) and non-target (blue) contributions are shown for each parent particle.

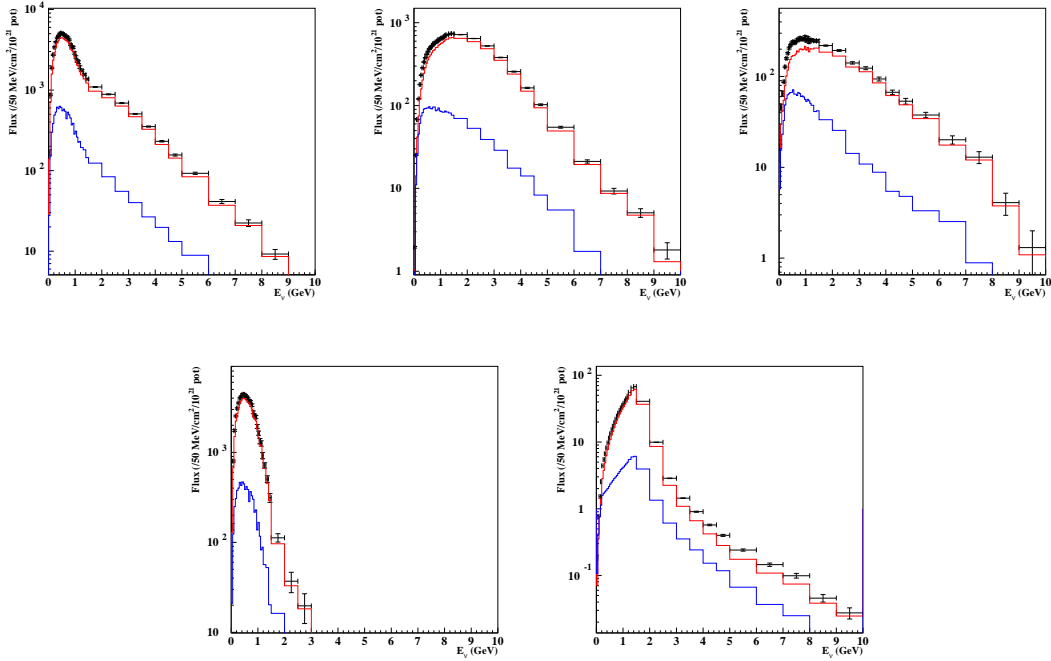


Figure B.10: ν_e flux from all contributions (top left), from K_{e3}^+ (top middle), from K_{e3}^0 (top right), from μ^+ (bottom left) and from π^+ (bottom right) decays at the far detector. Target (red) and non-target (blue) contributions are shown for each parent particle.

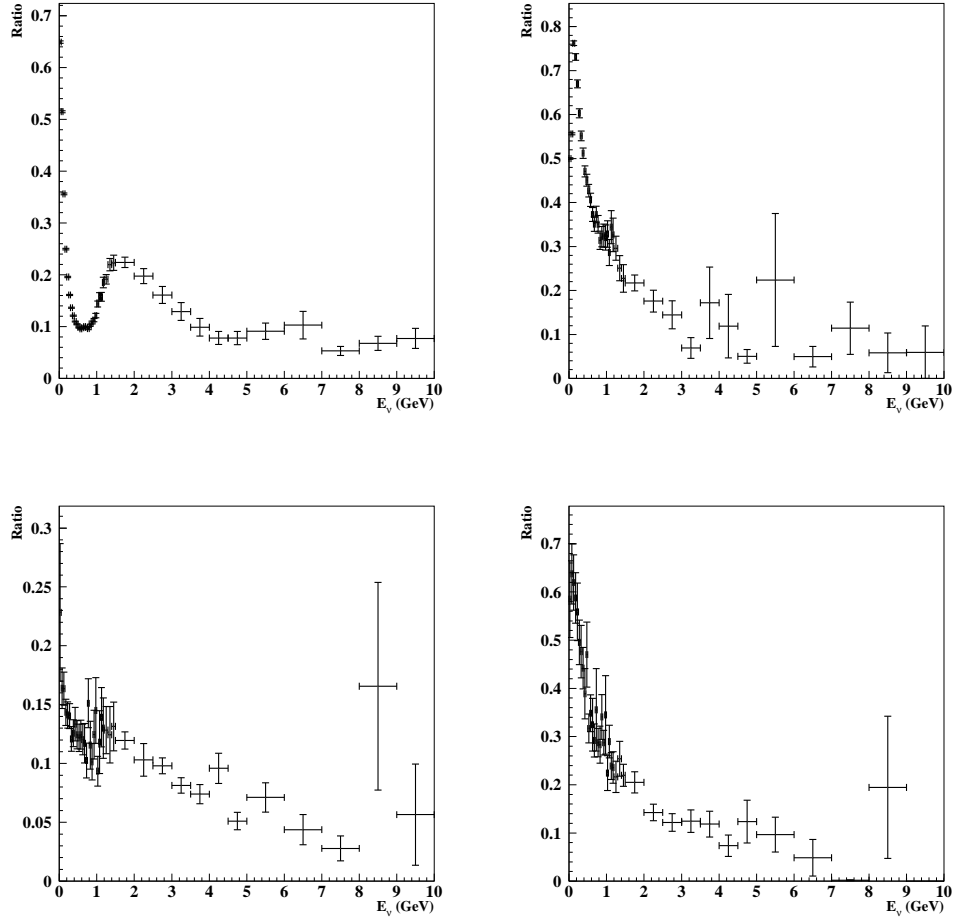


Figure B.11: Ratio of indirect contribution over total contribution for ν_μ (top left), $\bar{\nu}_\mu$ (top right), ν_e (bottom left) and $\bar{\nu}_e$ (bottom right) fluxes at the near detector.

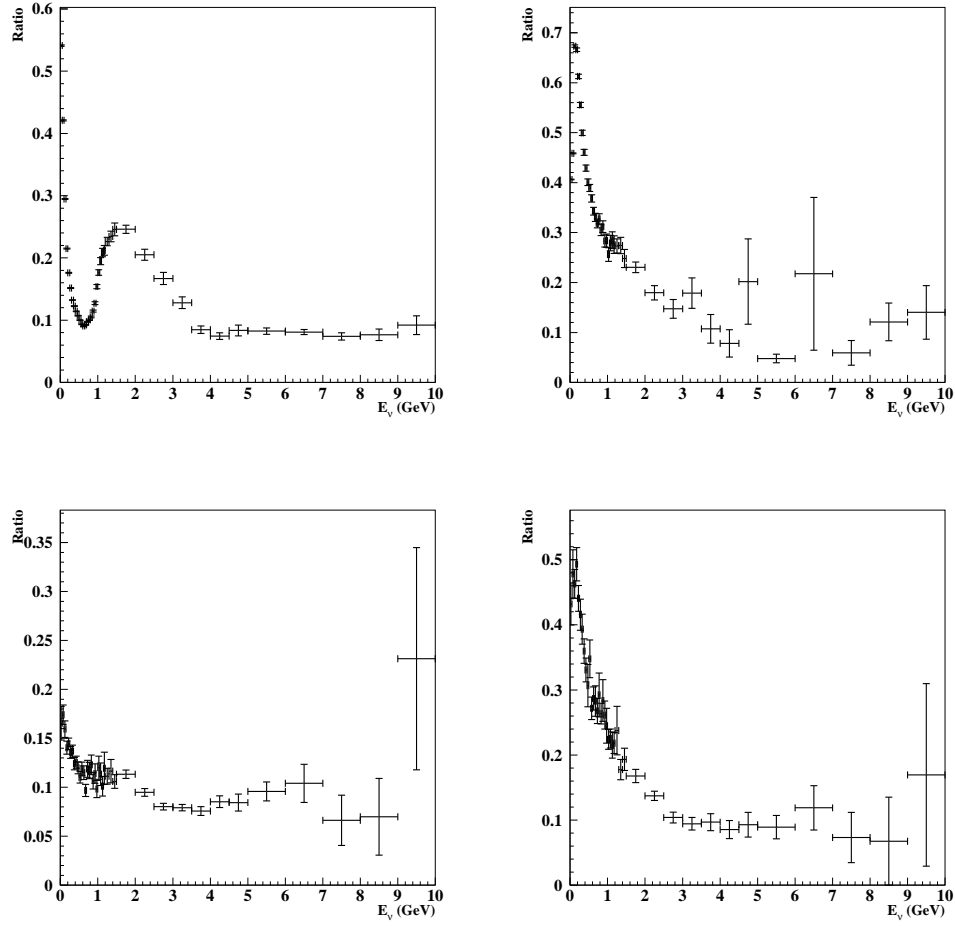


Figure B.12: Ratio of indirect contribution over total contribution for ν_μ (top left), $\bar{\nu}_\mu$ (top right), ν_e (bottom left) and $\bar{\nu}_e$ (bottom right) fluxes at the near detector.

Appendix C

$\{p, \theta\}$ phase space distributions

Phase space of hadrons producing neutrinos in the near and far detectors for contributions described in Section 2.3.1 and Section 2.3.2 are shown in this appendix.

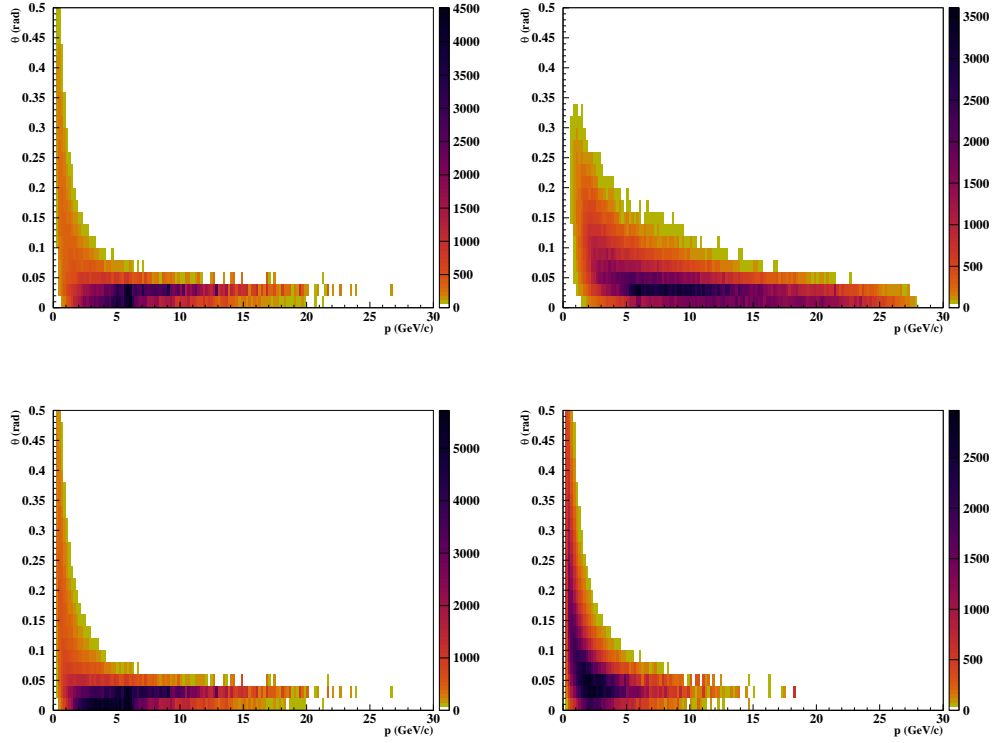


Figure C.1: The $\{p, \theta\}$ distributions of secondary π^- giving neutrinos in the far detector for the direct (top left) and indirect (top right) contributions, and of parent π^- for the target (bottom left) and non-target (bottom right) contributions are shown.

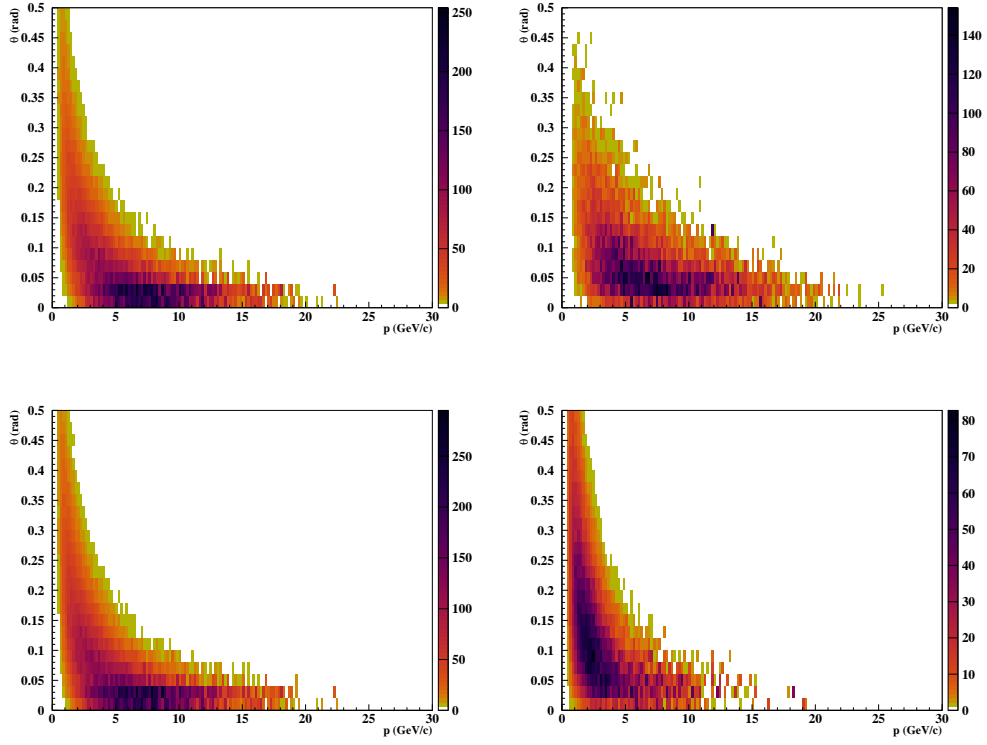


Figure C.2: The $\{p, \theta\}$ distributions of secondary K^- giving neutrinos in the far detector for the direct (top left) and indirect (top right) contributions, and of parent K^- for the target (bottom left) and non-target (bottom right) contributions are shown.

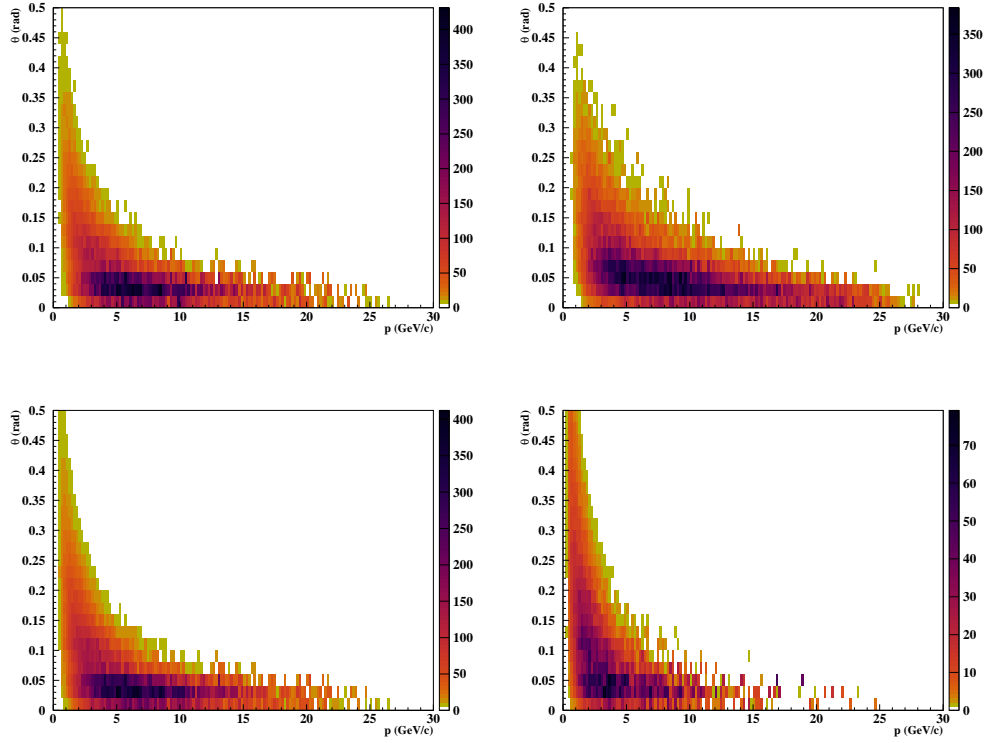


Figure C.3: The $\{p, \theta\}$ distributions of secondary K_L^0 giving neutrinos in the far detector for the direct (top left) and indirect (top right) contributions, and of parent K_L^0 for the target (bottom left) and non-target (bottom right) contributions are shown.

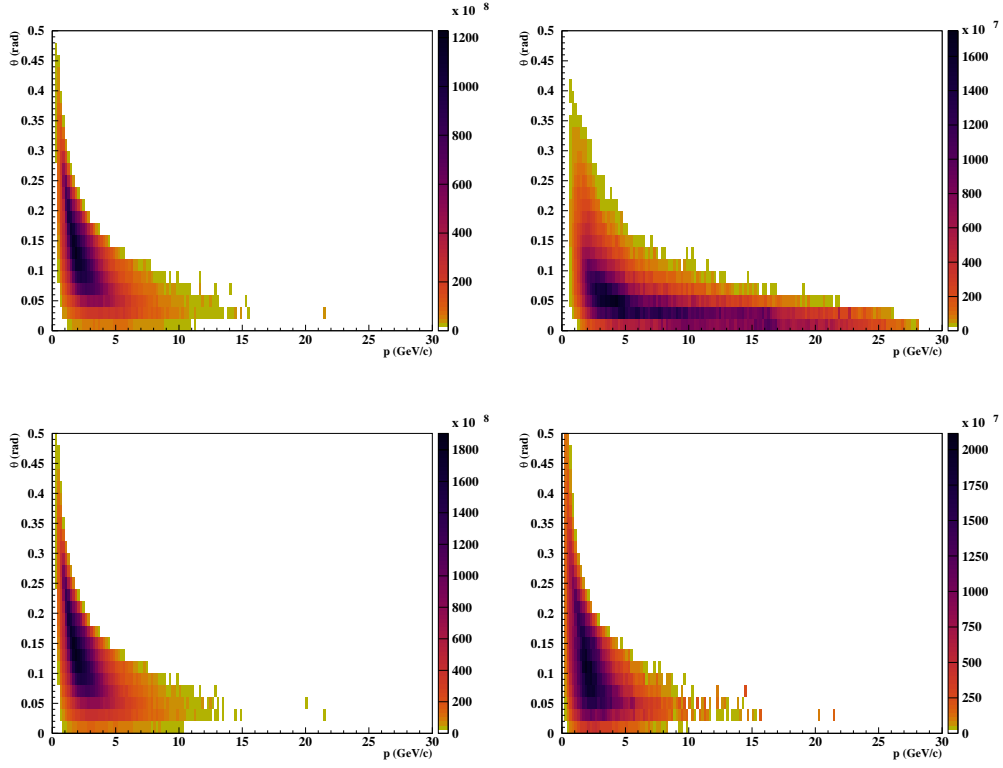


Figure C.4: The $\{p, \theta\}$ distributions of secondary π^+ giving neutrinos in the near detector for the direct (top left) and indirect (top right) contributions, and of parent π^+ for the target (bottom left) and non-target (bottom right) contributions are shown.

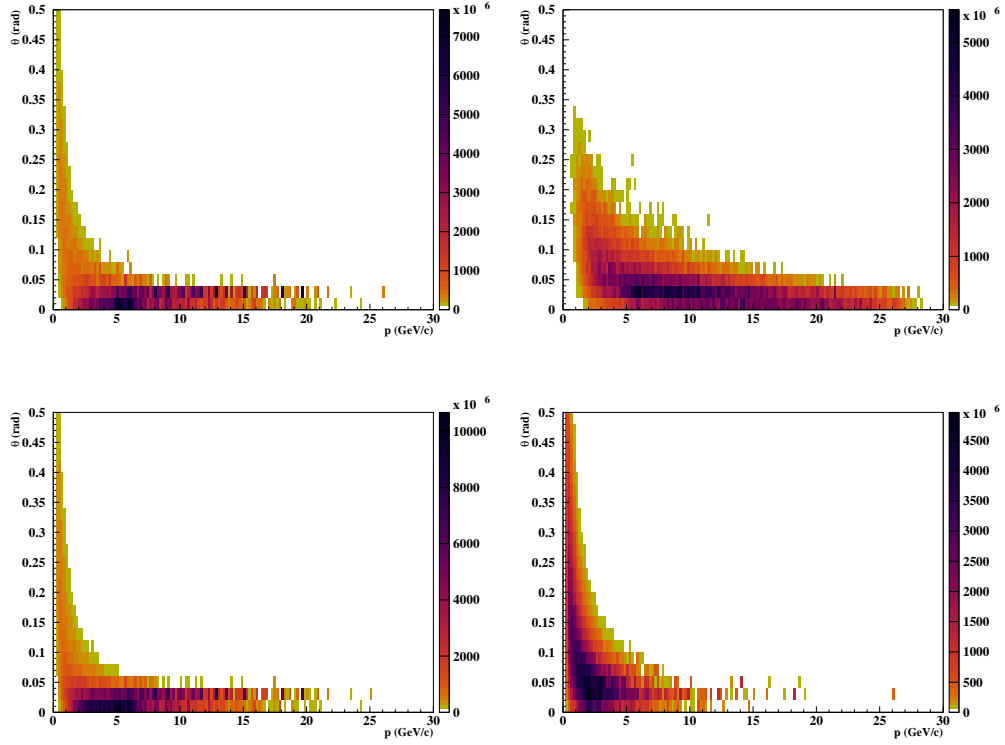


Figure C.5: The $\{p, \theta\}$ distributions of secondary π^- giving neutrinos in the near detector for the direct (top left) and indirect (top right) contributions, and of parent π^- for the target (bottom left) and non-target (bottom right) contributions are shown.

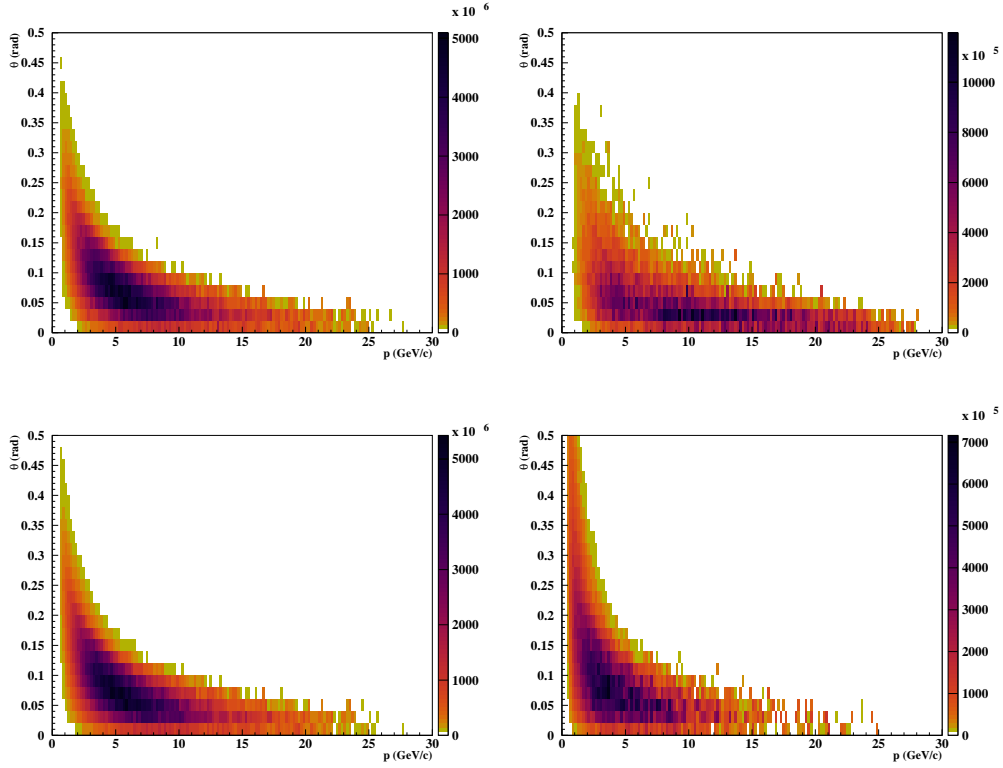


Figure C.6: The $\{p, \theta\}$ distributions of secondary K^+ giving neutrinos in the near detector for the direct (top left) and indirect (top right) contributions, and of parent K^+ for the target (bottom left) and non-target (bottom right) contributions are shown.

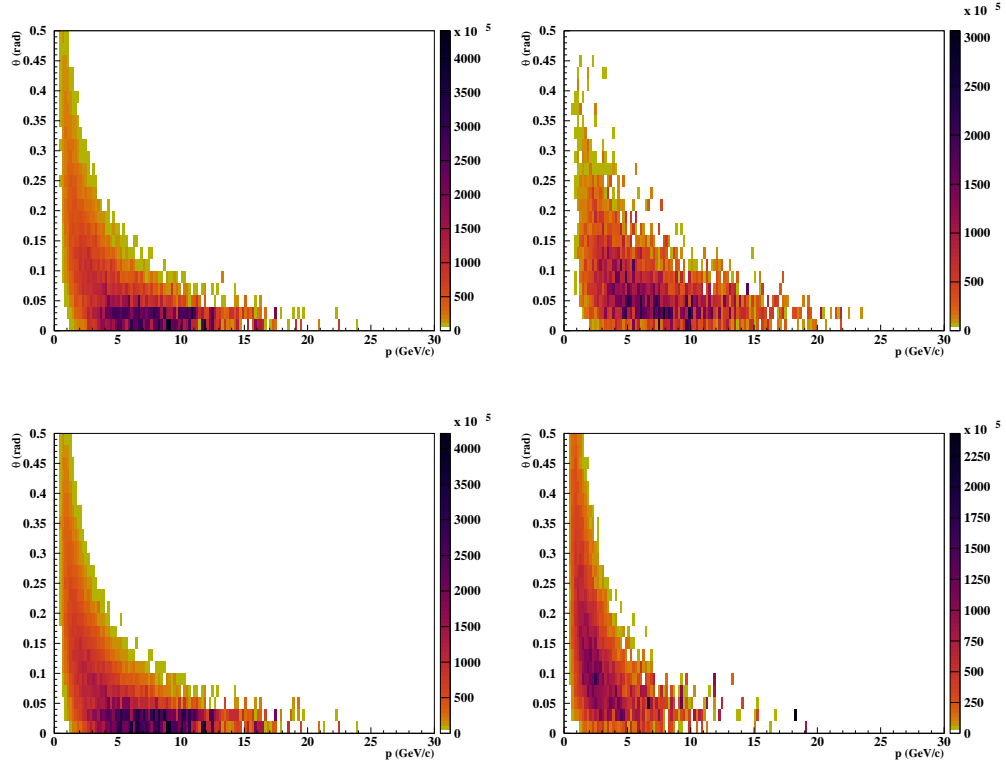


Figure C.7: The $\{p, \theta\}$ distributions of secondary K^- giving neutrinos in the near detector for the direct (top left) and indirect (top right) contributions, and of parent K^- for the target (bottom left) and non-target (bottom right) contributions are shown.

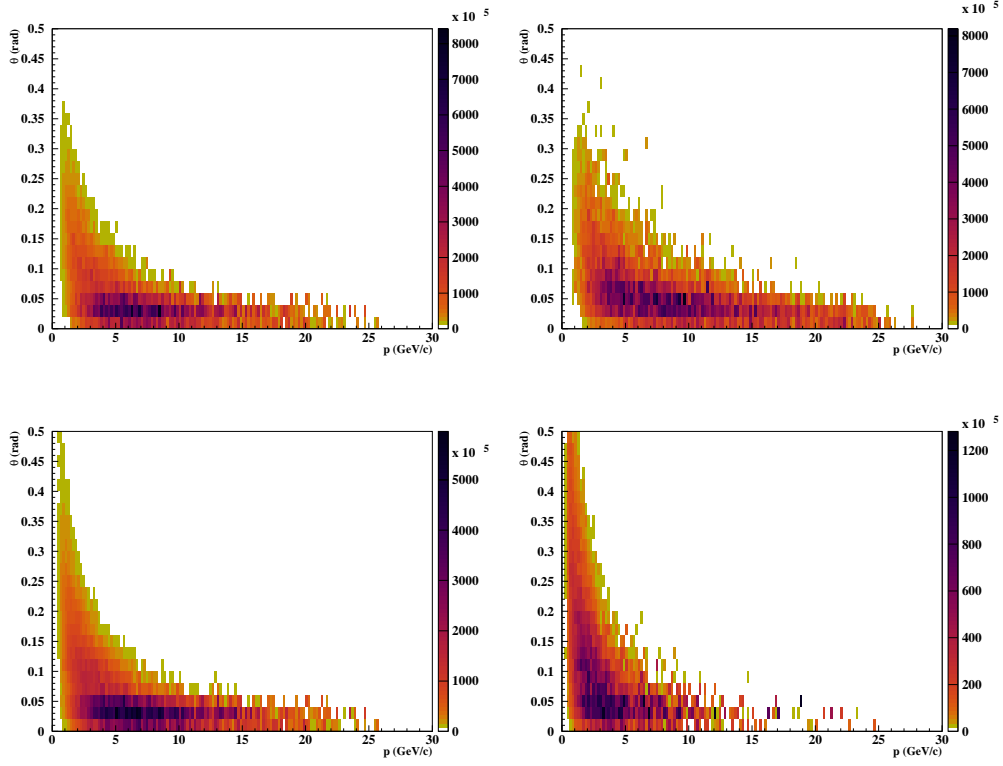


Figure C.8: The $\{p, \theta\}$ distributions of secondary K_L^0 giving neutrinos in the near detector for the direct (top left) and indirect (top right) contributions, and of parent K_L^0 for the target (bottom left) and non-target (bottom right) contributions are shown.

Appendix D

Raw yields of positively charged pions on target

$z = 1$						
Δp [GeV/c]	$dn_{\pi}^{NA61}/dp (\times 10^{-3})$ [/(GeV/c)/p.o.t.]	$\pm \text{stat.}$	$\pm \text{syst.}$	$dn_{\pi}^{FLUKA}/dp (\times 10^{-3})$ [/(GeV/c)/p.o.t.]	$\pm \text{stat.}$	$\pm \text{syst.}$
$20 < \theta < 100 \text{ mrad}$						
0.8-1.6	0.294	0.0653	0.00625	0.272	0.0215	0.00438
1.6-2.4	0.849	0.098	0.018	0.921	0.043	0.0148
$40 < \theta < 100 \text{ mrad}$						
2.4-3.2	0.968	0.098	0.0206	1.09	0.0469	0.0176
3.2-4	0.957	0.109	0.0204	1.18	0.045	0.019
4-4.8	0.773	0.098	0.0235	0.966	0.0469	0.0166
4.8-6.4	0.571	0.0544	0.0174	0.678	0.0274	0.0117
6.4-8	0.299	0.0381	0.0091	0.427	0.0196	0.00735
8-9.6	0.169	0.0326	0.00941	0.165	0.0147	0.0081
9.6-12.8	0.0789	0.0163	0.0044	0.0767	0.00733	0.00376
12.8-16	0.0218	0.00816	0.00121	0.0186	0.0044	0.000911
$100 < \theta < 160 \text{ mrad}$						
0.8-1.6	0.827	0.0871	0.0176	0.852	0.0411	0.0137
1.6-2.4	1.18	0.12	0.025	1.4	0.0509	0.0225
2.4-3.2	1.13	0.109	0.0241	1.46	0.0528	0.0236
3.2-4	0.816	0.098	0.0173	1.02	0.0489	0.0165
4-5.6	0.299	0.049	0.0091	0.49	0.0225	0.00843
5.6-7.2	0.131	0.0272	0.00397	0.194	0.0137	0.00333
7.2-10.4	0.0354	0.0109	0.00197	0.0298	0.0044	0.00146
$160 < \theta < 280 \text{ mrad}$						
0.8-1.6	1.9	0.12	0.0405	2.4	0.0685	0.0388
1.6-2.4	1.09	0.109	0.0231	1.53	0.0509	0.0247
$160 < \theta < 240 \text{ mrad}$						
2.4-4	0.413	0.049	0.00879	0.415	0.0215	0.0067
$160 < \theta < 200 \text{ mrad}$						
4-7.2	0.0408	0.0136	0.00124	0.0596	0.00587	0.00103

Table D.1: Raw yields of positively charged pions in data (left) and simulation (right) for the first longitudinal bin along the target and different angular intervals. Quoted yields are normalized to 114885 p.o.t. in data and 639355 p.o.t. in the simulation.

$z = 2$						
Δp [GeV/c]	$dn_{\pi}^{NA61}/dp (\times 10^{-3})$ [/(GeV/c)/p.o.t.]	$\pm \text{stat.}$	$\pm \text{syst.}$	$dn_{\pi}^{FLUKA}/dp (\times 10^{-3})$ [/(GeV/c)/p.o.t.]	$\pm \text{stat.}$	$\pm \text{syst.}$
$20 < \theta < 100 \text{ mrad}$						
0.8-1.6	0.729	0.0871	0.0155	0.794	0.0372	0.0128
1.6-2.4	1.75	0.142	0.0372	2.13	0.0626	0.0343
$40 < \theta < 100 \text{ mrad}$						
2.4-3.2	2.71	0.196	0.0576	2.82	0.0763	0.0454
3.2-4	2.95	0.185	0.0627	3.19	0.0881	0.0515
4-4.8	2.71	0.185	0.0824	2.88	0.0822	0.0496
4.8-6.4	1.76	0.109	0.0534	1.99	0.0441	0.0343
6.4-8	1.05	0.0817	0.0319	1.1	0.0342	0.0189
8-9.6	0.501	0.049	0.0279	0.627	0.0254	0.0307
9.6-12.8	0.239	0.0245	0.0134	0.257	0.0122	0.0126
12.8-16	0.0626	0.049	0.00349	0.0767	0.00684	0.00376
$100 < \theta < 160 \text{ mrad}$						
0.8-1.6	1.61	0.12	0.0342	1.61	0.0587	0.0259
1.6-2.4	2.03	0.142	0.0433	2.63	0.0744	0.0425
2.4-3.2	2.06	0.142	0.0437	2.72	0.0646	0.0439
3.2-4	1.51	0.131	0.0322	1.79	0.0646	0.0288
4-5.6	0.783	0.0708	0.0238	0.989	0.0342	0.017
5.6-7.2	0.462	0.049	0.0141	0.347	0.0196	0.00597
7.2-10.4	0.0734	0.0136	0.0041	0.085	0.00635	0.00417
$160 < \theta < 280 \text{ mrad}$						
0.8-1.6	2.74	0.142	0.0583	3.51	0.0822	0.0565
1.6-2.4	1.63	0.131	0.0347	2.25	0.0665	0.0363
$160 < \theta < 240 \text{ mrad}$						
2.4-4	0.56	0.0544	0.0119	0.595	0.0245	0.0096
$160 < \theta < 200 \text{ mrad}$						
4-7.2	0.0762	0.0136	0.00232	0.0611	0.00587	0.00105

Table D.2: Raw yields of positively charged pions in data (left) and simulation (right) for the second longitudinal bin along the target and different angular intervals. Quoted yields are normalized to 114885 p.o.t. in data and 639355 p.o.t. in the simulation.

$z = 3$						
Δp [GeV/c]	$dn_{\pi}^{NA61}/dp (\times 10^{-3})$ [/(GeV/c)/p.o.t.]	$\pm \text{stat.}$	$\pm \text{syst.}$	$dn_{\pi}^{FLUKA}/dp (\times 10^{-3})$ [/(GeV/c)/p.o.t.]	$\pm \text{stat.}$	$\pm \text{syst.}$
$20 < \theta < 100 \text{ mrad}$						
0.8-1.6	0.598	0.0762	0.0127	0.649	0.0332	0.0105
1.6-2.4	2.14	0.152	0.0456	2.17	0.0646	0.035
$40 < \theta < 100 \text{ mrad}$						
2.4-3.2	2.47	0.174	0.0525	2.57	0.0744	0.0415
3.2-4	2.92	0.196	0.062	3.02	0.0744	0.0487
4-4.8	2.24	0.174	0.0682	2.6	0.0783	0.0448
4.8-6.4	1.71	0.103	0.052	1.8	0.0431	0.0309
6.4-8	1.13	0.0817	0.0342	0.981	0.0323	0.0169
8-9.6	0.571	0.0599	0.0319	0.528	0.0244	0.0259
9.6-12.8	0.256	0.0299	0.0143	0.235	0.0112	0.0115
12.8-16	0.0843	0.0163	0.0047	0.0694	0.00587	0.0034
$100 < \theta < 160 \text{ mrad}$						
0.8-1.6	1.28	0.109	0.0273	1.27	0.0469	0.0205
1.6-2.4	1.58	0.131	0.0335	1.98	0.0626	0.0319
2.4-3.2	1.55	0.131	0.0328	2.25	0.0724	0.0363
3.2-4	1.36	0.12	0.0289	1.6	0.0587	0.0259
4-5.6	0.691	0.0762	0.021	0.775	0.0303	0.0133
5.6-7.2	0.305	0.0381	0.00927	0.281	0.0176	0.00483
7.2-10.4	0.0816	0.0136	0.00455	0.0567	0.00587	0.00278
$160 < \theta < 280 \text{ mrad}$						
0.8-1.6	2.23	0.142	0.0474	2.77	0.0685	0.0446
1.6-2.4	1.52	0.131	0.0324	1.94	0.0626	0.0312
$160 < \theta < 240 \text{ mrad}$						
2.4-4	0.424	0.0544	0.00902	0.45	0.0215	0.00725
$160 < \theta < 200 \text{ mrad}$						
4-7.2	0.0571	0.0136	0.00174	0.0528	0.00538	0.000908

Table D.3: Raw yields of positively charged pions in data (left) and simulation (right) for the third longitudinal bin along the target and different angular intervals. Quoted yields are normalized to 114885 p.o.t. in data and 639355 p.o.t. in the simulation.

$z = 4$						
Δp [GeV/c]	$dn_{\pi}^{NA61}/dp (\times 10^{-3})$ [/(GeV/c)/p.o.t.]	$\pm \text{stat.}$	$\pm \text{syst.}$	$dn_{\pi}^{FLUKA}/dp (\times 10^{-3})$ [/(GeV/c)/p.o.t.]	$\pm \text{stat.}$	$\pm \text{syst.}$
$20 < \theta < 100 \text{ mrad}$						
0.8-1.6	0.533	0.0762	0.0113	0.547	0.0313	0.00883
1.6-2.4	1.7	0.131	0.0361	1.61	0.0548	0.0259
$40 < \theta < 100 \text{ mrad}$						
2.4-3.2	1.78	0.142	0.0379	1.98	0.0626	0.0319
3.2-4	2.32	0.152	0.0493	2.12	0.0607	0.0342
4-4.8	1.91	0.152	0.0582	1.9	0.0665	0.0328
4.8-6.4	1.35	0.098	0.041	1.28	0.0362	0.022
6.4-8	0.664	0.0599	0.0202	0.693	0.0264	0.0119
8-9.6	0.419	0.049	0.0234	0.355	0.0186	0.0174
9.6-12.8	0.141	0.0218	0.00789	0.134	0.00929	0.00659
12.8-16	0.0435	0.0109	0.00243	0.0396	0.00489	0.00194
$100 < \theta < 160 \text{ mrad}$						
0.8-1.6	1.07	0.109	0.0227	0.882	0.043	0.0142
1.6-2.4	1.24	0.12	0.0264	1.27	0.0509	0.0205
2.4-3.2	1.46	0.131	0.031	1.61	0.0567	0.026
3.2-4	1.22	0.109	0.0259	1.13	0.0489	0.0182
4-5.6	0.452	0.0544	0.0137	0.567	0.0254	0.00975
5.6-7.2	0.245	0.0381	0.00745	0.223	0.0147	0.00383
7.2-10.4	0.068	0.0136	0.00379	0.0538	0.00538	0.00264
$160 < \theta < 280 \text{ mrad}$						
0.8-1.6	1.86	0.142	0.0396	2.06	0.0548	0.0332
1.6-2.4	0.925	0.098	0.0197	1.45	0.0528	0.0233
$160 < \theta < 240 \text{ mrad}$						
2.4-4	0.277	0.0381	0.0059	0.35	0.0196	0.00564
$160 < \theta < 200 \text{ mrad}$						
4-7.2	0.0381	0.0109	0.00116	0.0347	0.00391	0.000597

Table D.4: Raw yields of positively charged pions in data (left) and simulation (right) for the fourth longitudinal bin along the target and different angular intervals. Quoted yields are normalized to 114885 p.o.t. in data and 639355 p.o.t. in the simulation.

$z = 5$						
Δp [GeV/c]	$dn_{\pi}^{NA61}/dp (\times 10^{-3})$ [/(GeV/c)/p.o.t.]	$\pm \text{stat.}$	$\pm \text{syst.}$	$dn_{\pi}^{FLUKA}/dp (\times 10^{-3})$ [/(GeV/c)/p.o.t.]	$\pm \text{stat.}$	$\pm \text{syst.}$
$20 < \theta < 100 \text{ mrad}$						
0.8-1.6	0.305	0.0544	0.00648	0.342	0.0254	0.00552
1.6-2.4	1.1	0.109	0.0234	1.07	0.0469	0.0173
$40 < \theta < 100 \text{ mrad}$						
2.4-3.2	1.46	0.12	0.031	1.43	0.0548	0.0231
3.2-4	1.61	0.12	0.0342	1.44	0.0548	0.0233
4-4.8	1.26	0.12	0.0384	1.32	0.0509	0.0227
4.8-6.4	0.8	0.0653	0.0243	0.825	0.0293	0.0142
6.4-8	0.49	0.0599	0.0149	0.45	0.0215	0.00774
8-9.6	0.228	0.0326	0.0127	0.213	0.0156	0.0105
9.6-12.8	0.087	0.0163	0.00486	0.0816	0.00635	0.004
12.8-16	0.0218	0.00816	0.00121	0.0166	0.00293	0.000815
$100 < \theta < 160 \text{ mrad}$						
0.8-1.6	0.664	0.0762	0.0141	0.647	0.0313	0.0104
1.6-2.4	0.849	0.098	0.018	0.917	0.0411	0.0148
2.4-3.2	0.957	0.0653	0.0204	1.15	0.0489	0.0186
3.2-4	0.729	0.0979	0.0155	0.735	0.0411	0.0119
4-5.6	0.332	0.0381	0.0101	0.434	0.0205	0.00747
5.6-7.2	0.163	0.0326	0.00496	0.146	0.0117	0.00251
7.2-10.4	0.0462	0.0136	0.00258	0.0347	0.00391	0.0017
$160 < \theta < 280 \text{ mrad}$						
0.8-1.6	1.24	0.109	0.0264	1.33	0.0489	0.0214
1.6-2.4	0.773	0.0871	0.0164	0.919	0.0411	0.0148
$160 < \theta < 240 \text{ mrad}$						
2.4-4	0.223	0.0326	0.00474	0.255	0.0156	0.00411
$160 < \theta < 200 \text{ mrad}$						
4-7.2	0.0354	0.0109	0.00108	0.0279	0.00391	0.000479

Table D.5: Raw yields of positively charged pions in data (left) and simulation (right) for the fifth longitudinal bin along the target and different angular intervals. Quoted yields are normalized to 114885 p.o.t. in data and 639355 p.o.t. in the simulation.

$z = 6$						
Δp [GeV/c]	$dn_{\pi}^{NA61}/dp (\times 10^{-3})$ [/(GeV/c)/p.o.t.]	$\pm \text{stat.}$	$\pm \text{syst.}$	$dn_{\pi}^{FLUKA}/dp (\times 10^{-3})$ [/(GeV/c)/p.o.t.]	$\pm \text{stat.}$	$\pm \text{syst.}$
$0 < \theta < 40 \text{ mrad}$						
0.8-1.6	0.501	0.0762	0.0106	0.485	0.0293	0.00782
1.6-2.4	1	0.109	0.0213	1.11	0.0469	0.0179
2.4-3.2	1.2	0.109	0.0254	1.35	0.0528	0.0218
3.2-4	1.63	0.152	0.0347	1.44	0.0528	0.0233
4-4.8	1.38	0.131	0.042	1.33	0.0528	0.0229
4.8-6.4	1.18	0.0871	0.0357	1.1	0.0333	0.0189
6.4-8	1	0.0817	0.0304	0.773	0.0264	0.0133
8-9.6	0.626	0.0653	0.0349	0.529	0.0235	0.0259
9.6-12.8	0.403	0.0381	0.0225	0.274	0.0132	0.0134
12.8-16	0.15	0.0218	0.00835	0.138	0.0112	0.00678
16-19.2	0.0707	0.0163	0.00395	0.0469	0.00489	0.0023
19.2-22.4	0.0381	0.0136	0.00212	0.00635	0.00147	0.000312
$40 < \theta < 80 \text{ mrad}$						
0.8-1.6	0.544	0.0762	0.0116	0.571	0.0332	0.00921
1.6-2.4	1.07	0.109	0.0227	1.02	0.043	0.0165
2.4-3.2	0.947	0.098	0.0201	0.931	0.043	0.015
3.2-4	0.675	0.0762	0.0143	0.669	0.0352	0.0108
4-5.6	0.544	0.0599	0.0165	0.555	0.0235	0.00955
5.6-7.2	0.354	0.0435	0.0108	0.325	0.0176	0.00558
7.2-10.4	0.201	0.0299	0.0112	0.143	0.0088	0.007
10.4-13.6	0.0571	0.0136	0.00319	0.0494	0.00538	0.00242
13.6-16.8	0.0109	0.00544	0.000607	0.00684	0.00244	0.000336
$80 < \theta < 160 \text{ mrad}$						
0.8-1.6	0.218	0.0544	0.00463	0.203	0.0196	0.00328
1.6-2.4	0.392	0.0653	0.00833	0.444	0.0293	0.00716
$80 < \theta < 140 \text{ mrad}$						
2.4-4	0.544	0.0544	0.0116	0.528	0.0235	0.00851
$80 < \theta < 120 \text{ mrad}$						
4-7.2	0.209	0.0245	0.00637	0.213	0.0108	0.00367

Table D.6: Raw yields of positively charged pions in data (left) and simulation (right) for the sixth longitudinal bin (downstream face of the target) along the target and different angular intervals. Quoted yields are normalized to 114885 p.o.t. in data and 639355 p.o.t. in the simulation.

Appendix E

Efficiencies and corrections

At the current stage of the analysis presented in Chapter 3, only the time-of-flight efficiency is used for the calculation of the NA61 based re-weighting factors for T2K. Other factors are simply listed in the following table for completeness.

$z = 6$	$0 < \theta < 40$ mrad									
Δp [GeV/ c]	ϵ_{TOF}	\pm_{stat} \pm_{syst}	ϵ_{REC}	\pm_{stat} \pm_{syst}	ϵ_{EXT}	\pm_{stat} \pm_{syst}	C_{ACC}	\pm_{stat} \pm_{syst}	C_{LOSS}	\pm_{stat} \pm_{syst}
0.8-1.6	0.986	$^{0.0069}_{0.0037}$								
1.6-2.4	0.956	$^{0.0125}_{0.0170}$								
2.4-3.2	0.943	$^{0.0168}_{0.0074}$								
3.2-4	0.938	$^{0.0181}_{0.0037}$								
4-4.8	0.956	$^{0.0164}_{0.0038}$								
4.8-6.4	0.952	$^{0.0135}_{0.0021}$								
6.4-8	0.957	$^{0.0141}_{0.0073}$								
8-9.6	0.956	$^{0.0164}_{0.0028}$								
9.6-12.8	0.949	$^{0.0144}_{0.0038}$								
12.8-16	0.944	$^{0.0180}_{0.0013}$								
16-19.2	0.989	$^{0.0112}_{0.0042}$								
19.2-22.4	0.924	$^{0.0326}_{0.0332}$								
$40 < \theta < 80$ mrad										
0.8-1.6	0.946	$^{0.0175}_{0.0166}$								
1.6-2.4	0.963	$^{0.0182}_{0.0022}$								
2.4-3.2	0.941	$^{0.0285}_{0.0083}$								
3.2-4	0.898	$^{0.0432}_{0.0316}$								
4-5.6	0.964	$^{0.0205}_{0.0040}$								
5.6-7.2	0.937	$^{0.0307}_{0.0028}$								
7.2-10.4	0.962	$^{0.0187}_{0.0035}$								
10.4-13.6	0.963	$^{0.0257}_{0.0234}$								
13.6-16.8	0.960	$^{0.0392}_{0.0185}$								
$80 < \theta < 160$ mrad										
0.8-1.6	0.959	$^{0.0202}_{0.0067}$								
1.6-2.4	0.951	$^{0.0336}_{0.0103}$								
2.4-4 [†]	0.927	$^{0.0288}_{0.0163}$								
4-7.2 [‡]	0.971	$^{0.0194}_{0.0134}$								

Table E.1: Time-of-flight, reconstruction and extrapolation efficiencies, and acceptance, pion loss and feed-down corrections for the sixth longitudinal bin (downstream face of the target) and angular bins $0 < \theta < 40$ mrad, $40 < \theta < 80$ mrad and $80 < \theta < 160$ mrad. The time-of-flight efficiency is computed from a data set of 114885 p.o.t., while all other efficiencies and corrections are computed for 639355 p.o.t. in the simulation.

[†]: bin stops at 140 mrad, [‡]: bin stops at 120 mrad.

Appendix F

Re-weighting factors

$z = 1$						
Δp [GeV/c]	$(1/\epsilon_{TOF}^{NA61})dn_{\pi}^{NA61}/dp (\times 10^{-3})$ [/(GeV/c)/p.o.t.]	$\pm\text{stat.}$	$\pm\text{syst.}$	$w(p, \theta)$	$\pm\text{stat.}$	$\pm\text{syst.}$
$20 < \theta < 100$ mrad						
0.8-1.6	0.298	0.0662	0.0064	1.0983	0.25915	0.05982
1.6-2.4	0.888	0.1032	0.0246	0.9638	0.12069	0.06045
$40 < \theta < 100$ mrad						
2.4-3.2	1.028	0.1056	0.0233	0.9439	0.10516	0.05822
3.2-4	1.021	0.1178	0.0221	0.8661	0.10523	0.05698
4-4.8	0.808	0.1035	0.0248	0.8365	0.11456	0.05971
4.8-6.4	0.600	0.0578	0.0183	0.8806	0.09192	0.06041
6.4-8	0.313	0.0401	0.0098	0.7320	0.09949	0.05821
8-9.6	0.177	0.0343	0.0099	1.0701	0.22851	0.09523
9.6-12.8	0.083	0.0172	0.0047	1.0795	0.24679	0.09561
12.8-16	0.023	0.0086	0.0013	1.2406	0.55112	0.10574
$100 < \theta < 160$ mrad						
0.8-1.6	0.875	0.0896	0.0228	1.0260	0.11618	0.06072
1.6-2.4	1.220	0.1274	0.0263	0.8716	0.09638	0.05700
2.4-3.2	1.202	0.1211	0.0276	0.8218	0.08795	0.05685
3.2-4	0.910	0.1119	0.0347	0.8868	0.11711	0.06362
4-5.6	0.311	0.0517	0.0096	0.6339	0.10947	0.05662
5.6-7.2	0.140	0.0289	0.0042	0.7199	0.15756	0.05762
7.2-10.4	0.037	0.0114	0.0021	1.2314	0.42318	0.10559
$160 < \theta < 280$ mrad						
0.8-1.6	1.982	0.1278	0.0431	0.8257	0.05824	0.05657
1.6-2.4	1.143	0.1207	0.0271	0.7497	0.08303	0.05624
$160 < \theta < 240$ mrad						
2.4-4	0.446	0.0537	0.0120	1.0741	0.14059	0.06195
$160 < \theta < 200$ mrad						
4-7.2	0.042	0.0145	0.0015	0.7055	0.25302	0.05871

Table F.1: Raw yields of positively charged pions in data (left) corrected for the time-of-flight efficiency, and corresponding re-weighting factors (right) for the first longitudinal bin along the target and different angular intervals. Quoted yields are normalized to 114885 p.o.t. in data and 639355 p.o.t. in the simulation.

$z = 2$						
Δp [GeV/c]	$(1/\epsilon_{TOF}^{NA61})dn_{\pi}^{NA61}/dp (\times 10^{-3})$ [/(GeV/c)/p.o.t.]	$\pm\text{stat.}$	$\pm\text{syst.}$	$w(p, \theta)$	$\pm\text{stat.}$	$\pm\text{syst.}$
$20 < \theta < 100 \text{ mrad}$						
0.8-1.6	0.740	0.0885	0.0160	0.9311	0.11972	0.05769
1.6-2.4	1.831	0.1497	0.0508	0.8615	0.07487	0.05887
$40 < \theta < 100 \text{ mrad}$						
2.4-3.2	2.877	0.2144	0.0652	1.0231	0.08113	0.05924
3.2-4	3.146	0.2064	0.0681	0.9830	0.06996	0.05833
4-4.8	2.840	0.1996	0.0869	0.9829	0.07458	0.06238
4.8-6.4	1.844	0.1172	0.0563	0.9251	0.06221	0.06123
6.4-8	1.097	0.0871	0.0344	0.9977	0.08505	0.06304
8-9.6	0.524	0.0521	0.0293	0.8381	0.09000	0.08120
9.6-12.8	0.252	0.0261	0.0141	0.9808	0.11167	0.08951
12.8-16	0.066	0.0520	0.0037	0.8608	0.68028	0.08239
$100 < \theta < 160 \text{ mrad}$						
0.8-1.6	1.704	0.1249	0.0443	1.0570	0.08644	0.06117
1.6-2.4	2.116	0.1532	0.0455	0.8022	0.06234	0.05626
2.4-3.2	2.191	0.1638	0.0503	0.8042	0.06307	0.05664
3.2-4	1.684	0.1585	0.0642	0.9423	0.09495	0.06496
4-5.6	0.811	0.0759	0.0252	0.8208	0.08201	0.05957
5.6-7.2	0.494	0.0538	0.0148	1.4237	0.17463	0.07162
7.2-10.4	0.076	0.0143	0.0043	0.8982	0.18096	0.08470
$160 < \theta < 280 \text{ mrad}$						
0.8-1.6	2.855	0.1541	0.0620	0.8158	0.04803	0.05645
1.6-2.4	1.721	0.1500	0.0408	0.7651	0.07038	0.05641
$160 < \theta < 240 \text{ mrad}$						
2.4-4	0.605	0.0605	0.0163	1.0155	0.10983	0.06099
$160 < \theta < 200 \text{ mrad}$						
4-7.2	0.078	0.0146	0.0027	1.2805	0.26803	0.07188

Table F.2: Raw yields of positively charged pions in data (left) corrected for the time-of-flight efficiency, and corresponding re-weighting factors (right) for the second longitudinal bin along the target and different angular intervals. Quoted yields are normalized to 114885 p.o.t. in data and 639355 p.o.t. in the simulation.

$z = 3$						
Δp [GeV/c]	$(1/\epsilon_{TOF}^{NA61})dn_{\pi}^{NA61}/dp (\times 10^{-3})$ [/(GeV/c)/p.o.t.]	$\pm\text{stat.}$	$\pm\text{syst.}$	$w(p, \theta)$	$\pm\text{stat.}$	$\pm\text{syst.}$
$20 < \theta < 100 \text{ mrad}$						
0.8-1.6	0.607	0.0773	0.0131	0.9360	0.12848	0.05777
1.6-2.4	2.236	0.1622	0.0622	1.0281	0.08058	0.06157
$40 < \theta < 100 \text{ mrad}$						
2.4-3.2	2.625	0.1901	0.0594	1.0196	0.07950	0.05918
3.2-4	3.105	0.2177	0.0672	1.0266	0.07627	0.05889
4-4.8	2.341	0.1862	0.0719	0.9005	0.07656	0.06087
4.8-6.4	1.792	0.1119	0.0547	0.9990	0.06682	0.06265
6.4-8	1.176	0.0873	0.0369	1.1983	0.09734	0.06737
8-9.6	0.598	0.0635	0.0334	1.1318	0.13112	0.09886
9.6-12.8	0.270	0.0318	0.0151	1.1463	0.14606	0.09984
12.8-16	0.090	0.0174	0.0050	1.2878	0.27291	0.10903
$100 < \theta < 160 \text{ mrad}$						
0.8-1.6	1.361	0.1128	0.0353	1.0673	0.09684	0.06132
1.6-2.4	1.636	0.1408	0.0352	0.8281	0.07599	0.05654
2.4-3.2	1.647	0.1479	0.0378	0.7319	0.06980	0.05587
3.2-4	1.517	0.1442	0.0578	0.9483	0.09659	0.06512
4-5.6	0.720	0.0813	0.0222	0.9287	0.11100	0.06143
5.6-7.2	0.325	0.0413	0.0098	1.1582	0.16411	0.06562
7.2-10.4	0.084	0.0143	0.0048	1.4991	0.29701	0.12358
$160 < \theta < 280 \text{ mrad}$						
0.8-1.6	2.321	0.1505	0.0504	0.8401	0.05833	0.05672
1.6-2.4	1.603	0.1483	0.0380	0.8275	0.08110	0.05712
$160 < \theta < 240 \text{ mrad}$						
2.4-4	0.458	0.0594	0.0123	1.0189	0.14080	0.06100
$160 < \theta < 200 \text{ mrad}$						
4-7.2	0.059	0.0145	0.0020	1.1138	0.29790	0.06761

Table F.3: Raw yields of positively charged pions in data (left) corrected for the time-of-flight efficiency, and corresponding re-weighting factors (right) for the third longitudinal bin along the target and different angular intervals. Quoted yields are normalized to 114885 p.o.t. in data and 639355 p.o.t. in the simulation.

$z = 4$						
Δp [GeV/c]	$(1/\epsilon_{TOF}^{NA61})dn_{\pi}^{NA61}/dp (\times 10^{-3})$ [/(GeV/c)/p.o.t.]	$\pm\text{stat.}$	$\pm\text{syst.}$	$w(p, \theta)$	$\pm\text{stat.}$	$\pm\text{syst.}$
$20 < \theta < 100$ mrad						
0.8-1.6	0.541	0.0773	0.0117	0.9887	0.15205	0.05839
1.6-2.4	1.778	0.1392	0.0493	1.1115	0.09498	0.06303
$40 < \theta < 100$ mrad						
2.4-3.2	1.896	0.1536	0.0429	0.9601	0.08351	0.05841
3.2-4	2.466	0.1695	0.0534	1.1603	0.08634	0.06068
4-4.8	2.001	0.1632	0.0615	1.0532	0.09348	0.06384
4.8-6.4	1.418	0.1050	0.0432	1.1120	0.08818	0.06495
6.4-8	0.693	0.0634	0.0218	0.9981	0.09900	0.06307
8-9.6	0.438	0.0518	0.0245	1.2343	0.15960	0.10540
9.6-12.8	0.149	0.0230	0.0083	1.1102	0.18777	0.09784
12.8-16	0.046	0.0115	0.0026	1.1589	0.32393	0.10055
$100 < \theta < 160$ mrad						
0.8-1.6	1.127	0.1121	0.0293	1.2788	0.14166	0.06504
1.6-2.4	1.288	0.1277	0.0278	1.0100	0.10795	0.05863
2.4-3.2	1.554	0.1469	0.0356	0.9637	0.09723	0.05856
3.2-4	1.357	0.1306	0.0517	1.2011	0.12675	0.07192
4-5.6	0.468	0.0579	0.0145	0.8259	0.10858	0.05965
5.6-7.2	0.262	0.0408	0.0078	1.1725	0.19859	0.06591
7.2-10.4	0.071	0.0143	0.0040	1.3176	0.29649	0.11095
$160 < \theta < 280$ mrad						
0.8-1.6	1.943	0.1484	0.0420	0.9419	0.07616	0.05785
1.6-2.4	0.972	0.1080	0.0230	0.6706	0.07842	0.05540
$160 < \theta < 240$ mrad						
2.4-4	0.299	0.0414	0.0081	0.8555	0.12748	0.05849
$160 < \theta < 200$ mrad						
4-7.2	0.040	0.0116	0.0014	1.1305	0.35853	0.06804

Table F.4: Raw yields of positively charged pions in data (left) corrected for the time-of-flight efficiency, and corresponding re-weighting factors (right) for the fourth longitudinal bin along the target and different angular intervals. Quoted yields are normalized to 114885 p.o.t. in data and 639355 p.o.t. in the simulation.

$z = 5$						
Δp [GeV/c]	$(1/\epsilon_{TOF}^{NA61})dn_{\pi}^{NA61}/dp (\times 10^{-3})$ [/(GeV/c)/p.o.t.]	$\pm\text{stat.}$	$\pm\text{syst.}$	$w(p, \theta)$	$\pm\text{stat.}$	$\pm\text{syst.}$
$20 < \theta < 100 \text{ mrad}$						
0.8-1.6	0.309	0.0552	0.0067	0.9031	0.17448	0.05736
1.6-2.4	1.149	0.1149	0.0319	1.0705	0.11680	0.06227
$40 < \theta < 100 \text{ mrad}$						
2.4-3.2	1.551	0.1300	0.0351	1.0792	0.09933	0.05998
3.2-4	1.719	0.1319	0.0372	1.1961	0.10247	0.06117
4-4.8	1.321	0.1273	0.0405	0.9970	0.10344	0.06267
4.8-6.4	0.840	0.0699	0.0256	1.0184	0.09220	0.06300
6.4-8	0.512	0.0630	0.0160	1.1383	0.15048	0.06601
8-9.6	0.239	0.0344	0.0134	1.1231	0.18112	0.09825
9.6-12.8	0.092	0.0172	0.0051	1.1265	0.22888	0.09844
12.8-16	0.023	0.0086	0.0013	1.3852	0.57462	0.11526
$100 < \theta < 160 \text{ mrad}$						
0.8-1.6	0.702	0.0782	0.0183	1.0835	0.13167	0.06164
1.6-2.4	0.881	0.1039	0.0189	0.9606	0.12116	0.05801
2.4-3.2	1.017	0.0759	0.0234	0.8837	0.07582	0.05760
3.2-4	0.811	0.1105	0.0309	1.1042	0.16250	0.06921
4-5.6	0.344	0.0406	0.0106	0.7938	0.10084	0.05904
5.6-7.2	0.174	0.0347	0.0052	1.1961	0.25712	0.06646
7.2-10.4	0.048	0.0142	0.0027	1.3861	0.43920	0.11573
$160 < \theta < 280 \text{ mrad}$						
0.8-1.6	1.293	0.1134	0.0281	0.9761	0.09284	0.05828
1.6-2.4	0.812	0.0955	0.0192	0.8839	0.11120	0.05782
$160 < \theta < 240 \text{ mrad}$						
2.4-4	0.241	0.0354	0.0065	0.9441	0.15022	0.05982
$160 < \theta < 220 \text{ mrad}$						
4-7.2	0.036	0.0116	0.0013	1.3030	0.45515	0.07255

Table F.5: Raw yields of positively charged pions in data (left) corrected for the time-of-flight efficiency, and corresponding re-weighting factors (right) for the fifth longitudinal bin along the target and different angular intervals. Quoted yields are normalized to 114885 p.o.t. in data and 639355 p.o.t. in the simulation.

$z = 6$							
Δp [GeV/c]	$(1/\epsilon_{TOF}^{NA61})dn_{\pi}^{NA61}/dp (\times 10^{-3})$ [/(GeV/c)/p.o.t.]	$\pm\text{stat.}$	$\pm\text{syst.}$	$w(p, \theta)$	$\pm\text{stat.}$	$\pm\text{syst.}$	
$0 < \theta < 40 \text{ mrad}$							
0.8-1.6	0.507	0.0773	0.0110	1.0456	0.17148	0.05911	
1.6-2.4	1.048	0.1147	0.0290	0.9437	0.11080	0.06012	
2.4-3.2	1.269	0.1177	0.0288	0.9400	0.09462	0.05821	
3.2-4	1.746	0.1661	0.0377	1.2146	0.12387	0.06143	
4-4.8	1.452	0.1396	0.0443	1.0957	0.11405	0.06463	
4.8-6.4	1.234	0.0929	0.0376	1.1218	0.09100	0.06513	
6.4-8	1.045	0.0870	0.0328	1.3487	0.12127	0.07091	
8-9.6	0.654	0.0689	0.0365	1.2368	0.14148	0.10563	
9.6-12.8	0.425	0.0407	0.0237	1.5518	0.16637	0.12658	
12.8-16	0.159	0.0232	0.0088	1.1449	0.19185	0.09960	
16-19.2	0.071	0.0165	0.0040	1.5238	0.38637	0.12470	
19.2-22.4	0.041	0.0148	0.0027	6.5025	2.77215	0.53917	
$40 < \theta < 80 \text{ mrad}$							
0.8-1.6	0.575	0.0778	0.0149	1.0061	0.14828	0.06039	
1.6-2.4	1.107	0.1159	0.0238	1.0829	0.12212	0.05956	
2.4-3.2	1.005	0.1083	0.0231	1.0796	0.12653	0.06016	
3.2-4	0.751	0.0878	0.0287	1.1240	0.14406	0.06977	
4-5.6	0.564	0.0638	0.0175	1.0165	0.12279	0.06325	
5.6-7.2	0.377	0.0473	0.0113	1.1645	0.15894	0.06576	
7.2-10.4	0.209	0.0316	0.0118	1.4650	0.23876	0.12094	
10.4-13.6	0.059	0.0143	0.0036	1.2028	0.31811	0.10780	
13.6-16.8	0.011	0.0057	0.0007	1.6553	1.02721	0.13792	
$80 < \theta < 160 \text{ mrad}$							
0.8-1.6	0.227	0.0553	0.0049	1.1134	0.29172	0.06003	
1.6-2.4	0.411	0.0698	0.0098	0.9269	0.16877	0.05837	
$80 < \theta < 140 \text{ mrad}$							
2.4-4	0.587	0.0604	0.0158	1.1109	0.12454	0.06257	
$80 < \theta < 120 \text{ mrad}$							
4-7.2	0.215	0.0265	0.0075	1.0105	0.13450	0.06513	

Table F.6: Raw yields of positively charged pions in data (left) corrected for the time-of-flight efficiency, and corresponding re-weighting factors (right) for the sixth longitudinal bin along the target and different angular intervals. Quoted yields are normalized to 114885 p.o.t. in data and 639355 p.o.t. in the simulation.

Bibliography

- [1] B. Pontecorvo. Report of the Chalk River Laboratory. *Report P.D.-141*, 1945.
- [2] F. Reines and C. L. Cowan. Detection of the free neutrino. *Phys. Rev.*, 92(3):830–831, Nov 1953.
- [3] M. Goldhaber, L. Grodzins, and A. W. Sunyar. Helicity of neutrinos. *Phys. Rev.*, 109(3):1015–1017, Feb 1958.
- [4] G. Danby et al. Remarks Concerning the Recent High-Energy Neutrino Experiment. *Phys. Rev. Lett.*, 10:260–262, 1963.
- [5] M. L. et al. Perl. Evidence for anomalous lepton production in $e^+ - e^-$ annihilation. *Phys. Rev. Lett.*, 35(22):1489–1492, Dec 1975.
- [6] Precision electroweak measurements on the Z resonance. *Phys. Rept.*, 427:257–454, 2006.
- [7] V. Lyubushkin. PhD thesis. JINR, Dubna. 2009.
- [8] V. Lyubushkin et al. [NOMAD Collaboration]. A Study of Quasi-Elastic Muon (Anti)Neutrino Scattering in the NOMAD Experiment. *Eur. Phys. J.*, C63:355, 2009.
- [9] B. Pontecorvo. Mesonium and antimesonium. *Sov. Phys. JETP*, 6:429, 1957.
- [10] L. Bonolis. Bruno Pontecorvo: From slow neutrons to oscillating neutrinos. *Am. J. Phys.*, 73:487–499, 2005.
- [11] S. Hatakeyama et al. Measurement of the flux and zenith-angle distribution of upward through-going muons in Kamiokande II+III. *Phys. Rev. Lett.*, 81:2016–2019, 1998.
- [12] V. N. Gavrin et al. SAGE: The Soviet-American GALLIUM solar neutrino experiment. *Nucl. Phys. Proc. Suppl.*, 28A:75–81, 1992.
- [13] P. Anselmann et al. GALLEX solar neutrino observations: Complete results for GALLEX II. *Phys. Lett.*, B357:237–247, 1995.

- [14] Y. Fukuda et al. Evidence for oscillation of atmospheric neutrinos. *Phys. Rev. Lett.*, 81:1562–1567, 1998.
- [15] S. Abe et al. *arXiv:0801.4589*.
- [16] K. Nakamura et al. Neutrino mass, mixing and oscillations. *JPG*, 37:075021, 2010.
- [17] B. Aharmim et al. Electron energy spectra, fluxes, and day-night asymmetries of B-8 solar neutrinos from the 391-day salt phase SNO data set. *Phys. Rev.*, C72:055502, 2005.
- [18] J. N. Bahcall, S. Basu, and A. M. Serenelli. . *Astrophys. J.*, 165:400, 2006.
- [19] E. Kh. Akhmedov. Do charged leptons oscillate? *JHEP*, 09:116, 2007.
- [20] E. Kh. Akhmedov and J. Kopp. Neutrino oscillations: quantum mechanics vs. quantum field theory. *JHEP*, 04:008, 2010.
- [21] J.-M. Levy. On ultra-relativistic approximations, unobservable phases and other hand-waving in the derivation of the neutrino oscillation length. *arXiv:0901.0408*, 2009.
- [22] H. J. Lipkin. Quantum theory of neutrino oscillations for pedestrians: Simple answers to confusing questions. *Phys. Lett.*, B642:366–371, 2006.
- [23] B. Kayser. Neutrino Mass, Mixing, and Flavor Change. *arXiv:0804.1497*, 2008.
- [24] A. de Gouvêa. Tasi lectures on neutrino physics. *arXiv:0411274v1*, 2004.
- [25] Stephen J. Parke. Neutrino oscillation phenomenology. FERMILAB-PUB-07-767-T.
- [26] A. Yu. Smirnov. The MSW effect and solar neutrinos. *arXiv:0305106*, 2003.
- [27] Arpesella C. et al. The Borexino Collaboration. *Phys. Lett.*, B658:101, 2008.
- [28] Hiroshi Nunokawa, Stephen J. Parke, and Renata Zukanovich Funchal. What fraction of boron-8 solar neutrinos arrive at the earth as a $\nu(2)$ mass eigenstate? *Phys. Rev.*, D74:013006, 2006.
- [29] T. Araki et al. Measurement of neutrino oscillation with KamLAND: Evidence of spectral distortion. *Phys. Rev. Lett.*, 94:081801, 2005.
- [30] Ahn M. et al. The K2K Collaboration. *Phys. Rev.*, D74:072003, 2006.
- [31] Michael D. et al. The MINOS Collaboration. *Phys. Rev. Lett.*, 97:191801, 2006.

- [32] P. Adamson et al. Measurement of the neutrino mass splitting and flavor mixing by minos. *Phys. Rev. Lett.*, 106(18):181801, May 2011.
- [33] M. De Serio. Tau neutrino appearance in the CNGS muon neutrino beam: The OPERA experiment. *Nucl. Phys. Proc. Suppl.*, 169:321–325, 2007.
- [34] Aguilar A. et al. The LSND Collaboration. *Phys. Rev.*, D64:112007, 2001.
- [35] Armbruster B. et al. The KARMEN Collaboration. *Phys. Rev.*, D65:112001, 2002.
- [36] Aguilar-Arevalo A. et al. The MiniBooNE Collaboration. *Phys. Rev. Lett.*, 98:231801, 2007.
- [37] G. Mention et al. The Reactor Antineutrino Anomaly. *Phys. Rev.*, D83:073006, 2011.
- [38] A. de Gouvêa, B. Kayser, and R. N. Mohapatra. Manifest cp violation from majorana phases. *Phys. Rev. D*, 67(5):053004, Mar 2003.
- [39] Olga Mena, Hiroshi Nunokawa, and Stephen J. Parke. NOvA and T2K: The race for the neutrino mass hierarchy. *Phys. Rev.*, D75:033002, 2007.
- [40] M. Apollonio et al. Search for neutrino oscillations on a long base-line at the CHOOZ nuclear power station. *Eur. Phys. J.*, C27:331–374, 2003.
- [41] F. Boehm et al. Search for Neutrino Oscillations at the Palo Verde Nuclear Reactors. *Phys. Rev. Lett.*, 84:3764–3767, 2000.
- [42] T. Akiri. The Double Chooz experiment. *Nucl. Phys. Proc. Suppl.*, 215:69–71, 2011.
- [43] J. K. Ahn et al. RENO: An Experiment for Neutrino Oscillation Parameter θ_{13} Using Reactor Neutrinos at Yonggwang. 2010.
- [44] J.P. Ochoa-Ricoux. The Daya Bay neutrino oscillation experiment. *Nucl. Phys. Proc. Suppl.*, 217:140–142, 2011.
- [45] K. Abe et al. The T2K Experiment. 2011.
- [46] Ayres D. S. et al. The NOvA Collaboration. *arXiv:hep-ex/0503053*.
- [47] Y. Itow and *al.* The JHF-Kamiokande neutrino project. 2001.
- [48] Magali Besnier. The contribution of near detectors to the T2K neutrino measurements. *J. Phys. Conf. Ser.*, 203:012105, 2010.
- [49] T. Kobayashi. Status of T2K experiment. *Proceedings Neutrino2010 Conference*.

- [50] J.-M. Levy. Kinematics of an off-axis neutrino beam. *arXiv:1005.0574v1*, 2010.
- [51] Y. Fukuda et al. The Super-Kamiokande detector. *Nucl. Instrum. Meth.*, A501:418–462, 2003.
- [52] Y. Ashie et al. A Measurement of Atmospheric Neutrino Oscillation Parameters by Super-Kamiokande I. *Phys. Rev.*, D71:112005, 2005.
- [53] <http://jnusrv01.kek.jp/kensh/t2k-na49>.
- [54] K. et al. [T2K Collaboration] Abe. Indication of Electron Neutrino Appearance from an Accelerator-produced Off-axis Muon Neutrino Beam. 2011.
- [55] C. Giganti. Contribution to the eps-hp 2011, grenoble, france.
- [56] R. Brun, F. Bruyant, M. Maire, A. C. McPherson, and P. Zancarini. GEANT3. CERN-DD-EE-84-1.
- [57] <http://www.staff.uni-mainz.de/zeitnitz/Gcalor/gcalor.html>.
- [58] R. Brun. PAW — Physics Analysis Workstation, <http://paw.web.cern.ch/paw>.
- [59] Sacha E. Kopp. Accelerator neutrino beams. *Phys. Rept.*, 439:101–159, 2007.
- [60] J. Smith and R. Vogt. Charm and bottom quark production cross sections near threshold. *Z. Phys.*, C75:271–276, 1997.
- [61] S. Frixione. Charm and bottom production at fixed target experiments. *Frascati Phys. Ser.*, 7:3–21, 1997.
- [62] C. Lourenco and H. K. Wohri. Heavy flavour hadro-production from fixed-target to collider energies. *Phys. Rept.*, 433:127–180, 2006.
- [63] K. Nakamura and others [Particle Data Group]. *J. Phys.*, G37:075021, 2010.
- [64] N. Abgrall et al. Neutrino flux prediction, t2k technical note 038.
- [65] <http://root.cern.ch/drupal/content/vmc>.
- [66] N. Abgrall, J. M. Levy, and B. Popov. Predictions of neutrino fluxes for T2K: NA61 analysis and data taking strategy. *NA61/T2K Internal Note 001*.
- [67] P. Astier et al. Prediction of neutrino fluxes in the NOMAD experiment. *Nucl. Instrum. Meth.*, A515:800–828, 2003.

- [68] G. Ambrosini et al. Measurement of charged particle production from 450-GeV/c protons on beryllium. *Eur. Phys. J.*, C10:605–627, 1999.
- [69] E. Aliu et al. Evidence for muon neutrino oscillation in an accelerator- based experiment. *Phys. Rev. Lett.*, 94:081802, 2005.
- [70] M. G. Catanesi et al. Measurement of the production cross-section of positive pions in p Al collisions at 12.9-GeV/c. *Nucl. Phys.*, B732:1–45, 2006.
- [71] S. Agostinelli et al. G4—a simulation toolkit. *Nuclear Instruments and Methods in Physics Research Section A: Accelerators, Spectrometers, Detectors and Associated Equipment*, 506(3):250 – 303, 2003.
- [72] A. A. Aguilar-Arevalo et al. The Neutrino Flux prediction at MiniBooNE. *Phys. Rev.*, D79:072002, 2009.
- [73] M. G. Catanesi *et al.* Measurement of the production cross-section of positive pions in the collision of 8.9 GeV/c protons on beryllium. *Eur. Phys. J. C*, 29:52, 2007.
- [74] M. Bonesini, A. Marchionni, F. Pietropaolo, and T. Tabarelli de Fatis. On particle production for high energy neutrino beams. *Eur. Phys. J.*, C20:13–27, 2001.
- [75] <http://jnusrv01.kek.jp/Indico/>.
- [76] V. Galymov et al. Neutrino flux uncertainty for 10a data analysis, t2k technical note 039.
- [77] M. Apollonio et al. Comparison of large-angle production of charged pions with incident protons on cylindrical long and short targets. *Phys.Rev.*, C80:065204, 2009.
- [78] N. Antoniou and *al.* [NA49-future Collaboration]. *CERN-SPSC-2006-034*, 2006.
- [79] N. Antoniou and *al.* [NA61/SHINE Collaboration]. *CERN-SPSC-2007-019*, 2007.
- [80] N. Antoniou and *al.* [NA61/SHINE Collaboration]. *CERN-SPSC-2007-004*, 2007.
- [81] N. Abgrall and *al.* [NA61/SHINE Collaboration]. *CERN-SPSC-2008-018*, 2007.
- [82] N Abgrall et al. Measurements of Cross Sections and Charged Pion Spectra in Proton-Carbon Interactions at 31 GeV/c. *Phys. Rev. C.*, 84:034604, 2011.

- [83] S. Afanasiev and *al.* [NA49 Collaboration]. *Nucl. Instrum. Meth. A*, 430, 1999.
- [84] K. Matsuoka, contributions to the T2K beam MC group meetings, 2009-2010.
- [85] K. Werner. *Nucl. Phys. A*, 525, 1991.
- [86] M. Posiadala. PhD thesis in preparation. University of Warsaw, Warsaw. 2011.
- [87] S. Murphy. PhD thesis in preparation. University of Geneva, Geneva. 2011.
- [88] T. Palczewski. PhD thesis in preparation. University of Warsaw, Warsaw. 2011.
- [89] Yoshiaki Teramoto. Explicit calculation of track extrapolation error. *Nuclear Instruments and Methods in Physics Research*, 449:344 – 355, 1999.
- [90] Steve Baker and Robert D. Cousins. Clarification of the use of chi-square and likelihood functions in fits to histograms. *Nuclear Instruments and Methods in Physics Research*, 221(2):437 – 442, 1984.
- [91] Nelson H. Goodness of fit for poisson distributed data.
- [92] Heinrich J. G. The log-likelihood ratio of the poisson distribution for small μ .
- [93] James F. Minuit, function minimization and error analysis. CERN Long Writup D506.
- [94] A. Haesler, contributions to the NA61/T2K analysis meetings, 2011.
- [95] T. Eichten et al. Particle production in proton interactions in nuclei at 24-GeV/c. *Nucl. Phys.*, B44:333–343, 1972.
- [96] J. V. Allaby et al. Total and absorption cross-sections of pi-, k- and anti-p in the momentum range 20-65 gev/c. *Yad. Fiz.*, 12:538–557, 1970.
- [97] N. Abgrall et al. Beam update for 2010a nue analysis using run i+ii data.
- [98] N. Abgrall. Contribution to the t2k beam workshop, august 2011, tokai, japan.
- [99] Y. Hayato. NEUT. *Nucl. Phys. Proc. Suppl.*, 112:171–176, 2002.
- [100] Alexis A. Aguilar-Arevalo et al. Measurement of ν_μ and $\bar{\nu}_\mu$ induced neutral current single π^0 production cross sections on mineral oil at $E_\nu \sim O(1\text{GeV})$. *Phys. Rev.*, D81:013005, 2010.

- [101] N. Abgrall et al. Characterization of a high resolution triple Gas Electron Multiplier (GEM) detector. *Nucl. Phys. Proc. Suppl.*, 172:234–236, 2007.
- [102] N. Abgrall et al. Time Projection Chambers for the T2K Near Detectors. *Nucl. Instrum. Meth.*, A637:25–46, 2011.
- [103] J. Bouchez et al. Bulk micromegas detectors for large TPC applications. *Nucl. Instrum. Meth.*, A574:425–432, 2007.
- [104] F. Reines, C. L. Cowan, F. B. Harrison, H. W. Kruse, and A. D. McGuire. Detection of the free neutrino: A confirmation. *Science*, 124(3212):103–104, Jul 1956.
- [105] J. Rich. Quantum mechanics of neutrino oscillations. *Phys. Rev. D*, 48(9):4318–4325, Nov 1993.
- [106] S. Raby. The oscillating neutrino. *Los Alamos Science*, (25), 1997.
- [107] A. Rubbia. Introduction to neutrino physics. *Cours du 3eme cycle de la Suisse romande*, Summer 2006.
- [108] T. Layda. New results from the CHARM-II experiment. In *Les Arcs 1991, Proceedings, Electroweak interactions and unified theories* 79-86.
- [109] A. Ichikawa. Status of the T2K long baseline neutrino oscillation experiment. *Proceedings TAUP09 Conference*.